

MOLECULAR CLOUDS AND STAR FORMATION IN THE INNER GALAXY

Andrew John Rigby

A thesis submitted in partial fulfilment of the
requirements of Liverpool John Moores University
for the degree of Doctor of Philosophy

May 2016

For John, Stella, Dennis and Margaret,
who are such excellent and admirable people,
and a constant source of inspiration.

Declaration

The work presented in this thesis was carried out at the Astrophysics Research Institute, Liverpool John Moores University. Unless otherwise stated, it is the original work of the author. While registered as a candidate for the degree of Doctor of Philosophy, for which submission is now made, the author has not been registered as a candidate for any other award. This thesis has not been submitted in whole, or in part, for any other degree.

Andrew John Rigby
Astrophysics Research Institute
Liverpool John Moores University
IC2 Liverpool Science Park
146 Brownlow Hill
Liverpool
L3 5RF
UK

ANDREW JOHN RIGBY

MAY 2016

Abstract

A detailed understanding of the process of star formation is crucial for modern astrophysics. Stars form from the gravitational collapse of molecular gas clouds; it is the process by which cold molecular gas is transformed into the stars and planets that make up the many billions of galaxies in the observable Universe. However, there are a number of open questions that have yet to be answered and a comprehensive theory that explains and predicts how, where and why stars and their clusters form proves elusive.

One such open question is how does the environment, on both local scales and galactic scales, influence star formation? The enormous radiative and mechanical outputs of high-mass stars ($M \gtrsim 8 M_{\odot}$) are known to have a strong impact on their surroundings and are able to erode their natal molecular clouds via their stellar winds, ionizing radiation and supernovae. It has been proposed that the shock fronts at the edges of expanding HII regions might trigger subsequent generations of star formation (e.g. Elmegreen & Lada, 1977; Bertoldi, 1989), and there are observational studies to support this (e.g. Thompson et al., 2012). It has also been proposed that large-scale effects such as the spiral structure of galaxies like the Milky Way might trigger the formation of stars in otherwise quiescent gas (e.g. Dobbs et al., 2008), though observations within the Galaxy appear to suggest that spiral arms are playing only a minor role, if any, in the triggering of

star formation (e.g. Moore et al., 2012; Eden et al., 2015).

To answer this question, and others concerning star formation, large samples of imminently and currently star-forming regions are required, and surveys of the plane of the Milky Way in various tracers are providing the data to acquire these. Molecular clouds are the initial conditions for star formation, and a complete theory of star formation must necessarily involve a detailed understanding of molecular clouds. In this thesis a survey of molecular gas in the Inner Galaxy known as CHIMPS is presented; these data provide measurements of denser and more optically thin molecular gas at a higher angular resolution than preceding surveys and over a significant area of the first quadrant of the Galactic plane. The combination of CHIMPS data with data from other surveys, such as Hi-GAL, allows the star-forming content of clumps of dense molecular gas to be studied.

The clumps of molecular emission identified within CHIMPS appear to be highly turbulent in nature, and are over-pressurized with respect to the encompassing neutral gas. This would appear to suggest that they are transient features in a highly dynamic interstellar medium. The efficiency of star formation within the CHIMPS clumps is not found to vary significantly on kiloparsec scales between the spiral arms and their inter-arm regions, with the exception of the Scutum-Centaurus arm, within which the current level of star formation per unit gas mass appears to be somewhat suppressed. On a clump-to-clump basis, the distribution of star formation efficiency is log-normal, indicating that the efficiency is determined by many random processes, with no single dominant agent.

The conclusion is that it is turbulence that controls the star formation efficiency, which is powered on a wide range of scales from the feedback of high-mass stars to the shear induced by the rotation of the entire Galaxy.

Publications

Much of the work presented in Chapter 2 has been published in the journal *Monthly Notices of the Royal Astronomical Society*.

Rigby, A. J., Moore, T. J. T., Plume, R., et al. 2016, ‘CHIMPS: the $^{13}\text{CO}/\text{C}^{18}\text{O}$ ($J = 3 \rightarrow 2$) Heterodyne Inner Milky Way Plane Survey’, MNRAS, 456, 2885

Acknowledgements

First of all, I would like to thank my supervisor Toby Moore for all of his efforts and his patience throughout my studentship. His calm demeanour has been immeasurably helpful during the stressful times, and he has been a pleasure to work with. I would also like to thank my collaborators David Eden, James Urquhart, Mark Thompson and René Plume who are a fantastically amiable and bright bunch. Malcolm Curry and David Berry also deserve a special mention for their tireless support with JCMT data reduction and Starlink applications that solved countless headaches.

I must thank my wonderful girlfriend Rachel Piggott for her unceasing support over throughout my undergraduate and postgraduate years, and I also extend sincere thanks to Rachel's parents John and Lorna, who put me up and provided proper dinners during the last few months, which eased the write-up considerably. My parents deserve enormous thanks for providing incredible support, and for giving me the freedom to fully explore my interests, and I owe my brother Chris a great debt of gratitude for everything he's done for me over the years. I have had an excellent group of fellow students at the ARI, and I must thank Richard Williams, Helen Jermak and Caroline Caldwell in particular for being such affable colleagues.

I am grateful to all of the teachers, lecturers and mentors I have had at all

levels of education, and who have all played a part in getting me to this point. I have been encouraged and inspired a great deal by a handful of individuals in particular, so I extend heartfelt thanks my primary school teacher John Shepley, my sixth form maths teacher Gary Baum and, at university, Professors Phil James and Carole Mundell.

Finally, I am grateful to the Science and Technology Facilities Council for funding my PhD, and for the support of the Royal Astronomical Society for overseas travel.

ANDREW JOHN RIGBY

MAY 2016

“If you wish to make an apple pie from scratch,
you must first invent the Universe.”

– *Carl Sagan*

Contents

Declaration	iii
Abstract	iv
Publications	vi
Acknowledgements	vii
Contents	x
List of Tables	xiv
List of Figures	xv
Glossary	xix
1 Introduction	1
1.1 Molecular clouds	2
1.1.1 Basic physical properties	2
1.1.2 Formation	5
1.1.3 Observations of molecular gas	6
1.1.4 Observations of the dust continuum	11
1.1.5 Scaling relations and the origin of substructure	12
1.2 High-mass star formation	18

1.3	Spontaneous and triggered star formation	22
1.4	The effects of large-scale Galactic structure on star formation . . .	26
1.4.1	The structure of the Galaxy	26
1.4.2	Impact on star formation	28
1.5	Surveys of the Galactic plane	30
1.6	Thesis outline	36
2	CHIMPS	38
2.1	38
2.1.1	Observations	38
2.1.2	Data reduction	41
2.2	The data	43
2.2.1	Overview	43
2.2.2	Extracting the emission	47
2.2.3	Integrated position–position maps	50
2.2.4	Integrated position–velocity maps	54
2.3	Data access	56
2.4	Comparison with GRS and COHRS	57
2.5	Example CHIMPS data	62
3	A voxel-by-voxel determination of the column density of molec-	
	ular gas in CHIMPS	68
3.1	Optical depth	71
3.2	Excitation temperature	79
3.3	Column density	84
3.4	Uncertainties	86
3.4.1	Random uncertainties	86

3.4.2	Systematic uncertainties	90
3.4.3	Total uncertainties	92
3.5	Discussion	93
4	Physical properties of the CHIMPS clumps	98
4.1	The CHIMPS source catalogue	99
4.2	Kinematic distances	102
4.3	Resolving the kinematic distance ambiguity	105
4.3.1	Sources with simple KDA solutions	107
4.3.2	Association with ATLASGAL sources	108
4.3.3	Association with RMS sources	110
4.3.4	Association with BGPS sources	110
4.3.5	Association with GRS sources	112
4.3.6	Association with CHIMPS sources	113
4.3.7	Summary of distance assignments	114
4.4	The uncertainties on kinematic distances	117
4.5	Basic physical properties	123
4.6	Dynamic state	132
5	Studies of the star formation efficiency	138
5.1	Hi-GAL & CHIMPS associations	140
5.2	The cloud-to-cloud star formation efficiency	146
5.2.1	Determination of L/M	146
5.2.2	L/M in the spiral arms	149
5.2.3	L/M as a function of Galactocentric distance	156
6	Discussion and conclusions	160
6.1	CHIMPS	160

6.2	Galactic structure in CHIMPS	161
6.3	The nature of CHIMPS clumps	163
6.3.1	Size and density	163
6.3.2	Timescales	165
6.3.3	Pressure	166
6.3.4	Virial state	169
6.4	Variations in star formation efficiency	170
6.4.1	Variations between spiral arms	170
6.4.2	Variations as a function of Galactocentric radius	172
6.5	The lognormality of L/M	175
7	Future Work	178
7.1	Testing spiral arm models	178
7.2	Extracting the filamentary content of CHIMPS	179
7.3	Identifying complexes of emission	181
7.4	Spatial frequency analysis	184
A	Parameters used in the CHIMPS data reduction	186
A.1	ORAC-DR parameters	186
A.2	FellWalker parameters	187
B	Radiative transfer analysis	189
C	Hi-GAL 70 μm velocity assignments	196
	Bibliography	217

List of Tables

1.1	Physical properties of molecular clouds, clumps and cores	5
1.2	Properties of commonly observed CO rotational emission lines . . .	10
1.3	CO and dust surveys of the northern Inner Galactic plane	34
3.1	Summary of the input data for the column density calculation . . .	71
4.1	Summary of the KDA resolutions	117
4.2	A comparison of the kinematic and parallax distances of four CHIMPS sources	122
5.1	Spiral arm and inter-arm assignments of the CHIMPS clumps . . .	151
5.2	Summary of the $\log_{10}(L_{70}/M_{13\text{CO}})$ distributions of CHIMPS clumps in spiral arm and inter-arm regions	155
5.3	Mean $\log_{10}(L_{70}/M_{13\text{CO}})$ in Galactocentric distance bins	158

List of Figures

1.1	A <i>Hubble</i> image of Bok globules in NGC 281	3
1.2	A <i>Spitzer</i> view of the infrared dark cloud G011.11-0.12	17
1.3	An artist’s impression of the Milky Way	27
2.1	Histograms of the voxel values in CHIMPS	44
2.2	Histograms of the noise (rms) of the CHIMPS spectra	46
2.3	Noise (rms) maps for the CHIMPS data	46
2.5	Map of the CHIMPS ^{13}CO (3–2) emission integrated over velocity	51
2.6	Map of the CHIMPS C^{18}O (3–2) emission integrated over velocity	52
2.7	Emission in CHIMPS ^{13}CO (3–2), integrated over 6 velocity ranges	53
2.8	Position–velocity diagrams for the CHIMPS data, integrated over latitude	55
2.9	One-dimensional profiles of the CHIMPS data	59
2.10	Examination of the G34 region in CHIMPS and other data	63
2.11	Close-ups of W43, the filament at $l = 37.4^\circ$ and W49A in the CHIMPS data	67
3.1	The behavior of optical depth as a function of the ^{13}CO (3–2) to C^{18}O (3–2) brightness temperature ratio	74
3.2	A comparison of the 3σ and 5σ threshold in the C^{18}O (3–2) cubes	75

3.3	An example of the ^{13}CO optical depth calculated from CHIMPS ^{13}CO (3–2) and COHRS ^{12}CO (3–2)	77
3.4	Histogram of the τ (^{13}CO) values calculated from ^{13}CO (3–2) and ^{12}CO (3–2)	78
3.5	The relationship between the ratio of brightness temperatures of ^{13}CO (3–2) and ^{13}CO (1–0), and the and excitation temperatures	82
3.6	An example of the excitation temperature calculated from CHIMPS ^{13}CO (3–2) and GRS ^{13}CO (1–0)	83
3.7	The relationship between column density, excitation temperature and optical depth	84
3.8	An example of the column density calculated from CHIMPS ^{13}CO (3–2) and GRS ^{13}CO (1–0)	85
3.9	The distributions of uncertainties in the excitation temperatures and column densities induced by the use of a lower angular reso- lution excitation temperature map in the LTE analysis	89
3.10	Histograms of the systematic fractional errors on voxels of optical depth, excitation temperature and column density	91
3.11	Histogram of the total fractional errors on the integrated column densities of CHIMPS clouds	93
3.12	Excitation temperature map for CHIMPS	96
3.13	Integrated column density map for CHIMPS	97
4.1	The geometry of the kinematic distance ambiguity	104
4.2	Distance distributions of the CHIMPS clumps	115
4.3	A top-down view of the distribution of resolved CHIMPS sources in the Galaxy	116
4.4	The dispersion of clump v_{LSR} compared to the tangential velocity	118

4.5	Errors on derived kinematic distances	119
4.6	A comparison of the masses derived for clumps in CHIMPS and of the masses of their ATLASGAL counterparts	125
4.7	A comparison of the mass–radius relationships of the CHIMPS clumps and GRS clouds	126
4.8	Distributions of the mass, radius and density of the CHIMPS clumps	128
4.9	CHIMPS completeness tests	130
4.10	The completeness limit of CHIMPS clumps as a function of helio- centric distance	130
4.11	Distributions of the virial parameter, excitation temperature and turbulent pressure	134
4.12	Velocity dispersion, density and turbulent pressure as a function of clump size	137
5.1	Example CHIMPS spectra for Hi-GAL 70 μm sources	143
5.2	Position–velocity diagram for the 70 μm sources	144
5.3	Position–velocity diagram of the 70 μm sources with a CHIMPS association	145
5.4	Example fields showing the CHIMPS and 70 μm associations . . .	146
5.5	The multiplicity of 70 μm Hi-GAL sources with a CHIMPS clump association.	147
5.6	The distributions of $\log_{10}(L_{70}/M_{13\text{CO}})$ for all CHIMPS clumps and complete between 2 and 12 kpc.	149
5.7	The spiral arm assignments of CHIMPS clumps	150
5.8	Distributions of $\log_{10}(L_{70}/M_{13\text{CO}})$ within the spiral arms	152
5.9	A top-down view of the spiral arm assignments of CHIMPS clumps	153
5.10	$L_{70}/M_{13\text{CO}}$ as a function of Galactocentric distance	157

6.1	CHIMPS position–velocity diagram, overlaid with two spiral arm models, and the giant molecular filaments of Ragan et al. (2014) .	163
6.2	The density distributions of GRS clouds, and ATLASGAL and CHIMPS clumps	165
6.3	The dynamical timescales of CHIMPS clumps and GRS clouds . .	165
6.4	Turbulent and thermal pressure of CHIMPS clumps as a function of Galactocentric distance	167
6.5	The relationship between $L_{70}/M_{13\text{CO}}$ and P_{turb}	174
7.1	The <i>Spitzer</i> view of IC342	180
7.2	Longitudinal profile of $L_{70}/M_{13\text{CO}}$ in the CHIMPS survey	185

Glossary

Term	Definition
ALMA	The Atacama Large Millimeter Array
APEX	The Atacama Pathfinder Experiment
ATLASGAL	The Apex Telescope Large Area Survey of the Galaxy (Schuller et al., 2009)
BeSSeL	The Bar and Spiral Structure Legacy Survey (Brunthaler et al., 2011)
BGPS	The Bolocam Galactic Plane Survey (Aguirre et al., 2011)
CHIMPS	The CO Heterodyne Inner Milky Way Plane Survey (Rigby et al., 2016)
COHRS	The CO High Resolution Survey (Dempsey, Thomas & Currie, 2013)
CORNISH	The Coordinated Radio and Infrared Survey for High-Mass Star Formation (Hoare et al., 2012)
FWHM	Full-width at half-maximum
GMC	Giant molecular cloud
GRS	The Galactic Ring Survey (Jackson et al., 2006)
HARP	The Heterodyne Array Receiver Programme (Buckle et al., 2009)
HiCA	HI continuum absorption
HiSA	HI self-absorption
HMSF	High-mass star formation
IRDC	Infrared dark cloud
ISM	Interstellar medium
JCMT	The James Clerk Maxwell Telescope
JPS	The JCMT Plane Survey (Moore et al., 2015)
KDA	Kinematic distance ambiguity
LTE	Local thermodynamic equilibrium
PDF	Probability distribution function
RMS	The Red MSX Source survey (Lumsden et al., 2013)
rms	root-mean-square
SFE	Star formation efficiency
VGPS	The VLA Galactic Plane Survey (Stil et al., 2006)
YSO	Young stellar object

Chapter 1

Introduction

The conversion of gas into stars is one of the most fundamental processes required to build an observable universe such as our own. Without stars, we would not have galaxies or planets or black holes. Stellar feedback plays a critical role in shaping the galaxies we see around us, particularly through the stellar winds and ionising radiation of high-mass stars, and disperses the heavy elements through supernovae. If we wish to acquire a detailed understanding of galaxies, planets, and black holes, then we must also have a detailed understanding of star formation.

At the most basic level, the recipe for star formation is relatively simple; if the initial conditions of a cloud of molecular gas and dust cause it to collapse under its own gravity, then it will continue to contract and heat up until the nuclear fusion of hydrogen may begin, and a hydrostatic equilibrium is achieved. However, a comprehensive and vital understanding of the precise physics of this process for both individual stars, and a galactic ensemble remains elusive.

As new stars are formed, they immediately begin to impact their surroundings via their radiation and, in the case of short-lived high-mass stars (with masses in

excess of $\sim 8 M_{\odot}$), the supernovae that mark the end of their lives. Accordingly, it is not sufficient to understand the formation of individual stars, since the formation of one star may influence the process for a neighbouring collapsing cloud. The impact of recent and incipient star formation on the surrounding material is highly complex, and a number of significant open questions remain. How do high-mass stars form, and what role does their feedback play in the formation of neighbouring stars? What is the origin of the apparent universality of the initial mass function? Molecular clouds are the initial conditions for star formation, and so any understanding of star formation must necessarily also explain the origin of molecular clouds, so how do they form? How does spiral structure affect star formation? What controls the star formation rate and efficiency? This thesis seeks to address the last three of these questions.

1.1 Molecular clouds

1.1.1 Basic physical properties

Molecular clouds are the birthplaces of stars, and make up the very coldest and densest regions of the interstellar medium (ISM). They exist in various forms and sizes, ranging from the Bok globules (see Figure 1.1) preferentially found nearby which have masses of $\sim 10 M_{\odot}$ contained within ~ 0.5 pc (e.g. Clemens & Barvainis, 1988; Clemens, Yun & Heyer, 1991), to giant molecular clouds (GMCs) which contain a total mass of $\sim 10^6 M_{\odot}$ and covering ~ 100 pc (e.g. Roman-Duval et al., 2010). Molecular clouds are generally found to have velocity dispersions an order of magnitude larger than expected from their thermal properties alone (e.g. Larson, 1981; Rathborne et al., 2009), and this is generally interpreted as evidence of turbulence.



Figure 1.1: A *Hubble* image of Bok globules, seen in absorption against emission from the star-forming region NGC 281. This is a four-colour composite image made using ACS images in the B , V , $H\alpha$ and R filters. Image credit: NASA, ESA, and The Hubble Heritage Team (STScI/AURA). Acknowledgment: P. McCullough (STScI)

Molecular clouds contain a range of substructures within them, characterised observationally by their sizes and densities as ‘clumps’ and ‘cores’. In general, clumps are referred to as objects which appear to be the precursors of star clusters, and cores are suspected to be the immediate precursors of individual or multiple star systems. These scenarios are difficult to distinguish observationally, and the structures visible within such observations are largely determined by the spatial resolution of the instrument in use. The approximate physical properties of molecular clouds, clumps and cores are summarised in Table 1.1.

The structure of molecular clouds may be described as hierarchical (e.g. Blitz & Stark, 1986; Rosolowsky et al., 2008), with the densest observable features

lying within an envelope of lower density gas, and also as fractal or multi-fractal (e.g. Falgarone, Phillips & Walker, 1991; Stutzki et al., 1998; Combes, 2000); the morphology of molecular clouds is found to be self-similar when a small region of one observation is studied at higher angular resolution. This kind of internal structure of molecular clouds is thought to arise as a consequence of turbulent motions of the constituent gas, driven on a range of scales from stellar feedback to galactic shear (e.g. Elmegreen & Scalo, 2004; Scalo & Elmegreen, 2004).

In recent years, the *Herschel* infrared Galactic Plane Survey (Hi-GAL; Molinari et al., 2010b) and the *Herschel* Gould Belt Survey (André et al., 2010), carried out with the *Herschel* Space Observatory (Pilbratt et al., 2010) and covering the wavelength range of 70–500 μm , have revealed that networks of filamentary structures dominate the interiors of molecular clouds (André et al., 2010; Molinari et al., 2010a; Men’shchikov et al., 2010; Arzoumanian et al., 2011). Although the importance of filaments has been suspected for some time (e.g. Schneider & Elmegreen, 1979), the ubiquity of such morphology, seen in these highly sensitive high-angular resolution submillimetre dust continuum surveys, has brought about a renewed focus on gas flows in filaments in both observational and theoretical studies (André et al., 2014). Moreover, filaments are found to be the sites of the vast majority of star-forming cores (Polychroni et al., 2013; Könyves et al., 2015).

The temperatures of molecular clouds are typically ~ 10 K, a value controlled by the balance of heating and cooling processes. The most basic and ubiquitous heating agent of molecular clouds is energy injection from cosmic rays (Glassgold & Langer, 1973a,b). In addition to cosmic rays, if a molecular cloud contains recent or ongoing star formation, then it will contain regions which are being heated and ionised by stellar radiation. In the absence of star formation, the outer layers of a molecular cloud may serve to absorb incident cosmic rays and

Table 1.1: Physical properties of molecular clouds, clumps and cores

Property	Clouds ^a	Clumps ^b	Cores ^b
Mass (M_{\odot})	10^2 – 10^6	30 – 10^2 ^c	0.2 – 30 ^d
Size (pc)	1–50	0.3–3	0.03–0.2
Density (cm^{-3})	50–800	10^2 – 10^4	10^4 – 10^6
Temperature (K)	4–8	10–20	8 – 13 ^d
Velocity width (km s^{-1})	0.3–3.0	0.3–3.0	0.1–0.3

^a Molecular cloud properties from the Galactic Ring Survey (Roman-Duval et al., 2010).

^b Physical properties of clumps and cores from Bergin & Tafalla (2007) excluding:

^c Clump masses from the Bolocam Galactic Plane Survey (Dunham et al., 2011)

^d Core masses and temperatures from Polychroni et al. (2013).

radiation, and the coldest gas will be found in the densest central regions due to self-shielding. The gas of a molecular cloud is cooled through the rotational and vibrational line emission of its constituent molecules, particularly CO (Goldsmith & Langer, 1978) while dust grains can contribute both to the cooling and heating. In regions with densities in the range 10^3 – 10^5 cm^{-3} , some molecules can freeze out onto dust grains, becoming ineffective coolants (e.g. Hocuk, Cazaux & Spaans, 2014).

1.1.2 Formation

The lifetimes of molecular clouds, whether they are relatively short- or long-lived, are a matter of uncertainty. There are a number of studies which claim that they do not exist for long, with Elmegreen (2000), for example, finding that molecular clouds last for only one or two crossing times, defined as R/σ_v , the cloud radius divided by its velocity dispersion.

Since the establishment of the ISM as an inherently dynamic environment,

the older picture of inert molecular clouds existing in a state of quasi-equilibrium prior to star formation was revised, and the picture of molecular clouds as largely transient features has prevailed. There have historically been two primary ideas for molecular cloud formation and consensus on the formation mechanism for molecular clouds has not yet been reached; they may form in a ‘top-down’ mode, from large-scale gravitational, hydrodynamic (e.g. Kelvin-Helmholtz), or magnetic instabilities induced by the collision of streams of neutral atomic gas (e.g. Elmegreen, 1979; Hartmann, Ballesteros-Paredes & Bergin, 2001; Heitsch et al., 2006; Kim & Ostriker, 2006) otherwise supported by thermal or turbulent pressure, or they may form in a ‘bottom-up’ manner by the accumulation of previously existing independent molecular sub-units through cloud–cloud collisions (e.g. Kwan, 1979; Roberts & Stewart, 1987).

The method of growing GMCs through the collision of smaller clouds requires timescales of $\gtrsim 2 \times 10^8$ years (Kwan, 1979), but the photodissociation and mechanical disruption of molecular clouds by HII regions is estimated to take only $\sim 10^7$ years (Blitz & Shu, 1980). The collisional growth of smaller molecular clouds alone is therefore too slow to be solely responsible for GMC formation, at least for clouds with masses of $\sim 10^6 M_{\odot}$, but may play a subdominant role in the process.

The top-down scenarios begin with the presence of flows of atomic gas that are powered by a combination of Galactic shear, spiral density waves, supernovae and interactions between galaxies. The turbulent instabilities induced by the collision of neutral streams provide the environment within which densities can be high enough to allow the formation of H_2 . One of the strengths of the collisional flow scenario is that it naturally produces the ubiquitous complex internal structure observed in molecular clouds (e.g. Heitsch et al., 2006). Elmegreen (1979)

proposed that molecular clouds condense, by dint of self-gravity, out of the dust lanes formed by the induced compression and shocking of gas by a passing spiral density wave. Self-gravity was found not to be necessary condition to form GMCs by Dobbs et al. (2008), who found that high densities in atomic gas may result from spiral structure as the spiral shock compresses the ISM, an effect exacerbated by orbit crowding, thus facilitating cooling of the gas and leading to H₂ formation.

1.1.3 Observations of molecular gas

Molecular clouds are composed overwhelmingly of molecular hydrogen, H₂, and inert atomic helium; adopting a solar abundance, the mean molecular weight of molecular gas is $\mu = 2.3$, taking helium into account (Allen, 1973). At typical molecular cloud temperatures (~ 10 K), however, these species are practically invisible; H₂ molecules do not possess a permanent dipole moment, and so do not radiate via the electric dipole rotational transitions which are easily excited in other ISM molecules. In addition, the lowest lying quadrupole transitions of H₂ have small transition probabilities and require excitation temperatures of $\gtrsim 500$ K, much higher than those typically found in the cold molecular ISM.

Carbon monoxide (CO) is the second most abundant molecule in the ISM and is present wherever H₂ exists. CO has low-lying rotational energy levels which are excited at temperatures of ~ 5 K and it is therefore an ideal tracer for cold H₂, with a number of rotational transitions that are accessible to millimetre and submillimetre telescopes. The relative abundance of CO compared to H₂ is measured by comparing the column density of H₂ derived from dust extinction or emission (assuming a dust-to-gas ratio) to the column density of CO, and is generally considered to be $X(\text{H}_2/\text{CO}) \sim 10^4$. Frerking, Langer & Wilson (1982)

place the abundance of CO at $X(\text{H}_2/\text{CO})^{-1} \sim 8.5 \times 10^{-5}$, and Blake et al. (1987) report a similar abundance ratio of $X(\text{H}_2/\text{CO})^{-1} \sim 1.4 \times 10^{-4}$ in the Orion molecular cloud.

This relationship between CO and H₂, however, is not a constant one. In regions where their respective formation and destruction processes do not strike the same balance, the abundance ratio $X(\text{H}_2/\text{CO})$ can vary, with variations having been observed across environments such as the Galactic centre (e.g. Sodroski et al., 1995) and outer Galaxy (e.g. Brand & Wouterloot, 1995), and within high-latitude molecular clouds (e.g. Paradis et al., 2012). H₂ formation is thought to occur overwhelmingly on the surfaces of dust grains (Gould & Salpeter, 1963; Hollenbach & Salpeter, 1971; Vidali et al., 2005), by a process which is many orders of magnitude more efficient than the alternative and highly improbable radiative combination scenario, $\text{H} + \text{H} \rightarrow \text{H}_2 + \gamma$. The dust grains' irregular surfaces are highly efficient at holding hydrogen atoms, and will do so long enough for their combination to occur. At typical temperatures of ~ 10 K in the cold neutral ISM, any hydrogen atom sticking to a dust grain will almost certainly evaporate in molecular form.

There are a number of isotopologues of CO which are frequently observed in addition to the most common isotopologue ¹²CO, which easily becomes optically thick, that trace H₂ to much higher optical depths due to their relative rarity. ¹³CO and C¹⁸O are the most commonly observed isotopologues with a review of interstellar abundances placing their relative abundances at $X(^{12}\text{CO}/^{13}\text{CO}) \approx 77$, and $X(^{12}\text{CO}/\text{C}^{18}\text{O}) \approx 560$ (Wilson & Rood, 1994). Abundance ratios are typically calculated by comparing the intensity of molecular lines in rare species or in highly optically thin regions. The abundance ratios vary across the Galaxy, with ISM values departing from the ratios found in the Solar System, and there

have been many reports of a gradient going from low abundance ratios of $^{12}\text{C}/^{13}\text{C}$ in the Galactic centre, to much higher values far out in the disc (e.g. Langer & Penzias, 1990). Nucleosynthesis within stars is the root of the variations in the abundances of carbon, nitrogen and oxygen, which depend on the star formation history, stellar evolution and the recycling of interstellar gas in a Galaxy such as our own.

The lowest-lying rotational emission lines of CO fall in the millimetre and submillimetre wavelength regimes, making them accessible from telescopes such as the 15 metre James Clerk Maxwell Telescope (JCMT) and the Atacama Large Millimeter Array (ALMA). The rotational energy of the J th level of a rigid diatomic molecule, such as CO, is given by:

$$E_J = \frac{\hbar^2}{2I} J(J+1) \quad (1.1)$$

where the moment of inertia, I , of the molecule is given by $I = \mu_m r^2$. The reduced mass μ_m of a diatomic molecule with constituent atoms of mass m_1 and m_2 , is given by $\mu_m = (m_1 m_2)/(m_1 + m_2)$, and the equilibrium separation of the C and O atoms of CO is $r = 0.112$ nm.

In average ISM conditions, the CO molecules are excited by a combination of collisions, most likely with H_2 , and the absorption of photons. In regions of dense gas, there is a critical density, n_{crit} , at which the rate of the spontaneous emission of a photon (denoted by the Einstein coefficient A_{ji}) is equal to the rate of collisions (given by $n\sigma v$), and can be approximated as:

$$n_{\text{crit}} = \frac{A_{ji}}{\sigma \langle v \rangle}, \quad (1.2)$$

where σ is the collisional cross section (typically $\sim 10^{-15}$ cm $^{-2}$) and $\langle v \rangle$ is the

time-averaged velocity, related to the gas temperature by $\langle v \rangle \approx \sqrt{3k_{\text{B}}T/m}$. Where the CO density exceeds n_{crit} , the energy levels are thermalised, and the radiative line intensity is determined by the gas temperature and column density, whereas below n_{crit} , the intensity has an additional dependence on volume density. The quantity $\sigma\langle v \rangle$ is an approximation of the collision rate coefficient, C_{ji} . While sub-thermal emission from CO can occur below the critical density, the emission is likely to be weak. The frequencies, excitation energies and critical densities of the lowest-lying (and most frequently observed) rotational transitions of the most common CO isotopologues are given in Table 1.2.

In synthetic observations of molecular clouds simulated using smoothed particle hydrodynamics (SPH), Duarte-Cabral & Dobbs (2016) find that CO is a good tracer of the density peaks of H_2 , but misses diffuse gas. CO-dark molecular gas is expected where H_2 densities fall below the critical density, but in cool ($T \lesssim 20$ K) and dense ($n \gtrsim 10^5 \text{ cm}^{-3}$) environments CO can also ‘freeze-out’ of the gas phase onto the surfaces of dust grains. Depletion factors of ~ 10 are typical in dense regions (e.g. Caselli et al., 1999; Pon et al., 2016), but depletion factors of up to 80 have been observed in the densest regions of infrared dark clouds (IRDCs; Fontani et al., 2012).

1.1.4 Observations of the dust continuum

In addition to molecules such as CO, dust grains consisting of tens to hundreds of atoms are another important tracer of molecular clouds and their structures, despite making up only $\sim 1\%$ of the ISM by mass. Nearby ($\lesssim 500$ pc) molecular clouds, such as the aforementioned Bok globules, can show up as optical absorption features against a background of stellar light and at greater distances their more massive IRDC counterparts have column densities large enough for them

Table 1.2: The lowest-lying rotational emission lines of the most common isotopologues of CO using recent collision rate coefficients.

Isotopologue	Transition	E/k_B (K)	A_{ij} (s^{-1}) ^a	C_{ij} ($cm^3 s^{-1}$) ^b	n_{crit} (cm^{-3}) ^c	ν (GHz) ^d
^{12}CO	$J = 1 \rightarrow 0$	5.5	7.2×10^{-8}	3.3×10^{-11}	1.9×10^3	115.271
^{13}CO	$J = 1 \rightarrow 0$	5.3	6.3×10^{-8}	3.3×10^{-11}	1.7×10^3	110.201
$C^{18}O$	$J = 1 \rightarrow 0$	5.3	6.3×10^{-8}	3.3×10^{-11}	1.7×10^3	109.782
^{12}CO	$J = 2 \rightarrow 1$	11.1	6.9×10^{-7}	7.2×10^{-11}	6.3×10^3	230.538
^{13}CO	$J = 2 \rightarrow 1$	10.6	6.0×10^{-7}	7.2×10^{-11}	5.4×10^3	220.399
$C^{18}O$	$J = 2 \rightarrow 1$	10.5	6.0×10^{-7}	7.2×10^{-11}	5.5×10^3	219.560
^{12}CO	$J = 3 \rightarrow 2$	16.6	2.5×10^{-6}	7.9×10^{-11}	1.6×10^4	345.796
^{13}CO	$J = 3 \rightarrow 2$	15.8	2.2×10^{-6}	7.9×10^{-11}	1.4×10^4	330.588
$C^{18}O$	$J = 3 \rightarrow 2$	15.7	2.2×10^{-6}	7.9×10^{-11}	1.4×10^4	329.331

^a Einstein A -coefficients are taken from LAMBDA (Schöier et al., 2005).

^b Collision rate coefficients are from Yang et al. (2010).

^c Critical densities calculated for an excitation temperature of 10 K.

^d Frequencies provided by NASA's Jet Propulsion Laboratory Molecular Spectroscopy catalogue (Pickett et al., 1998).

These critical densities use a more complex calculation than Equation 1.2 that includes all possible collisional de-excitations and accounts for an ortho/para- H_2 abundance ratio of 0.001:0.999 at 10 K (Flower, Pineau Des Forêts & Walmsley, 2006). Adapted from a code provided by J. Mottram (private communication).

to show up in absorption at mid-infrared wavelengths (e.g. Carey et al., 1998; Peretto & Fuller, 2009).

The level of absorption of background starlight by dust leads to the direct determination of the column density of molecular hydrogen, $N(\text{H}_2)$. Bohlin, Savage & Drake (1978) developed a widely used conversion from reddening to the column density of atomic and molecular hydrogen:

$$\langle (N(\text{HI}) + 2N(\text{H}_2))/E(B - V) \rangle = 5.8 \times 10^{21} \text{cm}^{-2} \text{mag}^{-1}, \quad (1.3)$$

which, through adoption of the standard Fitzpatrick (1999) extinction law $R_V = A_V/E(B - V) = 3.1$, may be rewritten as:

$$N(\text{H}_2)/A_V = 9.4 \times 10^{20} \text{cm}^{-2} \text{mag}^{-1}. \quad (1.4)$$

The thermal emission of dust grains can be directly observed by far-infrared, submillimetre and millimetre telescopes, and assuming the dust grains can be described by a single temperature, a direct calculation of the column density averaged over a telescope beam can be made (e.g. Schuller et al., 2009):

$$N(\text{H}_2) = \frac{F_\nu R_{\text{gd}}}{B_\nu(T_{\text{D}})\Omega\kappa_\nu\mu m_{\text{H}}}, \quad (1.5)$$

where F_ν is the beam-integrated flux density, R_{gd} is the gas-to-dust mass ratio, $B_\nu(T_{\text{D}})$ is the Planck function evaluated at the dust temperature T_{D} , Ω is the solid angle of the beam, κ_ν is the dust absorption coefficient, μ is the mean molecular mass and m_{H} is the mass of a hydrogen atom. The dust absorption coefficient is usually interpolated from the measurements by Ossenkopf & Henning (1994), and the dust emission is assumed to be optically thin, which is almost always true at wavelengths of ~ 1 mm.

1.1.5 Scaling relations and the origin of substructure

The interiors of molecular clouds are observed to be highly substructured in both spatial and spectral dimensions, a matter which is thought to arise as a result of turbulence. The virial parameter, α_{vir} , is frequently used in the literature to describe the dynamical state of a molecular cloud (e.g. Bertoldi & McKee, 1992; Dib et al., 2007; Dobbs, Burkert & Pringle, 2011). It is the ratio of a molecular cloud's gravitational energy to its kinetic energy:

$$\alpha_{vir} = \frac{5\sigma_v^2 R_c}{GM_c}, \quad (1.6)$$

for a uniform density spherical gas cloud, where G is Newton's gravitational constant, σ_v is the line-of-sight velocity dispersion, R_c is the radius of the cloud and M_c is its mass. If $\alpha_{vir} = 1$ then the cloud is in virial equilibrium. If α_{vir} is greater than unity, then the cloud is unbound. Heyer et al. (2009) analysed molecular clouds from the Galactic Ring Survey (GRS; Jackson et al., 2006), and found that the majority are in virial equilibrium. It is worth mentioning that there is probably a selection effect at work here; where $\alpha_{vir} > 1$, clouds will disperse over a signal-crossing time, and where $\alpha_{vir} < 1$ the molecular or dust emission of over-dense sub-regions will disappear on a free-fall timescale.

In a seminal paper, Larson (1981) measured various trends between the size, mass and velocity dispersions of molecular clouds in the literature, and found them to have approximately power-law forms, and these have become known as 'Larson's Laws'. Larson's relationships relate size (L) and linewidth (σ_v):

$$\sigma_v = 1.10 L^{0.38}, \quad (1.7)$$

mass (M) and linewidth:

$$\sigma_v = 0.42 M^{0.20}, \quad (1.8)$$

and size and mean volumetric density $\langle n(\text{H}_2) \rangle$:

$$\langle n(\text{H}_2) \rangle = 3400 L^{-1.10}, \quad (1.9)$$

where velocity dispersions, sizes, masses and densities are quoted in units of km s^{-1} , pc, M_\odot and cm^{-3} , respectively. Larson's interpretation of the size–linewidth relationship was that there is no preferred length scale for turbulent motions under a simple hierarchy of sizes. In this picture, the structure emerges as a consequence of the cascade of energy in turbulent eddies, similar to Kolmogorov's law for incompressible fluids, which has a form $\sigma_v \propto L^{0.33}$. The size–linewidth and density–linewidth relations were later revised to $\sigma_v \propto L^{0.5}$ and $n \propto L^{-1}$ (e.g. Solomon et al., 1987; Myers & Goodman, 1988), with the interpretation that these ought to arise as a consequence of the approximate virial equilibrium of clouds. The combination of all three Larson relations leads to the conclusion that the column density, the volume density multiplied by the cloud size, is approximately constant, regardless of the cloud size.

The Larson relationships have been largely reproduced in many surveys of both the Galaxy and external galaxies (e.g. Bolatto et al., 2008), and are generally regarded as evidence that molecular clouds are universally both in approximate virial equilibrium and supported by turbulence. Shetty et al. (2012) find a similar slope to the size–linewidth relation for clouds in the Central Molecular Zone (CMZ) albeit with systematically higher linewidths. This would appear to suggest that the Larson relationships hold, even in extreme environments.

Departures have been seen, however, with a study of the molecular clouds

identified by the ^{13}CO Galactic Ring Survey (Heyer et al., 2009) exhibiting an exponent of the structure function $v_0 = \sigma_v/R^{1/2}$ that is not constant as implied by the simplified version of Larson’s laws, but varies systematically with the surface density $\Sigma^{1/2}$. Dobbs, Burkert & Pringle (2011) argue that the properties of the GRS clouds as reported by Heyer et al. (2009) actually show that they have virial parameters exceeding unity, and so are generally unbound. While it remains true that the denser regions within the clouds do become bound in order to form stars, the clouds are predominantly *globally* unbound. In numerical simulations Clark & Bonnell (2004) found that self-gravitating clumps are naturally generated within the supersonically turbulent interiors of molecular clouds. The implication is that global self-gravity of a molecular cloud is not a necessary condition for star formation.

The mass spectrum of molecular clouds with masses $> 10^5 M_\odot$ was found by Roman-Duval et al. (2010) to be described a power law of the form: $N(M) \propto M^{-1.64 \pm 0.25}$, consistent with a previous result of Williams & McKee (1997) who found a power law with an exponent of -1.6 for clouds with masses less than $10^6 M_\odot$. Moving into the substructure of molecular clouds, similar mass functions have been found for clumps (Kramer et al., 1998), and this similarity continues down to the core mass function (e.g. André et al., 2010) and again to the apparently universal stellar initial mass function (IMF; Bastian, Covey & Meyer, 2010).

The column density probability distribution function (PDF) of molecular clouds is both predicted (e.g. Vazquez-Semadeni, 1994) and observed (e.g. Rathborne et al., 2014) to follow a lognormal distribution, at least at low densities. This lognormality arises from the central limit theorem, and should be expected when any particular cell of gas experiences a series of random and independent

compressions through turbulent shocks (Ostriker, Stone & Gammie, 2001). At high column densities, however, the PDF departs from lognormality and a power-law tail arises, seen in dust observations (Rathborne et al., 2014; Schneider et al., 2015) but not with CO or ^{13}CO (Goodman, Pineda & Schnee, 2009) due to the limitations of those observations at high column density described in Section 1.1.3. The power-law tail has been interpreted as being the result of the cores and filaments for which gravity has become significant, and that will go on to form stars.

When observed at high spatial resolution and with dense-gas tracers, molecular clouds exhibit a strongly filamentary structure (e.g. Molinari et al., 2010b; André et al., 2010; Arzoumanian et al., 2011) and the ubiquity of such structures in both star-forming and quiescent molecular clouds suggests that they play an important role in star formation. An apparently universal filament width of ~ 0.1 pc was found by Arzoumanian et al. (2011), who highlight that this width approximately corresponds to the sonic scale at which turbulence becomes subsonic in diffuse gas (Padoan et al., 2001), and a consistent width has since been measured by a number of other studies (e.g. Benedettini et al., 2015; Kainulainen et al., 2016) and produced in simulations (e.g. Kirk et al., 2015).

Molecular filaments are observed to consist of bundles of approximately cylindrical velocity-coherent components (Hacar et al., 2013; Tafalla & Hacar, 2015). Hacar et al. (2013) suggest that supersonic linewidths observed in more massive filaments are the result of a superposition of bundles of filaments at distinct velocities with sonic linewidths that have decoupled from the turbulence. Hacar et al. (2016) report observations of a 6 pc long filament in the nearby (~ 150 pc) Musca cloud that exhibits a sub- or trans-sonic non-thermal velocity dispersion ($\sigma_{\text{NT}}/c_s \lesssim 1$) and comparably subsonic velocity dispersions have also been seen

in dense cores (Pineda et al., 2010). These linewidths depart from Larson’s size–linewidth relation and may be an indication the these structures have decoupled from the turbulent ISM, a condition that is necessary for star formation.

Tafalla & Hacar (2015) proposed a ‘fray and fragment’ scenario in which a collision between two supersonic flows results in the generation of the filamentary bundles (also see Padoan et al., 2001), which evolve through the combined effects of turbulence and self-gravity. The filaments may split into a network of further smaller filaments, and where the gas has exceeded a critical mass-per-unit-length, self-gravity becomes important and the filament fragments into a chain of cores. Smith et al. (2016) suggest that the smaller sub-filaments arise as a result of the dissipation of turbulence onto smaller scales, and arise fromioi short wavelength (or high wavenumber) turbulent modes.

Infrared polarisation measurements by Sugitani et al. (2011) found that the main filaments in Serpens South preferentially have orientations perpendicular to magnetic field lines, with sub-filaments orientated parallel to the field lines, and the same behaviour was seen in dust polarisation measurements of two IRDCs by Pillai et al. (2015). These authors suggest that the elongation of the sub-filaments parallel to the magnetic field lines indicate that the sub-structures may be inflows of material toward the main filament, or outflows of gas from the embedded cluster. MHD simulations by Federrath (2016) find that the inclusion of turbulence in addition to self-gravity produces filaments with subsonic velocity dispersions that agree well with the supposedly universal width of ~ 0.1 pc .

Star-forming cores appear to be preferentially found within filaments (Polychroni et al., 2013; Könyves et al., 2015), and their intersections (known as ‘hub-filament systems’) are observed to host both young clusters (Myers, 2011; Schneider et al., 2012) and high-mass clumps (e.g. Peretto et al., 2013), which are

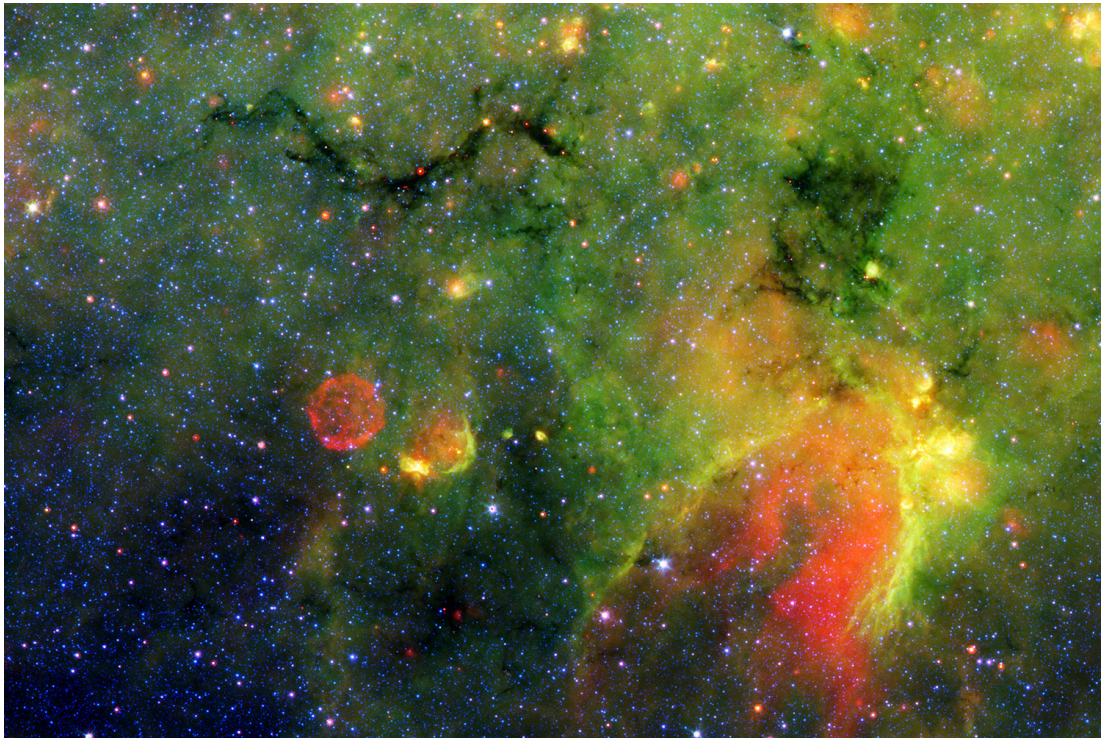


Figure 1.2: A three-colour composite *Spitzer* image of the infrared dark cloud G011.11-0.12, with the 3.6 and 8.0 μm IRAC bands shown in blue and green, and the red is a 24 μm image from MIPS. Image credit: NASA/JPL-Caltech.

thought to be the precursors of high-mass stars. Pillai et al. (2015) suggested that the strong magnetic fields observed in the Milky Way's two most massive known IRDCs indicate a vital role of magnetic fields in the formation of high-mass stars. Magneto-hydrodynamic (MHD) simulations by Hennebelle (2013) find that the inclusion of magnetic fields increases the level of filamentary substructure produced by hydrodynamic simulations alone. The author suggests that they arise as a consequence of energy-dissipating flows and that magnetic fields along their length helps preserve the velocity coherence.

Collectively, these studies indicate that filamentary structures appear to link molecular clouds and star formation. The hints of a particular connection of filaments and magnetic fields to the formation of high-mass stars, which present a number of problems to our understanding, are compelling.

1.2 High-mass star formation

High mass stars ($M \gtrsim 8 M_{\odot}$) play an enormous role in the shaping of the cosmos. Their fantastic output of radiation and energy in the forms of ionising photons, stellar winds and supernovae has a dramatic effect on their surroundings. Their impact ranges from the reionisation of the Universe to the evolution of galaxies through their feedback into the ISM and the synthesis of heavy elements. It is vital, then, that a comprehensive understanding of the formation and evolution of high-mass stars is acquired, but high-mass star formation (HMSF) is poorly understood and presents problems for theorists and observers alike (Zinnecker & Yorke, 2007; Tan et al., 2014; Schilke, 2016).

Large samples of sites of ongoing high-mass star formation are difficult to obtain due to their intrinsic rarity. There are very few local star-forming regions which are massive enough to sample sufficiently far up the IMF to contain high-mass stars. For example, the Orion Nebula Cluster lies at a distance of around 415 pc (Menten et al., 2007), and is thought to contain perhaps just two high-mass stars in the formation process, with masses of $\sim 7\text{--}20 M_{\odot}$ (Matthews et al., 2010) and $\sim 10\text{--}15 M_{\odot}$ (Plambeck et al., 2013). This observational limitation is compounded by the fact that high-mass stars form and evolve more rapidly than lower-mass stars, but also mitigated to some extent by the greater distances at which high-mass stars can be seen due to their greater luminosities.

In the ‘classical’ picture of star formation, an isothermal sphere of gas gravitationally collapses to form a star, but this model has several major difficulties in describing the formation of high mass stars. In this model, the rate of accretion of material onto the forming protostar yields formation timescales of over 10^6 Myr (Shu, 1977) which are unrealistically long for high-mass stars (Stahler, Palla & Ho, 2000). The Kelvin-Helmholtz timescales for such high-mass stars

are shorter than these accretion timescales, meaning that the stars must continue accretion during the main sequence. However, high-mass stars exert a strong radiative pressure on surrounding gaseous material, which can efficiently halt the inwards collapse of the gas, so it is not clear how accretion can continue once HII regions emerge. Wolfire & Cassinelli (1987) found that, in the spherical model, accretion rates exceeding $10^{-3} M_{\odot} \text{yr}^{-1}$ are required to overcome the outwards radiation pressure exerted by the most massive forming stars; either a method of achieving these extreme accretion rates, or a model of non-spherical accretion must be found.

Over the last decade or so, two main families of HMSF models have emerged – the so-called *turbulent core accretion* (e.g. McKee & Tan, 2003) and *competitive accretion* (e.g. Bonnell et al., 2001; Bonnell & Bate, 2006) models. The core accretion models uphold the spherical assumption and HMSF proceeds as a scaled-up version of low-mass star formation with the exception that the accretion rate is determined by the supersonic turbulent velocity dispersion as opposed to the isothermal sound speed, and thus reaches sufficiently high values. In these models, each individual pre-stellar core will produce one star and the final mass of the forming star is determined by the mass of that core. These models naturally predict that the core mass function and the initial stellar mass function should be directly related, and high-mass stars are able to form in isolation.

Competitive accretion models describe the accretion of gaseous material onto stars which share a common gravitational potential (Bonnell & Bate, 2006). Here, the stars which lie at the centre of the gravitational potential will accrete matter via the Bondi–Hoyle mechanism at an accelerated rate when compared to stars forming further from the centre towards which the ambient gas is funnelled. At early times, the low-mass protostars at the centre of the potential can accrete

those components of the turbulent surrounding gas with the lowest relative velocity, and as the proto-high-mass star accretes more material, it begins to accrete gas with a higher relative velocity, increasing the rate of accretion. As time goes on, the most central, and now most massive stars, continue to dominate the accretion of the ambient gas, and so the mass distribution of low mass stars is set by fragmentation. These models naturally explain the origin of observed mass segregation and the location of the most massive stars in the centre of OB associations and young stellar clusters (e.g. Hillenbrand & Hartmann, 1998). In competitive accretion models, the final stellar mass is not determined by any initial ‘seed’ core.

Both families of HMSF models manage to successfully produce some observation results, but fall down on others. For example, the McKee & Tan (2003) model requires that the density profile of the collapsing core is strongly peaked with $\rho \sim r^{-1.5}$, but Dobbs, Bonnell & Clark (2005) demonstrated that turbulence does not act in an equivalent manner to isotropic pressure, and that such centrally condensed cores with masses of $30 M_{\odot}$ would fragment into ≈ 20 smaller stars. The competitive accretion model requires an initially *strongly* gravitationally bound cloud, but Krumholz, McKee & Klein (2005) point out that this is generally not observed to be the case (e.g. Larson, 1981).

The magnetic fields present in filaments, discussed in Section 1.1.5, present some insights and potential solutions to these problems. The inflows of gas onto filaments from sub-filaments that lie parallel to magnetic field lines help supply the mass needed for high-mass cores, as the competitive accretion models of HMSF require and numerical simulations suggest that strong magnetic fields may help suppress the fragmentation problem of the core accretion models (Comerçon, Hennebelle & Henning, 2011; Myers et al., 2013); magnetic fields appear

to be consistent with both HMSF models. Strong magnetic fields have also been observed sites of ongoing star formation (Girart et al., 2013; Zhang et al., 2014b), suggesting that they may continue to play a significant dynamical role even after star formation begins.

Contemporary observations point towards a model of HMSF theories that must incorporate aspects of both of these models. After collating observational and theoretical evidence, Zinnecker & Yorke (2007) proposed an evolutionary timeline for HMSF, which has been advanced over the intervening years, that consists of four main observational stages:

1. A pre-stellar phase in which a high-mass clump is gravitationally bound, but does not exhibit mid-IR emission or any other evidence of an embedded object or objects.
2. The high-mass clumps collapse under self-gravity, fragmenting into cores containing protostars that gain mass through accretion discs. As the protostellar temperatures increase, the envelope of clump gas is heated, and radiative pumping incites 6.7 GHz class II methanol maser emission (e.g. Menten, 1991; Walsh et al., 2003; Urquhart et al., 2015).
3. The accreting young stellar object (YSO) swells and contracts. Numerical simulations by Hosokawa, Yorke & Omukai (2010) show that for high accretion rates, in excess of $10^{-4} M_{\odot} \text{ yr}^{-1}$, accretion causes the protostar to swell in size, reaching a radius of $\sim 100 R_{\odot}$. At this size, the effective temperature is very low and accretion can continue. When a mass of $\sim 10 M_{\odot}$ is reached, the Kelvin-Helmholtz timescale is shorter than the accretion timescale, the protostar begins to contract, and the temperature rises once again. An upper limit of $\sim 30 M_{\odot}$ can be reached by accretion before the

protostar reaches the zero-age main-sequence (ZAMS). These swollen high-mass YSOs (HMYSOs) are extremely luminous (with 10^3 – $10^5 L_{\odot}$) but do not yet emit ionising radiation, and therefore do not have any associated HII region.

4. The formation and growth of HII regions occurs once the high-mass star has reached the ZAMS and hydrogen burning has begun. The ionising radiation now present will initially create a hyper-compact HII region, followed in stages by ultra-compact and compact HII regions before emerging from the clump as a ‘classical’ HII region that can be seen at optical wavelengths.

Urquhart et al. (2014b) have collected a large sample of methanol masers, high-mass YSOs and compact HII regions associated with high-mass clumps, finding that they are in broad agreement with this evolutionary sequence. Numerical simulations of high-mass protostars by Davies et al. (2011) find that the luminosity distribution of YSOs in the Galaxy are best described by models in which the accretion rate increases over time during the accretion phase, and models with constant or decreasing accretion rates do not fit the observations. A sample of HMYSOs were found by Mottram et al. (2011) to suggest that the HMYSO phase lasts for roughly 7×10^4 to 4×10^5 years, depending on the YSO mass, and that the compact HII region phase has a duration of $\sim 3 \times 10^5$ years.

The samples collated by these studies, and those available from other large-scale Galactic plane surveys (discussed in Section 1.5) will allow targeted sub-arcsecond resolution follow-up observations to be made of all HMSF regions in the Milky Way as we move into the era of ALMA, offering tantalizing new insights into HMSF.

1.3 Spontaneous and triggered star formation

One of the foundations of modern astrophysics, provided by James Jeans at the turn of the 20th century, is a critical mass limit known as the Jeans mass, M_J . It describes the maximum mass at which the thermal energy of a self-gravitating sphere of idealised gas can support itself against collapse. It can be derived from the virial equilibrium where $2T + \Omega = 0$ (T being the kinetic and Ω the gravitational energy) and is given in the following way:

$$M_J = \left(\frac{3}{4\pi\rho} \right)^{\frac{1}{2}} \left(\frac{5k_B T}{G\mu m_H} \right)^{\frac{3}{2}}, \quad (1.10)$$

where ρ is the mean gas density, k_B is Boltzmann's constant, T is the gas temperature, μ is the mean molecular mass of the gas and m_H is the mass of a hydrogen atom. A sphere of ideal gas with a mass greater than M_J will undergo gravitational collapse, resulting in the formation of stars, and there are a myriad of astrophysical processes which can induce gravitational collapse of molecular gas. Although the Jeans mass represents a simplified situation, neglecting the effects of rotation and magnetic fields, it remains a fundamental estimator of the dynamical condition of molecular clouds.

While there are a multitude of processes which can cause a gas region to begin gravitational collapse, it can be said that there are two paradigms for star formation: *spontaneous* and *triggered* star formation. In spontaneous star formation, the collapsing regions of gas are caused by overdensities which naturally arise in the turbulent gas motions. For example, the aforementioned numerical study of Clark & Bonnell (2004) showed that self-gravity and gravitational collapse can occur in quiescent regions of a turbulent medium. The turbulent fragmentation models of Padoan & Nordlund (2002) and Padoan, Haugbølle & Nordlund (2012)

are able to reproduce the stellar IMF for stars with masses greater than 1–2 M_{\odot} directly from the probability density function of the turbulence, finding that only cores with sufficient gravity to be able to overcome the thermal and magnetic energy will collapse into protostars. In these models, the IMF above M_J is determined by the (power-law) velocity power spectrum, and below M_J the IMF follows the lognormal density PDF.

The triggered star formation paradigm requires a triggering agent, such as the ionising radiation from a high-mass star or a shockwave from a supernova, which imparts energy or momentum into a previously sub-critical cloud or clump of molecular gas. The induced compression of the molecular gas causes it to become gravitationally unstable and collapse. There are two models for triggered star formation which are emphasised in the literature currently: that of radiation-driven implosion (Bertoldi, 1989; Bisbas et al., 2011) and the collect and collapse model (Elmegreen & Lada, 1977; Whitworth et al., 1994)

In the radiation-driven implosion (Bertoldi, 1989) model, the ionisation front of an HII region propagates out to the Strömgen radius, and the strong winds from O stars will then drive the expansion of this ionised bubble. A dense shell of neutral gas forms ahead of the ionisation front, with a typically irregular density structure. Observations of these regions typically display clumps with a cometary tail extending away from the ionising source, and bright rims on the side of the cloud adjacent to the ionising source. These clumps have become gravitationally unstable after the passage of the shockwave, and will go on to form stars. Simulations by Bisbas et al. (2011) demonstrate that it is possible for the ionising flux to trigger this star formation.

Elmegreen & Lada (1977) proposed the collect and collapse model of triggered star formation in which OB groups at the edge of a molecular cloud provide

ionisation and shock fronts which propagate into the molecular gas. Dense gas is accumulated between the two fronts and becomes gravitationally unstable, leading to a new generation of stars. They predicted that the enhanced temperatures in the shocked gas caused by the HII region would mean that star formation would proceed to preferentially produce high-mass stars. This next generation of high-mass OB stars will then drive their own ionisation-shock fronts into surrounding molecular material, and the process continues with a wave of propagating *sequentially triggered* star formation.

Collisions between molecular clouds are also thought to trigger star formation (e.g. Kimura & Tosa, 1996; Anathpindika, 2010; Inoue & Fukui, 2013). As two clouds collide, the bow shock which is formed between them becomes susceptible to dynamical instabilities, and collapses to a filament in the direction of the collision axis containing high-mass pre-stellar cores (Anathpindika, 2010). The three dimensional isothermal magnetohydrodynamic simulations of Inoue & Fukui (2013) find that the cores have large effective Jeans masses due to the high strength of the magnetic fields induced in the compressed layer and the cores are threaded by magnetic fields which are preferentially perpendicular to the filament. This mechanism in particular has been proposed as the origin of the rich high-mass star clusters NGC 3603 (Fukui et al., 2014), Westerlund 2 (Furukawa et al., 2009), M20 (Torii et al., 2011) and RCW 38 (Fukui et al., 2016).

In practice it is extremely difficult to distinguish between the triggered and spontaneous modes of star formation without being able to observe a particular region evolve over time. For example, Thompson et al. (2012) found a statistical overdensity of YSOs on the rims of expanding bubbles surrounding HII regions, surmising that as much as $\sim 30\%$ of the field population of stars may result from such triggering. A similar result was found by Kendrew et al. (2012) who

report that 67% of high-mass YSOs and compact or ultra-compact HII regions are associated with a bubble. There is a debate as to whether studies like this might be the result of observational bias, and one can envisage the bubble expanding rapidly until it reaches a dense clump of gas that may already have been collapsing to form stars, or sweeping up and moving already star-forming material. In a study of hydrodynamical simulations involving the feedback from O-type stars, Dale, Haworth & Bressert (2015) find that none of the techniques used to identify triggering used in 67 papers increase the probability of correctly determining the triggered origin of any given star by a factor of more than 2.

1.4 The effects of large-scale Galactic structure on star formation

1.4.1 The structure of the Galaxy

The Milky Way is thought to be a barred spiral Galaxy of type Hubble type SBb or SBc (e.g. Hodge, 1983; Dame, Hartmann & Thaddeus, 2001; Benjamin et al., 2005). An approximation of the main observed features of the Milky Way is shown in Figure 1.3, but its exact structure is not well known. The location of the Solar System within its disc means that accurately determining distances to other objects in the Galactic plane is extremely difficult; aside from issues arising from peculiar motions, objects residing within the orbit of the Sun have two distance solutions for their line-of-sight velocities – a problem known as the kinematic distance ambiguity (KDA, discussed in more detail in Section 4.2). Consequently the exact spiral structure is not established.

The last few decades have seen a lively debate as to the number of spiral arms

that the Milky Way has, whether there are two (e.g. Churchwell et al., 2009) , three (e.g. Solomon et al., 1987) or four (e.g. Reid et al., 2009; Hou & Han, 2014; Urquhart et al., 2014a) main spiral arms. The number of arms observed may depend on the tracer used and it has been argued, for example, that the overall stellar distribution is best matched by a two-armed model while the distributions of HII regions, atomic and molecular gas and star formation tracers are better described by four arms. Since this thesis concerns molecular gas and the formation of stars, it is the predominantly four-armed models that shall be used.

In a matter of comparatively universal acceptance, the Galaxy is thought to be barred. The structure in the centre of the Galaxy is thought to consist of a main bar, which is ~ 3 kpc in radius and lies at an angle of 20° northward with respect to the Sun-Galactic centre axis (Binney et al., 1991; Dwek et al., 1995) and a second structure known as the long bar with a 4 kpc radius and which subtends an angle of $\sim 43^\circ$ with respect to the Sun-Galactic centre axis (Hammersley et al., 2000; Amôres et al., 2013).

Georgelin & Georgelin (1976) measured the radial velocities of 268 HII regions and, after resolving the KDAs, concluded that the distribution was fitted well by four spiral arms. This model formed the basis for the more recent four-armed model of Taylor & Cordes (1993), which was updated by Cordes (2004), and it is this model that is adopted for this thesis. The four main arms in the latter case are known as the Perseus, Sagittarius, Scutum–Centaurus and Norma arms.

There are a number of other significant structures that have been identified in addition to the four main spiral arms of the Galaxy. There are the Near- (e.g. Oort, 1977) and Far-3 kpc arms (Dame & Thaddeus, 2008), and the Sun resides in a minor arm known variously as the Orion Spur, Local Spur or Local Arm (e.g. Blaauw, 1985), and Stark & Lee (2006) found evidence of a structure between

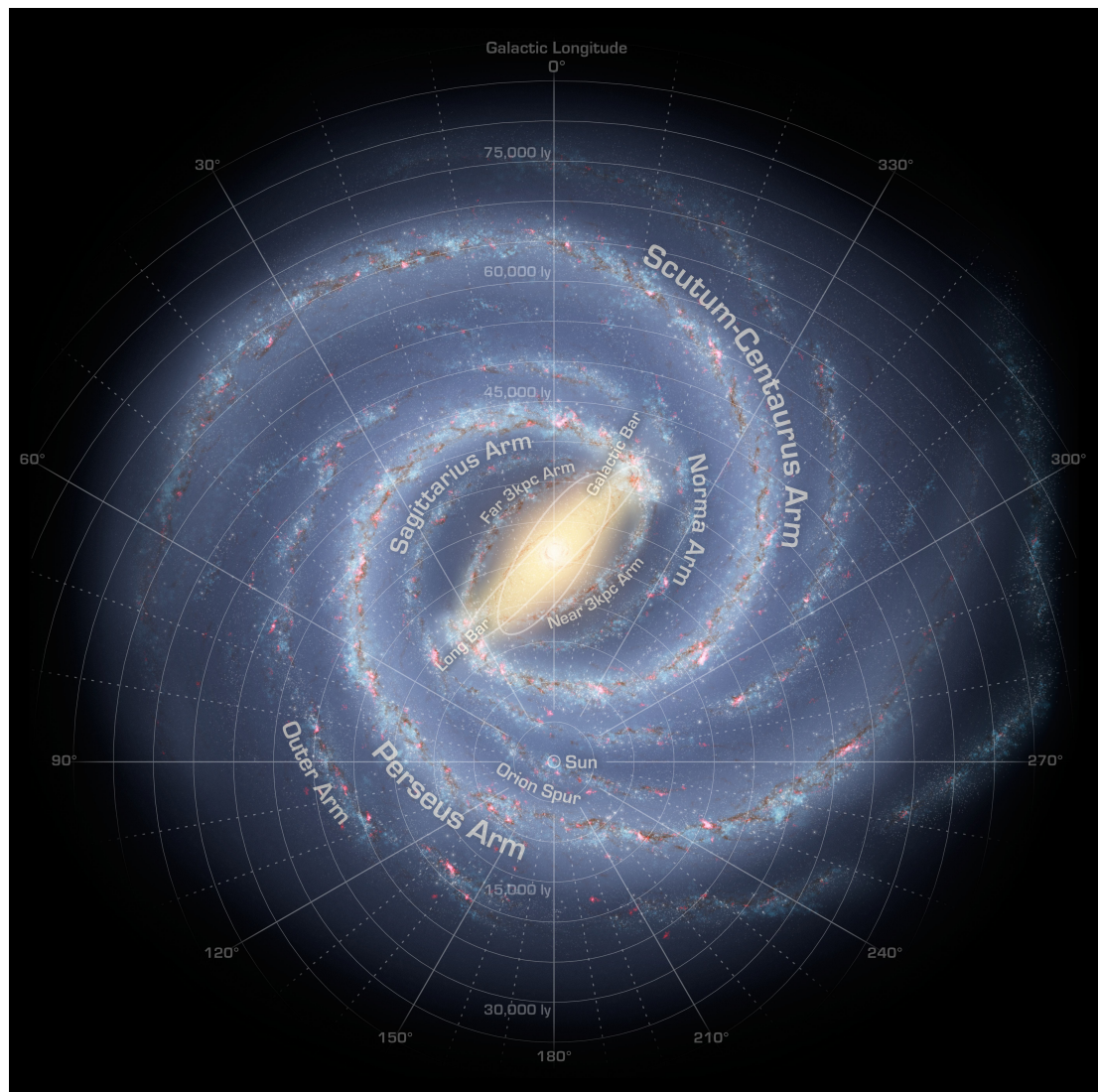


Figure 1.3: An artist's impression of what the Milky Way might look like from a face-on view. This image was created by Robert Hurt of the Spitzer Science Center in consultation with Robert Benjamin at the University of Wisconsin-Whitewater and is described in Churchwell et al. (2009).

the Scutum–Centaurus and Sagittarius spiral arms.

1.4.2 Impact on star formation

Operating at the interface between physical processes which dominate on the scale of HII regions and molecular clouds, and effects induced by the larger scale of galactic structure features, is the shear imposed on molecular clouds by the differential rotation curve of the Galaxy. The models of Tan (2000) predict that the star formation rate in galaxy discs should be elevated in regions with a higher shear rate, and similarly the star formation rate should be lower in regions with lower shear. Seigar (2005) found a correlation between the shear rate and an indicator for the specific star formation rate (i.e. star formation rate per unit mass). A recent study by Dib et al. (2012) finds no significant correlation between the shear parameter and star formation efficiency for molecular clouds in the Galactic Ring Survey. It appears that shear in molecular clouds imposed by Galactic rotation has a very minor effect, if any, on star formation.

The significance of spiral arms in determining a galaxy’s star-forming behaviour is equivocal. Specifically, it is unknown whether spiral arms actually trigger star formation or if they simply gather the precursor material which will be triggered by some other agent. Heyer & Terebey (1998) observed a 28:1 contrast ratio between molecular gas in arms and inter-arm regions, and concluded that molecular gas in spiral arms must condense from atomic gas being compressed as it enters the spiral shock region, a scenario that was reproduced in simulations by Dobbs, Bonnell & Pringle (2006). Observations by Seigar & James (2002) saw an enhancement in the rate of star formation traced by H α emission where *K*-band stellar spirals were present in 20 galaxies, also finding that this enhancement correlates well with an indicator of the strength of spiral

shocks. A study by Foyle et al. (2010) found an enhancement in the star formation efficiency for spiral arms when compared to inter-arm regions in a sample of 2 grand design spiral galaxies of less than 10%. Additionally, this study found that the ratio of H_2/HI shows no significant enhancement in arm regions compared to inter-arm regions. Momose et al. (2010) report a factor of 2 increase in both the star formation rate and efficiency in the spiral arms compared to the central bar. In a recent paper, Koda, Scoville & Heyer (2016) examine the molecular gas fraction in the Milky Way from archival molecular gas and HI data, finding an azimuthal (i.e. arm/inter-arm) variation of $\sim 20\%$ within the inner 6 kpc of the Galaxy, where the molecular gas fraction stays $\gtrsim 50\%$. In the outer Galaxy, defined as being more than 6 kpc from the Galactic centre, they find that the molecular gas is localized to the spiral arms, and becomes predominantly atomic in the inter-arm regions.

Moore et al. (2012) found that $\sim 70\%$ of the increase in the star formation rate density associated with spiral arms in the Galaxy can be attributed to simple source crowding. They ascribe the remaining increase to an increase in the number of embedded high-mass YSOs per unit mass of gas in the Sagittarius arm, though the increase in efficiency in the Perseus arm is attributed to an increase in the luminosity of the high-mass YSOs. The enhanced efficiency in the latter implies a top-heavy IMF in the W49A star-forming complex. The authors suggest that the W49A complex is exceptional, in agreement with other authors (Roberts et al., 2011; Nagy et al., 2012) who suggest that it has conditions comparable to starburst galaxies, whereas the major star-forming regions in the Sagittarius and Scutum arms (W51 and W43 respectively) can be expected from a normal distribution of star-forming regions. Similar conclusions were reached by Eden et al. (2015) who found that the ratio of infrared YSO luminosity to the mass of molec-

ular clouds is slightly enhanced in the spiral arms, but such enhancements may arise out of patchy or intermittent star formation, or be artefacts of a small sample. The efficiency of formation of clumps from clouds has also been observed to be invariant when arm and inter-arm regions are compared (Eden et al., 2012; Eden et al., 2013). Urquhart et al. (2014a) also found that, excluding the Galactic centre, the high-mass star formation rate per unit mass of molecular gas is largely constant across the Galaxy. In light of the most recent results, it appears that spiral arms are playing a minor role in triggering star formation in our Galaxy.

1.5 Surveys of the Galactic plane

In the last couple of decades, surveys of significant fractions of the Galactic plane have become feasible at wavelengths which are able to probe the initial conditions of star formation. These surveys cover atomic and molecular gas, as well as dust continuum structures, YSOs and HII regions. Here follows a summary of the main surveys that are relevant to this study.

Neutral atomic hydrogen in the first quadrant was observed in the VLA Galactic Plane Survey (VGPS; Stil et al., 2006) survey of the 21 cm (1420 MHz) hyperfine emission. The VGPS covers a longitude range of $18^\circ \leq l \leq 67^\circ$, with coverage in latitude between $|b| \leq 1.3^\circ$ and $|b| \leq 2.3^\circ$ with an angular resolution of 1 arcminute and 1.56 km s^{-1} velocity resolution. Atomic hydrogen was covered more recently by another multi-tracer survey; The HI OH, Recombination Line survey of the Milky Way (THOR; Bihr et al., 2015) mapped the 21 cm HI line along with 4 OH lines and 19 H α recombination lines over $15^\circ \leq l \leq 67^\circ$ and $|b| \leq 1^\circ$ at ~ 20 arcseconds angular resolution.

For molecular gas, Dame et al. (1987) compiled the first well-sampled CO

($J = 1-0$) survey of the entire Galactic plane. This was a composite of a number of separate surveys made with a 1.2 m telescope in New York City and another similar facility at Cerro Tololo in Chile. The composite survey covered $\sim 7700 \text{ deg}^2$ of the sky – almost one fifth of the entire sky. This survey was largely superseded by the survey of Dame, Hartmann & Thaddeus (2001), another composite CO ($J = 1-0$) survey which built on the aforementioned one, with 16 times more spectra, at angular resolutions better by up to a factor of ~ 3 (up to 0.125°) and achieving ten times the sensitivity. The position–velocity diagrams of these surveys, in particular, allowed the spiral structure of the whole Galaxy to be seen in detail for the first time.

In this thesis the CO Heterodyne Inner Milky Way Plane Survey (CHIMPS; Rigby et al., 2016) is presented, a survey of dense molecular gas which was carried out at the JCMT. CHIMPS observed approximately 18 deg^2 of the first quadrant of the Inner Galaxy, between $28^\circ \lesssim l \lesssim 46^\circ$ in Galactic longitude and $|b| \lesssim 0.5^\circ$ in latitude. The $J = 3-2$ transition of ^{13}CO and C^{18}O were observed simultaneously, with an angular resolution of 15 arcseconds, and with 200 km s^{-1} of velocity coverage in 0.5 km s^{-1} channels.

CHIMPS complements other recent molecular gas surveys such as the Galactic Ring Survey (GRS; Jackson et al., 2006), which mapped the region $18^\circ \leq l \leq 55.7^\circ$ and $|b| \leq 1^\circ$ in $^{13}\text{CO} (1-0)$ from the 14 metre Five College Radio Astronomy Observatory (FCRAO). With angular resolution of 46 arcseconds and a 0.21 km s^{-1} velocity channel width, these data and their catalogues of molecular clouds (Rathborne et al., 2009; Roman-Duval et al., 2010) have been widely used for studies of the Inner Galaxy. Since ^{13}CO is a more optically thin tracer than the ^{12}CO of the aforementioned Dame surveys, the total molecular gas mass in the Galaxy ought to be better traced in this survey. The CO High-Resolution Survey

of the Galactic plane (COHRS; Dempsey, Thomas & Currie, 2013) of ^{12}CO (3–2) is ongoing at the JCMT and has currently charted an area of $17.5^\circ \leq l \leq 50.25^\circ$ with a width of $|b| \leq 0.25^\circ$, and with $|b| \leq 0.5^\circ$ for two small segments with an angular resolution of 14 arcseconds in 1 km s^{-1} -wide velocity channels. Another molecular gas survey of the first quadrant is going at the 45 metre Nobeyama Radio Observatory (NRO); FUGIN, the FOREST Ultra-wide Galactic plane survey In Nobeyama will simultaneously observe the $J = 1-0$ transition of ^{12}CO , ^{13}CO and C^{18}O in two segments, covering parts of the Inner Galaxy with $10^\circ \lesssim l \lesssim 50^\circ$ and Outer Galaxy with $198^\circ \lesssim l \lesssim 236^\circ$. FUGIN offers an improvement in angular resolution over the GRS, providing a JCMT-matching 15 arcsecond beam, but at a lower spectral resolution of 1.3 km s^{-1} .

The Southern Galactic plane has been historically surveyed more sparsely and less systematically in molecular gas, but a number of surveys are ongoing, and two in particular are being carried out from the 14 metre Atacama Pathfinder Experiments (APEX). The Three-mm Ultimate Mopra Milky Way Survey (ThrUMMS; Barnes et al., 2015) is observing the $J = 1-0$ transitions of ^{12}CO , ^{13}CO , C^{18}O and CN simultaneously at 1 arcminute angular resolution and with 0.3 km s^{-1} velocity resolution and SEDIGISM, which will cover $-60^\circ \leq l \leq 18^\circ$ in ^{13}CO and C^{18}O in the $J = 2-1$ transition is also under way at APEX.

In the submillimetre regime, the APEX Telescope Large Area Survey of the Galaxy (ATLASGAL; Schuller et al., 2009) surveyed the Inner Galaxy in $870 \mu\text{m}$ dust continuum, covering longitudes of $280^\circ < l < 60^\circ$ and latitudes of $|b| < 1.5^\circ$ for the most part, with the outer 20° in longitude in the Southern sky being covered in latitude by $-2^\circ < b < 1^\circ$ in order to account for the warp of the Galactic plane. The Bolocam Galactic Plane Survey (BGPS; Aguirre et al. 2011) has surveyed the dust continuum of 170 deg^2 of the Galactic plane at 1.1 mm

with an effective angular resolution of 33 arcseconds. It consists of an unbiased contiguous section covering longitudes of $-10^\circ \leq l \leq 90.5^\circ$ with a latitude coverage of $|b| \leq 0.5^\circ$, flaring to $|b| \leq 1.5^\circ$ at $75.5^\circ \leq l \leq 87.5^\circ$ to cover Cygnus X, and making several further $|b| \leq 1.5^\circ$ excursions and has four further targeted regions covering IC1396, NGC 7538, W3/4/5 and Gem OB1. The JCMT Galactic Plane Survey (JPS; Moore et al., 2015) has surveyed six equally-spaced regions covering approximately 5° in longitude and 1.7° in latitude, centred on $l = 10^\circ, 20^\circ, 30^\circ, 40^\circ, 50^\circ$ and 60° simultaneously at $450 \mu\text{m}$ and $850 \mu\text{m}$, with an angular resolution of 14 arcseconds.

These ground-based continuum surveys are joined by the space-based *Herschel* infrared Galactic Plane Survey (Hi-GAL; Molinari et al., 2010b), which has mapped the entire Galactic plane with a latitude coverage of $|b| \leq 1^\circ$ at 70, 160, 250, 350 and $500 \mu\text{m}$, with beam sizes ranging from 6 to 35 arcseconds. The *Planck* satellite also covered the Galactic plane at $350 \mu\text{m}$ and 5 cm wavelengths (Planck Collaboration et al., 2011), though, at 5 arcminutes, the angular resolution is too low to resolve the interior structures of molecular clouds.

The Hi-GAL, ATLASGAL, BGPS and JPS surveys together provide a census of the dense gas and star-forming clumps in the Galactic plane. With a range of wavelength and sensitivity coverage, they complement each other to provide coverage of the spectral energy distributions of dust structures over a large wavelength range. The main characteristics of the major CO and dust continuum surveys used in this thesis are summarised, for reference, in Table 1.3.

These molecular gas and dust continuum surveys are the most heavily referred to in this thesis, but there are a number of other surveys that are mentioned to a lesser extent, covering infrared wavelengths and in various radio continua. In the near infrared regime, the ongoing UKIDSS Galactic Plane Survey (Lucas

Table 1.3: The main molecular line and dust continuum surveys of the Inner Northern Galactic plane that have been used in this thesis.

Molecular line survey	Tracer	ν (GHz)	Resolution	Approximate coverage	Sensitivity (K channel ⁻¹)	Reference
CHIMPS	¹³ CO (3–2),	330.588	15 arcsec	27.5° < l < 46.3°	0.6	Rigby et al. (2016)
	C ¹⁸ O (3–2)	329.331	0.5 km s ⁻¹	$ b < 0.5^\circ$ –50 < $v_{\text{LSR}} < 150$ km s ⁻¹		
COHRS	¹² CO (3–2)	345.796	14 arcsec 1 km s ⁻¹	10.25° < l < 55.25° $ b < 0.25^\circ$ with $ b < 0.5^\circ$ patches –35 < $v_{\text{LSR}} < 150$ km s ⁻¹	1.0	Dempsey et al. (2013)
GRS	¹³ CO (1–0)	110.201	46 arcsec 0.21 km s ⁻¹	18° < l < 55.7° $ b < 1^\circ$ –5 < $v_{\text{LSR}} < 135$ km s ⁻¹	0.13	Jackson et al. (2006)

Dust cont. survey	Band (μm)	Bandwidth (μm)	Resolution (arcsec)	Approximate coverage	Sensitivity (mJy beam ⁻¹)	Reference
ATLASGAL	870	150	19	–60° < l < 60° $ b < 0.5^\circ$	50–70	(Schuller et al., 2009)
BGPS	1100	190	33	–10.5° < l < 90.5° $ b < 0.5^\circ$	11–53	(Aguirre et al., 2011)
Hi-GAL	70, 160, 250, 350 & 500	25, 80, 83, 117 & 167	5, 13, 18, 25 & 36	Full 360° in l $ b < 1^\circ$	16.6, 26.8, 12.8 17.6 & 14.9	(Molinari et al., 2010b)
JPS	450 & 850	32 & 85	14 (at 850 μm)	7° < l < 63°, $ b < 0.8^\circ$ in six ~ 5 deg ² patches	12–19 (at 850 μm)	(Moore et al., 2015)

et al., 2008) is surveying $15^\circ \leq l \leq 107^\circ$ and $142^\circ \leq l \leq 230^\circ$ with $|b| \leq 5^\circ$, and a narrower excursion into the Galactic Centre, in J , H and K bands down to the 18th magnitude. Moving into the mid-infrared wavelengths, *Spitzer*'s Galactic Legacy Infrared Mid-Plane Survey Extraordinaire (GLIMPSE; Benjamin et al., 2003; Churchwell et al., 2009) has provided a global view of the Milky Way through various surveys at 3.6, 4.5, 5.8 and 8.0 μm , with unprecedented depth (15th magnitude) and a 2 arcsecond angular resolution. The *Spitzer* survey MIPS GAL complements GLIMPSE with its Inner Galaxy survey at 24 and 70 μm , covering $-62^\circ \leq l \leq 63^\circ$ with a total latitude coverage of $|b| \leq 1^\circ$, and flaring to $|b| \leq 5^\circ$ in the Galactic Centre. The *Wide-field Infrared Survey Explorer* (WISE; Wright et al., 2010) encompassed the Galactic plane in its survey of the whole sky at wavelengths at 3.4, 4.6, 12 and 22 μm at angular resolutions between 6 and 12 arcseconds.

In addition to these unbiased contiguous surveys of the Galaxy, there have been a number of multi-tracer targeted follow-up surveys that have particularly targeted tracers of HMSF. The Red MSX Source survey (RMS; Lumsden et al., 2013) targeted sources that were found, through combination of *Midcourse Space Experiment* (MSX) and the Two Micron All-Sky Survey (2MASS), to have mid-infrared colours indicating the presence of embedded YSOs. These sources were extensively followed up with targeted spectral observations of molecular lines, radio continuum and H and K -band spectroscopy to characterise the YSOs, HII regions and planetary nebulae in the sample, and other survey data, such as those of *WISE* were used when required.

The Coordinated Radio and Infrared Survey for High-Mass Star Formation (CORNISH; Hoare et al., 2012; Purcell et al., 2013) used the Very Large Array (VLA) to survey 5 GHz continuum at arcsecond resolution, cataloguing ultra-

compact HII regions over $10^\circ \leq l \leq 65^\circ$ and $|b| \leq 1^\circ$. The Methanol Multi-beam survey (MMB; Caswell et al., 2010) scoured the Galactic plane, searching for 6.7 GHz methanol maser emission, sources almost always found with HMSF (Urquhart et al., 2015) with a ~ 6 arcminute beam at the Parkes telescope, with ~ 2 arcsecond-resolution follow-up with the Australia Telescope Compact Array. The full MMB coverage is $-174^\circ \leq l \leq 60^\circ$ with $|b| \leq 2^\circ$, and it has detected 972 6.7 GHz methanol masers (Caswell et al., 2010; Green et al., 2010; Caswell et al., 2011; Green et al., 2012; Breen et al., 2015). The 6.7 GHz MMB sources have also been followed up with observations of 12.2 GHz maser emission (Breen et al., 2012b,a, 2014, 2016), which have always been found to be cospatial with 6.7 GHz emission, and 45.3% of 6.7 GHz sources are found to have an associated 12.2 GHz counterpart.

All of these surveys, and many others not mentioned here, are continuing to provide a staggering wealth of data that enable research into many aspects of astrophysics. In this era of Galactic plane surveys, astronomers are able to create large and statistically significant samples of molecular clouds, clumps, cores, YSOs, HII regions, masers, and so on, that hope to answer some of the unsolved problems about the fundamental process of star formation.

1.6 Thesis outline

This thesis presents recent results from the dense molecular gas survey CHIMPS and, through combination with a number of other Galactic plane surveys listed in Section 1.5, examines an analogue of star formation efficiency over the survey area. The overarching aim is to help bridge the gap between our understanding of the effects of large-scale Galactic structure and smaller scale triggering agents

on the star formation process.

In Chapter 2, the observations and data reduction for the CHIMPS survey are described, and a number of regions are examined to check their consistency and draw comparisons with data from other surveys. Some physical properties of the emission seen in CHIMPS are calculated in Chapter 3, initially, before distance assignments allow the determination of sizes, masses and further physical properties in Chapter 4. The star-forming content of the sources identified within CHIMPS is examined in Chapter 5. The various results of these studies, and the conclusions drawn from them are discussed in Chapter 6 before, finally, plans for future studies are outlined in Chapter 7.

Chapter 2

CHIMPS

To facilitate a study of star formation over a significant section of the Galaxy, a spectral survey of molecular gas was carried out, covering approximately 19 deg^2 of the inner Northern Galactic plane. The survey is known as CHIMPS: the CO Heterodyne Inner Milky Way Plane Survey. In this Chapter, the observations making up the survey are described first, followed by descriptions of the data reduction and source extraction and finally some analyses that follow directly from the observations. The work in this Chapter has largely been published in Rigby et al. (2016).

2.1 Observations and data reduction

2.1.1 Observations

CHIMPS is a spectral survey covering the $J = 3-2$ rotational transitions of ^{13}CO at 330.587 GHz and C^{18}O at 329.331 GHz. The observations were made using the Heterodyne Array Receiver Program (HARP; Buckle et al., 2009) on the 15 m James Clerk Maxwell Telescope (JCMT) in Hawaii. The observations

cover approximately 19 deg^2 in the region $27.5^\circ \lesssim l \lesssim 46.4^\circ$ and $|b| \leq 0.5^\circ$, and were taken over a total of eight semesters, beginning in March 2010. The most recent data presented here were taken in 2014 June, and the proposal IDs are: m10ac06, m10au13, m10bu28, m11au05, m12bc19, m12bu37, m13au31, m13bu28, s13bu03 and s14au04.

HARP is a 16-receptor focal-plane array receiver operating over a submillimetre frequency range of 325–375 GHz. The receptors are superconductor–insulator–superconductor heterodyne detectors arranged in a 4×4 grid, each separated by 30 arcseconds on the sky. The Auto-Correlation Spectral Imaging System (Buckle et al., 2009) backend was used in conjunction with HARP, configured to use a 250 MHz bandwidth with 4096 frequency channels of width 61.0 kHz. The velocity width per channel is 0.055 km s^{-1} giving each CHIMPS observation $\sim 200 \text{ km s}^{-1}$ of usable velocity coverage. In the kinematic local standard of rest (LSRK) the velocity window was placed at -50 to 150 km s^{-1} at $l = 28^\circ$, and shifts with increasing Galactic longitude to -75 to 125 km s^{-1} at $l = 46^\circ$ in order to follow the Galactic velocity gradient. This range covers expected velocities of the regions associated with the Scutum–Centaurus tangent, and the Sagittarius, Perseus and Norma arms.

The observations were taken in a position-switching raster (on-the-fly) mode with off-positions measured below the Galactic plane with a latitude offset of $\Delta b = -1.5^\circ$ for each observation. This observation mode scans across the area of sky by the desired width filling the image with the first few rows of pixels. When the scan reaches the edge of the sky region, the array is shifted in a direction perpendicular to the scan direction before scanning over the field again in the reverse direction. In this way, each point of sky is covered by multiple receptors. This process is repeated until the required area of sky is covered, and a second

scan is then made by passing over the same area with a scan direction orthogonal to that of the first scan. A 1/2 array scan spacing was used, which shifts the array by half of its width in a direction perpendicular to the scan direction when it completes each row, before the scan direction is reversed. The raw data are written continuously as the telescope scans, in a time series format. This results in a sample spacing of 7.3 arcseconds which, in conjunction with a 0.25 s sample time, produces data cubes covering an area of $\sim 21 \times 21$ arcminutes in approximately one hour. A small number of observations, however, are slightly larger or smaller in size as discussed later on in this section.

As part of the standard operating procedure at JCMT, pointing accuracy is checked between most observations, and is generally found to be approximately 2 arcseconds in both azimuth and elevation. Tracking accuracy is better than 1 arcsecond over the course of a typical ~ 1 hour observation. The spectra are calibrated as the observations are made, using the three-load chopper-wheel method of Kutner & Ulich (1981). Intensities are thereby placed on the T_A^* (corrected antenna temperature) scale, which corrects for atmospheric attenuation, ohmic losses within the telescope, and rearward scattering and spillover. This T_A^* scale is then calibrated absolutely by observations of spectral standards (listed online¹) that are carried out on a nightly basis. Calibrated peak and integrated intensities of the standards must fall within 20% of the standard values, or else the receiver is re-tuned and calibration is repeated. The calibration uncertainty and pointing accuracy for the CHIMPS data are estimated in Section 2.2.1.

The T_A^* intensities can be converted to main beam brightness temperature (T_{mb}) by using the relation $T_{\text{mb}} = T_A^*/\eta_{\text{mb}}$ adopting the mean detector efficiency $\eta_{\text{mb}} = 0.72$ (Buckle et al., 2009). All intensities reported in this Chapter are on

¹ <http://www.eaobservatory.org/jcmt/instrumentation/heterodyne/calibration/>

the T_A^* scale unless stated otherwise.

The tiling pattern for the observations varies over three sections. In the section spanning $27.5^\circ \lesssim l \lesssim 32.8^\circ$, the cubes were observed such that the edges of the map are aligned in the equatorial coordinate system. For longitudes of $32.8^\circ \lesssim l \lesssim 44.1^\circ$, the cubes have the same dimensions as the lower longitude section, but are parallel to Galactic longitude and latitude. This tiling pattern was more efficient since no time was spent observing latitudes $|b| > 0.5^\circ$. The change in tiling pattern was due to an update to the observation setup for HARP raster maps which made it possible to observe square maps aligned with Galactic coordinates. The final $44.1^\circ \lesssim l \lesssim 46.4^\circ$ section was observed contemporaneously with the lowest longitude section, and consequently the observation edges are aligned with the equatorial gridlines. In the latter section the cubes also have slightly different dimensions; 18 of the cubes here measure approximately 22 arcmin along each side, and 10 cubes measure ~ 7.5 arcmin along each side; the smaller observations were to fill holes which were not covered by the original tiling pattern.

2.1.2 Data reduction

The raw time series data were reduced using the ORAC-DR data reduction pipeline (Jenness et al., 2015) which is built on the Starlink (Currie et al., 2014) packages CUPID (Berry et al., 2007), KAPPA (Currie et al., 2008) and SMURF (Jenness et al., 2008); specifically, the NARROWLINE reduction recipe was used, which is optimized for Galactic targets with narrow line widths (compared to the bandwidth) and small velocity gradients. The reduction pipeline transforms the raw time series spectra into spectral data cubes with longitude, latitude and velocity (l, b, v) axes. The reader may find more detailed descriptions of the pipeline in

Dempsey, Thomas & Currie (2013) and Jenness et al. (2015). The default quality assurance parameters were used as listed in table 2 of Dempsey, Thomas & Currie (2013). The pixel size used is 7.6 arcseconds, half of the beamwidth at this frequency and, to increase signal-to-noise, the spectral axis was re-binned into 0.5 km s^{-1} velocity channels.

Baseline subtractions were carried out using a fourth-order polynomial fit which was found to have sufficient flexibility to fit both linear and typical non-linear baselines well. Such bad baselines may result from external interference, for example (cf. Currie, 2013). Prior to reduction, an average spectrum was generated for each time series observation by integrating over the time and position axes to determine a velocity window containing any strong emission. These velocity windows were then masked out for the baseline subtraction by the software in order to avoid fitting the baseline polynomial to any broad emission features. The ORAC-DR parameters are listed in Appendix A.1.

The reduced data cubes each contain a variance array component determined for each spectrum from the system noise temperature by the SMURF utility MAKE-CUBE within the reduction pipeline. Upon output from ORAC-DR, the reduced cubes have undersampled edges caused by the change in direction of the scanning pattern when generating the raster maps, which also have low signal-to-noise ratios (SNRs). The cubes are cropped to remove these unwanted edge features. After cropping, there is a small overlap region (typically ≈ 1 arcmin) between adjacent tiles that results in a reduced noise level when adjacent tiles are mosaicked (see Figure 2.3).

There are a number of cases where the observation in a particular location has been repeated, and the duplicate observations were co-added using the MOSAIC_JCMT_IMAGES recipe from Starlink's PICARD package (Gibb, Jenness &

Economou, 2013), which is contained within ORAC-DR. All of the files that make up these combined cubes have been made available, should the user wish to co-add them in a different way, or use a single observation.

Additionally, a number of data cubes were taken when several of the 16 HARP receptors were unusable – sometimes with as few as 11 active receptors. If any further receptors are rejected by ORAC-DR, the reduced data cubes may contain locations with no valid spectra. This effect results in data cubes containing a regular grid of blank spectra at the particular locations which received no sampling. These blank voxels (three-dimensional pixels) were filled in using an interpolation routine (KAPPA:FILLBAD) which estimates a voxel value from adjacent voxels in the l – b plane. These interpolated spectra tend to have high variance values.

Throughout this thesis, three-dimensional (l, b, v) pixels are referred to as ‘voxels’, and the term ‘pixels’ is used to describe array elements making up either a two-dimensional l – b image, or as the elements of an l – b plane from an (l, b, v) cube.

2.2 The data

2.2.1 Overview

The CHIMPS survey data presented in this thesis cover a total of approximately 19 square degrees. A histogram of all voxel values in both isotopologues is shown in Figure 2.1. The voxel values can be modelled as being normally distributed about a mean value of -0.06 K in both cases, with a standard deviation of 0.6 and 0.7 K in the ^{13}CO and C^{18}O data, respectively. For optically thin gas at an excitation temperature of 10 K, typical of molecular clouds (e.g.

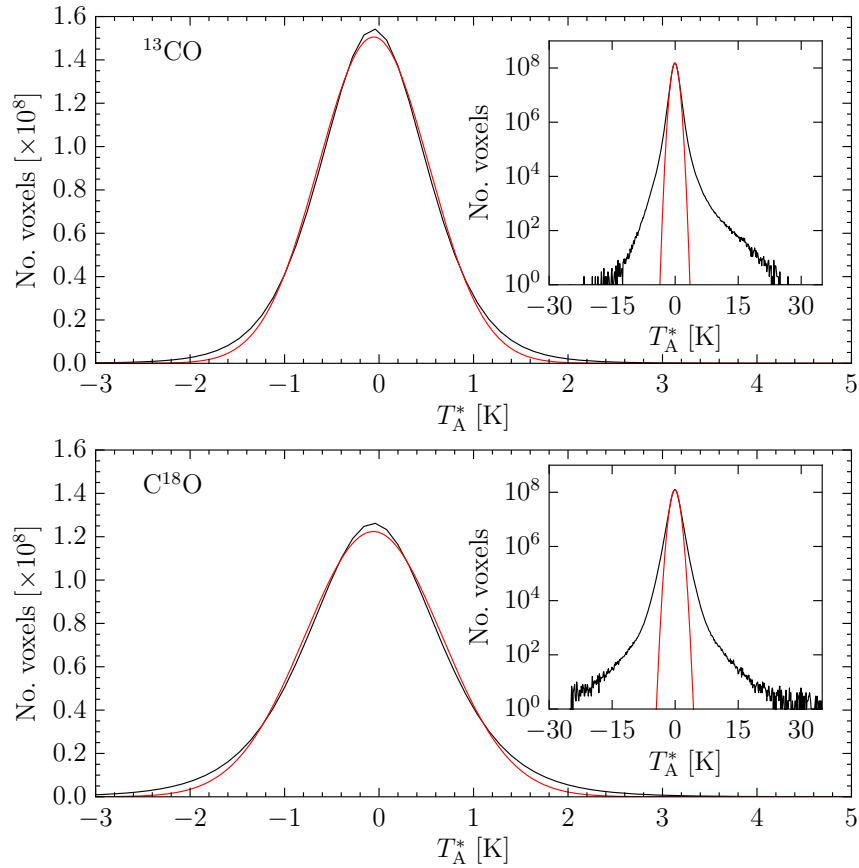


Figure 2.1: Histogram of all voxels in CHIMPS for ^{13}CO (top) and C^{18}O (bottom). The red lines show the Gaussian fits with the functions $1.51 \times 10^8 \exp[-(T_{\text{A}}^* + 0.06)^2 / 2 \times 0.58^2]$ and $1.22 \times 10^8 \exp[-(T_{\text{A}}^* + 0.06)^2 / 2 \times 0.73^2]$ for ^{13}CO (3–2) and C^{18}O (3–2), respectively. The bin width is 0.12 K. The insets show the Gaussian fits on a logarithmic scale.

Polychroni, Moore & Allsopp, 2012), these sensitivities correspond to gas column densities of $N(^{13}\text{CO}) \sim 3 \times 10^{14} \text{ cm}^{-2}$ and $N(\text{C}^{18}\text{O}) \sim 4 \times 10^{14} \text{ cm}^{-2}$, or $N(\text{H}_2) \sim 3 \times 10^{20} \text{ cm}^{-2}$ and $N(\text{H}_2) \sim 4 \times 10^{21} \text{ cm}^{-2}$ for ^{13}CO (3–2) and C^{18}O (3–2), respectively, assuming abundance ratios of $X(^{12}\text{CO}/^{13}\text{CO}) = 77$ (Wilson & Rood, 1994), $X(^{12}\text{CO}/\text{H}_2) \sim 8.5 \times 10^{-5}$ and $X(\text{C}^{18}\text{O}/\text{H}_2) \sim 1.7 \times 10^{-7}$ (Frerking, Langer & Wilson, 1982). For comparison, a higher excitation temperature of 30 K would imply a sensitivity to corresponding to a column densities of $N(^{13}\text{CO}) \sim 1 \times 10^{14} \text{ cm}^{-2}$.

There is a strong wing towards the higher positive brightness temperatures in the ^{13}CO distribution which can be identified as voxels containing emission, and a smaller wing extends out to negative antenna temperatures. The former is much stronger in ^{13}CO than C^{18}O where emission is weaker. The negative wings can be attributed to those observations which have significantly higher-than-average noise levels. The overall distribution is the convolution of the noise distributions for each individual observation, with the addition of detected emission in the positive antenna temperature wing. The 330 GHz band lies on the edge of an atmospheric absorption feature (Buckle et al., 2009, fig. 20), whereby transmission is lower at lower frequencies; as the lower frequency emission line, the C^{18}O data suffer more from the resulting attenuation and hence have broader noise wings in its voxel distribution.

A histogram of the root-mean-square (rms) values of every spectrum in the survey is shown in Figure 2.2. These values were determined by taking the square root of each pixel in the two-dimensional variance arrays that are produced for each observation in the data reduction process. Both distributions peak at values close to the standard deviations of the normal distributions in Figure 2.1. The rms noise map for each CHIMPS isotopologue is shown in Figure 2.3. The variation of noise across the map is caused by a combination of varying weather conditions, airmasses and variations in the numbers of active receivers on the HARP instrument over the course of the observations. It is also possible to see the lower noise where duplicated or repeated observations have been co-added.

Buckle et al. (2009) estimated that the HARP data have a calibration uncertainty of 15%. To check the accuracy of this figure for the CHIMPS data, the uncertainty in the calibration was calculated directly by comparing six observations that were made twice. These observations were those centred on the

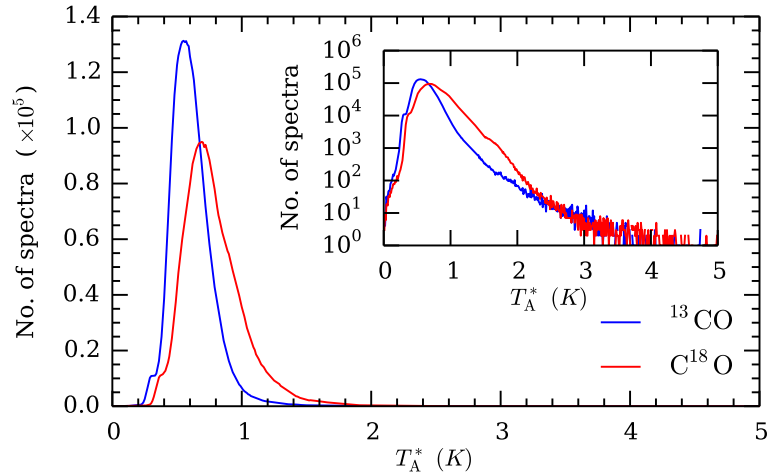


Figure 2.2: Histograms of the noise values in the CHIMPS data. The blue line shows the noise values for the ^{13}CO (3–2) data while the red line shows the noise values for the C^{18}O (3–2) data. The bin width is 0.01 K. The inset shows the same distributions on a logarithmic scale.

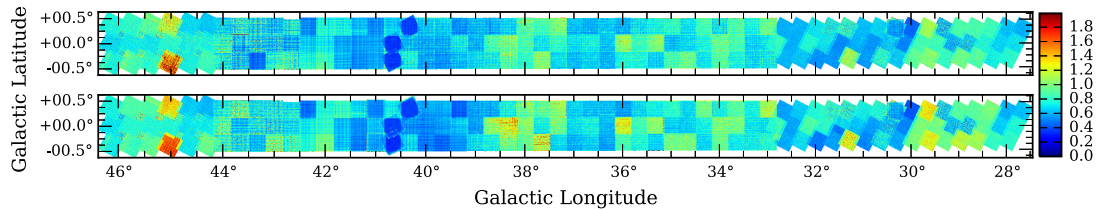


Figure 2.3: Noise (rms) maps for the CHIMPS data. Top: ^{13}CO (3–2). Bottom: C^{18}O (3–2). The intensity scale is in T_A^* (K).

(l, b) coordinates: $(30.35^\circ, 0.30^\circ)$, $(30.69^\circ, 0.30^\circ)$, $(31.02^\circ, 0.30^\circ)$, $(40.33^\circ, 0.33^\circ)$, $(40.66^\circ, 0.00^\circ)$ and $(40.66^\circ, -0.33^\circ)$. The observations were integrated over their velocity range, smoothed with a Gaussian kernel with a 3 pixel full-width half-maximum (FWHM) to an effective resolution of 27.4 arcseconds to increase the SNR, and masked to exclude any pixels with $\text{SNR} < 10$. To determine the relative accuracy of repeated measurements, the quantity $([T_A^*]_1 - [T_A^*]_2)/[T_A^*]_1$ was calculated for each pair of pixel values with the same sky position, where $[T_A^*]_1$ and $[T_A^*]_2$ refer to the two measurements made at each position. The resulting distribution is shown in Figure 2.4, and a normal distribution fit finds a standard deviation of 0.144, indicating that the 15% calibration uncertainty is well

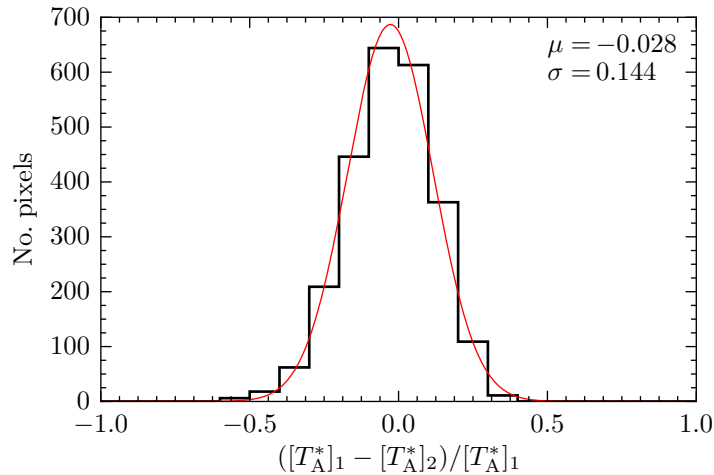


Figure 2.4: The distribution of the relative corrected antenna temperatures for pixels with repeated measurements (black histogram) is found to be well fitted by a normal distribution (red) with a mean of -0.028 and a standard deviation of 0.144 .

matched to these data. These repeated observations were also used to check pointing accuracy, and after smoothing the data slightly to an angular resolution of 16 arcseconds, the mean difference in sky position between the centroids of a sample of four bright and compact sources visible in these velocity-integrated images was found to be ~ 3 arcseconds.

2.2.2 Extracting the emission

The fully reduced (l, b, v) data cubes contain a significant number of emission-free voxels since the bandwidth is much greater than the velocity width of emission features, even in the brightest regions of the Galactic plane such as the Scutum tangent. In order to avoid integrating large numbers of noise voxels in each spectrum to form an integrated intensity map with a significant noise component, a source extraction was carried out.

To do this, the entire 19 square degrees of CHIMPS were mosaicked in several sections using KAPPA:WCSMOSAIC which uses a Lanczos kernel of the form

$\text{sinc}(\pi x)\text{sinc}(s\pi kx)$, where x is the pixel offset from the input pixel, to assign pixel values in the mosaicked image’s pixel grid. A spatial smoothing was then applied using a Gaussian kernel with a FWHM of 3 pixels in order to account for the beam profile as well as a small smoothing effect caused by the re-gridding of pixels in the mosaicking routine, resulting in an effective resolution of 27.4 arcseconds.

A SNR cube of each survey section in both isotopologues was produced using `KAPPA:MAKESNR`, which divides the intensity of each voxel by the square root of the variance value of the spectrum to which the voxel belongs. The emission generally occupies a small part of the spectrum, so the fact that the emission is not masked out before calculating the variance is of little consequence. A spatial filtering routine (`CUPID:FINDBACK`) was next applied to subtract an estimate of the background from each spectrum, and to minimise the regular noise features which appear in the CHIMPS cubes due to variations in sensitivity between receptors which are discussed in Section 2.2.1.

The source extraction algorithm ‘FellWalker’ (Berry, 2015) in the `CUPID` routine `FINDCLUMPS` was applied to the background-subtracted SNR cubes. For each voxel, `FellWalker` examines its neighbouring voxels for any higher values, moving to the highest value within the search volume if possible. If no adjacent voxels have a higher value, then the search radius is increased (up to a user-defined maximum search radius), and a jump is made to the new highest voxel value found. When a peak is reached and there are no higher values in the neighbourhood, a clump is defined, and all voxels which lead to that peak are designated as being part of the clump. There is an additional criterion for the minimum number of voxels required for a clump to be defined, in an attempt to reduce false positives from noise spikes, which was set to the minimum allowed value of

16 (corresponding to a cubic source of width 2.5 pixels). FellWalker was chosen for this study over the ClumpFind algorithm (Williams, de Geus & Blitz, 1994) because comparisons by Berry (2015) on a sample of simulated Gaussian clumps found that the FellWalker results are less dependent on the specific parameter settings than for ClumpFind.

Source extraction was carried out on the SNR cubes instead of the intensity cubes so that the effects of the varying background over the 178 individual cubes would not cause either faint sources that have good signal-to-noise in regions of low background to be missed, or false positives to present a significant issue. The background in the original cubes varied significantly between individual observations taken over the course of 4 years due to a varying number of active receptors and the variable weather conditions the data were taken under. A similar approach is used in Moore et al. (2015) who also found that the best results were achieved using FellWalker on SNR maps.

The parameters used for the FellWalker source extraction are listed in Appendix A.2. For the extraction of ^{13}CO sources, the noise level was regarded as all voxels with $\text{SNR} < 3$, and sources were required to have a peak with $\text{SNR} > 5$. Due to comparative rarity of C^{18}O compared to ^{13}CO the criteria for extraction of C^{18}O sources had to be less exacting; the SNR threshold below which voxels are considered noise was lowered 2, though sources were still required to have a peak with $\text{SNR} > 5$.

Varying the FellWalker parameters, of course, produces different results in both the output catalogues and masks. The minimum number of voxels required for a clump was set to 16, corresponding to a cuboid with a width of 2.5 voxels in each of the three axes. If this threshold is reduced, then the likelihood of mistakenly identifying spurious noise artefacts as clumps of emission increases.

The minimum peak SNR for a clump to be detected was set to 5 so that the occurrence of false positives can be mitigated, and accordingly the minimum dip in SNR between adjacent clumps for them to be considered separate was also set to 5. A smaller value for either of these parameters results in more clumps being found due to the inclusion of more false positives, or the fragmentation of clumps into several smaller ones. Clumps which touch the edges of the survey were excluded because their extent outside of the survey is unknown.

In the final stage of FellWalker, an iterative cleaning routine is applied that replaces the clump index of every voxel with the most commonly occurring value found within a local volume of $3 \times 3 \times 3$ voxels. A test of the number of clumps found by FellWalker with the parameters listed in Appendix A.2, but varying the number of cleaning iterations applied found that each additional iteration reduces the number of clumps found by $\sim 10\%$, and only converges after ~ 50 iterations. At this point, visual inspection shows that clumps of emission have clearly been joined up too liberally, and so only two such iterations were applied in the CHIMPS source extraction, a number which was found to yield agreeable results upon visual inspection.

The masks generated from the smoothed $^{13}\text{CO} (3-2)$ and $\text{C}^{18}\text{O} (3-2)$ emission were applied to the native resolution $^{13}\text{CO} (3-2)$ and $\text{C}^{18}\text{O} (3-2)$ data, respectively, to produce the emission maps of Section 2.2.3. However, only the smoothed $^{13}\text{CO} (3-2)$ emission mask and clump catalogue are used throughout the remainder of this thesis since $\text{C}^{18}\text{O} (3-2)$ emission is relatively sparse and weak. The $^{13}\text{CO} (3-2)$ catalogue produced by FellWalker is discussed in Section 4.1.

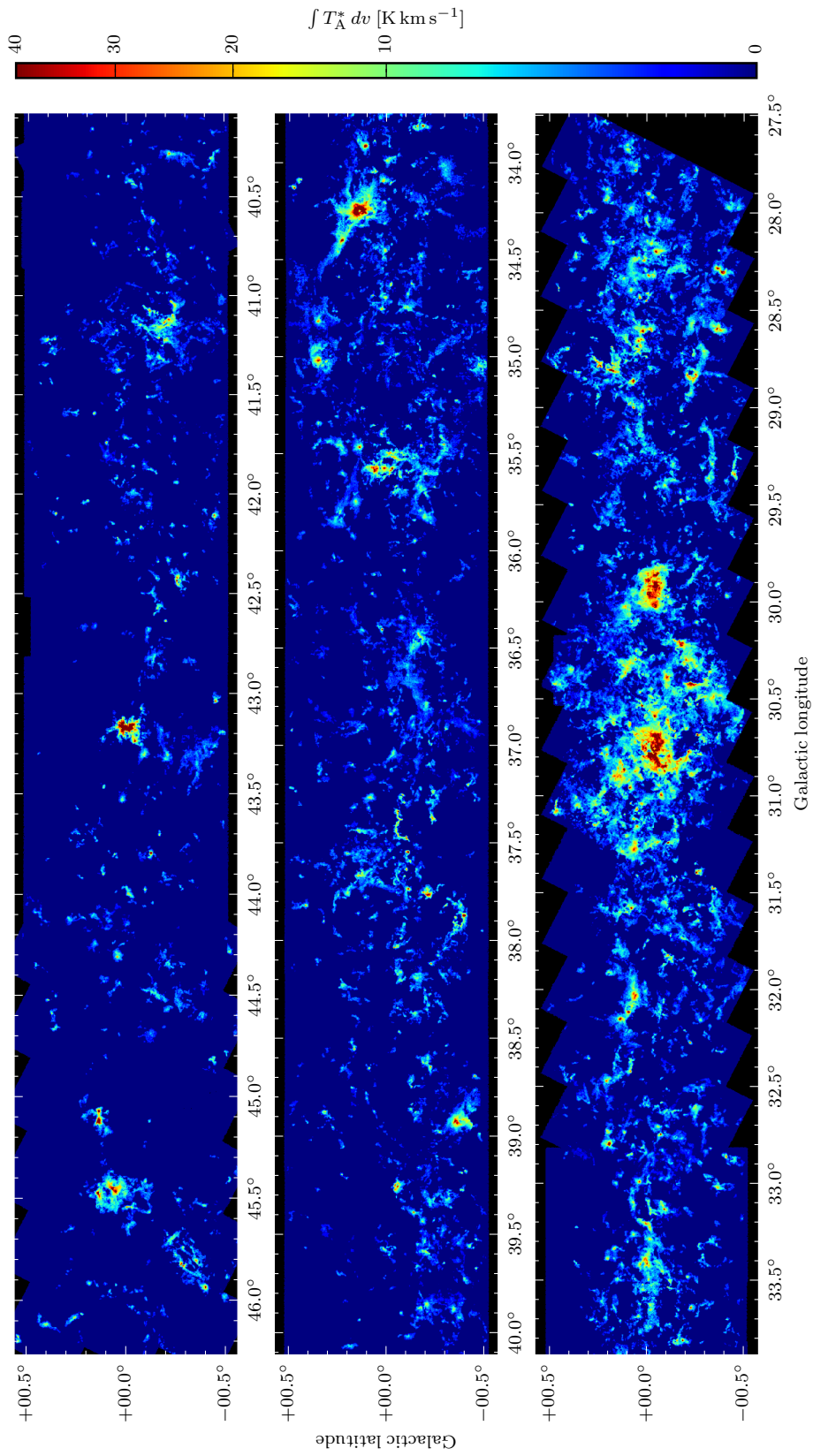


Figure 2.5: The integrated emission (T_A^*) in CHIMPS ^{13}CO (3–2). All voxels with a SNR above 5 are included, and any voxels containing emission above a SNR of 3 which is assigned to a clump with a peak SNR of more than 5 are also included. Each spectrum was integrated over all velocity channels.

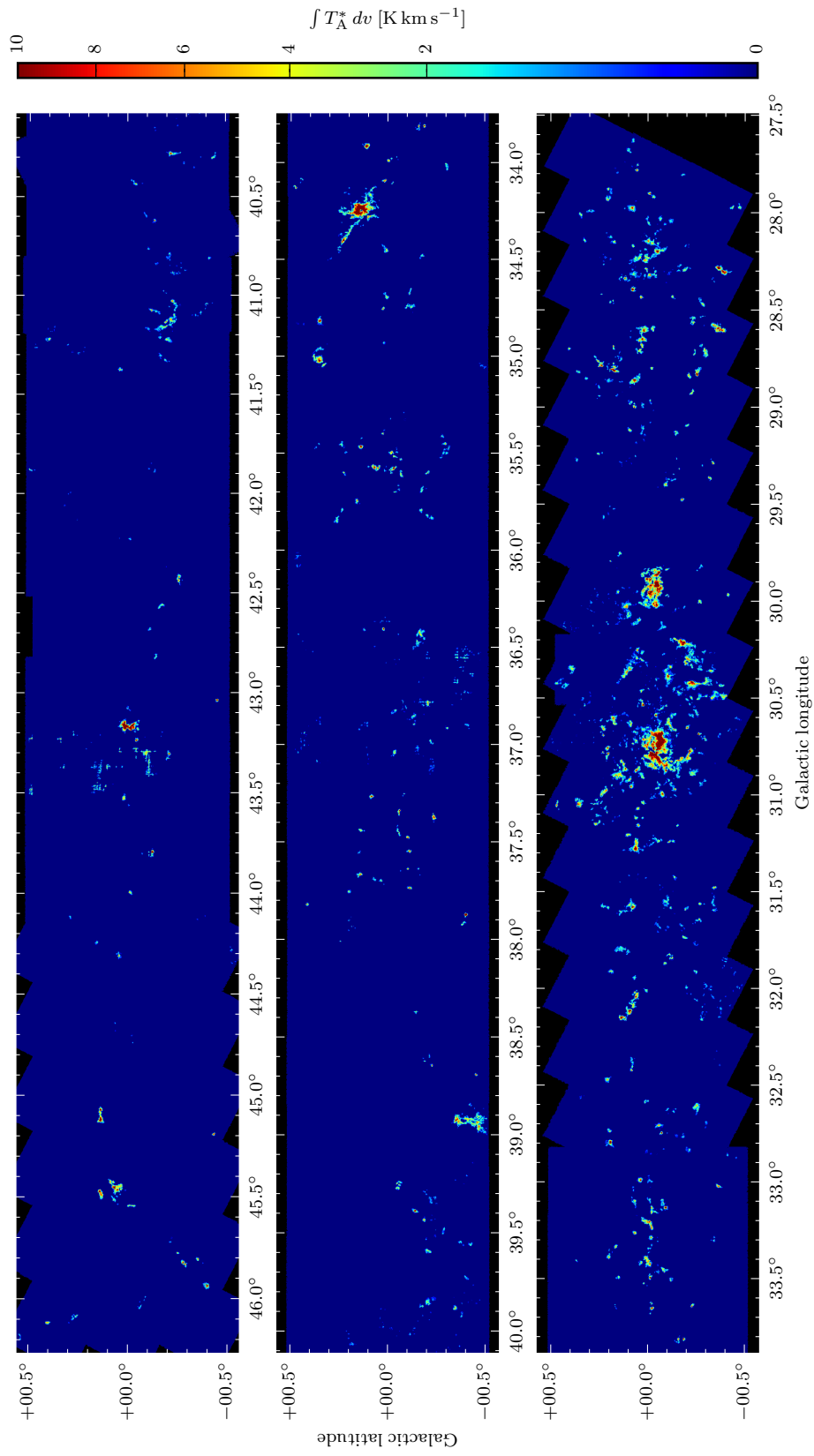


Figure 2.6: The integrated emission (T_A^*) in CHIMPS C^{18}O (3–2). All voxels with a SNR above 5 are included, and any voxels containing emission above a SNR of 2 which is assigned to a clump with a peak SNR of more than 5 are also included. Each spectrum was integrated over all velocity channels

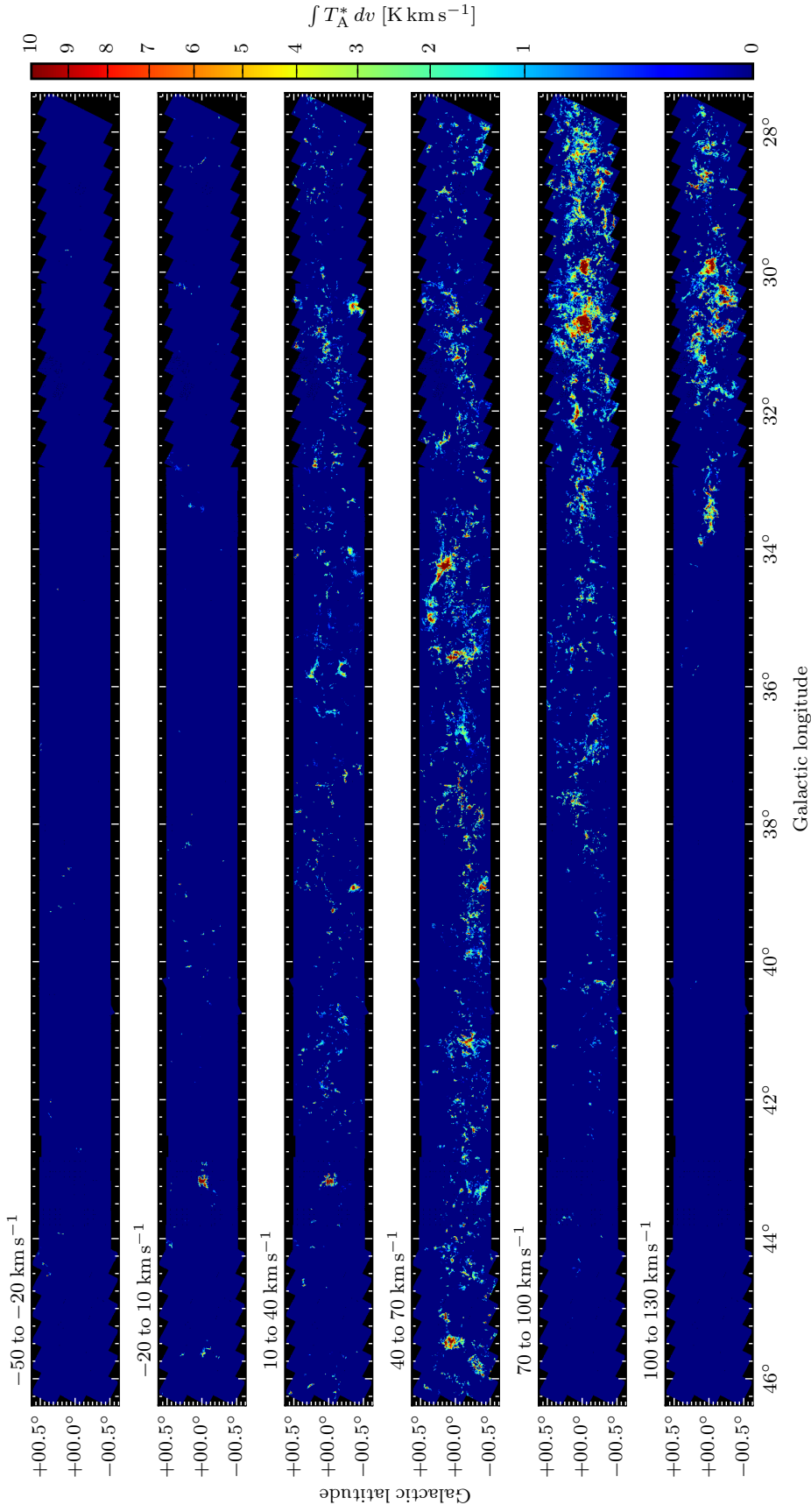


Figure 2.7: Integrated emission (T_A^*) of the ^{13}CO data of CHIMPS split into 30 km s^{-1} channels. All emission with a SNR of 5 or higher is shown, and additionally any emission with a SNR of at least 3, which is related to a clump with a peak SNR of 5 or more. The units of the intensity scale are K km s^{-1} .

2.2.3 Integrated position–position maps

Figures 2.5 and 2.6 show the integrated ^{13}CO (3–2) and C^{18}O (3–2) emission, respectively, with $\text{SNR} > 5$ (measured for each individual spectrum) in CHIMPS, integrated over all velocity channels. This emission additionally includes any emission with $\text{SNR} > 3$ in the case of ^{13}CO (3–2), or $\text{SNR} > 2$ in the case of C^{18}O (3–2), which was assigned to an extracted clump. As a result of the FellWalker parameters used, any voxels containing emission which has a SNR of over 3 or 2 in ^{13}CO or C^{18}O respectively, but is not assigned to $\text{SNR} > 5$ clump are not included in the integrated emission of Figures 2.7 or 2.8 either. There is much more emission visible in the ^{13}CO (3–2) images due to the higher abundance of ^{13}CO relative to C^{18}O . The brightest regions in the survey are some of the most massive star-forming regions in the Galaxy, and the W43 and W49A complexes are clearly visible at $l = 30.7^\circ$ and 43.1° , respectively. In the C^{18}O (3–2) emission map of Figure 2.6, there are a small number of places where noise features have been extracted by FellWalker; for example there are such noise features at $l = 43.3^\circ$, $b = -0.01^\circ$ and $l = 36.5^\circ$, $b = -0.035^\circ$. These appear due to the lowering of the detection threshold to $\text{SNR} > 2$ for the C^{18}O data, which was necessary to enable the fainter emission to be seen, but real clumps also emerge which were not visible using the same detection limits as for the ^{13}CO . Figure 2.7 shows the ^{13}CO (3–2) emission integrated over 30 km s^{-1} velocity windows, allowing emission features to be separated along the line of sight and fainter clouds to become more visible than in Figure 2.5.

2.2.4 Integrated position–velocity maps

Figure 2.8 shows the position–velocity diagrams for the ^{13}CO and C^{18}O emission, integrated over the latitude axis. The spiral arms are clearly visible in the

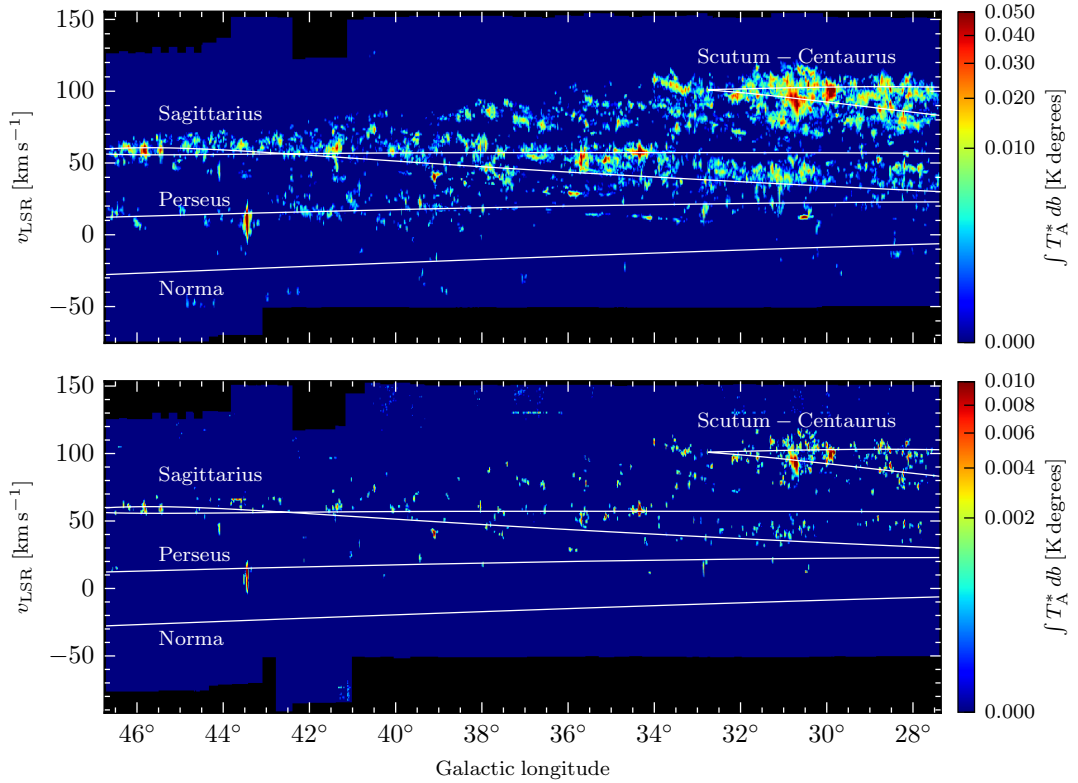


Figure 2.8: Position–velocity diagrams for the ^{13}CO (*top*) and C^{18}O (*bottom*) emission (T_{A}^*) with a SNR of at least 3 in CHIMPS in which the emission was integrated over the latitude axis. The colour mapping uses a third-root intensity scale, and has units of K degrees. Each pixel in the longitude axis is the sum of 10 pixels at the same velocity. The overlaid white lines are the spiral arm loci of the four-arm model of Taylor & Cordes (1993), updated in Cordes (2004), projected into the longitude–velocity plane.

^{13}CO map as continuous streams of emission, with inter-arm regions also visible as relatively emission-free regions separating the arms. Spiral arms have been overlaid which derive from the models of Taylor & Cordes (1993) and Cordes (2004), with the position–velocity–space projections calculated in Urquhart et al. (2013b). The molecular gas traced by CHIMPS fits reasonably well with this four-arm model, though there are some significant deviations. There is little emission visible which falls on the locus of the distant Norma arm, though a shift of $10\text{--}20\text{ km s}^{-1}$ towards negative velocities across the CHIMPS region would be consistent with a number of emission features visible here.

There is a significant quantity of emission lying between the Scutum–Centaurus and Sagittarius arms, which has been seen before in ^{13}CO (1–0) (Lee et al., 2001; Stark & Lee, 2006), though not with this clarity. The structure of this emission is much clearer in CHIMPS than in Dame, Hartmann & Thaddeus (2001), Lee et al. (2001), GRS, or COHRS and has a number of possible explanations. First, this emission could be a minor spiral arm which lies in-between the Scutum–Centaurus and Sagittarius spiral arms. This is suggested by a potential loop feature that extends from the low-longitude end of the survey up to a tangent at approximately $l = 39^\circ$, spanning approximately $60\text{--}90\text{ km s}^{-1}$ in velocity. Secondly, this could be an extension of the Scutum–Centaurus arm itself, with an elongated tangent region reaching up to roughly 39° in longitude. Thirdly, this could be a bridging structure of the kind described by Stark & Lee (2006) or some similar spur structure, which does not extend far enough to be considered an arm in its own right. Finally, it is possible that this region contains a number of spurs which form their own coherent structures in this parameter space, and which generally extend for several degrees. These coherent objects in position–velocity space might also be one origin of filaments (see Ragan et al., 2014), and arise through the shear of dense regions due to Galactic rotation in the simulations of Dobbs (2015). Tests to distinguish between these scenarios are regrettably beyond the scope of this work.

Emission in the C^{18}O map is much more sparse, though the broad emission from W49A is a prominent feature, and its compact size makes it stand out when compared to the other bright regions such as W43. W49A contains a cluster of ultra-compact HII regions (Urquhart et al., 2013b), with powerful H_2O maser outflows (Smith et al., 2009) and strong bipolar outflows seen in ^{12}CO ($J = 1 \rightarrow 0$) (Scoville et al., 1986). There are a small number of noise features

also visible in the C¹⁸O map, which are usually easy to identify as they tend to appear at the low- or high-velocity ends of the spectral band. An example of such a noise feature can be seen extending from $\sim 36^\circ$ to 37.5° at $\sim 130 \text{ km s}^{-1}$.

2.3 Data access

The CHIMPS data are available to download from the CANFAR archive². The data are presented in the FITS format and are available primarily as mosaics which each make up approximately 1 square degree, available at intervals of half a degree. In addition to these mosaics, the individual cubes which each represent a single observation (or several observations for the co-added cubes) are available, along with the variance arrays for the mosaics and individual cubes. The integrated emission maps in $l-b$ and $l-v$ space of Section 2.2.3 can also be downloaded. The data are presented in T_{A}^* with data cubes in units of K, and the integrated $l-b$ and $l-v$ maps have units of K degrees and K km s^{-1} respectively.

The raw data can be downloaded from the Canadian Astronomy Data Centre's JCMT Science Archive using the Project IDs listed in Section 2.1.

2.4 Comparison with GRS and COHRS

The GRS mapped the inner Galactic plane in ¹³CO (1–0) at an angular resolution approximately three times lower than CHIMPS. Since the critical density of the $J = 1-0$ transition is also lower than that of $J = 3-2$ ($\sim 10^3 \text{ cm}^{-3}$ and $\sim 10^4 \text{ cm}^{-3}$ at 10 K, respectively), the molecular gas traced by CHIMPS is much more concentrated spatially (and presumably traces higher column densities) than in GRS, allowing us to see the dense cores and filaments which appear

² <http://dx.doi.org/10.11570/16.0001>

to be almost ubiquitous and closely associated with the star formation seen in continuum surveys such as Hi-GAL (Molinari et al., 2010b).

Figure 2.9 shows the integrated intensity l , b and v profiles for the GRS over the extent of the CHIMPS region, and of the two CHIMPS tracers. In each case, the profiles show the intensity normalised to the peak intensity in the profile and integrated over both orthogonal axes. For the two CHIMPS tracers, the extracted emission described in Section 2.2.3 was used to make the profiles, whereas the GRS data were integrated over all velocity channels. In the longitudinal profile (integrated over latitude and velocity), the regions of strongest emission in the GRS are generally coincident with a peak in the CHIMPS data, though the $\text{C}^{18}\text{O}(3-2)$ only appears at the highest column density regions. The peak in the longitudinal profile at $l \approx 34.2^\circ$, for example, is much more sharply peaked in $\text{C}^{18}\text{O}(3-2)$ than $^{13}\text{CO}(3-2)$ which is itself more sharply peaked than the $^{13}\text{CO}(1-0)$, possibly indicating self-absorption in the ^{13}CO spectrum, or greater turbulence in the lower density material. Additionally, the star-forming region W49A located at $l \approx 43.2^\circ$ stands out with a strong, sharp peak in $^{13}\text{CO}(3-2)$.

The latitudinal profiles (integrated over longitude and velocity) also display a trend of increasing sharpness in denser gas tracers and at higher resolution as expected, and the normalised intensity of $^{13}\text{CO}(3-2)$ is close to zero at the limits of the survey. It is therefore reasonable to suggest that our latitude range for CHIMPS is not missing significant quantities of emission in the inner Galactic plane. The two ^{13}CO transitions have profiles which are asymmetric about $b = 0^\circ$ which can be attributed to both the warp in the Milky Way's disc, and a parallax effect caused by the position of the Sun between 4 and 30 pc above the Galactic plane (de Vaucouleurs & Malik, 1969; Stenholm, 1975; Bahcall & Bahcall, 1985).

The velocity profiles (integrated over longitude and latitude) are again more

sharply peaked in the CHIMPS tracers compared to GRS as the diffuse gas component becomes transparent, leaving the distributions of gas denser than $\sim 10^4 \text{ cm}^{-3}$. The C^{18}O peak at $\approx 130 \text{ km s}^{-1}$ which is not seen in the other tracers is caused by noise artefacts that appear as a result of the less stringent noise criteria applied to this isotopologue described in Section 2.2.2.

In comparison to COHRS, a JCMT survey of ^{12}CO (3–2) covering much of the CHIMPS area, there is significantly less faint and extended emission in the CHIMPS data. The higher optical depths and self-absorption in the ^{12}CO data suppress the emission peaks and there is an additional effect of photon pumping at high optical depths which reduces the effective critical density of ^{12}CO (3–2), enhancing emission from more diffuse gas. These effects combine to reduce the contrast between the between high- and low-column density regions in the COHRS data. There is, therefore, more contrast between the faint and bright emission in CHIMPS and massive cores appear to have a steeper density profile as more of the densest gas can be observed. This means that it is possible to deduce dense gas masses in CHIMPS with greater accuracy, and the sensitivity in terms of column density is less complex due to the lesser contribution of photon pumping.

A region centred on Galactic coordinates $l = 34.25^\circ$, $b = +0.15^\circ$ and with the velocity range $v_{\text{lsr}} = 45 - 70 \text{ km s}^{-1}$ (hereafter the ‘G34 region’, also known by the identifier IRAS 18507+0110), which contains a number of ultra-compact HII regions seen in the Red MSX Source survey (Lumsden et al., 2013), is shown in Figure 2.10. This region lies at a distance of 4.0 kpc based on the water maser parallax measurements of G34.26+0.15 (Hofner & Churchwell, 1996), and has a Galactocentric distance of $\sim 4.5 \text{ kpc}$, based on the Galactic rotation curve of Brand & Blitz (1993) and central velocity of 57.5 km s^{-1} . CHIMPS, COHRS

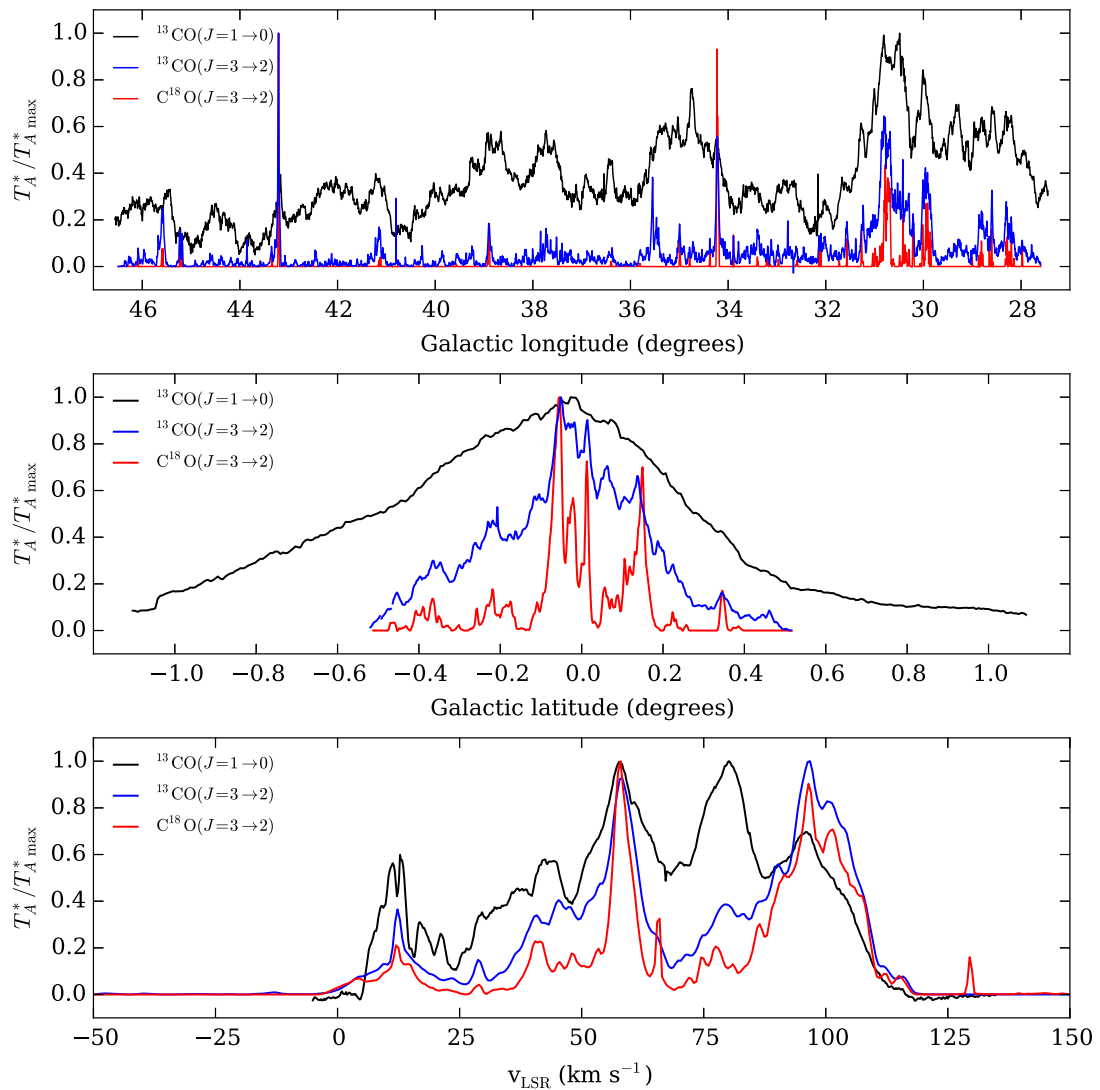


Figure 2.9: Integrated (one-dimensional) longitudinal, latitudinal, and velocity profiles for the GRS and the two CHIMPS isotopologues. In each case, the one-dimensional profile was created by integrating over the two orthogonal axes. The T_A^* intensity is normalized to the peak intensity in the profile.

and ATLASGAL (870 μm) imaging have been smoothed spatially using Gaussian kernels with FWHM of 43.4, 42.9 and 41.8 arcseconds respectively in order to match the 46 arcseconds resolution of the GRS and re-gridded to the GRS pixel size. Intensity scales in the various CO data were converted from T_{A}^* to T_{mb} by dividing by main beam efficiencies of $\eta_{\text{mb}} = 0.72$ and 0.61 for CHIMPS and COHRS, respectively (Buckle et al., 2009), and $\eta_{\text{mb}} = 0.48$ for GRS (Jackson et al., 2006).

The various CO cubes were aligned in three dimensions, and histograms (left column, second row from bottom) of the voxel-by-voxel intensity ratios of $^{13}\text{CO}(1-0)$, $^{12}\text{CO}(3-2)$, and $\text{C}^{18}\text{O}(3-2)$ with respect to $^{13}\text{CO}(3-2)$ are presented. The intensity ratio was measured only for voxels in which both species have an intensity above five times the rms value of all voxels each cube. In instances where both species are optically thin, the intensity ratio ought to be equal to the abundance ratio of the species. It is unlikely, however, that a significant number of voxels are optically thin in both species for any pairing. The black histogram, showing the intensity ratio distribution of $^{13}\text{CO}(1-0)$ to $^{13}\text{CO}(3-2)$, has a median value of 0.4. For optically thin gas at temperatures significantly greater than $h\nu/k$, this ratio should approach a value of one ninth since $T_{\text{R}}(J+1 \rightarrow J)/T_{\text{R}}(J \rightarrow J-1) = (J+1/J)^2$. Deviations from small τ in either transition, along with uncertainties in the intensity measurement contribute towards broadening this distribution.

The red histogram shows the intensity ratio of the two CHIMPS isotopologues, $\text{C}^{18}\text{O}(3-2)$ to $^{13}\text{CO}(3-2)$, and in the cases where both voxels are optically thin, the abundance ratio of C^{18}O to ^{13}CO should be recovered. At a Galactocentric distance of 4.5 kpc, the isotopic abundance ratios for $^{12}\text{C}/^{13}\text{C}$ (Milam et al., 2005) and $^{16}\text{O}/^{18}\text{O}$ (Wilson & Rood, 1994) indicate that an abundance ratio

of $C^{18}O/^{13}CO \sim 1/6$ should be expected, which is consistent with these measurements. The blue histogram which measures the intensity ratio of $^{12}CO(3-2)$ to $^{13}CO(3-2)$ has a median value of < 10 , whereas the Milam et al. (2005) relation predicts a value close to 50. It is unlikely that any optically thin $^{12}CO(3-2)$ emission is detected where $^{13}CO(3-2)$ is also recovered and so the intensity ratio is suppressed, and further reduced by self-absorption which is likely to be significant in this high optical depth transition.

The pixel-to-pixel correlations of $^{13}CO(1-0)$, $^{12}CO(3-2)$, $C^{18}O(3-2)$ and $870\ \mu\text{m}$ with $^{13}CO(3-2)$ of the integrated images for the G34 region are also presented in Figure 2.10. In the correlations between the different CO isotopologues there are strong optical depth effects visible where the denser tracer dominates in the brightest regions, and these effects are more significant in the integrated image, where any optically thin voxels are folded into an optically thick column. These distributions also contain noise pixels, though these are not significant when integrated over the velocity range, which make up the high concentration of points towards the origin. The correlation between $870\ \mu\text{m}$ and $^{13}CO(3-2)$ emission was measured only for pixels with intensities greater than five times the rms $870\ \mu\text{m}$ value. For the majority of eligible pixels a linear correlation is visible between dust and CO emission, extending from ~ 0 to $800\ \text{K km s}^{-1}$ in $^{13}CO(3-2)$ and ~ 0 to $50\ \text{Jy}$ in S_{870} , but there are a number of pixels in which the dust emission becomes significantly brighter. This could be caused by $^{13}CO(3-2)$ emission becoming optically thick where the brightest $870\ \mu\text{m}$ emission is, though these may also correspond to a small number of objects that are bright and compact in the continuum data but disappear into the background in the degraded-resolution $^{13}CO(3-2)$ image.

This study of the G34 region shows that the brightness temperatures mea-

sured within the CHIMPS data are consistent with comparable survey data, and demonstrate that they, when used in conjunction with data sets such as GRS and COHRS, provide a more complete picture.

2.5 Example CHIMPS data

Some sample close-ups of the CHIMPS data are illustrated in Figure 2.11 in which some of the interesting regions in the survey are examined in integrated $^{13}\text{CO}(3-2)$ (first from left column), $\text{C}^{18}\text{O}(3-2)$ (second from left column) maps, $^{13}\text{CO}(3-2)$ position-velocity space (second from right column) and the $70\ \mu\text{m}$ Hi-GAL images for comparison (right column). In each case, the CHIMPS data used contain the emission extracted according to Section 2.2.2.

The W43 star-forming region ($l = 30.75^\circ, b = -0.05^\circ$), illustrated in row (a) of Figure 2.11 is the largest region of bright and extended emission within CHIMPS (see Figure 2.5). At a distance of 5.5 kpc (Zhang et al., 2014a), W43 lies at the tangent of the Scutum–Centaurus arm and its meeting point with the near-end of the Long Bar (Nguyen Luong et al., 2011). The region presented has been integrated over a velocity range of $v_{\text{LSR}} = 80 - 110\ \text{km s}^{-1}$, identified by Nguyen Luong et al. (2011) as the central part of the cloud; indeed, this velocity range is extremely well matched by the CHIMPS spectra of the region in both $^{13}\text{CO}(3-2)$ and $\text{C}^{18}\text{O}(3-2)$. W43 is frequently referred to as a ‘mini-starburst’ (e.g. Motte, Schilke & Lis, 2003), implying a high star formation efficiency, and while it contains a high-column-density ridge known as ‘MM1’ with a high star-forming efficiency of 8% (Louvet et al., 2014), the region as a whole does not appear to be particularly unusual.

Eden et al. (2012) find that, while the fraction of mass in dense BGPS clumps

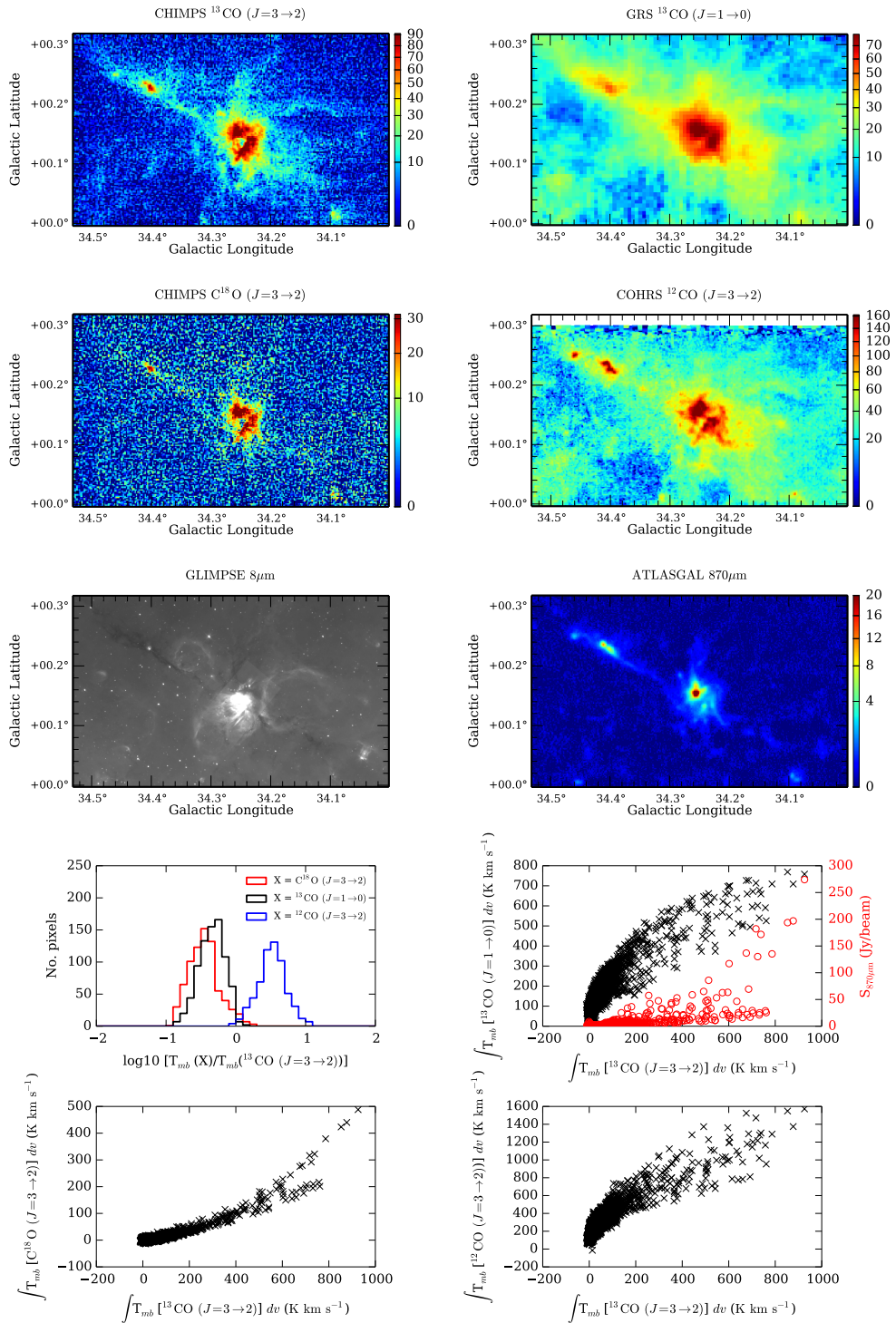


Figure 2.10: Top: images of the G34.2+0.1 region in the two CHIMPS isotopologues, and imaging from GRS, COHRS, GLIMPSE and ATLASGAL. The images are shown in their native resolution, and the CHIMPS, COHRS and GRS images are integrated over $45\text{--}70\text{ km s}^{-1}$. The units on the integrated T_{mb} intensity scales are K km s^{-1} , with the exception of the ATLASGAL image, which is in units of Jy per beam. A square-root scaling is used in each image. Bottom: histogram of the intensity ratios of the different species compared to ^{13}CO ($3\rightarrow 2$) calculated on a voxel-by-voxel basis for all voxels brighter than 5σ , and pixel-by-pixel correlations for all pixels in the integrated images.

compared to the mass in $^{13}\text{CO}(1-0)$ for clumps coincident with the W43 HII region is high, the median value of this quantity for all clumps in the region is not enhanced when compared to other regions along the same line of sight. Similarly Moore et al. (2012) and Eden et al. (2015) find that the star-formation efficiency averaged at this Galactocentric radius is also unexceptional, with all three studies suggesting that W43 is consistent with being part of a normal distribution of star-forming properties. W43 is also the subject of the recent pilot study for The HI, OH, Recombination Line Survey of the Milky Way (THOR; Bihl et al., 2015), who revise the mass in HI of the complex, finding a lower limit of $6.6 \times 10^6 M_{\odot}$.

A striking filament visible in the CHIMPS data (see Figure 2.5) is examined in row (b) of Figure 2.11, centred on $l = 37.4^{\circ}$, $b = -0.1^{\circ}$ and integrated over $50 - 65 \text{ km s}^{-1}$. The structure is coherent in position–velocity space, and so may be viewed as a single structure. With a single high-density ridge and little or no diffuse gas surrounding it, this filament appears to have an especially compact profile. The relatively low contrast of the filament in the $70 \mu\text{m}$ image compared to the molecular gas images suggests that the filament is largely cool, though the peaks at either end of the filament are associated with HII regions, such as HRDS G037.468–0.105 (Bania, Anderson & Balser, 2012) and IRAS 18571+0349 (Johnston et al., 2009), and several sites of massive star formation are also present. The filament lies at a distance of 9.6 kpc (Bania, Anderson & Balser, 2012), assuming that the coherence in position–velocity space implies a single distance, and contains a string of 1.1 mm clumps identified in the BGPS (Rosolowsky et al., 2010). The total length of the filament, following its shape, is approximately 14 arcmin, which corresponds to a length of 30 pc. Its width, which remains roughly constant across its length, is ~ 22 arcseconds corresponding to ~ 1 pc and implying an average aspect ratio of about 30.

Further comparison between the ^{13}CO (3–2) and $70\ \mu\text{m}$ images reveal diffuse material that appears to be missing in CHIMPS, and there are also several compact sources in the $70\ \mu\text{m}$ image which do not appear in the integrated position–position maps, but appear at different velocities in position–velocity space. The $70\ \mu\text{m}$ image would appear to show that the filament lies at the intersection of a small number of bubble edges, and when viewed alongside the CHIMPS data, there is a suggestion that these bubbles are sweeping up a significant quantity of gas culminating in the dense ridge of this filament.

Row (c) of Figure 2.11 is centred on $l = 43.18^\circ$, $b = -0.05^\circ$ and shows the massive star-forming region W49 integrated over the velocity range of -30 to $30\ \text{km s}^{-1}$. W49, located at a distance of $11.11\ \text{kpc}$ (Zhang et al., 2013), is associated with the brightest peak of emission visible in CHIMPS and is the most luminous ($\sim 10^7 L_\odot$ Sievers et al., 1991) star-forming region, and one of the most massive in the Galaxy ($M_{\text{gas}} \sim 1.1 \times 10^6 M_\odot$; Galván-Madrid et al., 2013). The emission in W49 is extremely broad, spanning $\approx 35\ \text{km s}^{-1}$ in ^{13}CO (3–2) traced by CHIMPS owing to high velocity bipolar outflows (Scoville et al., 1986), and its three-dimensional structure can be described as a hub-filament system, with filaments converging on the W49N and W49S clusters. The whole complex is thought to contain ~ 13 ultra-compact HII regions (Urquhart et al., 2013b), and contains sufficient mass to form several young massive clusters. Moore et al. (2012) find that the star formation in W49, which has a flatter-than-normal luminosity function, is exceptional in terms of its efficiency, and as such may be considered truly starburst-like.

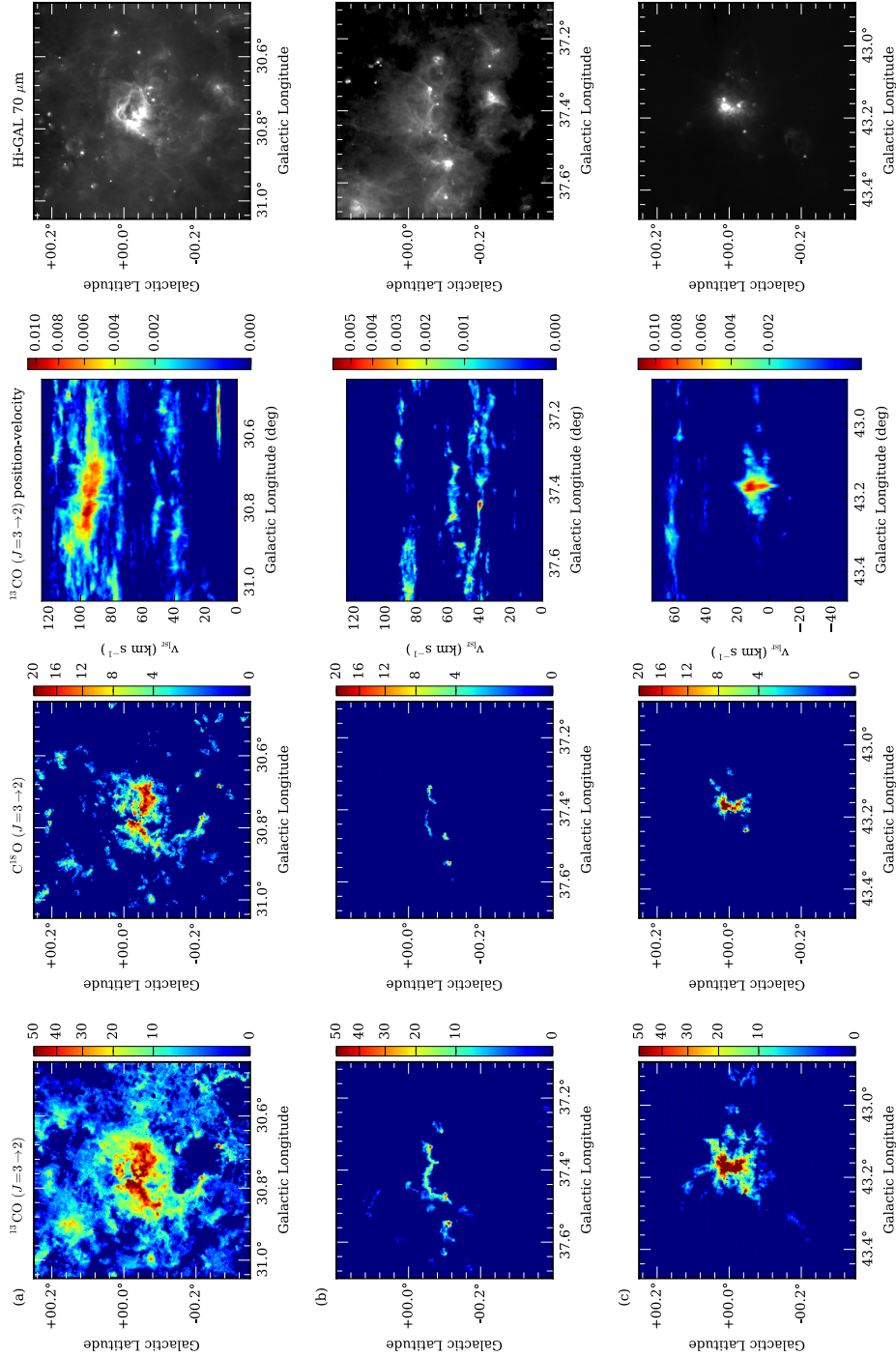


Figure 2.11: Close-ups of several interesting regions in the CHIMPS data: a) The W43 star-forming complex, centred on $l = 30.5^\circ$, $b = -0.05^\circ$ and integrated over $50 - 60 \text{ km s}^{-1}$; b) A filamentary structure centred on $l = 37.4^\circ$, $b = -0.1^\circ$ and integrated over $50 - 60 \text{ km s}^{-1}$; c) W49A star-forming complex centred on $l = 43.18^\circ$, $b = -0.05^\circ$ and integrated over -30 to 30 km s^{-1} . The first two columns from the left-hand side show the integrated intensity in ^{13}CO ($3\rightarrow 2$) and C^{18}O ($3\rightarrow 2$) respectively, while the third from left column shows the region integrated over latitude, and the fourth column shows the 70 μm images of regions from Hi-GAL. In the integrated images in the first and second columns, the intensity scale shows the integrated corrected antenna temperature T_A^* in units of K km s^{-1} , and the integrated T_A^* intensity scale of the position-velocity maps in the third column has units of K degrees.

Chapter 3

A voxel-by-voxel determination of the column density of molecular gas in CHIMPS

The CHIMPS data add to a publicly-available wealth of molecular survey data, particularly spectra of carbon monoxide. In this Chapter, the CHIMPS are combined with data from the GRS and COHRS surveys (described in Section 1.5; see Table 1.3 for a summary) to calculate physical properties of the clouds with fewer assumptions than would otherwise be needed. For example, it is common practice to adopt a single excitation temperature for a particular region under study in molecular gas or dust continuum, but the determination of the column density can be fairly sensitive to uncertainties – particularly underestimates – in the excitation temperature. This Chapter demonstrates a method of calculating $\tau(^{13}\text{CO})$ and T_{ex} , and thereby $N(^{13}\text{CO})$, on a voxel-by-voxel basis. In Chapter 4, distances to emission regions are determined, leading to the calculation of molecular gas masses and other physical properties.

It is necessary to begin this Chapter by establishing a number of shorthand conventions which are used to prevent some of the follow equations from becoming inundated with parentheses. The optical depth of ^{13}CO (3–2) and C^{18}O (3–2) emission shall be referred to as $\tau(^{13}\text{CO})$ and $\tau(\text{C}^{18}\text{O})$, respectively and the column density of ^{13}CO (3–2) is referred to by $N(^{13}\text{CO})$. It is important to bear in mind that column densities derived from ^{13}CO (3–2) would necessarily be lower than those determined from ^{13}CO (1–0) at the same angular resolution due to the high critical density of the $J = 3-2$ transition compared to $J = 1-0$.

In the equations that follow, the intensity of molecular line emission is referred to as the brightness temperature T_b , but the values in the data cubes in place of T_b are actually main beam brightness temperatures, T_{mb} . For extended emission (i.e. features larger than the beam size), T_b and T_{mb} are equivalent, but this is not the case for sources smaller than the beam, in which case T_{mb} is really a beam-averaged T_b . The main beam brightness temperatures for each voxel have been converted from their respective corrected antenna temperatures, T_{A}^* , in the native data formats. T_{mb} is determined from T_{A}^* by dividing by the relevant main beam efficiency η_{mb} . The main beam efficiencies for the CHIMPS, COHRS and GRS data cubes are 0.72, 0.61 and 0.48, respectively (see Section 2.4 for references).

Spectral survey data are typically available in the format of position-position-velocity cubes, which have spatial dimensions l and b , with a third Doppler-shifted velocity axis based on the rest frequency of the rotational emission line. Therefore, spectral molecular data have the advantage that it is possible to determine the various physical properties on a voxel-by-voxel (i.e. 3-dimensional) basis.

To determine the optical depths, excitation temperatures and column densities, an assumption that local thermodynamic equilibrium (LTE) may adequately describe the situation within the clouds is made. LTE describes conditions in

which the density exceeds the critical density (described in Section 1.1.3), and the excitation is dominated by collisions; the rotational energy levels of the CO molecules are populated according to the Boltzmann distribution, which is controlled solely by the temperature. A full derivation of the equations appearing in this Chapter is given in Appendix B.

The data used in this Chapter largely follow on from Section 2.4. As part of the source extraction described that Section, the CHIMPS cubes were smoothed using a Gaussian kernel with a 3-pixel FWHM. The image smoothing has two main practical effects: the SNR of emission is increased by reducing the noise level, but this comes at the price of effectively lowering the angular resolution. A 3-pixel FWHM kernel was found to be a suitable compromise between the enhancing the SNR of emission without degrading the resolution too much; after smoothing, the rms noise level drops from 0.58 K per channel to 0.14 K per channel (in units of T_A^*), and the angular resolution is effectively degraded from 15.2 to 27.4 arcseconds.

The reduction of the noise level in the CHIMPS data is vitally important for the determination of optical depths on a voxel-by-voxel basis because they are determined from the ratio of brightness temperatures, as will be described in Section 3.1. The optical depth is asymptotic (see Figure 3.1), increasing rapidly as the $C^{18}O$ brightness tends to the ^{13}CO brightness in optically thick regions. The danger is that where the brightness temperature ratio of ^{13}CO to $C^{18}O$ emission is underestimated, the optical depth can be *dramatically* overestimated, which will result in an anomalously high column density determination. The COHRS data are also used in the determination of optical depths, and so are also smoothed to an effective resolution of 27.4 arcseconds; the Gaussian kernel used was slightly narrower than that used for the CHIMPS data because the COHRS cubes already

Table 3.1: A summary of the necessary input for the column density calculation. The COHRS and GRS data have been resampled onto the CHIMPS voxel grid of $7.6 \text{ arcseconds} \times 7.6 \text{ arcseconds} \times 0.5 \text{ km s}^{-1}$.

Tracer	Survey	Native Resolution (arcsec)	Effective Resolution (arcsec)	Smoothing FWHM (arcsec)	Parameter calculated
$^{13}\text{CO} (3-2)$	CHIMPS	15.2	27.4	22.8	$\tau(^{13}\text{CO}), N(^{13}\text{CO})$
$\text{C}^{18}\text{O} (3-2)$	CHIMPS	15.2	27.4	22.8	$\tau(^{13}\text{CO})$
$^{12}\text{CO} (3-2)$	COHRS	16.6	27.4	21.8	$\tau(^{13}\text{CO})$
$^{13}\text{CO} (3-2)$	CHIMPS	15.2	46	43.4	T_{ex}
$^{13}\text{CO} (1-0)$	GRS	46	46	–	T_{ex}

had a small smoothing applied before their public release (cf. Dempsey, Thomas & Currie, 2013).

The excitation temperatures are determined from the ratio of brightness temperatures of the GRS $^{13}\text{CO} (1-0)$ data and the CHIMPS $^{13}\text{CO} (3-2)$, for which a version of the latter are smoothed spatially to match the 46 arcsecond resolution of the GRS cubes. For the sake of clarity, it is worth mentioning at this point that the column density cubes that are produced in this Chapter take on the 27.4 arcseconds of angular resolution. The required input data are summarised in Table 3.1.

3.1 Optical depth

The optical depth, $\tau(^{13}\text{CO})$ may be computed from the ratio of brightness temperatures of $^{13}\text{CO} (3-2)$ and another isotopologue observed in the same transition. By virtue of the heterodyne observing mode used in taking the CHIMPS data at JCMT, a measurement of the brightness in $\text{C}^{18}\text{O} (3-2)$ exists for every voxel in $^{13}\text{CO} (3-2)$. In addition to this, the central strip of the survey is also covered in $^{12}\text{CO} (3-2)$ thanks to COHRS. For the most part, the optical

depth is calculated from the ratio of brightness temperatures of ^{13}CO (3–2) and C^{18}O (3–2).

Assuming that the two isotopologues have the same excitation temperature, the optical depth in a voxel can be determined from the ratio of brightness temperatures of ^{13}CO and C^{18}O from the following relation (derived from Equation B.27 of Appendix B) :

$$\frac{T_{\text{b}}(^{13}\text{CO})}{T_{\text{b}}(\text{C}^{18}\text{O})} = \frac{1 - e^{-\tau(^{13}\text{CO})}}{1 - e^{-\tau(\text{C}^{18}\text{O})}}. \quad (3.1)$$

The relative optical depths of two different isotopologues depends only on their relative abundances, and so $\tau(\text{C}^{18}\text{O}) = \tau(^{13}\text{CO})/X(^{13}\text{CO}/\text{C}^{18}\text{O})$ where $X(^{13}\text{CO}/\text{C}^{18}\text{O})$ is the ratio of the relative abundances of ^{13}CO and C^{18}O . The distribution of the the ratio of brightness temperatures of two isotopologues is determined by the abundance ratio and the optical depth. In Figure 2.10, the ratio of main beam brightness temperatures, $T_{\text{mb}}(^{13}\text{CO})/T_{\text{mb}}(\text{C}^{18}\text{O})$, was calculated for the G34 region. Assuming a constant abundance ratio applies over the whole survey, the minimum value of this distribution corresponds to the most optically thin gas, and is therefore must have a value close to the abundance ratio. The minimum value in the histogram of $\log[T_{\text{mb}}(\text{C}^{18}\text{O})/T_{\text{mb}}(^{13}\text{CO})]$ is -1 , and therefore a value of 10 is adopted for the abundance ratio $X(^{13}\text{CO}/\text{C}^{18}\text{O})$.

Equation 3.1 cannot be solved analytically, and so must be solved numerically. For an initial estimate of the optical depth, an assumption that the ^{13}CO is optically thick where C^{18}O emission is present (i.e. $X(^{13}\text{CO}/\text{C}^{18}\text{O}) \gg 1$) allows Equation 3.1 to be simplified to:

$$\frac{T_{\text{b}}(^{13}\text{CO})}{T_{\text{b}}(\text{C}^{18}\text{O})} = \frac{1}{1 - e^{-\tau(^{13}\text{CO})/X(^{13}\text{CO}/\text{C}^{18}\text{O})}}. \quad (3.2)$$

This equation can be rearranged to allow the optical depth $\tau(^{13}\text{CO})$ to be extracted for a given brightness ratio:

$$\tau(^{13}\text{CO}) = -X(^{13}\text{CO}/\text{C}^{18}\text{O}) \ln \left[1 - \frac{T_b(\text{C}^{18}\text{O})}{T_b(^{13}\text{CO})} \right]. \quad (3.3)$$

Following the initial estimate of the optical depth, the optical depth may be determined more accurately using the iterative Newton–Raphson method which has the general form:

$$x_i = x_{i-1} - \frac{f(x_{i-1})}{f'(x_{i-1})}. \quad (3.4)$$

The Newton–Raphson method allows a function with no analytical solution to be approximated using an initial estimate and knowledge of the derivative. When the Newton–Raphson method is applied to Equation 3.1, the optical depth is estimated through application of:

$$\tau_i = \tau_{i-1} - \frac{\left(\frac{T_b(^{13}\text{CO})}{T_b(\text{C}^{18}\text{O})} (1 - e^{-\tau_{i-1}/X(^{13}\text{CO}/\text{C}^{18}\text{O})}) \right) - (1 - e^{-\tau_{i-1}})}{\left(\frac{T_b(^{13}\text{CO})}{T_b(\text{C}^{18}\text{O})} \frac{e^{-\tau_{i-1}/X(^{13}\text{CO}/\text{C}^{18}\text{O})}}{X(^{13}\text{CO}/\text{C}^{18}\text{O})} \right) - e^{-\tau_{i-1}}}. \quad (3.5)$$

The quantity given in Equation 3.3 is used as the first value, τ_0 , and Equation 3.5 is applied repeatedly until the latest estimate of τ , meaning $\tau(^{13}\text{CO})$, agrees with the previous estimate to within 0.1%. The application of this technique typically converges on a solution within 3 iterations, though in cases where more than 20 iterations are made without converging on a solution, the process is terminated and the optical depth is assumed to have no solution. Figure 3.1 illustrates the relationship between the ratio of brightness temperatures and optical depths calculated using this method.

To determine the optical depth for an isotopologue in a particular voxel,

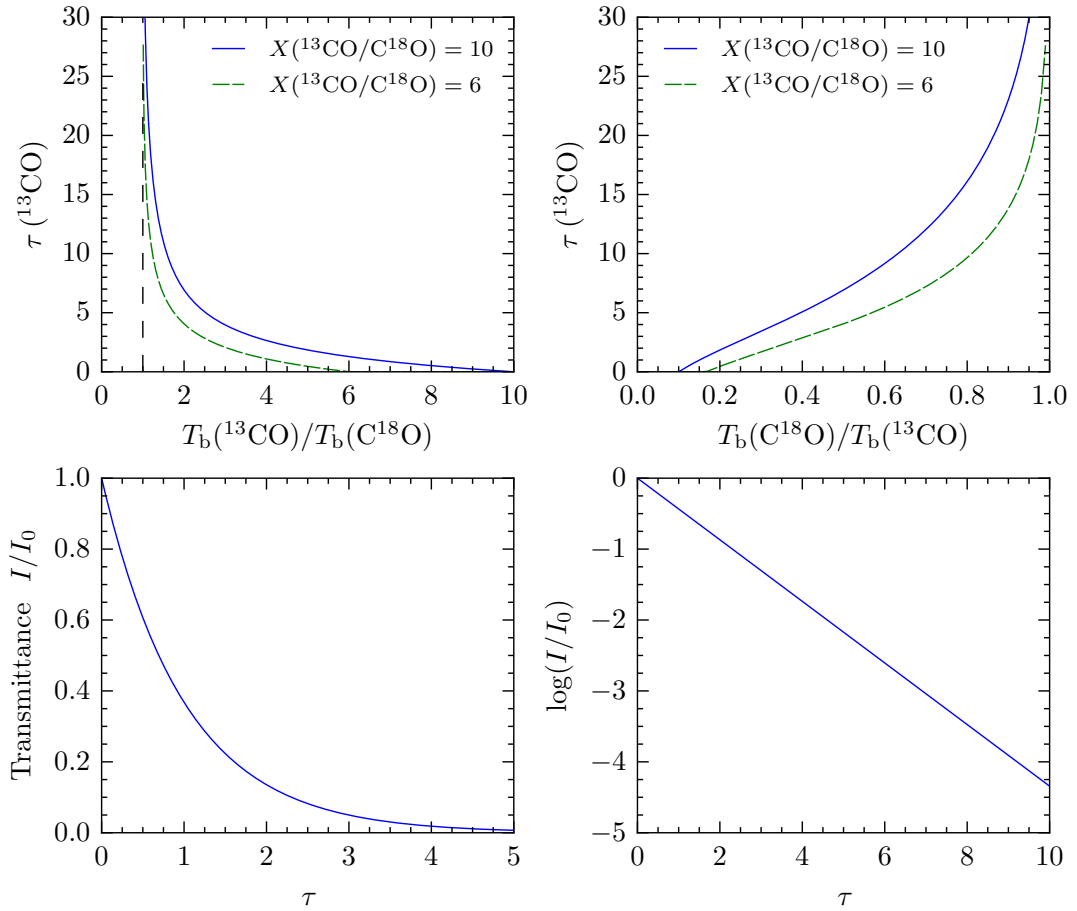


Figure 3.1: *Top row*: the behaviour of optical depth for different brightness temperature ratios of ^{13}CO (3–2) and C^{18}O (3–2) with the adopted abundance ratio of $X(^{12}\text{CO}/\text{C}^{18}\text{O}) = 10$ (blue line), and a slightly lower value of 6 (dashed green line) for comparison. *Bottom row*: the fraction of radiation transmitted through a medium as a function of optical depth.

it is necessary to have detected emission from two isotopologues (in the same transition) in that same position. The rms noise was calculated for each individual cube in each tracer by measuring the standard deviation of voxel values in the 50 velocity frames (i.e. 25 km s^{-1}) at the upper- and lower-velocity ends of each cube, which are overwhelmingly emission-free. A detection limit of at least 3 times the rms noise value was used for the ^{13}CO (3–2) emission, but it was necessary to be more stringent with the C^{18}O (3–2) emission, for which a detection limit of 5

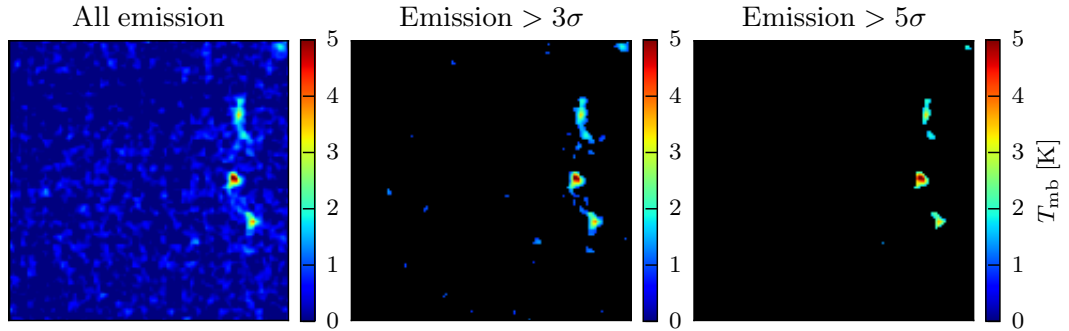


Figure 3.2: A comparison between the emission visible in the 27.4 arcsecond-resolution C^{18}O (3–2) cube with detection thresholds of 3 and 5 times the rms noise. These particular images are the $v_{\text{LSR}} = 96.5 \text{ km s}^{-1}$ velocity slice of the cube centred on $l = 32.17^\circ$, $b = 0.0^\circ$.

times the rms noise value was used. This latter stringency was required because at a detection level of 3 times the rms noise, in some cubes, noise artefacts can be seen which are aligned with the scan directions that may lead to artefacts in the column density maps. A comparison of the 3 and 5 times the rms thresholds is shown in Figure 3.2.

The combined effects of the lower abundance of C^{18}O compared to ^{13}CO , and its lower sensitivity in the CHIMPS data (with rms T_{A}^* of $\sim 0.7 \text{ K km s}^{-1}$ per channel for C^{18}O compared to $\sim 0.6 \text{ K km s}^{-1}$ per channel for ^{13}CO) means that it is not possible to calculate the optical depth of ^{13}CO for every voxel where ^{13}CO (3–2) emission is detected from C^{18}O (3–2). The COHRS ^{12}CO (3–2) emission was used to constrain the optical depth of ^{13}CO for those problematic voxels, though this approach has its own difficulties since COHRS does not extend to the same latitude coverage as CHIMPS. The COHRS data were re-gridded onto the same $7.6 \text{ arcsecond} \times 7.6 \text{ arcsecond} \times 0.5 \text{ km s}^{-1}$ voxel scale as the CHIMPS data using KAPPA:SQORST, and smoothed spatially using a Gaussian kernel with a 3-pixel FWHM to match the effective resolution of 27.4 arcseconds. The COHRS data were also aligned with the CHIMPS voxel grid using KAPPA:WCSALIGN so

that each CHIMPS voxel had a corresponding measurement from COHRS in a $^{12}\text{CO}(3-2)$ cube.

The optical depth in ^{12}CO may be calculated using the same approach as for $\tau(^{13}\text{CO})$ using Equations 3.1, 3.2, 3.3 and 3.5, but replacing the terms referring to ^{13}CO with those of ^{12}CO , and those referring to C^{18}O with those of ^{13}CO . The optical depth in ^{12}CO may be converted to that in ^{13}CO by simply dividing by the abundance ratio $X(^{12}\text{CO}/^{13}\text{CO})$, for which a value of 77 is adopted (Wilson & Rood, 1994).

Figure 3.3 illustrates an example of the determination of $\tau(^{13}\text{CO})$ for a velocity slice taken from the cube centred on $l = 32.17^\circ$, $b = 0.0^\circ$, at $v_{\text{LSR}} = 96.5 \text{ km s}^{-1}$. On the top row, the data from COHRS and CHIMPS used for the optical depth determination are displayed, after smoothing to a resolution of 27.4 arcseconds. The middle row shows the maps of the number of Newton–Raphson iterations required to arrive at a $\tau(^{13}\text{CO})$ solution, with the determinations from $\text{C}^{18}\text{O}(3-2)$ and $^{12}\text{CO}(3-2)$ shown in the left- and right-hand images, respectively, and the resulting $\tau(^{13}\text{CO})$ maps are shown on the bottom row. Almost universally, it took just one Newton–Raphson iteration to determine $\tau(^{13}\text{CO})$ from $^{12}\text{CO}(3-2)$, showing that the initial guess that the $^{13}\text{CO}(3-2)$ emission is optically thick (determined by Equation 3.3), is a good one. The boundary of the right-hand middle row image shows the extent of $^{13}\text{CO}(3-2)$ emission where $\text{SNR} > 3$, while the boundary visible in the left-hand middle row image shows the extent of the $\text{C}^{18}\text{O}(3-2)$ emission where $\text{SNR} > 5$.

A boundary is visible in the COHRS image in Figure 3.3 showing the lesser extent of the coverage of that survey in this region ($|b| < 0.25^\circ$) compared to that of CHIMPS. In fact, the COHRS survey covers only the lowest latitudes of the CHIMPS data, and consequently, $^{12}\text{CO}(3-2)$ data isn't available for a large

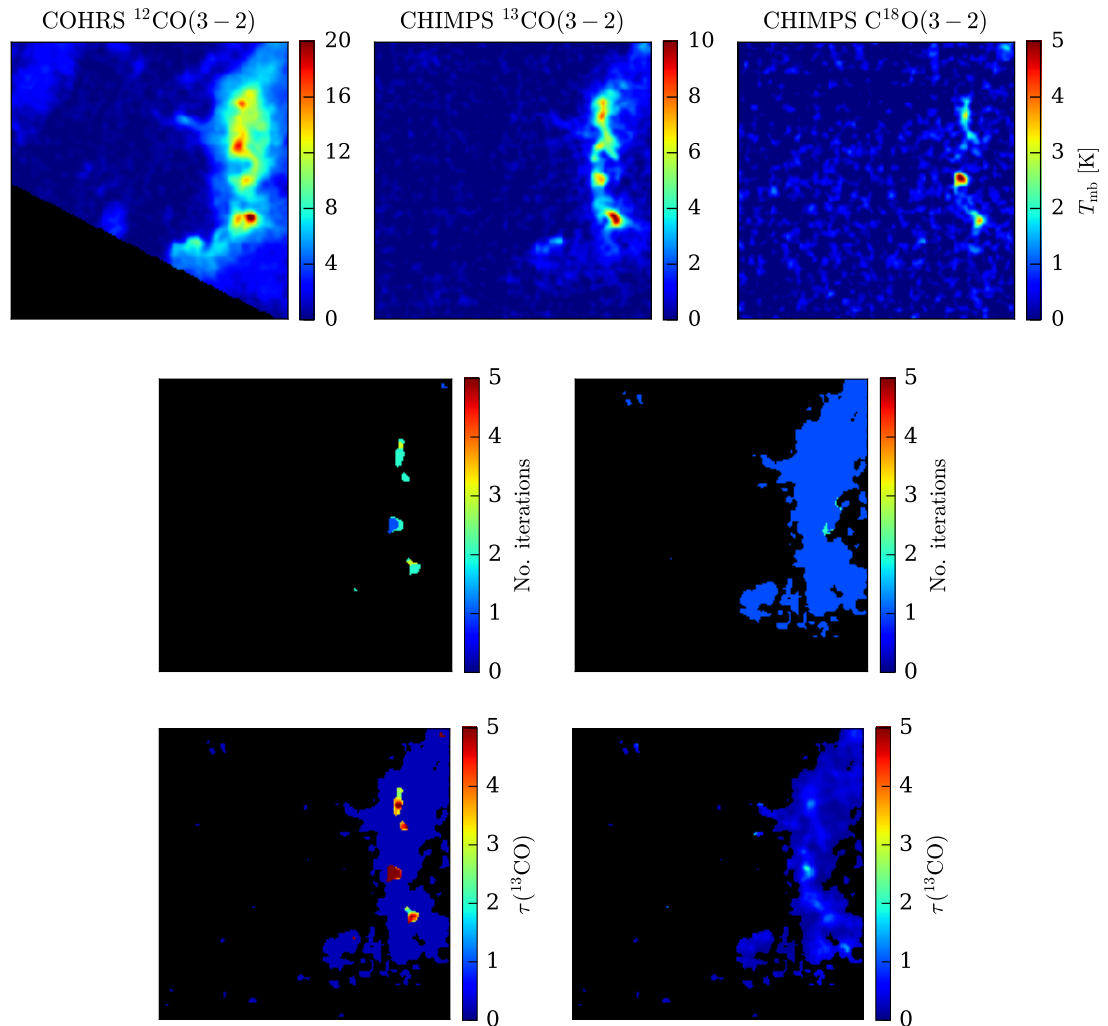


Figure 3.3: An example of the optical depth calculation for the cube centred on $l = 32.17^\circ$, $b = 0.0^\circ$, in the plane corresponding to $v_{\text{LSR}} = 96.5 \text{ km s}^{-1}$. *Top row*: intensity of emission in the 96.5 km s^{-1} plane for the three tracers. *Middle row*: Maps of number of Newton–Raphson iterations taken to converge on a solution for $\tau(^{13}\text{CO})$ calculated from $\text{C}^{18}\text{O}(3-2)$ (left) and $^{12}\text{CO}(3-2)$ (right) for each voxel in the plane. *Bottom row*: Maps of $\tau(^{13}\text{CO})$ determined from $\text{C}^{18}\text{O}(3-2)$ (left) and $^{12}\text{CO}(3-2)$ (right).

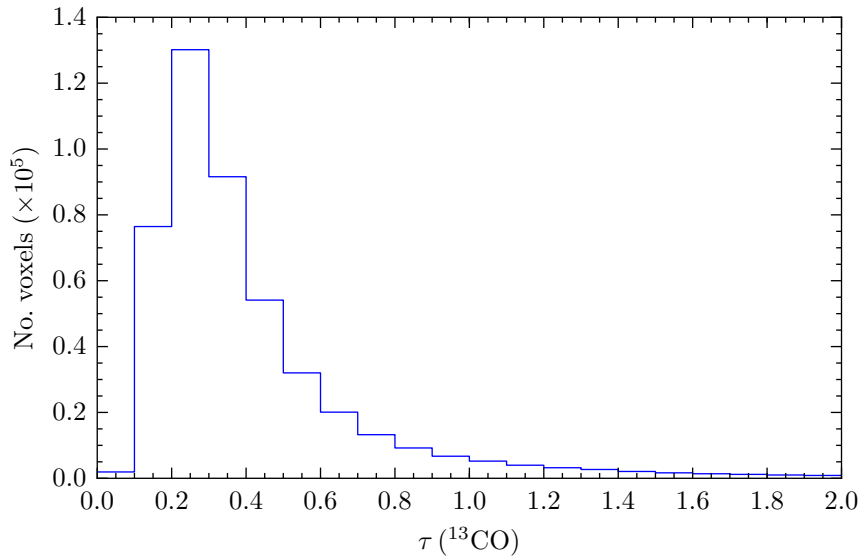


Figure 3.4: Histogram of $\tau(^{13}\text{CO})$ values calculated from ^{13}CO (3–2) and ^{12}CO (3–2) for voxels with above 3σ in ^{13}CO (3–2). This measurement was taken for 458,696 voxels in total.

amount of CHIMPS ($|b| < 0.5^\circ$). In order to maintain a consistent methodology for the optical depth determination over the full CHIMPS range, the COHRS data were not used directly in the calculation. Instead, the COHRS data were used to calculate the optical depth for a sample of 18 CHIMPS cubes centred on $b = 0.0^\circ$ and spaced at intervals of approximately one degree. These $\tau(^{13}\text{CO})$ cubes were assumed to be representative of the $\tau(^{13}\text{CO})$ behaviour over the whole survey, and allowed the optical depth to be inferred in regions not covered by COHRS. A histogram of the $\tau(^{13}\text{CO})$ values calculated for this subset is presented in Figure 3.4. The histogram peak at $\tau(^{13}\text{CO}) = 0.25$ was taken as the representative value in regions where ^{13}CO (3–2) was detected, but not C^{18}O (3–2).

There are a small number of locations where $T_{\text{mb}}(\text{C}^{18}\text{O}) > T_{\text{mb}}(^{13}\text{CO})$, which may be a result of the calibration uncertainty (typically $\sim 10\%$ in each T_{mb} value), or of self-absorption in the corresponding ^{13}CO (3–2) spectrum. Here, the optical depth has no solution since $\tau(^{13}\text{CO}) \rightarrow \infty$ as $T_{\text{b}}(\text{C}^{18}\text{O})/T_{\text{b}}(^{13}\text{CO}) \rightarrow 1$, and so

the optical depths were not calculated for these voxels.

3.2 Excitation temperature

The excitation temperature, T_{ex} , of molecular gas may be determined from observations of two or more transitions for a particular isotopologue, e.g. $^{13}\text{CO}(3-2)$ and $^{13}\text{CO}(1-0)$ if their optical depths are known. The closest match to the CHIMPS ^{13}CO data in another transition are the $^{13}\text{CO}(1-0)$ cubes from the GRS. Since the GRS data have a lower angular resolution than CHIMPS – 46 arcseconds compared to 15 arcseconds – the determination of excitation temperature must necessarily be done at a lower resolution. The GRS data were first interpolated onto a $7.6 \text{ arcsecond} \times 7.6 \text{ arcsecond} \times 0.5 \text{ km s}^{-1}$ voxel grid using KAPPA:SQORST and the CHIMPS data were smoothed spatially using a Gaussian kernel with a FWHM of 43.4 arcseconds to match the GRS resolution of 46 arcseconds. In the following approximation, it is assumed that the excitation temperatures on a resolution of 46 arcseconds adequately represents the excitation temperature distribution at 27.4 arcseconds. Although this is not necessarily true, there are currently no survey data in $^{13}\text{CO}(1-0)$ to match the CHIMPS resolution, and therefore some compromise must be made.

The excitation temperature is calculated from the ratio of brightness temperatures T_{b} using the following relation (derived in Equation B.28 of Appendix B):

$$R = \frac{T_{\text{b}32}}{T_{\text{b}10}} = \frac{1 - e^{-\tau_{32}} \nu_{32} \left(e^{\frac{h\nu_{32}}{k_{\text{B}}T_{\text{ex}}}} - 1 \right)^{-1} - T_{\text{bg}32}}{1 - e^{-\tau_{10}} \nu_{10} \left(e^{\frac{h\nu_{10}}{k_{\text{B}}T_{\text{ex}}}} - 1 \right)^{-1} - T_{\text{bg}10}} \quad (3.6)$$

where:

$$T_{\text{bg}32} = \frac{1}{e^{\frac{h\nu_{32}}{k_{\text{B}}T_{\text{bg}}}} - 1} \quad (3.7)$$

and

$$T_{\text{bg}10} = \frac{1}{e^{\frac{h\nu_{10}}{k_{\text{B}}T_{\text{bg}}}} - 1} \quad (3.8)$$

Here T_{bg} is the background radiation temperature, and has the value of 2.7 K (Fixsen, 2009), $T_{\text{b}32}$ and $T_{\text{b}10}$ refer to the brightness temperatures of ^{13}CO (3–2) and ^{13}CO (1–0), respectively, and τ_{32} and τ_{10} are the optical depths in ^{13}CO (3–2) and ^{13}CO (1–0), respectively.

The determination of τ_{10} requires observations of at least two species in the ($J = 1 \rightarrow 0$) transition. The lack of another isotopologue in the ($J = 1 \rightarrow 0$) transition at high angular resolution is one caveat of the proceeding methodology; the GRS ^{13}CO (1–0) has no inner Galaxy ^{12}CO (1–0) counterpart at similar resolution. The canonical public ^{12}CO (1–0) survey of Dame, Hartmann & Thaddeus (2001), has a resolution of only 8.5 arcmin, which is too low to generate any meaningful optical depths to use in conjunction with the CHIMPS data. To get around this issue, the excitation temperature may be determined from approximations of Equation 3.6 in optically thin and optically thick regimes.

In the optically thick case ($\tau \gg 1$), the quantity $(1 - e^{-\tau_{32}})/(1 - e^{-\tau_{10}})$ tends to unity (i.e. $\tau_{32} \approx \tau_{10}$), and in the optically thin case, this quantity tends to τ_{32}/τ_{10} . In the former case, the excitation temperature can therefore be determined from the ratio of brightness temperatures, R :

$$R_{\text{thick}} = \frac{T_{\text{b}32}}{T_{\text{b}10}} = \frac{\nu_{32}}{\nu_{10}} \frac{\left(e^{\frac{h\nu_{32}}{k_{\text{B}}T_{\text{ex}}}} - 1 \right)^{-1} - T_{\text{bg}32}}{\left(e^{\frac{h\nu_{10}}{k_{\text{B}}T_{\text{ex}}}} - 1 \right)^{-1} - T_{\text{bg}10}}. \quad (3.9)$$

In the latter case, the optical depth τ_{10} is still required, though the ratio τ_{32}/τ_{10}

depends only on the excitation temperature, and so can be determined from the ratio of radiation temperatures R . In Appendix B, Equation B.24 shows that:

$$\frac{\tau_{32}}{\tau_{10}} = 3e^{-\frac{3h\nu_{10}}{k_B T_{\text{ex}}}} \left(\frac{1 - e^{-\frac{h\nu_{32}}{k_B T_{\text{ex}}}}}{1 - e^{-\frac{h\nu_{10}}{k_B T_{\text{ex}}}}} \right), \quad (3.10)$$

and therefore the excitation temperature for optically thin regions can be calculated according to:

$$R_{\text{thin}} = \frac{T_{\text{b}32}}{T_{\text{b}10}} = 3e^{-\frac{3h\nu_{10}}{k_B T_{\text{ex}}}} \left(\frac{1 - e^{-\frac{h\nu_{32}}{k_B T_{\text{ex}}}}}{1 - e^{-\frac{h\nu_{10}}{k_B T_{\text{ex}}}}} \right) R_{\text{thick}}. \quad (3.11)$$

Equations 3.6, 3.9 and 3.11 have no analytical solutions for T_{ex} , and so must be solved numerically. For each voxel, a choice must be made as to whether to adopt the optically thin or optically thick solution. For the purposes of these observations, there is effectively a lower limit on the optical depth of 0.25 due to the approach used in Section 3.1, and wherever $\text{C}^{18}\text{O} (3-2)$ is detected, $\tau (^{13}\text{CO})$ is likely to be at a moderate optical depth of at least this value already. This value of the optical depth is in somewhat of a grey area between an optically thin and optically thick regime; this corresponds to a $\sim 20\%$ reduction in radiation intensity since $I/I_0 = 1 - e^{-\tau}$, and is therefore judged to be the boundary. Any voxels with $\tau > 0.25$ are taken to be optically thick, and any with $\tau \leq 0.25$ are optically thin. Practically, it is the detection, or non-detection of $\text{C}^{18}\text{O} (3-2)$ that determines whether the optically thin, or optically thick excitation temperature calculation is used.

Following this, the excitation temperature for each voxel is chosen, in the range $3\text{ K} \leq T_{\text{ex}} \leq 99\text{ K}$, which most closely matches the ratio of brightness temperatures given by R_{thin} or R_{thick} , sampled to the nearest whole degree. The

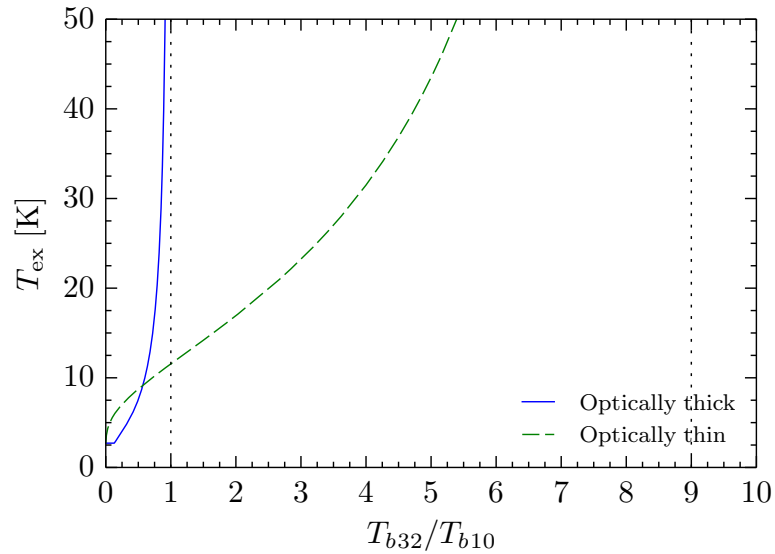


Figure 3.5: The relationship between the ratio of brightness temperatures of ^{13}CO (3–2) and ^{13}CO (1–0), and the derived excitation temperatures for the optically thick and optically thin regimes. The dotted lines show the asymptotes for the excitation temperature in each optical depth regime.

GRS data do not cover the CHIMPS data where $v_{\text{LSR}} < -5 \text{ km s}^{-1}$, and excitation temperatures in this range revert to the minimum of 3 K, accordingly. In the analysis of masses and other properties in Chapter 4, sources which have taken the minimum excitation temperature of 3 K are discarded since their masses would be erroneously large.

In any regions where $T_{b32} > T_{b10}$, Equation 3.9 cannot be solved, since the the ratio T_{b32}/T_{b10} should tend to unity. This situation may occur due to measurement uncertainties in the ^{13}CO (3–2) and ^{13}CO (1–0) data, which ought to be very similar in optically thick areas, or perhaps due to variations in the profile of the different telescope beams at this resolution. This could also arise due to temperature gradients along the line of sight, or different optical depths of ^{13}CO (3–2) and ^{13}CO (1–0). Smoothing the CHIMPS data to the GRS resolution naturally assumes that the GRS beam has a precisely Gaussian profile; the

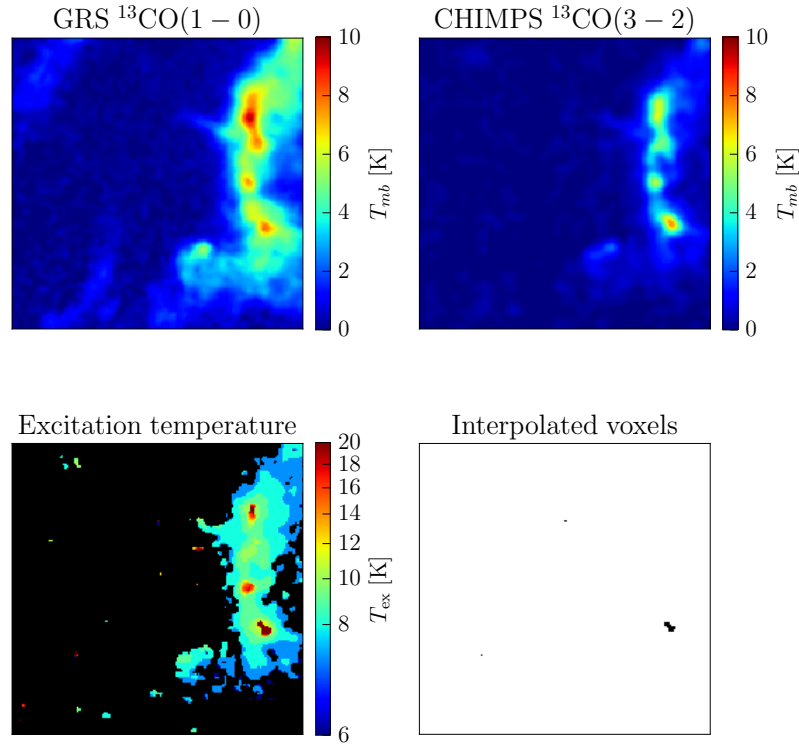


Figure 3.6: An example of the excitation temperature calculation for the cube centred on $l = 32.17^\circ$, $b = 0.0^\circ$, in the plane corresponding to $v_{\text{LSR}} = 96.5 \text{ km s}^{-1}$. *Top row*: intensity of emission in the 96.5 km s^{-1} plane for the two tracers. Both images have an angular resolution of 46 arcseconds, on a voxel grid of 7.6 arcseconds in l and b , and 0.5 km s^{-1} in velocity. *Bottom row*: The map of T_{ex} (left) and the mask (right) showing the voxels for which the excitation temperature was interpolated.

smoothed CHIMPS beam is dominated by the Gaussian kernel, but any deviations from this shape in the GRS data introduce errors in the brightness ratio. To get around this problem, voxels where T_{ex} is undefined in this way were interpolated using a 2-dimensional cubic spline. In these regions, the values of T_{ex} tend to be much higher than the surrounding area, and should be treated with care; overestimates of T_{ex} have little effect on the column density (see Figure 3.7) and so the impact of these interpolated- T_{ex} voxels is unlikely to be significant, but their impact on the overall distribution of T_{ex} in each cloud should be considered.

The process for determining the excitation temperature is illustrated in Fig-

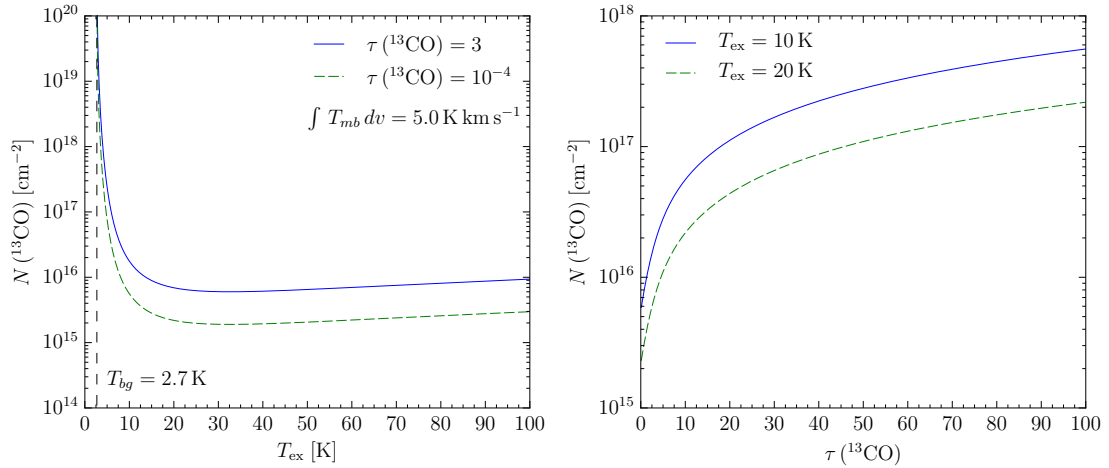


Figure 3.7: The relationships between column density, excitation temperature and optical depth for a ^{13}CO (3–2) main beam brightness temperature of 10 K in a 0.5 km s^{-1} velocity channel, typical of a CHIMPS peak.

ure 3.6 for the same velocity slice as in Figure 3.3, for which the input ^{13}CO (1–0) and ^{13}CO (3–2) images from GRS and CHIMPS are shown in the top row. The bottom row shows the resulting T_{ex} map alongside a mask which flags the voxels for which T_{ex} was interpolated.

3.3 Column density

With the determinations of the excitation temperatures and optical depths, Equation B.35 of Appendix B shows that it is now possible to calculate the column density for each voxel using the following relation for a generic rotational transition $j \rightarrow i$:

$$N_{ji} = \frac{3\epsilon_0 k_B}{2\pi^2 \nu_{ji} \mu^2 j} Z e^{\frac{hB_i(i+1)}{k_B T_{\text{ex}}}} \left(1 - e^{-\frac{h\nu_{ji}}{k_B T_{\text{ex}}}}\right)^{-1} \left(\frac{1}{e^{\frac{h\nu_{ji}}{k_B T_{\text{ex}}}} - 1} - \frac{1}{e^{\frac{h\nu_{ji}}{k_B T_{\text{bg}}}} - 1}\right)^{-1} \frac{\tau}{1 - e^{-\tau}} \int T_b(v) dv, \quad (3.12)$$

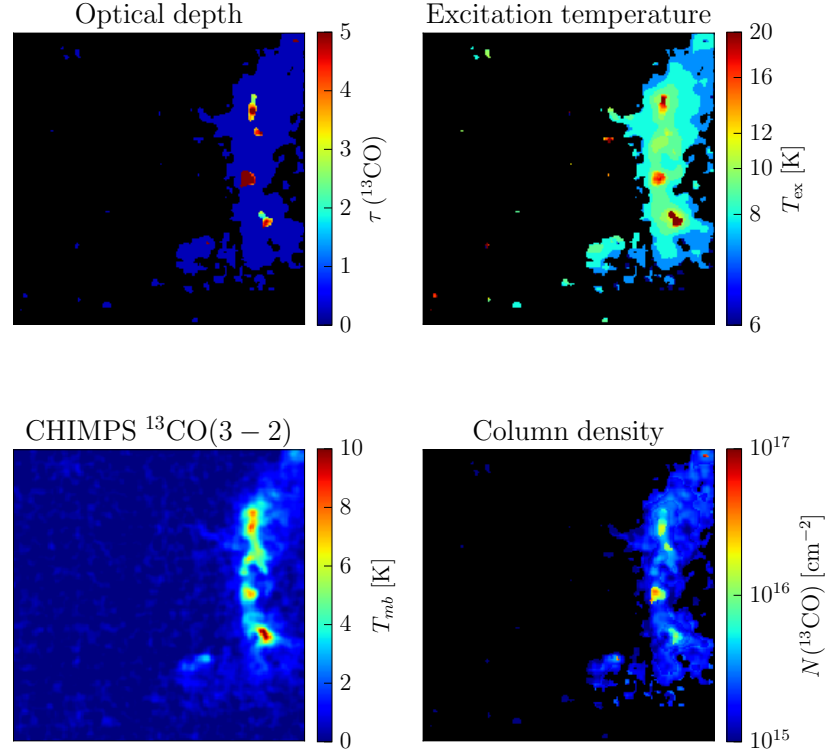


Figure 3.8: An example of the column density calculation for the cube centred on $l = 32.17^\circ$, $b = 0.0^\circ$, which is calculated from the maps of optical depth and excitation temperature.

where ϵ_0 is the permittivity of free space, k_B is Boltzmann's constant, ν_{ji} is the frequency of the $^{13}\text{CO}(3-2)$ emission line, μ is the dipole moment of ^{13}CO of 0.122 Debye, Z is the partition function and $B = h/8\pi^2 I$ relates to the moment of inertia given by $I = \mu_m r_{\text{CO}}^2$ where the reduced mass $\mu_m = m_{^{13}\text{C}} m_{\text{O}} / (m_{^{13}\text{C}} + m_{\text{O}})$ and the equilibrium separation of C and O atoms in CO is $r_{\text{CO}} = 0.113 \text{ nm}$. The background temperature, again, takes on the cosmic microwave background value of $T_{\text{bg}} = 2.7 \text{ K}$, and the partition function is approximated (Equation B.11 of Appendix B) as:

$$Z = \frac{k_B}{hB} \left(T_{\text{ex}} + \frac{hB}{3k_B} \right). \quad (3.13)$$

The final term in Equation 3.12, the integral of the brightness temperature over

the velocity channel, is simply the main beam brightness temperature of the ^{13}CO (3–2) map for the voxel multiplied by the channel width, which is modified by the preceding factor of $\tau/(1 - e^{-\tau})$ to account for the optical depth. It is worth noting that if the channel width is supplied in units of km s^{-1} then to convert from the implicit units on the column density of m^{-2} to cm^{-2} , the output must be multiplied by a factor of 0.1. If the optical depths and brightness temperatures are supplied in terms of ^{13}CO , then the column density calculated is that of ^{13}CO . Figure 3.8 shows the resulting column density map, alongside the three input maps required to generate it.

3.4 Uncertainties

The column density cubes contain both systematic and random errors. The systematic errors arise from the calibration error of the instruments used to take both the CHIMPS and GRS data, and these will vary from night to night, based on the performance of the receivers. The random errors are derived from the voxel-to-voxel noise in the data cubes, and so are directly related to the noise maps of Figure 2.3.

3.4.1 Random uncertainties

The random uncertainties can be estimated by using the variance arrays which accompany each ^{13}CO cube. The variance arrays, for which the arrays of standard deviation are illustrated in Figure 2.3, for each cube were processed and propagated by the KAPPA package during the 3-pixel smoothing applied by GAUSSMOOTH. The smoothing, by its nature, improves the signal-to-noise ratio at the expense of angular resolution; before smoothing, the mean noise value in the ^{13}CO

data according to the variance arrays was $\Delta T_{\text{mb}} \approx 0.88$ K, and after smoothing the average noise drops to $\Delta T_{\text{mb}} \approx 0.19$ K.

Each cloud in the CHIMPS catalogue, extracted by FellWalker, has an associated T_{ex} and $\tau(^{13}\text{CO})$ distribution. For each cloud, the variance values falling within its footprint were read in from the variance map of the smoothed data, centred at the position of the cloud's centroid l and b coordinates, and with a width in l and b based on the cloud's size in those axes. The median variance value from this area was assumed to be representative of the whole cloud, and the corresponding standard deviation was taken to be the T_{mb} representing the uncertainty of brightness temperature in the cloud. Along with the median excitation temperature and mean optical depth, a corresponding uncertainty in $N(^{13}\text{CO})$ was calculated by inserting these numbers into Equation 3.12. This value is the average uncertainty, per voxel, for the cloud in question, and so was multiplied by the number of voxels in the cloud to arrive at the total random uncertainty in that cloud. The distribution of the resulting fractional errors is close to normal, with a mean of 0.68 and a standard deviation of 0.20.

These calculations have assumed that the relative abundance ratios of ^{12}CO , ^{13}CO and C^{18}O have the same values throughout the survey volume. This is certainly not the case, and it is likely that the abundance ratios vary both randomly and systematically. There have been many studies finding correlations of abundances with Galactocentric distance (e.g. Wilson & Rood, 1994; Milam et al., 2005) and the scatter in the abundance ratios is generally much larger than the systematic rise over a Galactocentric distance range like that present in CHIMPS data, which is approximately $4 \leq R_{\text{GC}} \leq 12$ kpc (see Figure 4.2).

Over the range in Galactocentric distances covered by CHIMPS, the Wilson & Rood (1994) model implies that the $X(^{13}\text{CO}/\text{C}^{18}\text{O})$ abundance ra-

tio increases by $\sim 8\%$, but with a scatter of $\sim 40\%$ in the abundance ratio $X(^{13}\text{CO}/\text{C}^{18}\text{O})$. The abundance ratio influences the column densities (and hence masses) of molecular gas structures through the optical depth. In Equation 3.12, it can be seen for any individual voxel with an excitation temperature T_{ex} and ^{13}CO (3–2) brightness temperature, T_{b} , that the column density is proportional to $\tau/(1 - e^{-\tau})$. Since the optical depth is proportional to the abundance ratio, a scatter of $\sim 40\%$ in the abundance ratio would result in a further scatter of $\sim 18\%$ in the column density.

The abundance ratios $X(^{12}\text{CO}/\text{H}_2)$ and $X(^{12}\text{CO}/^{13}\text{CO})$ abundances are required predominantly for the conversion of $N(^{13}\text{CO})$ to $N(\text{H}_2)$, but since this Chapter concerns the determination of $N(^{13}\text{CO})$ only, a discussion of the error contribution in those abundance ratios is saved until Section 4.5.

In Section 3.2, the excitation temperature was determined at the GRS resolution of 46 arcseconds, and then used to determine the column density of ^{13}CO at 27.4 arcsecond resolution. This interpolation to higher resolution introduces a component of random error into the column density data as the true temperature distribution will be averaged over the larger beam area at lower resolution.

To estimate the magnitude of the random uncertainty on the column density cubes at 27.4 arcsecond resolution, which were created using the 46 arcsecond resolution excitation temperature cubes, a test was carried out using a 1 degree patch of the survey, consisting of nine cubes between $l = 43.0^\circ$ and $l = 44.0^\circ$. Since the morphology of molecular clouds appears to be fractal (see Section 1.1.1), it is reasonable to expect that errors induced by using 46 arcsecond resolution T_{ex} values to calculate column density at a resolution of 27.4 arcseconds would be similar to those induced by using T_{ex} values at even lower angular resolution to determine the column density at a resolution of 46 arcseconds.

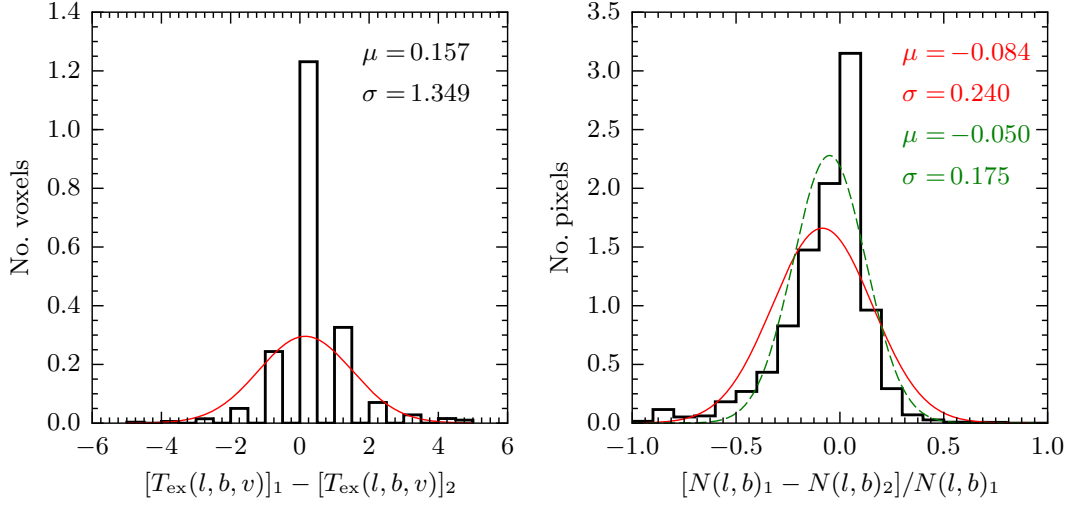


Figure 3.9: *Left*: Distribution of changes in T_{ex} voxel values in the $l = 43.0^\circ$ to 44.0° region when using the matching resolution T_{ex} cubes compared to the lower resolution cubes. *Right*: Distribution of changes to velocity-integrated column density pixel values in the same patch arising from the use of the lower-angular resolution T_{ex} information. The subscripts 1 and 2 refer to the calculations using the 46 arcsecond- and 77.2 arcsecond-resolution T_{ex} cubes, respectively.

To that end, a set of column density cubes were generated at 46 arcsecond resolution after smoothing the CHIMPS cubes to the GRS resolution, thus giving a benchmark for their determination using matching resolution T_{mb} and T_{ex} values. A further set of excitation temperature cubes were then generated after smoothing the ^{13}CO (3–2) and ^{13}CO (1–0) cubes to an angular resolution of 77.2 arcseconds, lower than 46 arcsecond resolution by the same factor as between the excitation temperature and column density cubes used in Sections 3.2 and 3.3. A second set of column density cubes was generated at 46 arcsecond resolution, but this time the excitation temperatures were taken from the 77.2 arcsecond resolution cubes.

In Figure 3.9, the uncertainties resulting from using the two different resolution T_{ex} values are presented. The left panel shows the difference in excitation temperature on a voxel-by-voxel basis between the cubes at 46 and 77.2 arcsec-

ond resolution. A normal distribution was fitted (overplotted in red), which has a standard deviation of 1.4 K, though there is a sharp peak in the bin centred on $\Delta T_{\text{ex}} = [T_{\text{ex}}(l, b, v)]_1 - [T_{\text{ex}}(l, b, v)]_2 = 0$ K that is not satisfactorily fitted by this distribution. In general, an uncertainty of ± 1 K on each voxel appears to be reasonable. In the right panel, the distribution of fractional differences in the column densities, integrated over velocity and on a pixel-by-pixel basis is presented. The velocity-integrated column density is the most relevant quantity for the calculation of masses for the CHIMPS clumps, which are determined in Chapter 4, and two normal distributions were fitted to these data. The red distribution is a best fit, which fits the negative tail best, with a standard deviation of 0.24, but the green dashed distribution fits better, by eye, to the majority of the values, and has a standard deviation of 0.175. Both distributions have a mean value of ≈ 0 , indicating that there was no significant systematic offset caused by the use of this method. The contribution to the random uncertainty on integrated column density values resulting from the use of this method was therefore assumed to be an intermediate value between these distributions, and so a value of $\pm 20\%$ was adopted.

3.4.2 Systematic uncertainties

To estimate the systematic uncertainties inherent in these calculations, the column density calculations were repeated several times for the cube used to demonstrate the process in this Chapter, centred on $l = 32.17^\circ$, $b = 0.0^\circ$, but with an intensity perturbation applied to the input. In Section 2.2.1, the calibration uncertainty of 15% in HARP data found by Buckle et al. (2009) was found to be extremely well matched by the CHIMPS data, while Jackson et al. (2006) estimate that the GRS data have a similar calibration uncertainty of 10–15%. In

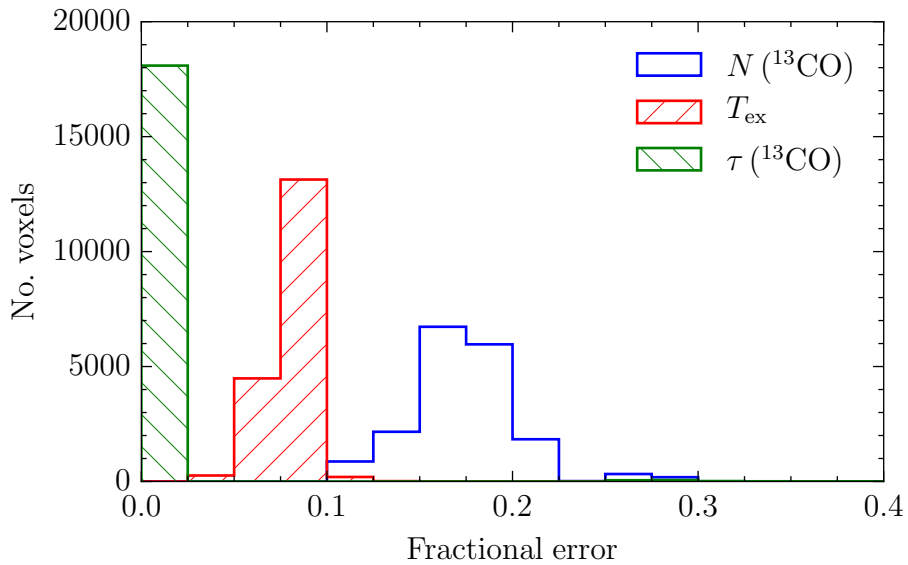


Figure 3.10: Histograms of the systematic fractional uncertainty on the voxels of optical depth, excitation temperature and column density for the CHIMPS cube centred on $l = 32.17^\circ$, $b = 0.0^\circ$.

reality, the calibration error has both systematic and random elements in the CHIMPS data; there is a systematic offset associated within all T_{mb} values in individual cubes caused by the calibration error each night, but also a random scatter caused by the varying calibration errors from night-to-night during the observations.

In total, optical depth, excitation temperature and column density cubes for the $l = 32.17^\circ$, $b = 0.0^\circ$ cube were calculated 20 separate times. Each time, the input CHIMPS data for both isotopologues were multiplied by a factor drawn from a normal distribution with a mean of 1.0 and a standard deviation of 0.15, and the GRS data were also multiplied by a separate factor drawn from the same distribution, in order to simulate the 15% calibration error for each cube. The $^{13}\text{CO} (3-2)$ and $\text{C}^{18}\text{O} (3-2)$ data cubes were multiplied by the same factor each time, since the same calibration would have been applied to the observations being made simultaneously.

The distribution of fractional errors on each voxel of the test cube are illustrated in Figure 3.10. The optical depth calculation does not suffer from systematic calibration errors, since the intensities of ^{13}CO (3–2) and C^{18}O (3–2) from which the optical depth is determined, will vary by the same factor. In the 20 realisations, the excitation temperatures vary by less than 10%, and column densities vary by about 10–20%. A value of 18% was adopted as fractional systematic error per cloud, accordingly.

3.4.3 Total uncertainties

Since the systematic uncertainties associated with the calibration errors and the varying $X(^{12}\text{CO}/\text{C}^{18}\text{O})$ abundance both contain significant random elements, the random and systematic uncertainties for each cloud are combined in quadrature. The resulting fractional errors on the integrated column density of each cloud are presented in Figure 3.11, with the distribution on a linear scale on the left panel, and with a logarithmic y-axis on the right panel. The fractional errors appear to be reasonably normally distributed about a mean value of ~ 0.75 with a standard deviation of ~ 0.18 . Despite the fact that on the linear scale the distribution appears to be well fitted by a normal distribution, a Shapiro-Wilk test finds that it is not a good fit, yielding a P value of $\sim 10^{-7}$. This is likely to be due to the presence of an extended wing in the distribution for those clouds with the largest fractional errors, visible in the right-hand panel of Figure 3.11. This wing is caused by a small number of clouds which contain spectra with the largest variances, corresponding to those data taken when several of the HARP receptors were not operational.

There is one cloud with an extremely large fractional error of 941. This appears to be a one-off since the second largest fractional error is 1.52. This

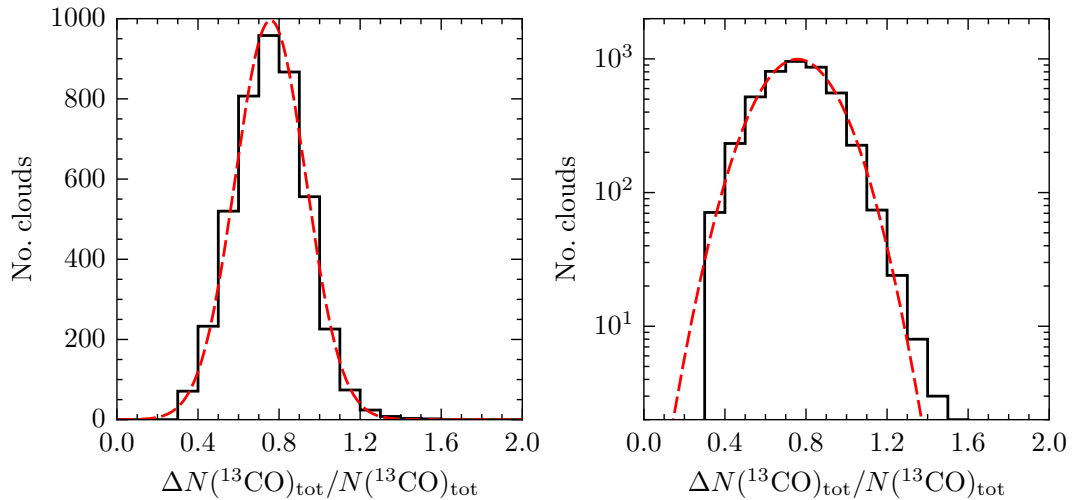


Figure 3.11: Distribution of the total fractional uncertainty on the integrated column density for all CHIMPS clouds with a valid column density measurement.

extreme fractional error is due to the fact that this particular cloud lies across the velocity boundary of -5 km s^{-1} at which the GRS $^{13}\text{CO} (1-0)$ data is no longer available. Consequently, the T_{ex} is undefined for half the cloud, in which region it takes on the background value of 2.7 K , causing a large uncertainty due to the asymptotic nature of $N(^{13}\text{CO})$ as T_{ex} tends to the background value.

3.5 Discussion

The cubes of these physical parameters are a valuable resource for studying molecular clouds and the conditions of star formation, but there are some important caveats that must be recognised in their usage. The effect of false positives are not discussed in this Section, but their rate is considered in Section 4.1.

Probably the most significant caveat with these data is that the column densities are likely to be underestimates in the majority of cases. This is evident in the sharp boundaries visible in the optical depth maps (e.g. Figure 3.3), and is mainly derived from the difficulties in detecting $\text{C}^{18}\text{O} (3-2)$. The underestimated

column density will propagate into the other physical parameters and properties derived from those values in Chapter 4.

The assumption of LTE must also be taken into account, which assumes that sub-thermal excitation is negligible. There is certain to be some component of sub-thermal emission in these data, but a full non-LTE analysis is beyond the scope of this work, and LTE is a reasonable approximation to make. The sub-thermal emission occurs where the gas density is below the critical density, in which case the gas temperature will be higher than the excitation temperature; the excitation temperature loses its physical significance where the energy level populations do not follow the Boltzmann distribution. This underestimate in the gas temperature will lead to overestimates in the column density (see Figure 3.7). In Chapter 4, the distribution of excitation temperatures of the molecular clumps extracted from the survey is shown to peak in the 7–8 K bin, which matches the expectation for molecular structures covering the size regime from cores, through clumps, to clouds (described in Table 1.1). Sub-thermal emission can therefore be assumed not to be a dominant effect here.

These calculations have enabled one of the first maps of the excitation temperature of molecular gas for a significant region of the Galactic plane to be produced. A map of the excitation temperature across the survey area can be found in Figure 3.12. Each pixel is the median T_{ex} in the spectrum at that position. Generally, the excitation temperature does not deviate much from ~ 10 K, though a number of the intensely star-forming regions do show considerable rises towards their centres. Such examples of regions with hot interiors can be found at the location of W49 ($l = 43.2^\circ$, $b = 0.0^\circ$) and the G34 region ($l = 34.3^\circ$, $b = 0.1^\circ$). A temperature gradient is visible across the filament located at $l = 37.4^\circ$, $b = -0.1^\circ$, which was discussed in Section 2.5. This temperature gradient would appear to

add weight to the idea that this filament is an expanding bubble rim, since it is warmer on the inside edge.

Figure 3.13 shows a map of the velocity-integrated column density of ^{13}CO (3–2) over the survey area on a logarithmic intensity scale. The morphology of this map is largely similar to the map of ^{13}CO (3–2) emission in Figure 2.5, with the exception that column density is enhanced by the optical depth in regions of C^{18}O (3–2) emission. The column density is illustrated in terms of the ^{13}CO gas column in order to limit the uncertainty in the various conversion factors required to display the H_2 column density, and it should be recalled that emission is visible only where the volume density is above the $J = 3-2$ critical density of 10^4 cm^{-3} . Broadly speaking, a factor of $\sim 10^6$ converts ^{13}CO to H_2 column density.

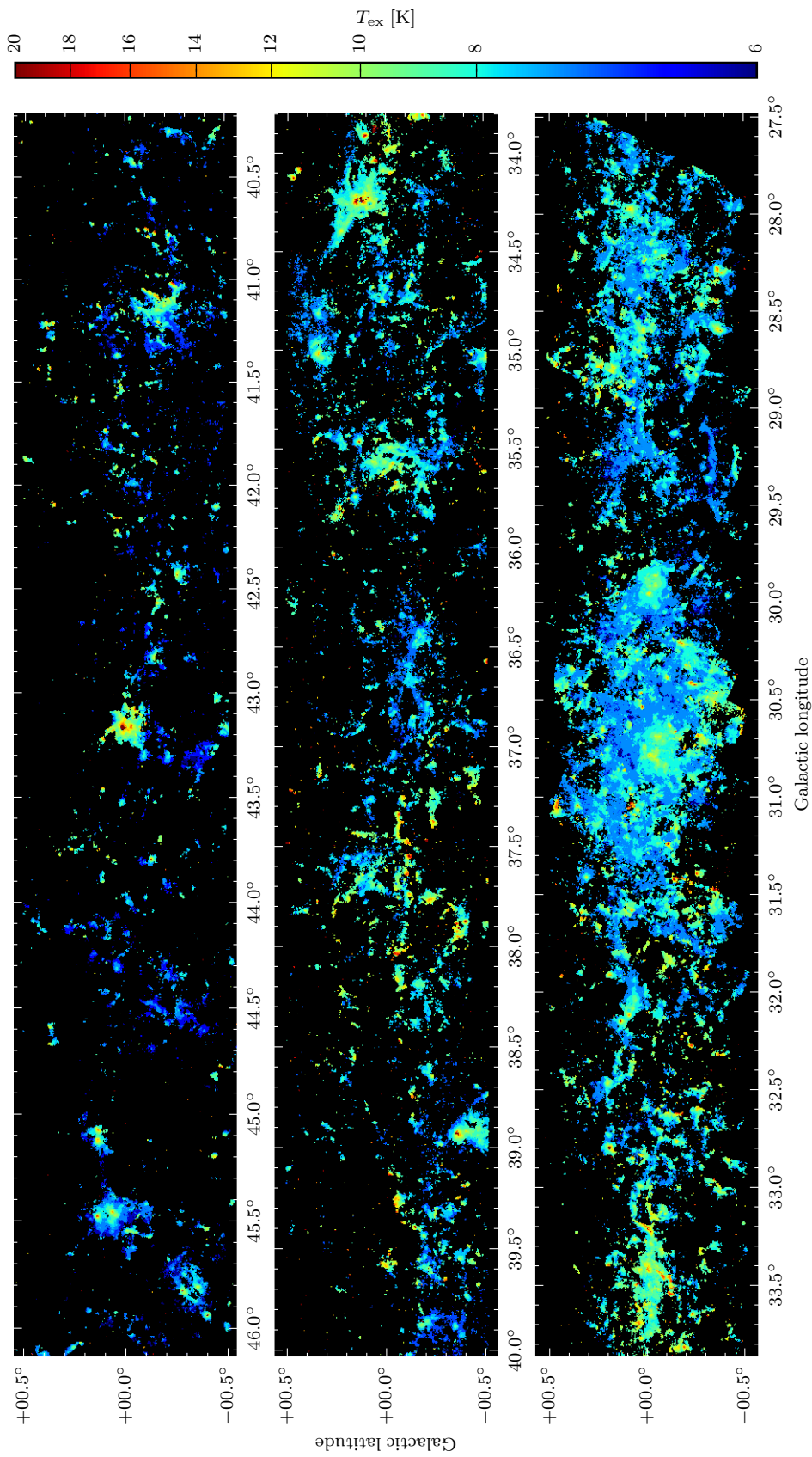


Figure 3.12: The excitation temperature map for CHIMPS. Each pixel value is the median excitation temperature from the spectrum at that position. A square root intensity scale has been adopted.

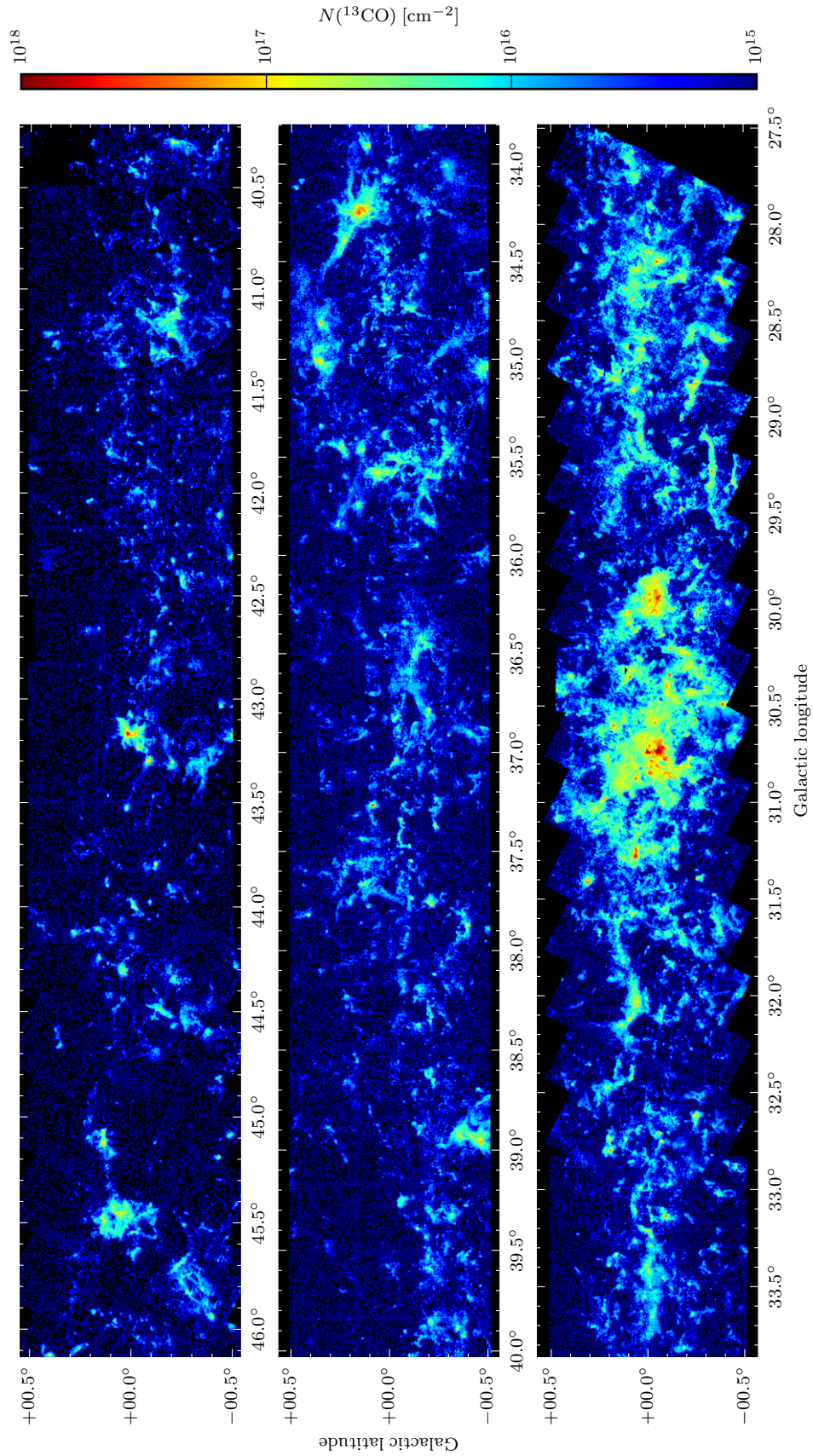


Figure 3.13: A map of the ^{13}CO column density in CHIMPS. Each pixel value is the sum of the column density spectrum at that position. The intensity scale is logarithmic.

Chapter 4

Physical properties of the CHIMPS clumps

CHIMPS constitutes one of the highest-resolution surveys of molecular clumps over a large area of the sky to date, and as such contains a vast quantity of information about dense gas structures that are likely to be the majority mass component of molecular clouds. The column densities and excitation conditions of the CHIMPS molecular gas determined in the previous Chapter are combined with the size and linewidth information extracted in Chapter 2, and kinematic distances in the following pages, allowing a wealth of additional properties for this population to be studied in detail.

Throughout this study, sources that have been extracted from the CHIMPS data are referred to as ‘clumps’, though we shall see in Section 4.5 that these sources match the properties for objects frequently described as clouds and cores, as well as clumps. The application of these terms depends to some extent on the spatial resolution, and this is to be expected if the structure of molecular clouds is indeed, as some suggest, fractal (e.g. Falgarone, Phillips & Walker, 1991).

4.1 The CHIMPS source catalogue

A source catalogue for the CHIMPS $^{13}\text{CO}(3-2)$ data was produced through the source extraction process detailed in Section 2.2.2. There were initially 4999 objects listed in this catalogue, but not all of these are genuine clumps of emission, and there are small number of noise features visible in the integrated extracted emission map of Figure 2.5.

The FellWalker masks have the same sizes and shapes as the $^{13}\text{CO}(3-2)$ cubes the extraction was applied to, as well as the cubes generated through the processes described in Chapter 3, but each voxel value is an integer that corresponds to the catalogued index of the clump to which that voxel was assigned. The FellWalker masks were used to extract the opacities, excitation temperatures and ^{13}CO column densities from their cubes, and the distributions of these quantities were measured for 4,990 of the 4,999 $^{13}\text{CO}(3-2)$ sources. The missing 9 sources can be identified as noise features in the $^{13}\text{CO}(3-2)$ cube which did not appear above the detection limit in the ancillary data cubes, and therefore have no corresponding optical depth, excitation temperature or column density value.

The shapes of molecular clouds are difficult to describe, and the FellWalker source extraction reports the intensity-weighted rms deviation of voxels from the centroid in the orthogonal l , b and v axes as opposed to the more common major and minor axes of an elliptical fit. For example, the quoted size of a source on a generic x -axis is determined in the following way:

$$size = \sqrt{\frac{\sum d_i x_i^2}{\sum d_i} - \left(\frac{\sum d_i x_i}{\sum d_i}\right)^2}, \quad (4.1)$$

where d_i is the background-subtracted intensity of the voxel at a distance x_i on the x axis from the centroid position.

As previously described, the source extraction was carried out on a map that has been smoothed to an effective resolution of 27.4 arcsec, and so both the applied smoothing and the intrinsic smoothing caused by the JCMT beam must be taken into account. The connection between the sizes reported (after smoothing) and the intrinsic source size, θ_0 , can be described in the following way:

$$size = \frac{1}{2.35} \sqrt{\theta_0^2 + \theta_{\text{beam}}^2 + \theta_{\text{smooth}}^2}, \quad (4.2)$$

where θ_0 describes the intrinsic angular size of the source and θ_{beam} and θ_{smooth} are the smoothing kernels caused by the 15.2 arcsecond JCMT beam and the 3 pixel-FWHM (22.8 arcsecond) Gaussian smooth, respectively. Assuming that the rms sizes reported in the FellWalker catalogue are equivalent to the standard deviation of a Gaussian profile, they may be converted into FWHMs by multiplying by a factor of 2.35 (more precisely this factor is $2\sqrt{2\ln 2}$).

The reported sizes in the l and b axes were deconvolved to remove the effects of the smoothing applied both manually and by the telescope beam according to Equation 4.2. The reported sizes are therefore calculated by:

$$size_{\text{deconvolved}} = \frac{\theta_0}{2.35} = \sqrt{size^2 - \left(\frac{\theta_{\text{beam}}}{2.35}\right)^2 - \left(\frac{\theta_{\text{smooth}}}{2.35}\right)^2}. \quad (4.3)$$

Although the intensity-weighted rms sizes are not strictly standard deviations, because the sources are not all perfectly Gaussian, this size deconvolution only makes a significant change to the reported source size for objects which are only slightly larger than the beam size, and such objects generally *are* compact and Gaussian-like. After deconvolution, any source with a negative deconvolved size is likely to have been a spurious noise artefact, and may be removed from the

catalogue. After removing those sources which have negative deconvolved sizes in both l and b axes, there are 4,617 CHIMPS clumps remaining.

The 373 sources that were removed for the source catalogue due to their undefined deconvolved sizes were examined visually in order to determine their nature. Approximately 40% of these sources are strong candidates to be genuine sources, appearing in at least two consecutive velocity channels, and may have negative deconvolved sizes due to being compact but sharply peaked; the intensity weighting of the source size calculated according to Equation 4.3 could lead to small source sizes for compact sources that have a strong central peak that falls rapidly with distance. Of the remaining 60% of rejected sources that were not obviously real, there are a number of kinds. Some of these are clearly noise artefacts that remain after smoothing with significant SNRs, while there are others for which it is difficult to distinguish by eye between being genuine sources or noise artefacts that fall on low-lying diffuse emission. There are also objects that appear to be fragments of complex regions of emission, and have been defined separately to other sources of which they ought to be part, possibly as a result of a noisy background. The estimate that 40% of the excluded sources are real is likely to be an underestimate to some extent, since a fraction of the remaining undefined sources are possibly real. However, the nature of all of these sources is doubtful to some extent, and it is better to exclude them from the sample for these analyses.

The catalogued peak intensity values are also modified by these reported smoothing effects, and should be rescaled according to:

$$peak_0 = peak(size/size_{deconvolved}), \quad (4.4)$$

before comparing them to values from other survey data. The total integrated intensity in a clump is unchanged by smoothing.

4.2 Kinematic distances

The centroid velocity v_{LSR} of a molecular cloud is determined by a number of factors. First and foremost, it is the Galactic rotation curve, controlled by the Galaxy's gravitational field, that dominates this value, as the rotation rate of the cloud around the Galactic centre varies with its distance from the centre. On top of this effect, there may be perturbations caused by processes in the local environment of the molecular cloud, such as spiral density waves or protostellar outflows.

To determine the kinematic distances to each of the CHIMPS clumps, the Galactic rotation curve of Brand & Blitz (1993) was adopted. The rotation curves of Clemens (1985) and Reid et al. (2009) are also frequently used to determine kinematic distances, but this work adopts the Brand & Blitz (1993) rotation curve in order to be consistent with the ATLASGAL measurements of Urquhart et al. (2014b), which are used in this Chapter. The differences in distances resulting from the choice of rotation curve are generally smaller than the uncertainties. These calculations require that the Galactocentric distance of the Sun, R_0 , and the Sun's circular velocity around the Galactic centre Θ_0 are known and, for the sake of consistency with other authors, the IAU values of $R_0 = 8.5 \pm 0.5$ kpc (Feast & Whitelock, 1997), and $\Theta_0 = 220 \pm 20$ km s⁻¹ (Kerr & Lynden-Bell, 1986) are adopted. The rotation curve has the form:

$$\frac{\Theta}{\Theta_0} = a_1 \left(\frac{R}{R_0} \right)^{a_2} + a_3, \quad (4.5)$$

where Θ and Θ_0 are the circular velocities of the molecular cloud and the Sun, respectively, R and R_0 are the Galactocentric distances of the molecular clouds and the Sun, respectively, $a_1 = 1.00767$, $a_2 = 0.0394$ and $a_3 = 0.0071$. This can be written equivalently in terms of the angular velocity, ω , and with $\omega_0 = \Theta_0/R_0$:

$$\frac{\omega}{\omega_0} = a_1 \left(\frac{R}{R_0} \right)^{a_2-1} + a_3 \left(\frac{R_0}{R} \right). \quad (4.6)$$

For a given centroid v_{LSR} of a molecular cloud, it is simple to calculate the angular velocity, which is given by:

$$\omega = \omega_0 + \frac{v_{\text{LSR}}}{R_0 \sin(l) \cos(b)}. \quad (4.7)$$

Since Equation 4.6 can not be solved analytically, ω was calculated as a look-up array for a range of Galactocentric distances from 2 to 17 kpc at intervals of 1 pc. For each molecular clump, its angular velocity ω was calculated from the centroid v_{LSR} , and the closest match in the look-up array allowed a Galactocentric distance to be determined.

While the v_{LSR} of a molecular cloud allows a Galactocentric distance consistent with the model to be determined easily, it is not always so easy to determine the distance to the cloud from Earth. According to the geometry outlined in Figure 4.1 and incorporating the correction for the source latitude, the heliocentric distance d_k of an object at a given position in (l, b, v) space is related to the Galactocentric distance by:

$$R = (d_k^2 \cos^2(b) + R_0^2 - 2R_0 d_k \cos(b) \cos(l))^{1/2}, \quad (4.8)$$

which has quadratic solutions for the heliocentric distance d of the form:

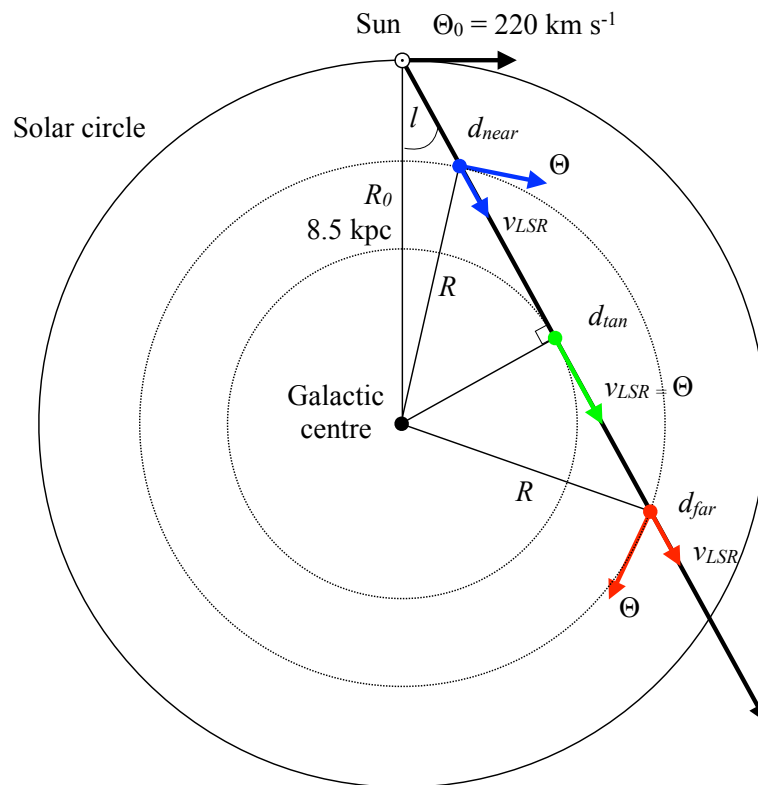


Figure 4.1: The geometry of the calculation of kinematic distances. In this top-down view, we do not see the effect of latitude which, at $|b| < 0.5^\circ$ for sources in CHIMPS, is regarded as negligible.

$$d_k = \frac{2R_0 \cos(b) \cos(l) \pm \sqrt{4R_0^2 \cos^2(b) \cos^2(l) - 4 \cos(b)^2 (R_0^2 - R^2)}}{2 \cos^2(b)}. \quad (4.9)$$

which, for sources lying on the Galactic plane with $b \approx 0^\circ$, can be simplified to:

$$d_k = R_0 \cos(l) \pm \sqrt{R^2 - R_0^2 \sin^2(l)}. \quad (4.10)$$

For objects which reside inside the Solar circle (i.e. with Galactocentric distances $R < 8.5$ kpc), there may be two real solutions to Equation 4.8. Some sources are located at the distance of the tangent-point along a particular line of sight, for which the near- and far-kinematic distances are equal. The kinematic distances for these sources are calculated as:

$$d_k = R_0 \frac{\cos(l)}{\cos(b)}. \quad (4.11)$$

4.3 Resolving the kinematic distance ambiguity

Resolving the kinematic distance ambiguity (KDA) is a problem that has attracted considerable effort in recent years, and a number of techniques have been used across the literature. The resolution depends, to some extent, on the nature of the source to which the distance is required. For example, in assigning kinematic distances to the IRDCs in the catalogue of Peretto & Fuller (2009), it is natural for Traficante et al. (2015) to adopt the near distances in cases of ambiguity, since IRDCs are identified in mid-infrared absorption and are necessarily located in front of a diffuse background.

The solution is less obvious for clouds or clumps seen in emission, which may

be seen at the far distance as well as the near distance. Where it is possible to supplement the spectra of the molecular gas tracer with HI spectra, such as those of the VLA Galactic Plane Survey (VGPS; Stil et al., 2006), the HI-self absorption (HiSA) technique is frequently adopted to break the KDA (e.g. Baker & Burton, 1979; Anderson & Bania, 2009; Roman-Duval et al., 2009; Eden et al., 2012; Urquhart et al., 2012). The HiSA technique works by looking for a self-absorption feature in HI spectra coincident with an emission peak in ^{13}CO , or a similar tracer of the molecular cloud. If an absorption feature is found at the velocity of the corresponding ^{13}CO emission, then the near-kinematic distance will be adopted on the assumption that the cold HI envelope surrounding the molecular cloud is being seen against the warmer diffuse HI background. Conversely, if no self-absorption is seen, then the far-kinematic distance solution will be taken.

Along a similar vein to the HiSA technique, there is another method for resolving the KDA utilising HI data that looks for HI absorption against a continuum source (HiCA; e.g. Roman-Duval et al., 2009; Urquhart et al., 2013b). Sources of 21 cm continuum emission, such as HII regions, tend to have much greater brightness temperatures than any cold HI associated with molecular clouds, and therefore any foreground clouds, between the observer and the cloud of interest, will show up as HI absorption features. If a cloud is located at the near distance, then only clouds with line-of-sight velocities less than that of the cloud containing the 21 cm continuum source will show up as absorption features. If the target cloud is located at the far distance, then absorption features may be seen for foreground clouds with velocities up to the terminal velocity (equivalently the tangential velocity) along that line of sight. This technique may be utilised for a molecular cloud or clump has been associated with a 21 cm continuum source. See Figure 2, Roman-Duval et al. (2009) for a schematic of this technique for

resolving the KDA.

Another method for resolving the KDA relies upon associating a cloud with a source that has a well defined distance. High-mass YSOs (HMYSOs) are frequently found to be the home to methanol, water and SiO masers, for which much more accurate distances can be assigned. Class II methanol masers at 6.7 and 12.2 GHz, for example, are generally extremely compact sources (~ 1 milliarcsecond) and so the geometric parallaxes of these sources can be measured with very long baseline interferometry facilities such as the Very Long Baseline Array (e.g. Reid et al., 2009). The Bar and Spiral Structure Legacy survey (BeSSeL; Brunthaler et al., 2011) is currently measuring accurate parallax distances to 400 high-mass star-forming regions, and will help provide a clearer picture of the structure of the Galaxy in years to come.

To solve the KDA for the CHIMPS sources, the KDA resolutions of publicly available data from other Galactic Plane surveys of star-forming regions and dust structures were exploited. By associating CHIMPS sources with molecular clouds or clumps, or YSOs and HII regions from these other surveys, it is possible to discriminate between the various kinematic solutions calculated as described in Section 4.2. CHIMPS sources were compared to sources from the source catalogues of ATLASGAL, RMS, BGPS and GRS, and in cases where an association could be made, the closest kinematic solution for the CHIMPS v_{LSR} was assigned.

4.3.1 Sources with simple KDA solutions

The easiest kinematic distances to assign are for those clumps which have no ambiguity; CHIMPS clumps which have either peak or centroid velocities of $v_{\text{LSR}} < 0 \text{ km s}^{-1}$ lie outside the Solar circle (i.e. with $R_{\text{GC}} > R_0$) have unphysical near distances, and so are assigned to the far distance. 52 of the original 4999

CHIMPS sources were assigned the far kinematic distance in this way, of which 43 are spatially resolved sources after the deconvolution described in Section 4.1. These sources have kinematic distances in the range of approximately 12.5–18 kpc.

There are similarly simple solutions, too, for some sources which lie at the distance of the tangent along that line of sight. Objects which are located at the tangent for a particular longitude are those in which the near- and far- kinematic solutions are equal. Owing to the velocity deviations from the rotation curve, there are a number of sources which have velocities which are greater than the maximum ‘terminal’ v_{LSR} permitted by the rotation curve that do not have real quadratic solutions, as the discriminant ($R^2 - R_0^2 \sin^2(l)$) becomes negative. These sources are assumed to be located at the tangential distance, and are consistent within the velocity uncertainty of having equal near- and far- kinematic solutions. These sources are located at the distance given by Equation 4.11. 380 sources with negative discriminants were assigned to the tangential KDA solution, and 346 of these are spatially resolved.

4.3.2 Association with ATLASGAL sources

The ATLASGAL survey of 870 μm dust continuum emission (Schuller et al., 2009) in the inner Galaxy is the most exhaustively catalogued census of star-forming clumps in the Milky Way. Urquhart et al. (2013a) matched ATLASGAL clumps from the Compact Source Catalogue (Contreras et al., 2013) to methanol masers with parallax distances from the MMB survey (Caswell et al., 2010) and Urquhart et al. (2013b) found the ATLASGAL clumps coincident with compact HII regions from the VLA 5 GHz survey CORNISH (Hoare et al., 2012) with maser parallax, spectroscopic or kinematic distances from the literature and derived new

kinematic distances to the remainder. Urquhart et al. (2014b) combined these two preceding catalogues with an additional sample of ATLASGAL clumps associated with HMYSOs and HII regions identified by the RMS survey (Lumsden et al., 2013), with assigned kinematic distances.

This combined catalogue of ATLASGAL clumps in Urquhart et al. (2014b) was used as a reference for the next step in the distance assignment of the CHIMPS clumps. A three-dimensional search was carried out, looking for ATLASGAL sources within a radius of 5 resolution elements, in each of the l , b and v axes, from the peak of emission of each CHIMPS source with an unresolved kinematic distance solution. This search radius equates to 75 arcseconds in the spatial axes, and 2.5 km s^{-1} in the velocity axis. 152 CHIMPS sources were assigned kinematic distance solutions in this manner, only one of which is a spatially unresolved source.

As an additional matching with ATLASGAL, the source catalogue of Wienen et al. (2015) was used to associate ATLASGAL and CHIMPS sources. The Wienen et al. (2015) catalogue does contain some clumps which have already appeared in the Urquhart et al. (2014b) catalogue, but the authors use a different technique to assign distances. They use the friends-of-friends algorithm (Huchra & Geller, 1982; Moore, Frenk & White, 1993; Berlind et al., 2006) to group together sources which lie in similar regions of l , b , v -space, and typically within a radius of 2 pc. They use spectra of NH_3 , N_2H^+ and CS to assign velocities to these groups, resolving the KDA with a combination of the HiSA and HiCA techniques applied to Hi spectra from the VGPS.

Of the 1131 sources in the catalogue of Urquhart et al. (2014b) and 1814 sources in the Wienen et al. (2015) catalogue, there are 653 clumps which appear in both catalogues, 230 (35%) of which have distance assignments differing by

more than 1 kpc. However, only 3% of the velocities assigned to those duplicate clumps differ by more than 5 km s^{-1} , which typically results in a kinematic distance deviation of only $\lesssim 0.5 \text{ kpc}$. A volumetric search was conducted around each remaining distance-unassigned CHIMPS source, again with search radius of 5 resolution elements, for ATLASGAL clumps appearing in Wienen et al. (2015). These ATLASGAL clumps have a quoted near, far or tangent KDA assignment, and so the CHIMPS sources which found matches were given the same solution, as opposed to taking the same distance. For CHIMPS sources assigned to duplicate ATLASGAL distances, preference is given to distances assigned in Urquhart et al. (2014b). A further 113 CHIMPS sources had distances assigned by association with the Wienen et al. (2015) catalogue, and they are all spatially resolved sources. Both of these ATLASGAL studies adopt the same rotation curve as is adopted for the CHIMPS sources – that of Brand & Blitz (1993) – and so the assigned kinematic distances ought to be in good agreement.

4.3.3 Association with RMS sources

A further catalogue of the YSOs falling within the CHIMPS region was acquired from the RMS Database Search Page¹. A total of 60 RMS YSOs fall in the CHIMPS area of $\sim 27.5^\circ$ - 46.5° and $|b| < 0.5^\circ$. A 3-dimensional 5-resolution element search was again carried out around the positions of CHIMPS clump peaks leading to the assignment of kinematic distances to a further 9 CHIMPS clumps. Only a small fraction of the RMS YSOs in this catalogue were associated with CHIMPS clumps in this search, but the likely explanation is that the YSOs which were not assigned to CHIMPS clumps in this step had already been assigned due to their appearance in the ATLASGAL catalogue of the preceding step. The

¹ http://rms.leeds.ac.uk/cgi-bin/public/RMS_SEARCH_PAGE.cgi

majority of the RMS-CHIMPS associations had therefore already been made. All of these CHIMPS clumps are spatially resolved.

4.3.4 Association with BGPS sources

Distances to the 1.1 mm dust continuum BGPS sources were assigned by Ellsworth-Bowers et al. (2013) using the so-called distance probability density function (DPDF) formalism, a Bayesian technique which uses ancillary datasets and models to resolve the KDA. The BGPS continuum sources have velocities assigned from a combination of spectra of the dense gas tracer HCO^+ ($J = 3-2$), acquired by follow-up observations, which are supplemented by spectra of the lower density tracer ^{13}CO ($1-0$) from the GRS. Synthetic $8\ \mu\text{m}$ images are produced from the 1.1 mm images by processing through a model of stellar and dust emission at mid-infrared wavelengths, with the dust continuum source being placed at varying distances. The morphology of the predicted absorption feature is then compared to the $8\ \mu\text{m}$ GLIMPSE imaging smoothed to the BGPS resolution, and the quality of the match informs the prior DPDF. This prior DPDF from the synthetic imaging is then combined with a prior DPDF given by an assumed model of the molecular gas distribution, and the clump distance with the maximum likelihood from these distributions is assigned. Ellsworth-Bowers et al. (2015) improved on and expanded this method by incorporating methanol and water maser parallax distances, resulting in a catalogue.

The Ellsworth-Bowers et al. (2015) catalogue was used to find associations of CHIMPS clumps with BGPS sources. Of the remaining CHIMPS clumps with no kinematic distance solution, 213 were found to be within 75 arcseconds and $2.5\ \text{km s}^{-1}$ of a BGPS source with a valid distance assignment. The kinematic solution with the best agreement to the BGPS distance was chosen to be the

solution to the KDA. Of these 213 sources with distance assignments, all but two of them are spatially resolved.

A further match with BGPS sources was carried out, but this time the catalogues of Eden et al. (2012) and Eden et al. (2013) were used. These studies calculated distances to BGPS sources falling in two regions, one covering $l = 28.5\text{--}31.5^\circ$, and one $l = 37.83\text{--}42.50^\circ$, with both regions extending to $|b| < 0.5^\circ$ in latitude. Spectra of $^{13}\text{CO}(1\text{--}0)$ and from the GRS, were extracted for each BGPS source and, in spectra where there were multiple emission peaks (and therefore ambiguous velocity assignments), these were supplemented with $^{13}\text{CO}(3\text{--}2)$ data from a previous reduction of what became CHIMPS data. Using these velocities, the BGPS sources were then associated with GRS clouds of Roman-Duval et al. (2009), from which kinematic distances were derived. In cases where there was no existing distance assignment from the GRS catalogue, or where BGPS clumps were found to have no GRS association, HI spectra from the VGPS were inspected and distances were assigned according to the HiSA method.

Once again, the CHIMPS clumps were matched to the BGPS sources, with velocities given by Eden et al. (2012) and Eden et al. (2013), by searching a volume with an extent of 75 arcseconds in l and b , and 2.5 km s^{-1} in v_{LSR} . A total of 164 CHIMPS clumps were associated with these BGPS sources, with 124 and 40 coming in the $l = 30^\circ$ and $l = 40^\circ$ patches, respectively. They are all spatially resolved.

4.3.5 Association with GRS sources

The $^{13}\text{CO}(1\text{--}0)$ GRS is probably the most directly comparable survey to CHIMPS; although the GRS traces more diffuse gas at lower resolution than CHIMPS, the

optical depths are much more closely matched than the emission in COHRS due to the use of the same isotopologue, ^{13}CO . Rathborne et al. (2009) describe two catalogues for the GRS – one for clumps and one for clouds. The cloud catalogue features sources that were extracted after applying a large smoothing, moving from a resolution of 46 arcseconds to an effective resolution of 6 arcminutes, re-sampled onto a 3 arcminute pixel grid. The GRS clouds, then, are the largest molecular gas structures which ought to represent the boundaries within which all star-forming clumps and cores are found. The GRS clumps are similar structures to the CHIMPS clumps, and are the sources found in the 46 arcsecond native resolution of those data, with a source extraction carried out only on emission which has been identified as a cloud. Distances to the emission peaks of the GRS clouds were identified by Roman-Duval et al. (2009), who used HI spectra from the VGPS with the HiSA and HiCA techniques to resolve the KDA.

The GRS clumps are comparable to those found within CHIMPS, and the data sets differ only by a factor of ~ 2 in both angular and spectral resolution when considering that the CHIMPS data used for the source extraction were smoothed to an angular resolution of 27.4 arcseconds. The other difference is that CHIMPS is biased towards denser (and slightly warmer) gas, but the GRS clumps should still be structures comparable to the CHIMPS clumps. It was therefore appropriate to search for associations of CHIMPS clumps and GRS clumps. A volumetric search was carried out, looking for GRS clumps with emission peak coordinates within 75 arcseconds in l and b , and 2.5 km s^{-1} in velocity of the position of CHIMPS emission peaks. 632 matches were found, and the CHIMPS distances were assigned according to the distances to the parent clouds of GRS clumps determined by Roman-Duval et al. (2009). 35 of the parent clouds had no distance assigned, and the corresponding CHIMPS clumps were therefore left in

the sample of unassigned distances. Distances to 597 of the remaining CHIMPS clumps were assigned distances according to their GRS clump associations, of which 588 are spatially resolved.

Another search was carried out to match CHIMPS clumps to the positions of the GRS *clouds*; CHIMPS centroid positions in l , b and v_{LSR} were checked for consistency with the catalogued positions of GRS clouds with assigned distances by Roman-Duval et al. (2009). An (l, b, v_{LSR}) cuboid search volume used was centred on the GRS l , b and v_{LSR} coordinates for clouds, with a tolerance of half of the quoted FWHM size in each axis. In any cases where a CHIMPS clump was consistent with the volumes of multiple GRS clouds, the one with the closest centroid velocity was chosen. In this way, distances were assigned to a further 886 CHIMPS clumps, and 834 of these are spatially resolved.

4.3.6 Association with CHIMPS sources

At this point, there are still 2593 of the original 4999 clumps in the CHIMPS catalogue that have yet to have the KDA resolved. For this remainder, the CHIMPS clumps that do have assigned kinematic distances were used as the references for those with unassigned distances. Wienen et al. (2015) used the friends-of-friends algorithm (Huchra & Geller, 1982; Moore, Frenk & White, 1993; Berlind et al., 2006) to define groups of ATLASGAL sources which are likely to be physically associated with each other to vastly reduce the number of KDAs to be solved. For each source, they find the neighbours which lie within a spatial tolerance of 0.3° and 10 km s^{-1} in velocity, a tolerance corresponding to the median molecular cloud size of GRS clouds from (Roman-Duval et al., 2009).

To assign KDA solutions to the remaining CHIMPS clumps, a similar scheme is adopted. A search was conducted around each remaining CHIMPS clump,

looking for nearby CHIMPS clumps with assigned distances. The search volume used was 0.3° in l and b , and 10 km s^{-1} in the velocity axis under the assumption that the CHIMPS clumps probably represent sub-units of molecular clouds like those seen in the GRS. In cases where a CHIMPS clump has more than one candidate association in the search volume, the closest match was favoured. 2318 of the remaining CHIMPS clumps were assigned kinematic distance solutions in this way, and 2081 of these are spatially unresolved sources.

4.3.7 Summary of distance assignments

The distance assignments for the 4999 CHIMPS clumps are summarised in Table 4.1. Each method described in the preceding Sections 4.3.1 to 4.3.6 is assigned a KDA method label in the ‘Method’ column. The resulting distribution of sources is shown for a top-down view of the Galaxy in Figure 4.3. There are 275 sources (229 spatially resolved ones) with no distance assignment. This sample presumably consists partly of noise artefacts, but there may also be a sample of isolated dense clumps that have not been detected. These warrant further investigation in the future.

The distributions of heliocentric and Galactocentric distances for the CHIMPS clumps are illustrated in Figure 4.2. The Galactocentric distance distribution shows peaks at the distances corresponding to spiral arms, with the Scutum–Centaurus, Sagittarius and Perseus arms being responsible for the peaks at 4.5, 6.5 and 8 kpc, respectively. In the distribution of heliocentric distances, the peak at ~ 8 kpc corresponds to the Scutum–Centaurus region, and consists of many sources that have the tangential KDA solution. The peaks at ~ 5 and 12 kpc both correspond to sources in the Sagittarius arm, which appears twice along these lines of sight at near- and far-distances. The Perseus arm also contributes

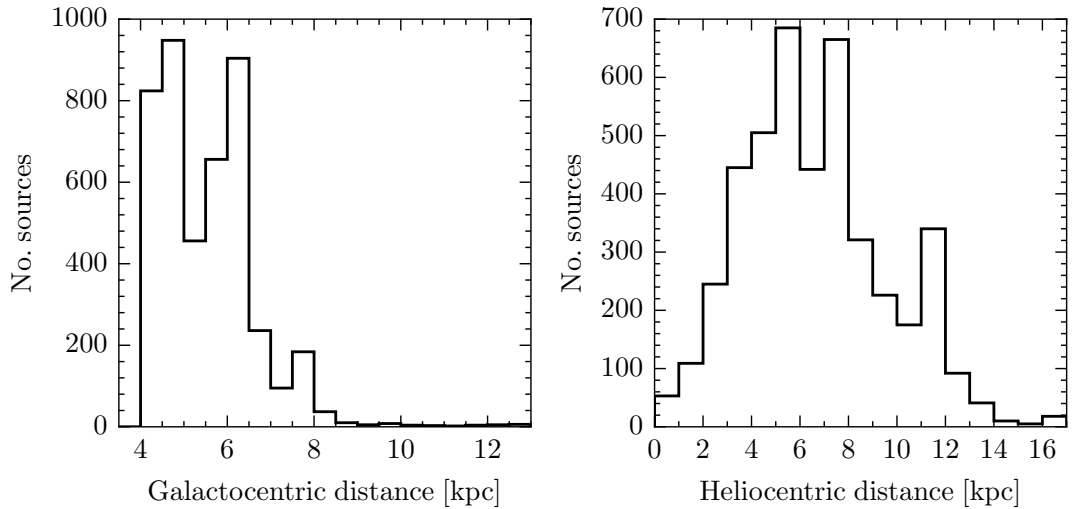


Figure 4.2: The Galactocentric and Heliocentric distance distributions of the CHIMPS clumps.

to sources in the 12 kpc heliocentric distance bin. The vast majority of CHIMPS clumps reside within 8 kpc of the Galactic centre, and 95% of them are closer than 12 kpc from the Sun.

4.4 The uncertainties on kinematic distances

There is a significant element of uncertainty on heliocentric distances calculated from these kinematics. The assumption being made is that the circular velocity (and thus v_{LSR}) of the cloud or clump is controlled only by the Galactic rotation curve, but in reality there are a number of processes which cause perturbations on top of this, with both systematic and random contributions. The shocks caused by the passage of a spiral arm may induce a systematic deviation of up to $\sim 20 \text{ km s}^{-1}$ (Roberts, 1969, 1972; Dobbs, Bonnell & Pringle, 2006), and there are also a number of effects that contribute to random deviations. Brand & Blitz (1993) found that random deviations occurring on the cloud-to-cloud scale are

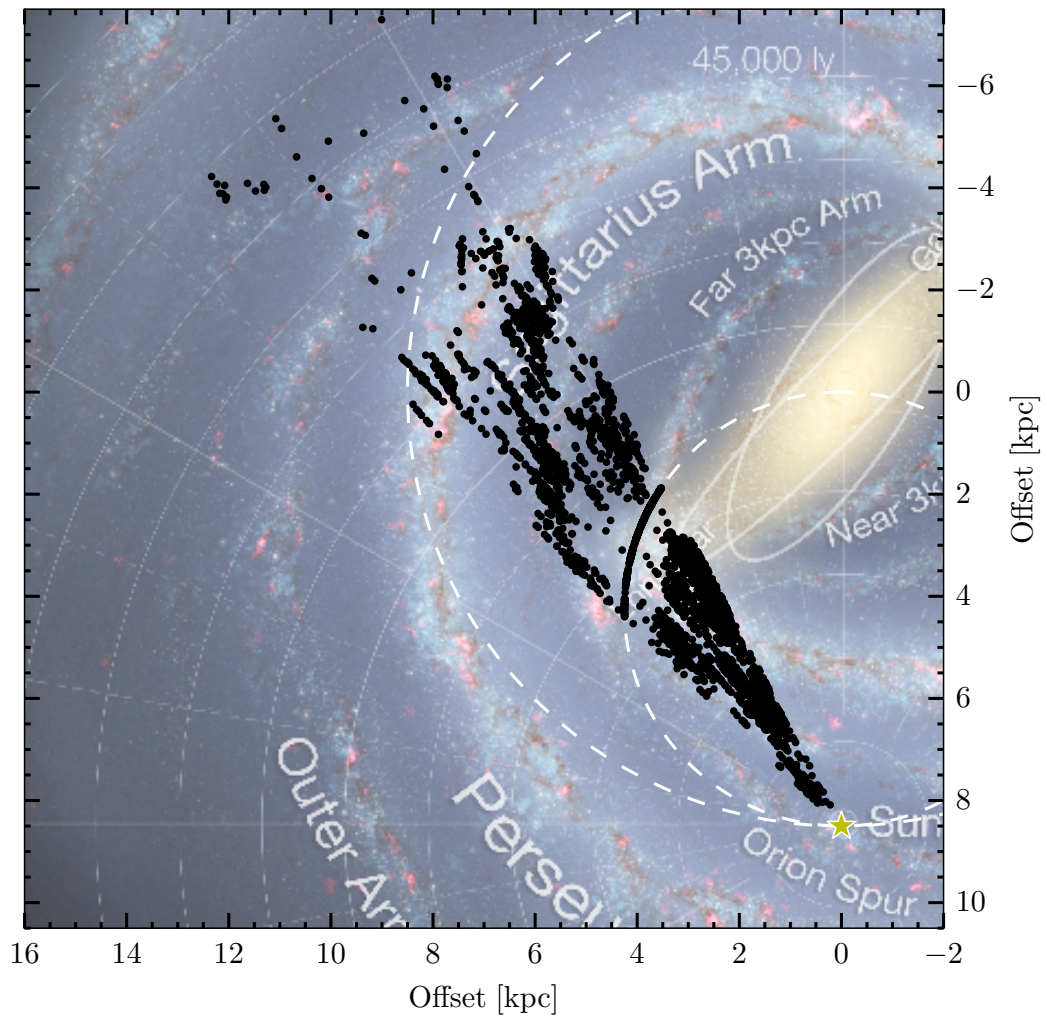


Figure 4.3: A top-down view of the distribution of spatially resolved CHIMPS sources in the Galaxy with the kinematic distances derived in this Chapter. The large dashed circle is the Solar circle, and the small dashed circle is the locus of the tangent points. The underlying image is an artist's impression, created by Robert Hurt of the Spitzer Science Center in consultation with Robert Benjamin at the University of Wisconsin-Whitewater, as described in Churchwell et al. (2009).

Table 4.1: A summary of the methodology used to resolve the KDA of CHIMPS sources

Method	Described in Section	Number of all sources assigned	of which are spatially resolved	Reference catalogue
negKDN	4.3.1	52	43	–
tangent	4.3.1	380	346	–
AGALa	4.3.2	152	151	Urquhart et al. (2014b)
AGALb	4.3.2	113	113	Wienen et al. (2015)
RMS	4.3.3	9	9	See Section 4.3.3
BGPSa	4.3.4	213	211	Ellsworth-Bowers et al. (2015)
BGPSb	4.3.4	164	164	Eden et al. (2012) and Eden et al. (2013)
GRScIp	4.3.5	525	516	Rathborne et al. (2009) and Roman-Duval et al. (2009)
GRScId	4.3.5	798	754	Roman-Duval et al. (2009)
CHIMPS	4.3.6	2318	2081	This work
	Total	4724	4388	
Unassigned		275	229	

generally $\sim 5 \text{ km s}^{-1}$ and that while the velocity residuals of individual molecular clouds could be as large as 40 km s^{-1} , the overall distribution is centred around 0 km s^{-1} with a standard deviation of 12.8 km s^{-1} . Clemens (1985) and Reid et al. (2009) estimate that these perturbations are on the order of 15 km s^{-1} , and so this value is adopted in order to maintain consistency with these authors as well as Brand & Blitz (1993) to estimate the uncertainty on the kinematic distances.

It is possible to estimate the distribution of velocity deviations from the adopted rotation curve for the CHIMPS data if all velocities greater than the terminal velocity are assumed to be due to the intrinsic velocity dispersion. The terminal velocity for any particular line of sight denoted by the longitude l is the velocity at which the Galactocentric radius is given by $R_{\text{GC}} = R_0 \sin(l)$. At the tangent points, there is no component of the velocity of the source in the plane of the sky, and the full magnitude of the velocity is along the line of

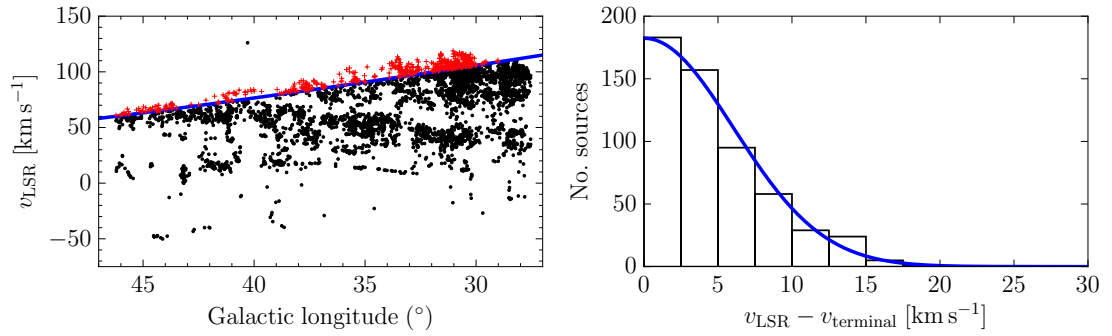


Figure 4.4: *Left panel:* position-velocity diagram of the CHIMPS sources, with the terminal velocity of the Brand & Blitz (1993) rotation curve overlaid in blue. The red crosses are the sources assigned the tangent distances by their negative discriminants, and the black points are the other CHIMPS sources. *Right panel:* deviations of the sources (red crosses) at the tangent region from the terminal velocity of the rotation curve at the objects' longitude coordinates. The blue line is the fitted normal distribution with a mean of 0 km s^{-1} and a standard deviation of 6 km s^{-1} .

sight. It is, therefore, the maximum velocity allowed for a source that is precisely following an orbit around the Galactic centre dictated by the rotation curve. The sources exceeding the terminal velocity appear to be normally distributed about the terminal velocity with a standard deviation of 6 km s^{-1} (see Figure 4.4); assuming that the distribution of velocity deviations is symmetric in positive and negative dispersions a Shapiro-Wilk test finds $W = 0.998$ and $p = 0.339$, indicating that that these velocities are normally distributed. The deviation from the terminal velocity appears to decrease as a function of longitude, but this is likely to be a selection effect caused by the decreasing inclination of the leading edges of the spiral arms with respect to the line of sight, and consequently a smaller component of the induced velocity difference is along the line of sight.

The uncertainty in the kinematic distance was calculated using a Monte Carlo technique; for each CHIMPS source, a velocity perturbation δv_{LSR} was added on to the centroid v_{LSR} from the catalogue, from which the distance was calculated. The perturbations were generated at random from a normal distribution with a mean of 0 km s^{-1} and a standard deviation of 15 km s^{-1} . This process was

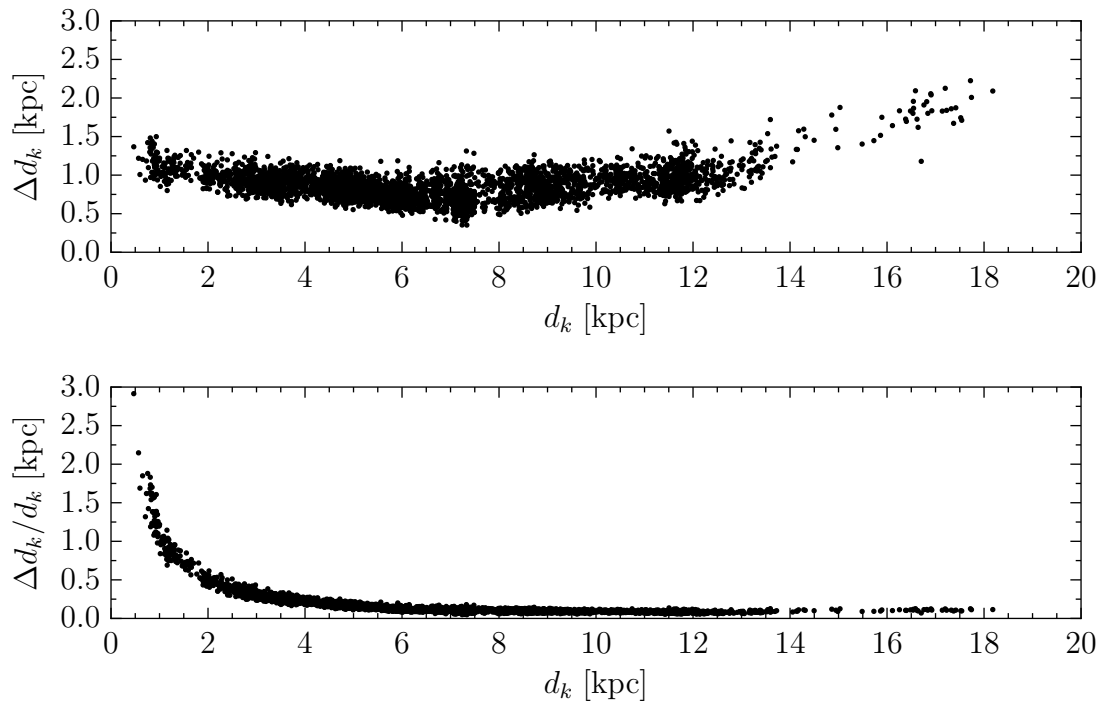


Figure 4.5: Absolute (*top*) and relative uncertainties (*bottom*) on the derived kinematic distances for the CHIMPS sources.

carried out with 50 random perturbations on the velocity of each clump, and accordingly the mean and standard deviation were recorded for each of the near, far and tangential kinematic distance solutions. The kinematic distance solutions are determined in Section 4.3, and the derived uncertainties on those distances are shown in Figure 4.5. For the 162 out of 4388 sources closer than ~ 2 kpc, the fractional errors on the heliocentric distances are extremely large ($\gtrsim 50\%$), and consequently for further analysis, these sources are removed from the sample.

The preceding error analysis for the kinematic distances naturally assumes that, at this point, that the correct solution to the KDA has been identified – an assumption that is not necessarily true. The determination of KDA solutions in stages naturally places a higher relative level of trust on the earlier matching methods; this order was chosen in order to reflect both the types of sources that have been considered, and generally placing a greater emphasis on sources which

have been analysed using by-eye rather than automated methods.

To verify the reliability of this method, a self-consistency check was made for those KDAs distinguished using the methods based on clump-matching, listed in Table 4.1 as AGALa, AGALb, RMS, BGPSa, BGPSb and GRScIp from Sections 4.3.2 to 4.3.5. A total of 1,176 CHIMPS sources, 1,164 of which that are spatially resolved, were assigned KDA solutions using these methods in the ordered approach. To check for self-consistency, a comparison was made by compiling a catalogue of all of the ATLASGAL, RMS and BGPS sources along with GRS clumps into a single catalogue, and searching for matches with the 4,228 spatially resolved CHIMPS clumps that do not have a solution assigned after resolving those with simple solutions in Section 4.3.1. Of these, 1,165 were found to match to solutions from the aforementioned combined ATLASGAL, RMS, BGPS and GRS clump catalogue, a difference of only 1 compared to the adopted method. The same KDA solution was found for 1,005 of these – an agreement level of 87%.

These distance assignments were propagated through the remaining method, by matching the clumps to GRS clouds and finally CHIMPS clumps with distance assignments as described in Sections 4.3.5 and 4.3.6, respectively. The same KDA solutions were found for 4,356 of the 4,724 CHIMPS clumps used in this Chapter - a 92% agreement. The discrepant 8% are the result of the sequential searches carried out which assumed a greater reliability of the ATLASGAL sample of Urquhart et al. (2014b) compared to that of Wienen et al. (2015), for example. From this discrepancy, it is clear that this assumed sequence of reliability in the various catalogues does not introduce a dominant source of bias in the distances (and hence masses, densities etc.) in the sample.

The use of multiple catalogues to break the KDA, which are themselves the result of different methods, does introduce a level of bias that is difficult

to quantify. The majority of the methods described in Sections 4.3.2 through to 4.3.5 rely on the inspection of HI spectra, but maser parallax distances also make up a portion of the ATLASGAL sample, for example, and the maximum likelihood method of resolving distances to BGPS clumps by Ellsworth-Bowers et al. (2013) also differs from these methods.

Parallax distances are the ideal solution to the KDA, and the MMB survey of 6.7 GHz methanol masers (amongst other types) described in Section 1.5 will provide more reliable distances for future studies. Distances determined from parallaxes are intrinsically more accurate as they do not rely on a model of the Galactic rotation curve, or precise knowledge of the distance to the Galactic centre. The high-mass star-forming region W49 in the Perseus spiral arm, for instance, has a parallax distance of $11.11^{+0.79}_{-0.69}$ kpc determined by Zhang et al. (2013) from very-long-baseline interferometry observations of 22 GHz H₂O masers as part of BeSSeL. There are 29 CHIMPS clumps lying in the region of W49, with longitudes in the range $43.08^\circ \leq l \leq 43.26^\circ$, latitudes in the range $-0.10^\circ \leq b \leq 0.11^\circ$ and velocities between 4.5 and 9 km s⁻¹ that appear to be associated with W49. With a mean kinematic distance of 11.9 kpc, a standard deviation of 0.4 kpc and a mean uncertainty of 1.1 kpc, the calculated kinematic distances are consistent with the maser parallax distance.

The W43 high-mass star-forming region located in the Scutum spiral arm, at $l \approx 30.7^\circ$ is also a suitable target for comparison with parallax measurements. Based on the parallax measurements of three 12 GHz methanol masers and a 22 GHz water maser, again as part of BeSSeL, Zhang et al. (2014a) report a distance of $5.49^{+0.39}_{-0.34}$ kpc to W43. Nguyen Luong et al. (2011) identified central region of W43 as lying in the velocity range of 80–110 km s⁻¹ at the near kinematic distance. There are 383 CHIMPS clumps at the near kinematic distance within the

Table 4.2: A comparison of the kinematic distances of four CHIMPS sources to the maser parallax distances of their associated ATLASGAL/MMB source

CHIMPS source	D_{CHIMPS} (kpc)	ATLASGAL source	D_{ATLASGAL} (kpc)
G035.390+00.018	6.9 ± 1.0	G035.399+00.026	6.1
G036.921+00.484	16.9 ± 1.7	G036.919+00.482	16.9
G038.117−00.232	6.7 ± 0.8	G038.119−00.229	7.3
G038.647+00.086	17.7 ± 2.0	G038.652+00.087	17.1

spatial area covered by the Zhang et al. (2014a) measurements of approximately $29.8^\circ \leq l \leq 31.6^\circ$ and satisfying the velocity criteria, with a mean kinematic distance of 5.8 kpc, a standard deviation of 0.4 kpc and a mean uncertainty of 0.7 kpc. This kinematic distance measurement is consistent with the Zhang et al. (2014a) maser parallax distance.

While the averaged distances to the large star-forming regions W43 and W49 are consistent with the parallax measurements, how do the determined kinematic distances to *individual* CHIMPS clumps compare with available parallax measurements? To investigate this, the ATLASGAL clumps in the catalogue of Urquhart et al. (2014b) that have MMB maser parallax distances were used to search for CHIMPS counterparts with independently-defined kinematic distances. There are four CHIMPS clumps that lie within 5 resolution elements ($76 \text{ arcseconds} \times 76 \text{ arcseconds} \times 2.5 \text{ km s}^{-1}$ in l , b and v , respectively) of such an ATLASGAL source, two of which had unique far kinematic distance solutions, and the other two are located at the tangent due to being above the terminal velocity. These four CHIMPS and ATLASGAL/MMB associations are detailed in Table 4.2, and the kinematic and parallax distances are found to be consistent for all of them.

4.5 Basic physical properties

With distances assigned to the clumps, it is now possible to determine their masses from their volume-integrated column densities. However, when adding up column density values, there is an overlap of the beam footprints at each sampling position, and therefore each voxel has been sampled multiple times. This is an effect caused by an overlap of the footprint of the beam since the sample spacing is less than half of the beam width. This oversampling factor can be calculated:

$$f_{\text{os}} = 1 + 4 \sum_{i=1}^6 \exp \left[-\frac{a_i^2}{b^2} 4 \ln 2 \right], \quad (4.12)$$

assuming a Gaussian beam profile where a is the sample spacing, b is the beam FWHM and $a_1 = a$, $a_2 = 2a$, $a_3 = \sqrt{2}a$, $a_4 = a_5 = \sqrt{5}a$, $a_6 = \sqrt{8}a$. The sample spacing of these observations is 7.2761 arcseconds, and the FWHM of the JCMT beam at this frequency is 15.224 arcseconds, resulting in an oversampling factor of $f_{\text{os}} = 4.93$. Each voxel in CHIMPS has been divided by f_{os} to remove this effect.

$$N(^{13}\text{CO})_{\text{tot}} = \frac{1}{f_{\text{os}}} \sum_{lbv} N(^{13}\text{CO})_{lbv}, \quad (4.13)$$

The clump mass can be determined from $N(^{13}\text{CO})_{\text{tot}}$ according to the following formula:

$$\frac{M}{M_{\odot}} = 2.24 \times 10^{32} X(\text{H}_2/^{13}\text{CO}) N(^{13}\text{CO})_{\text{tot}} \frac{\mu m_{\text{p}} p^2 d_{\text{k}}^2}{M_{\odot}}, \quad (4.14)$$

where p is the pixel size in arcseconds (in this case 7.6 arcseconds), and the numerical factor converts the angular pixel size to a spatial scale at the clump's kinematic distance d_{k} (in kpc), $X(\text{H}_2/^{13}\text{CO})$ is the abundance ratio of H_2 compared to ^{13}CO , μ is the mean mass per H_2 molecule, taken to be 2.72, accounting

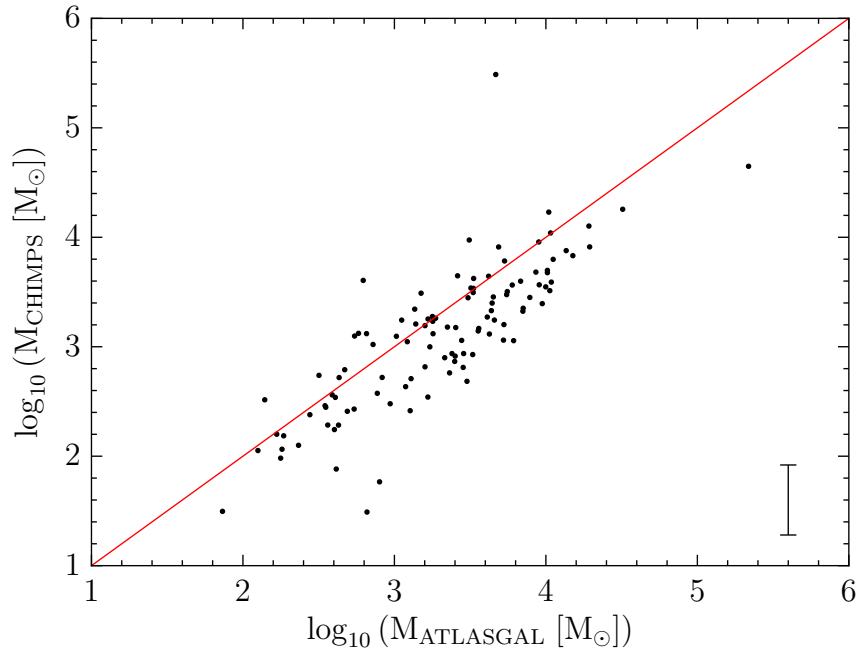


Figure 4.6: A comparison between the masses derived for a sample of CHIMPS clumps and their ATLASGAL counterparts. The line of equality is overlaid in red and the median error bar on the CHIMPS masses is shown in the lower right.

for a helium fraction of 0.25 (Allen, 1973), and m_p is the mass of a proton.

The value of $X(\text{H}_2/^{13}\text{CO})$ is determined from $X(^{12}\text{CO}/\text{H}_2)$ and $X(^{12}\text{CO}/^{13}\text{CO})$. For $X(^{12}\text{CO}/^{13}\text{CO})$, the local ISM value of 77 is adopted (Wilson & Rood, 1994), which is reasonable given that the Sun lies roughly in the middle of the Galactocentric distance range covered by the CHIMPS clumps. The scatter on the Wilson & Rood (1994) abundance ratio is $\sim 40\%$ at $R_{\text{GC}} = 4$ kpc and $\sim 25\%$ at $R_{\text{GC}} = 12$ kpc, and so a mean scatter of $\sim 30\%$ is adopted as the uncertainty on the value of $X(^{12}\text{CO}/^{13}\text{CO})$. The value of $X(^{12}\text{CO}/\text{H}_2)^{-1} = 8.5 \times 10^{-5}$ is adopted from Frerking, Langer & Wilson (1982), and the uncertainty is also taken to be $\pm 30\%$ (Bolatto, Wolfire & Leroy, 2013).

To compare the masses derived for the CHIMPS clumps with an independent measure, their ATLASGAL dust continuum counterparts were identified. Unique

associations between CHIMPS and ATLASGAL clumps were made by searching in a volume of $3 \times 3 \times 3$ CHIMPS resolution elements (i.e. 45 arcseconds in l and b , and 1.5 km s^{-1} in velocity) around the position of the peak $^{13}\text{CO} (3-2)$ intensity of each CHIMPS clump. There was one ATLASGAL clump that matched to three CHIMPS clumps and was therefore excluded, because the corresponding CHIMPS clumps are likely to have been divided along the line of sight. The remaining 112 ATLASGAL-CHIMPS associations generally agree very well within the quoted uncertainties, as can be seen in Figure 4.6; there is one anomalous measurement in which the CHIMPS mass is larger than the corresponding ATLASGAL mass by a factor of 100. The ATLASGAL masses appear to be systematically greater by a factor of ~ 1.5 to 2, though this should be expected when comparing masses derived from the full H_2 column density, as in ATLASGAL, to a higher-critical density tracer as in CHIMPS; the CHIMPS masses are necessarily missing a component of mass in the lower density regions.

The effective radius is determined from the rms sizes in the l and b axes as reported by FellWalker, after deconvolving to remove the smoothing effects of the beam, and applied before the source extraction (see Section 4.1):

$$R_{\text{eff}} = d_{\text{k}} \sqrt{\text{size}(l) \text{size}(b)}, \quad (4.15)$$

where $\text{size}(l)$ and $\text{size}(b)$ are the intensity-weighted rms deviations in the l and b axes, deconvolved to account for the beam smoothing and the applied smoothing (see Equation 4.3) and d_{k} is the assigned kinematic distance.

The mass–radius relationship for all CHIMPS clumps at a heliocentric distance of more than 2 kpc is displayed in Figure 4.7 alongside the GRS molecular clouds. A power-law fit using a fitting routine developed for quantities with bi-

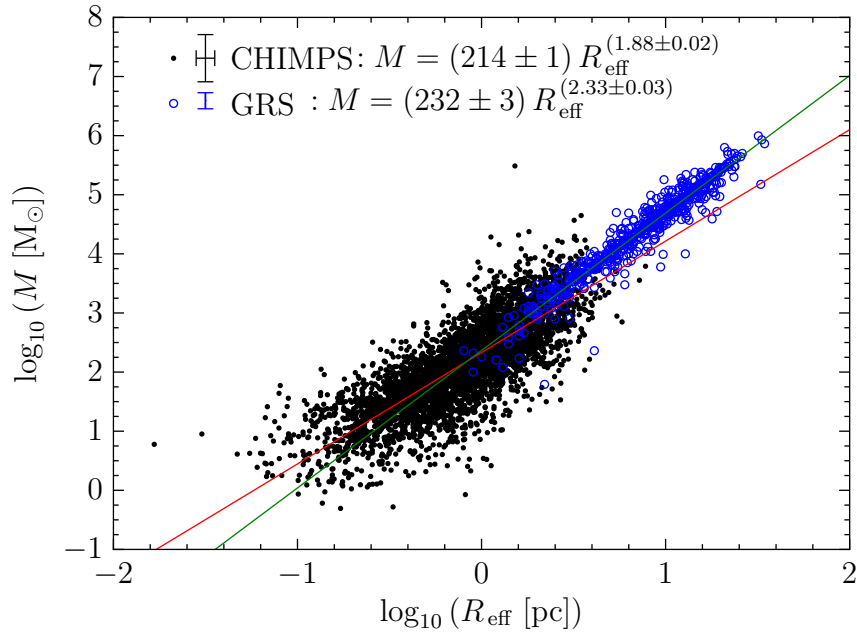


Figure 4.7: The mass–radius relationship for the CHIMPS clumps (black points) and, for comparison, the GRS clouds (open blue circles) with the best fit power laws and median error bars given in the upper left.

variate correlated errors and intrinsic scatter (BCES; Akritas & Bershady, 1996), finds that the relationship can be described as $M = (214 \pm 1) R_{\text{eff}}^{(1.88 \pm 0.02)}$ – a significantly shallower relationship than found for the molecular clouds of the GRS, for which Roman-Duval et al. (2010) found $M = (228 \pm 18) R^{(2.36 \pm 0.04)}$. The scatter on the CHIMPS data is much larger than that on the GRS, and probably relates to the large difference in resolution. The GRS clouds were extracted from data that had been smoothed to a resolution of 6 arcminutes, thereby removing substructure on small scales, whereas the CHIMPS clumps were extracted from data smoothed to 27.4 arcsecond resolution.

The determination of mass and radius naturally allows the average density to be determined. Assuming that matter in each clump is approximately spherical,

then the average number density may be calculated by:

$$n(\text{H}_2) = \frac{3}{4\pi} \frac{M}{\mu m_{\text{p}} R_{\text{eff}}^3}, \quad (4.16)$$

which, using the more appropriate units of M_{\odot} for mass and pc for the radius, has the form:

$$n(\text{H}_2) = 3.57 M R_{\text{eff}}^{-3}, \quad (4.17)$$

yielding the average number density in units of cm^{-3} .

The distributions of clump masses, radii and average densities are illustrated in Figure 4.8, with masses spanning from $\sim 10^{-1}$ to $10^5 M_{\odot}$, radii in the range ~ 0.03 to 10 pc and densities spanning ~ 10 to 10^5 cm^{-3} . Comparison with the canonical properties of clouds, clumps and cores listed in Table 1.1 would seem to suggest that, while the sources are referred to here as ‘clumps’, the objects extracted from the CHIMPS data span the full range of those structures. The shape of the mass distribution is determined by the mass function of the clumps, but there is also a significant contribution from various observational biases.

To estimate the completeness of the CHIMPS data, fake sources with varying peak brightness temperatures were injected into a sample of three of the CHIMPS cubes, chosen to represent different environments in the survey. These cubes were centred on $b = 0^\circ$, with $l = 29.83^\circ$, 35.66° and 38.00° , chosen to represent the crowded, intermediate and sparse environments, respectively. These cubes were also chosen because their noise levels are comparable to the mean rms noise of 0.58 K (see Figure 2.1) of the whole survey, with values of 0.51 , 0.50 and 0.57 K per channel for the $l = 29.83^\circ$, 35.66° and 38.00° cubes, respectively.

The synthesised sources have a constant FWHM extent of 3 voxels in each of the l , b and v axes (before smoothing), in order to simulate clumps of emission

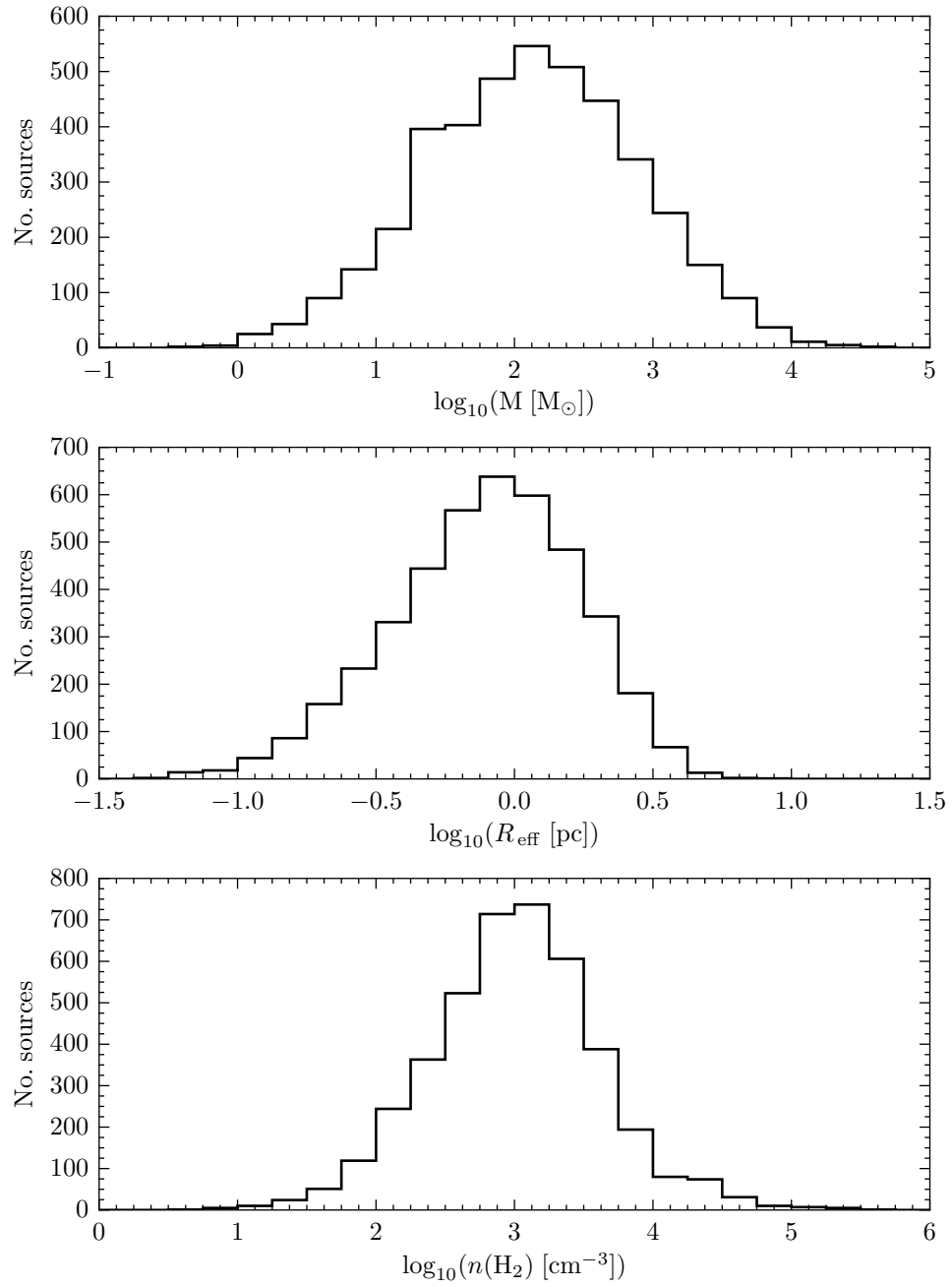


Figure 4.8: The distributions of mass, effective radius and average number density for the CHIMPS clumps. The number densities are calculated assuming uniform density spheres.

that are just spatially resolved. They also have identical peak T_{A}^* values, and the test was carried out by varying the peak T_{A}^* values over all integers in the range 1 to 20 K. After the source injection, the same processes were applied to the test cubes as were applied to the data cubes before the source extraction, described in Section 2.2.2, was carried out; the cubes were smoothed to a resolution of 27.4 arcseconds and SNR cubes were generated, on which the source extraction was carried out. For each cube 200 fake sources with identical sizes were injected in 50 realisations (to avoid crowding the cube), resulting in a total of 10,000 fake sources per peak intensity per cube.

The results of the completeness tests are presented in Figure 4.9. In the top panel, the recovery rate is illustrated as a function of the peak T_{A}^* value for the three test fields. In all fields, the recovery rate stays constant at $\sim 90\%$ for $T_{\text{A}}^* \gtrsim 3\text{ K}$, though slight deviations from this can be seen due to the crowding level, with the recovery rate of the crowded field being a few per cent lower than the intermediate and sparse fields. The lower steady recovery rate in the most crowded cube is due to source confusion, as injected sources land on stronger real emission features, and are consequently not recovered in the same position by FellWalker.

The lower panel of Figure 4.9 shows how the fraction of the integrated intensity (in K km s^{-1}) – the crucial quantity for the mass determination – recovered by FellWalker varies as a function of peak intensity. This ratio tends to $\sim 80\%$ of the integrated flux being recovered, and the form of this curve is determined by the fraction of the source intensity that lies below the noise level. For low-lying sources, a much greater fraction of the recovered intensity is lost below the detection threshold, and for sources with a peak intensity below $\sim 4\text{ K}$, more noise is present than genuine emission.

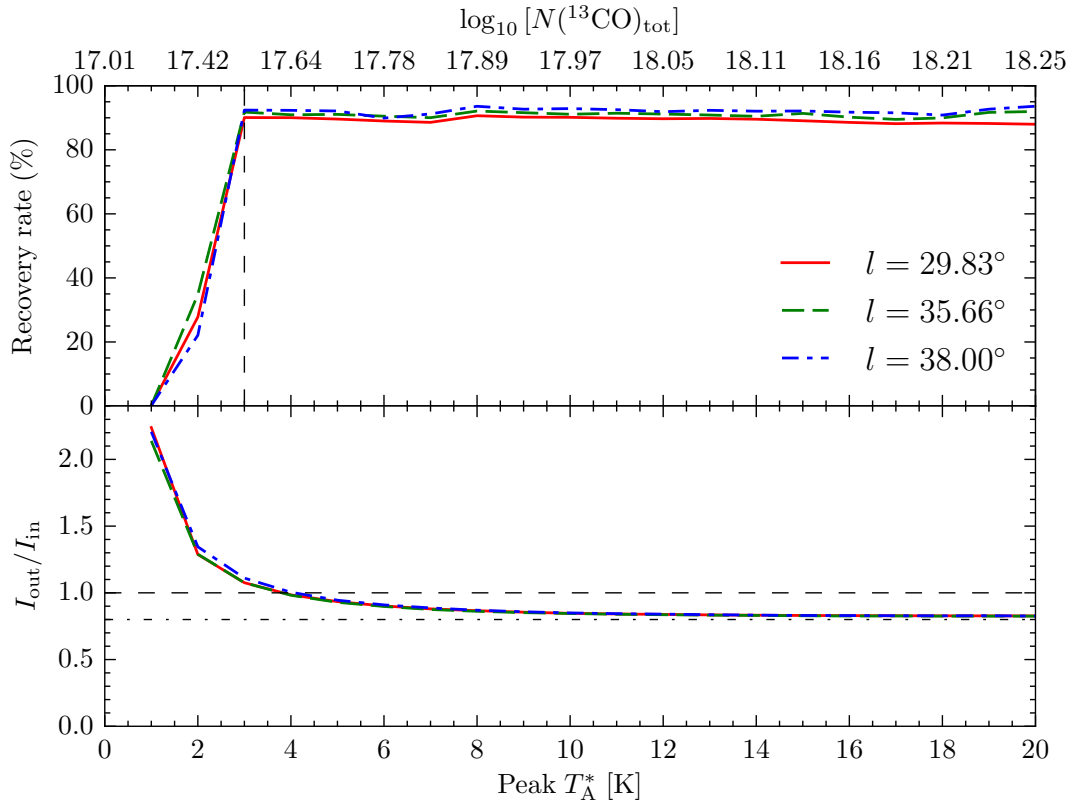


Figure 4.9: Results of the completeness tests. *Top*: Recovery rate of the 10,000 injected sources as a function of the peak T_{A}^* values. The dashed vertical line shows the adopted completeness limit, corresponding to an integrated column density of $10^{17.53} \text{ cm}^{-2}$. *Bottom*: The ratio of the integrated intensity of extracted sources to their injected integrated intensities as a function of peak T_{A}^* . The secondary axis gives the equivalent integrated column density of ^{13}CO , after integrating the input intensity over all voxels, assuming an excitation temperature of 8 K and an optical depth of 0.25.

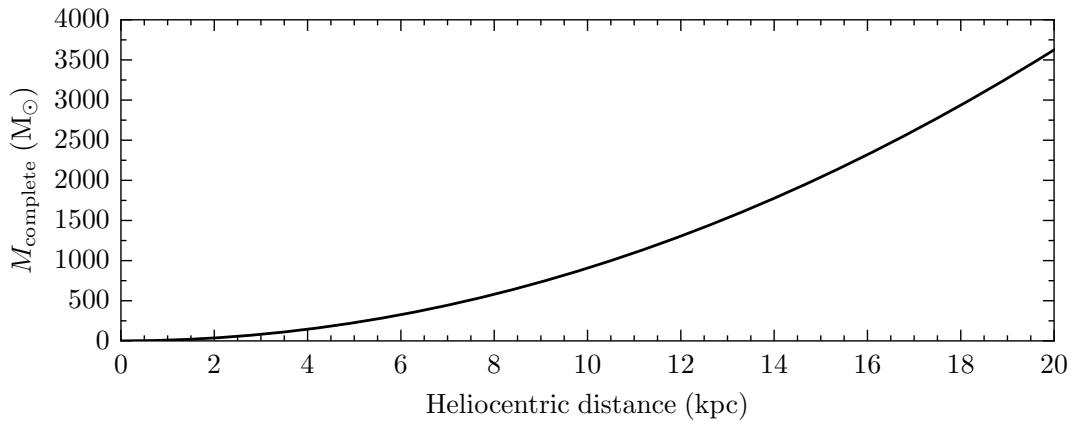


Figure 4.10: The completeness limit as a function of heliocentric distance, which may be described as $M_{\text{complete}} \approx 9.06 d_{\text{k}}^2$. For reference, the completeness limit at a distance of 10 kpc is approximately $1000 M_{\odot}$.

From the turnover in the recovery rate curves, a volume-integrated column density (see Equation 4.13) of $N(^{13}\text{CO}) = 10^{17.53} \text{ cm}^{-2}$ is adopted as the $\sim 80\%$ completeness level, corresponding to a total artificial source mass of $\sim 1000 M_{\odot}$ at a distance of 10 kpc. The completeness limit varies as a function of distance according to $M_{\text{complete}} \approx 9.06 d_{\text{k}}^2$, which is illustrated in Figure 4.10, though there are a number of important caveats with these completeness tests.

Firstly, since the noise level varies across the survey, the quoted completeness function $M_{\text{complete}} \approx 9.06 d_{\text{k}}^2$ does not apply to every cube, but represents the average completeness limit across the whole survey. The value taken from the turnover of these test cubes may be regarded as the average completeness level since these cubes have noise values close to the mean rms noise value of $\sim 0.6 \text{ K}$ per channel. The calculation of the completeness limit also makes the assumption that the optical depth is 0.25 for all voxels, which is the value assumed in Chapter 3 where $^{13}\text{CO} (3-2)$ is detected without $\text{C}^{18}\text{O} (3-2)$ emission. This is a reasonable assumption to make for the distant sources which are likely to be invisible in the weaker C^{18}O emission, with the implication that the quoted completeness limit is an underestimate.

A further caveat in this analysis is that these injected sources do not look like all of the sources in the survey. While there surely are many structures that are compact, like the just-resolved Gaussian sources injected, there are also many sources that have complex and irregular shapes, accompanied by irregular intensity profiles. These kinds of sources are extremely hard to replicate, and the quoted completeness limit, therefore, only really applies to compact sources.

4.6 Dynamic state

The dynamic state of the molecular clumps – whether they be expanding, collapsing or in some quasi-stable equilibrium – can be addressed by using the virial theorem. A virial equilibrium describes a state of affairs where the potential energy of a system is equal to twice its internal kinetic energy; MacLaren, Richardson & Wolfendale (1988) state a generalised form for the critical mass of a gas cloud for which virial equilibrium exists:

$$M_{\text{vir}} = \frac{(5 - 2n) \sigma^2 R}{(3 - n) G}, \quad (4.18)$$

where n is the index of a spherical mass with density distribution $\rho(r) \propto r^n$, σ is the three-dimensional velocity dispersion of a cloud with a radius R . For a uniform density sphere, this can be re-written as:

$$M_{\text{vir}} = 210 R_{\text{eff}} (\Delta v)^2, \quad (4.19)$$

for which Δv is the one-dimensional velocity FWHM in km s^{-1} , R_{eff} (defined in Equation 4.15) is the radius in parsecs and M_{vir} is the clump mass in units of M_{\odot} . The numerical factor of 210 arises from the assumption that the density profile of the gas is constant, corresponding to $n = 5/3$.

The virial parameter, $\alpha_{\text{vir}} = M_{\text{vir}}/M$ is often used to assess the virial state. When $\alpha_{\text{vir}} < 1$, the mass of the clump is greater than its virial mass, and the system is therefore collapsing; $\alpha_{\text{vir}} > 1$ suggests that the clump is dissipating as its velocity dispersion dominates gravity, and $\alpha_{\text{vir}} \sim 1$ describes a clump that is in approximate equilibrium.

The turbulent pressure can be determined according to:

$$P_{\text{turb}}/k_B = \mu m_p n(\text{H}_2) \sigma_v^2 / k_B, \quad (4.20)$$

which has units of K cm^{-3} , where k_B is Boltzmann's constant, and the 1-dimensional velocity dispersion $\sigma_{v_{\text{LSR}}}$ is supplied in units of m s^{-1} .

The distributions of virial parameter, temperature and turbulent pressure are shown in Figure 4.11. The peak of the virial parameter distribution lies at $\alpha_{\text{vir}} \approx 3$, which would seem to suggest that the majority of these clouds are unbound. However, the clump masses measured by CHIMPS do not describe the full picture since the $J = 3-2$ transition, with a critical density of $\sim 10^4 \text{ cm}^{-3}$, traces only the relatively dense gas. These clumps sit in a wider gravitational potential caused by all of the lower density molecular gas that CHIMPS doesn't trace. In addition, we know that the CHIMPS cloud masses have a number of factors which cause them to be systematically light, whether it be from the source extraction method (see Figure 4.9) or as a consequence of the finite sensitivity to $\text{C}^{18}\text{O}(3-2)$. It is likely that the peak of the distribution is really at lower α_{vir} , and that the clumps around the peak of this distribution are more-or-less in virial equilibrium; we can certainly say that the ratio of bound clumps to unbound ones is not quite so extremely low as would appear from a first glance at this distribution. Even considering a factor of a few as the systematic offset for the 'dark' mass in more diffuse gas, there is an extended tail towards high values where clumps have virial parameters up to 100 and beyond; such extreme value clumps must be either confined by external pressure or short-lived with respect to their dynamical timescales $L/\sigma_{v_{\text{LSR}}}$.

The mean and median excitation temperature distributions are fairly similar,

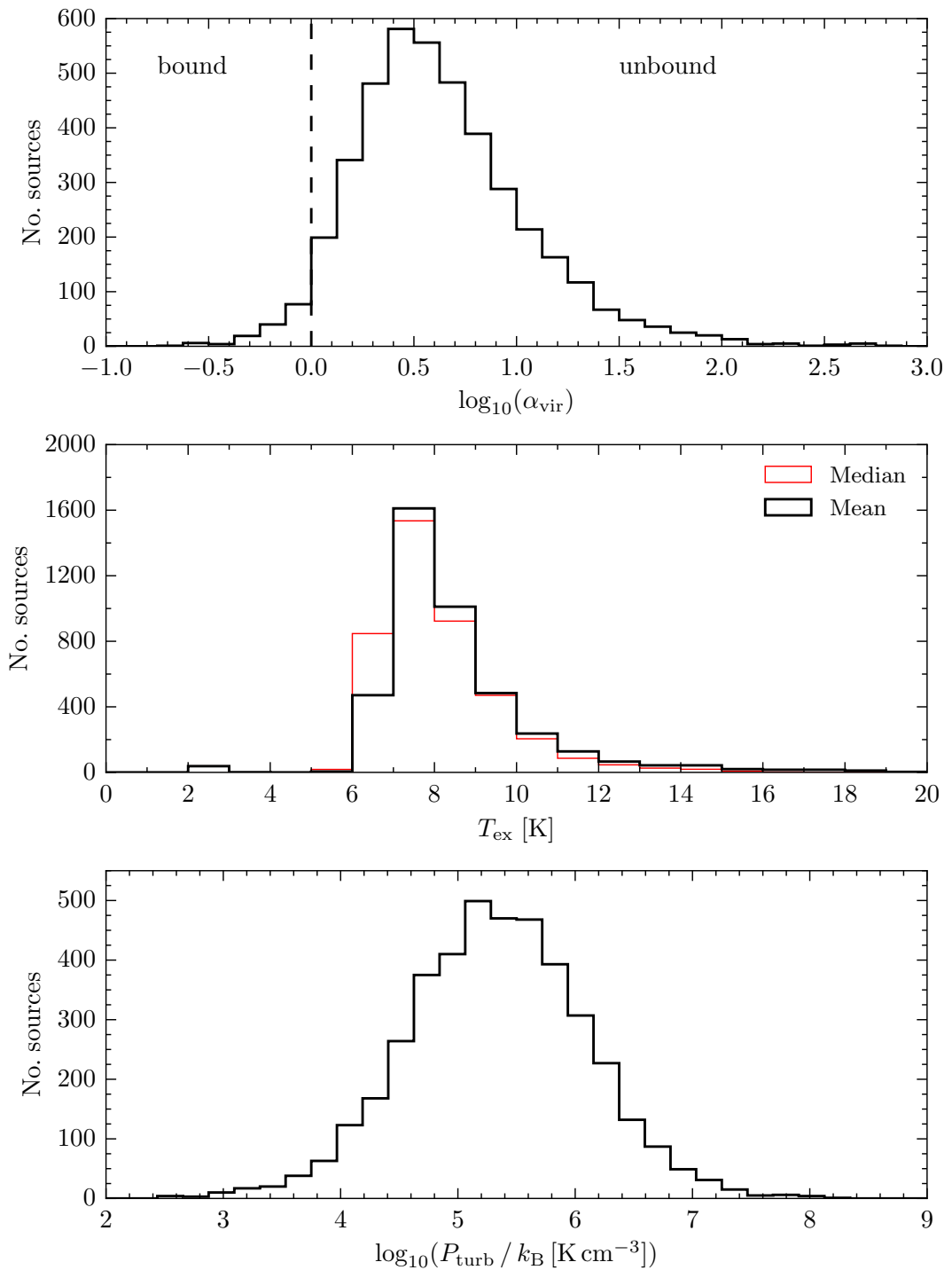


Figure 4.11: The distributions of the virial parameter, excitation temperature and turbulent pressure for the CHIMPS clumps.

with both peaking in the 7–8 K bin. To reiterate, the values in the histograms are the mean and median of the three-dimensional T_{ex} distribution which is associated with each clump; the mean of the mean excitation temperature distribution is 8.6 K while the mean of the median excitation temperature distribution is 8.2 K. These excitation temperatures are similar to the values reported for molecular clouds in the GRS (Rathborne et al., 2009; Roman-Duval et al., 2010) to which they are most comparable. The small number of clouds in the 2–3 K bin are those with centroid v_{LSR} of -5 km s^{-1} , falling outside of the GRS range and therefore reverting to the 3 K minimum value – the lowest integer above the lower limit set by the cosmic microwave background.

The turbulent pressure distribution appears to be lognormal, though a Shapiro-Wilk test finds some significant deviations, with a mean value of $P_{\text{turb}}/k_{\text{B}} = 2 \times 10^5 \text{ K cm}^{-3}$ and a standard deviation of 0.8 dex. For reference, the total mid-plane pressure in the solar neighbourhood has a value of $P/k_{\text{B}} \sim 10^5 \text{ K cm}^{-3}$, and $P/k_{\text{B}} \sim 10^9$ may be found in the Galactic centre (e.g. Rathborne et al., 2014).

In Figure 4.12 power-law fits to the size–linewidth, size–density, size–virial parameter and size–pressure relations are calculated using the BCES routine. The Spearman rank-correlation coefficient was calculated for each relationship, and they all show statistically significant correlations, with $\rho = 0.50, -0.63, -0.13$ and -0.21 for the size–linewidth, size–density, size–virial parameter and size–pressure relations, respectively. The scatter appears to be significant in each case, though the uncertainty on the angular sizes and linewidths are difficult to account for, and the irregular shapes of molecular clouds will contribute to the scatter.

The size–linewidth relationship is $\sigma_{v_{\text{LSR}}} = (0.67 \pm 0.01)L^{(0.39 \pm 0.01)}$, a power-law index that is consistent with the canonical Larson (1981) relation, which has an index of 0.38. There is a cut-off in the size–linewidth relationship at $\sigma_{v_{\text{LSR}}} =$

0.25 km s^{-1} , which is the minimum linewidth measurable from the CHIMPS data with 0.5 km s^{-1} velocity channels; if there are sources missed below this cut-off then this might cause the slope of this relationship to appear to be shallower than it really is. Across the literature, the size–linewidth relation is generally regarded to be an approximate measurement of $L \propto \sigma_v^{0.5}$ since revision by Myers & Goodman (1988), among others.

The size–density relation, however, does significantly depart from that of Larson (1981), with an index of -1.49 ± 0.03 compared to Larson’s -1.1 . The relationship (or lack thereof) between the virial parameter is consistent with Larson, who reported a power-law index of -0.14 compared to the CHIMPS value of -0.17 ± 0.03 (note that Larson’s ‘virial ratio’ is $1/\alpha_{\text{vir}}$ by this definition). There is a weak, but statistically significant negative correlation between turbulent pressure and clump size. The physical interpretation of these relationships is discussed in Chapter 6.

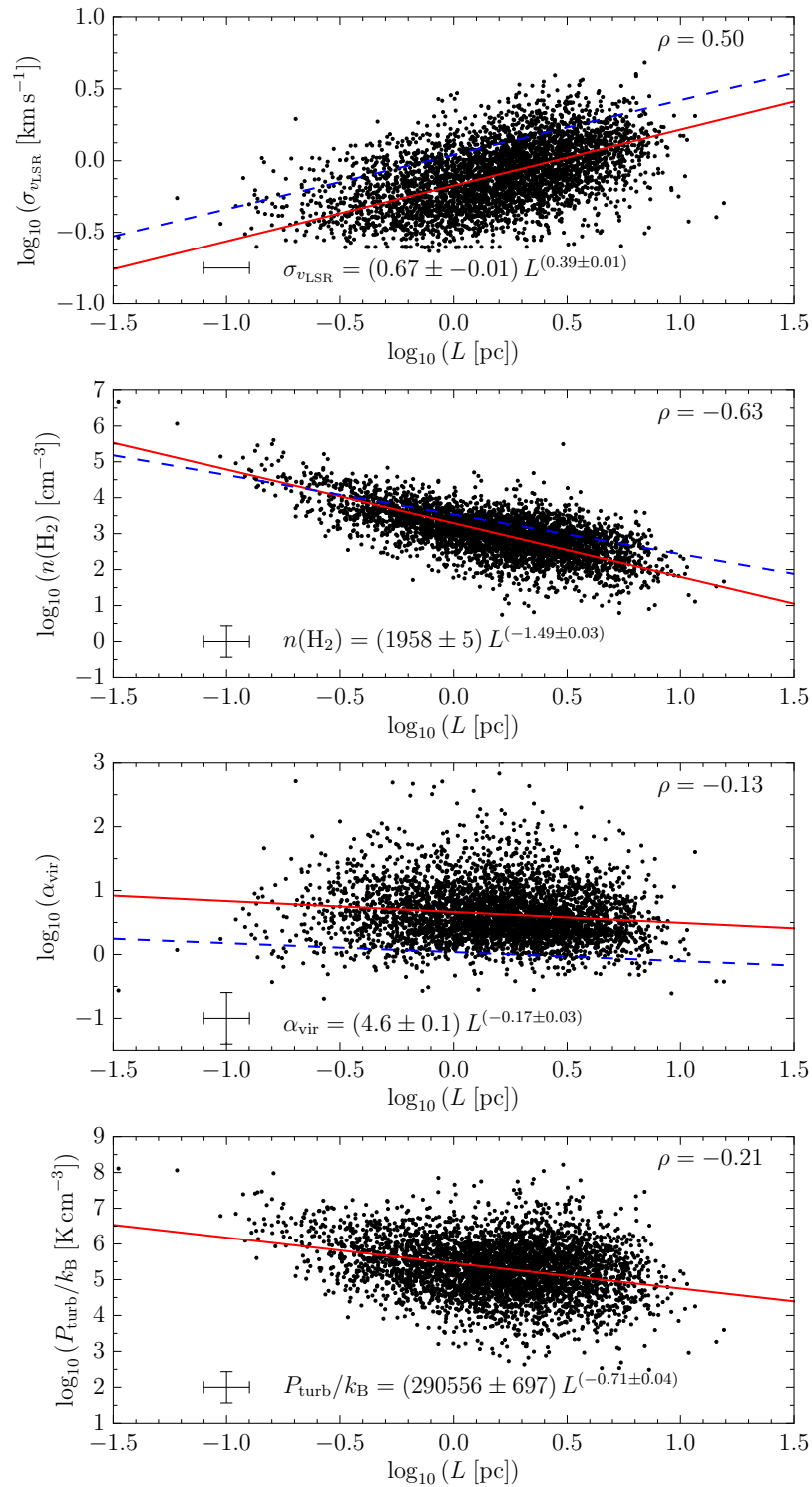


Figure 4.12: The size–linewidth, size–density and size–pressure relationships for the CHIMPS clumps. In each figure, the median error bars are given alongside the best fit power-law relationship. The size parameter L is defined as twice the effective radius to maintain the Larson (1981) formalism. The relationships derived in Larson (1981) are shown as blue dashed lines for reference, and the Spearman rank-order correlation coefficient, ρ is given in the top-right corner of each plot.

Chapter 5

Studies of the star formation efficiency

One way to gauge the importance of galactic environment on star formation would be to look for variations in SFE across a range of environments, and several such studies within the Milky Way and of external Galaxies have been carried out, though there are important strengths and weaknesses of both approaches. Milky Way studies offer far superior spatial resolutions providing the ability to resolve the sub-parsec scale of molecular cores and filaments, though this comes at the expense of accurate distance determinations, which are difficult to achieve in the Milky Way due to the position the Solar System within the Galaxy's disc.

A number of studies of the efficiency of star formation in the Milky Way have found results contrary to studies of external galaxies, with respect to the role played by large-scale features such as spiral arms. Moore et al. (2012) measured the SFE in the inner Milky Way disc by using the ratio of bolometric luminosity of YSOs from the RMS survey to the mass in GRS ^{13}CO -traced clouds, $L_{\text{bol}}/M_{\text{CO}}$, as a proxy measurement. The authors found that $\sim 70\%$ of the increase in SFR

associated with spiral arms was caused by source crowding, with an elevated high-mass YSO luminosity per unit molecular gas mass accounting for the remainder; the regions of high luminosity per unit gas mass tend to be located in a handful of extreme objects, such as W49 in the Perseus spiral arm. In similar studies, Eden et al. (2012); Eden et al. (2013) found that the efficiency of formation of dense clumps in the Milky Way, measured as the ratio of masses of 1.1 mm BGPS clumps to the masses of their parent GRS molecular cloud, appears to be unchanged across spiral arm and inter-arm environments.

A number of studies of external systems, however, have found conflicting results. Seigar & James (2002) found a significant enhancement of H α -traced star formation relative to K -band continuum spiral features within a sample of 20 spiral galaxies. James & Percival (2016) find that the bar-dominated regions of four spiral galaxies exhibit a dearth of star formation for timescales comparable to bar lifetimes of $\gtrsim 1$ Gyr. A study of the dense and molecular gas in the spiral galaxy M51 by Bigiel et al. (2016) found that gas with a high surface density and a high molecular gas fraction (traced by HCN/CO) tends to exhibit a low efficiency of star formation with respect to the dense gas (traced by IR/HCN).

The star formation efficiency of a molecular cloud may be parameterised by the ratio of the luminosity of any star formation occurring within its boundaries to the mass of the cloud, assuming a constant luminosity function (derived from a Universal IMF) and that the star formation timescale is short with respect to the cloud lifetime. In this Chapter, data from the CHIMPS and Hi-GAL surveys are combined to measure a proxy for the SFE. Associations are found between CHIMPS clumps and compact 70 μ m Hi-GAL sources; the luminosities of clumps of dust emission in the 70 μ m waveband have been found to correlate well with protostellar luminosity (Dunham et al., 2006, 2008), and are fairly

insensitive to external heating and disc geometry which can be a problem with 24 μm luminosity, for example.

5.1 Hi-GAL & CHIMPS associations

The compact source catalogues (Molinari et al., 2016) of the Hi-GAL survey at 70 μm and 160 μm were used to estimate the star-forming content of the CHIMPS clumps. The 70 μm and 160 μm catalogues contain 123,210 and 308,509 sources, respectively, covering an area of Hi-GAL defined by $-70^\circ \leq l \leq 68^\circ$ and $|b| \leq 1.0^\circ$.

Since the 70 μm luminosity correlates well with protostellar luminosity, the compact 70 μm Hi-GAL sources are adopted as the YSOs in the sample, though this selection can be strengthened; the 70 μm sources are also required to be associated with a counterpart at 160 μm , so that there is still at least some trace of an envelope remaining. This additional criterion increases the likelihood that the objects in the YSO sample are at a similar stage in their evolution.

A search was carried out using the elliptical footprints of the 70 μm and 160 μm sources given in the compact source catalogues, which provide centroid positions for each source, along with the FWHMs of the major and minor axes and a position angle. An association between sources of these two wavelengths was made where the elliptical footprints overlapped such that the central position of the 70 μm source was located inside the 160 μm ellipse, or vice versa. When the resulting catalogue is narrowed down to those objects falling within the CHIMPS range $27.50^\circ \leq l \leq 46.35^\circ$ and $|b| \leq 0.5^\circ$, that have a $\text{SNR} > 3$ at both 70 μm and 160 μm , and with a determined error, there are 5,377 YSO candidates which could potentially be matched with a CHIMPS clump.

In order to assign velocities to each of these YSO candidates, the entire

CHIMPS ^{13}CO (3–2) survey was mosaicked into a single data cube. This data cube necessarily had to be reduced in resolution so that the file size was manageable, and so that spectra could be extracted with moderate computing resources. The ^{13}CO (3–2) data cubes were smoothed in the l and b plane using a Gaussian kernel of FWHM 43 arcseconds, so that the original 15.2-arcsecond resolution was degraded by a factor of three. After smoothing, each cube was then re-binned onto 22.8 arcsecond pixels in the two spatial axes, and the spectral axis was also re-binned by a factor of two into 1 km s^{-1} channels. This reduces the size of each data cube, and hence the mosaic of the entire survey by a factor of eighteen; a side-effect the smoothing and re-binning is that the SNR of the spectra is increased, making velocity assignments more robust. In this low resolution mosaic, the standard deviation of all voxels, and hence the rms noise, is $\sim 0.08 \text{ K}$ per 1 km s^{-1} channel.

A spectrum was extracted from the CHIMPS ^{13}CO (3–2) mosaic at the centroid position of each of the 5,377 remaining $70 \mu\text{m}$ sources, and the velocity corresponding to the peak T_{A}^* value was assigned to that source. In cases where there are multiple peaks in the spectrum, the v_{LSR} corresponding to the brightest peak was assigned, on the assumption that the brightest peak is likely to correspond to the highest column density source. Of the 5,377 $70 \mu\text{m}$ sources in the catalogue, 106 had no available spectrum for their position, falling outside the precise footprint of the survey. Figure 5.2 shows the position–velocity diagram for all 5,271 of the $70 \mu\text{m}$ Hi-GAL sources with assigned velocities, and a fraction of these are clearly associated with noise artefacts; these are scattered across the entire velocity range, even at velocities beyond the terminal velocity of the Galactic rotation curve and, when compared to Figure 2.8, some are located where there is no emission. Most of these false positives will be inconsequential,

since they are located too far away in position–position–velocity–position–velocity space to be associated with a CHIMPS source. The rate of questionable velocity assignments which do result in associations can, however, be estimated.

Visual inspection of a sub-sample of 200 spectra (illustrated in Appendix C) of the 70 μm sources with a CHIMPS association reveals that, in the vast majority of cases, the v_{LSR} assignment is strong, however there are a small number of spectra which are either ambiguous, or do not contain any obvious emission. Of these 200 visually-inspected velocity assignments, 179 (89%) were deemed to have a strong velocity assignment, whereas 2 had poor velocity assignments and the remaining 19 were ambiguous, due to either the presence of multiple $^{13}\text{CO}(3-2)$ peaks with comparable peak T_{A}^* values in the same spectrum, or due to a relatively low SNR. This indicates that the velocity assignments may be used with confidence. Assuming that this randomly-selected sub-sample is representative of the full sample, a 90% rate of good velocity assignments is acceptable. Example spectra of the different quality assignments are shown in Figure 5.1, and the full sample of visually inspected spectra can be found in Appendix C.

With velocity assignments in place, it is possible to associate these 70 μm Hi-GAL sources with CHIMPS clumps (identified in Chapter 2, with physical properties calculated in Chapter 4) by using a 3-dimensional search in (l, b, v) space. For an association to be made, the elliptical 70 μm footprint must overlap the elliptical footprint in the l – b plane of the CHIMPS catalogue entry, for which the catalogued extents in the l and b axes, deconvolved according to Equation 4.3 in Section 4.1, are taken to represent the semi-major and semi-minor axes. In addition to this match in the l – b plane, the 70 μm source must also have a velocity consistent with the CHIMPS clump velocity. An uncertainty of 0.5 km s^{-1} –

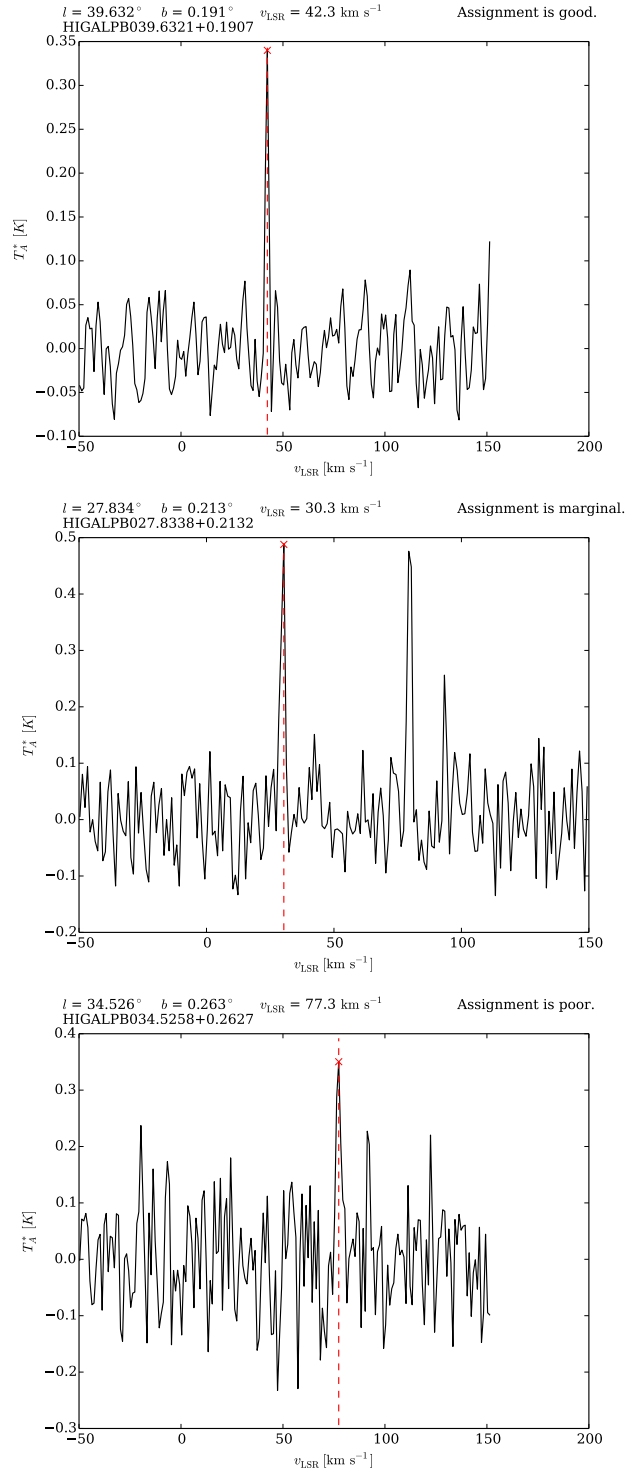


Figure 5.1: Examples of spectra from the positions of three 70 μm YSO candidates. The spectra in the top, middle and bottom panels demonstrate velocity assignments deemed to be good, marginal and poor, respectively. 90% of the velocity assignments in the inspected sample have good velocity assignments, with one clear peak with a good SNR, and the remaining 10% are made up of spectra similar to that the middle panel, where there are multiple peaks at good SNR, and the lower panel which have low SNR. The full sample of visually inspected spectra can be found in Appendix C.

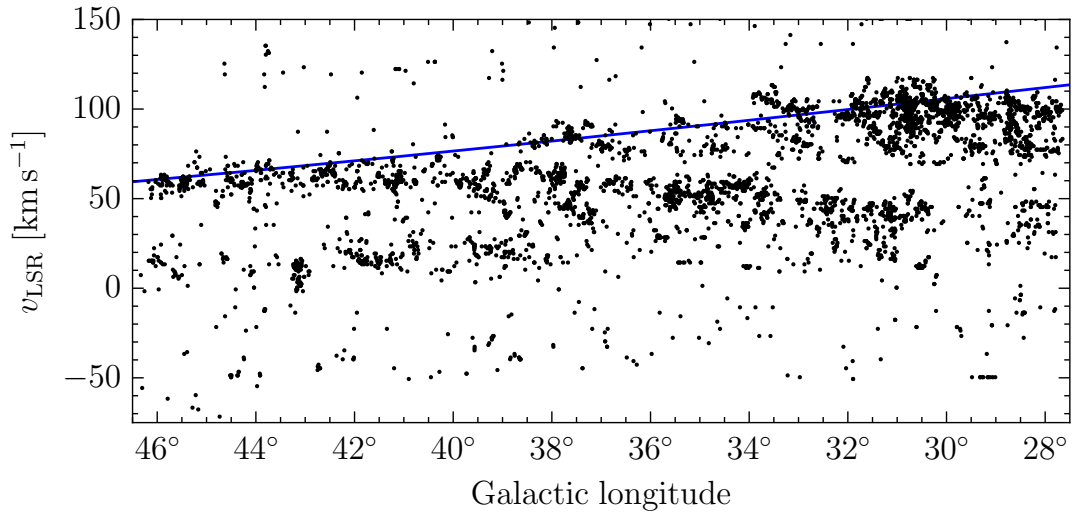


Figure 5.2: position–velocity diagram for all 5,271 Hi-GAL 70 μm sources with assigned velocities. Velocities which have been assigned by association with noise features in the ^{13}CO (3–2) data include those above the terminal velocity. The terminal velocity of the Brand & Blitz (1993) rotation curve is shown in blue.

half of the channel width – on the 70 μm velocity was adopted, and the tolerance on the CHIMPS clump velocity was given by the catalogued rms velocity extent. In cases where an individual 70 μm source is consistent with more than one CHIMPS clump, then the CHIMPS clump with the nearest centroid (normalised by the extent of the cloud) is chosen. Associations were identified between the 5,271 Hi-GAL 70 μm sources with velocity assignments and the 4,388 CHIMPS clumps with distance assignments that were determined to be spatially resolved in Section 4.3; in this manner 2,031 70 μm Hi-GAL sources were associated with 1,234 CHIMPS clumps, and these are displayed in position–velocity space in Figure 5.3.

A two-dimensional visualisation of two $0.3^\circ \times 0.3^\circ$ cutouts is displayed in Figure 5.4, with one centred roughly on W43 and the other centred on the filamentary structure at $l \approx 37.4^\circ$; the image is the integrated column density image from Figure 3.13. In this Figure, ellipses are shown in grey for all of the CHIMPS

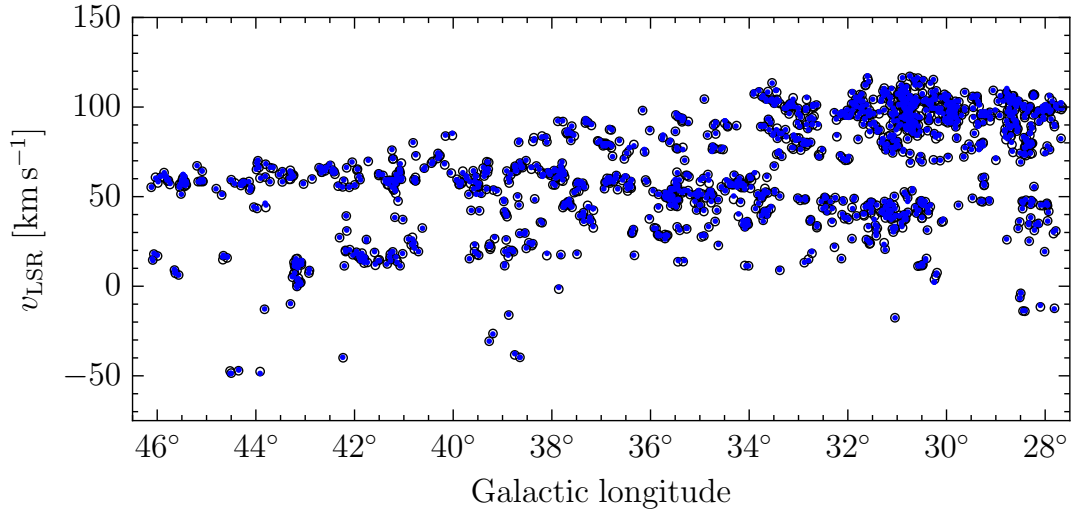


Figure 5.3: position–velocity diagram for the 2,031 70 μm Hi-GAL sources (blue dots) and their 1,234 CHIMPS associations (open circles).

clumps that have no associated 70 μm sources while the CHIMPS clumps with such associations are shown as white ellipses. The associated 70 μm sources are shown as red ellipses, connected to the centroid of their CHIMPS parent by red arrows. The black circles show the reported positions of the ^{13}CO (3–2) emission peaks from CHIMPS, also connected to the centroid of their parent clump by an arrow. The crowding of sources in W43 is highly apparent in the left panel of this Figure, demonstrating that the field is too crowded for a two-dimensional matching to be appropriate. Many of the clumps have peak positions which lie outside the elliptical footprint of the parent clump, highlighting the limitations in describing molecular structures within a compact source catalogue alone; this issue is discussed in more detail in Section 7.3.

The multiplicity of sources is illustrated in Figure 5.5. 3,154 (72%) of the CHIMPS clumps with distance assignments were found to have no 70 μm counterparts, while 798 (18%) clumps have a single 70 μm source. Of the remainder, the number of clumps decreases approximately exponentially with 70 μm source

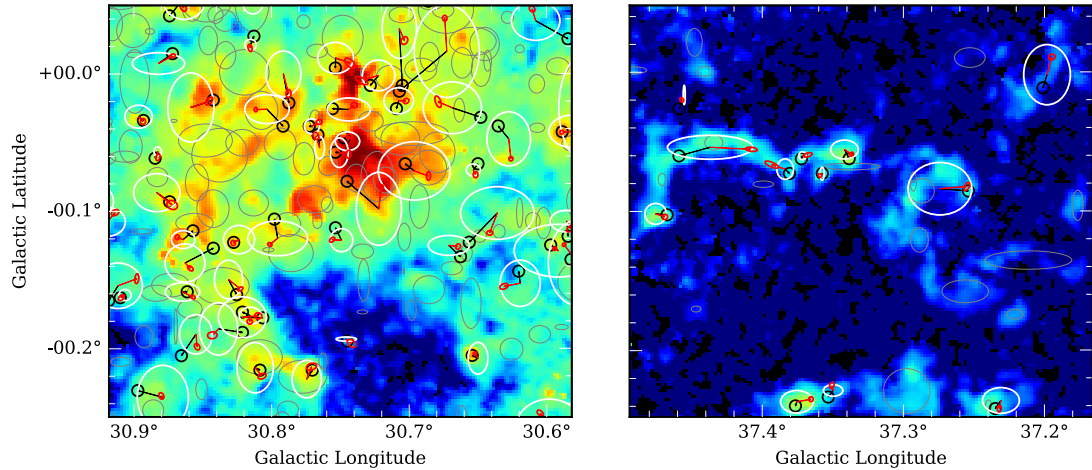


Figure 5.4: Two example fields demonstrating the source associations, with a close-up up of the W43 complex (left) and a filamentary structure (right). The white and grey ellipses represent the positions of CHIMPS clouds with and without $70\ \mu\text{m}$ associations, respectively, while the red ellipses are the $70\ \mu\text{m}$ sources with associations, connected by red arrows to the centroid of the parent CHIMPS clump, and the black circles show the positions of the ^{13}CO (3–2) peaks of each clump. The underlying image is the velocity-integrated column density map from Figure 3.13, and has the same intensity scale.

multiplicity, and there is a single clump with a mass of $9300 M_{\odot}$, a radius of 1.7 pc and the maximum of nine $70\ \mu\text{m}$ Hi-GAL counterparts.

5.2 The cloud-to-cloud star formation efficiency

5.2.1 Determination of L/M

With the CHIMPS clump and Hi-GAL $70\ \mu\text{m}$ source associations made, it is possible to calculate the SFE analogue, L_{70}/M . The masses of the CHIMPS clumps were calculated in Section 4.5, and so to produce a measurement comparable to other studies, the luminosity of $70\ \mu\text{m}$ sources must now be determined. Since both luminosity and mass determinations are inversely proportional to the square of the distance, this quantity is distance-independent, and therefore any problems in the distance assignment will not affect this measurement; this quantity is only

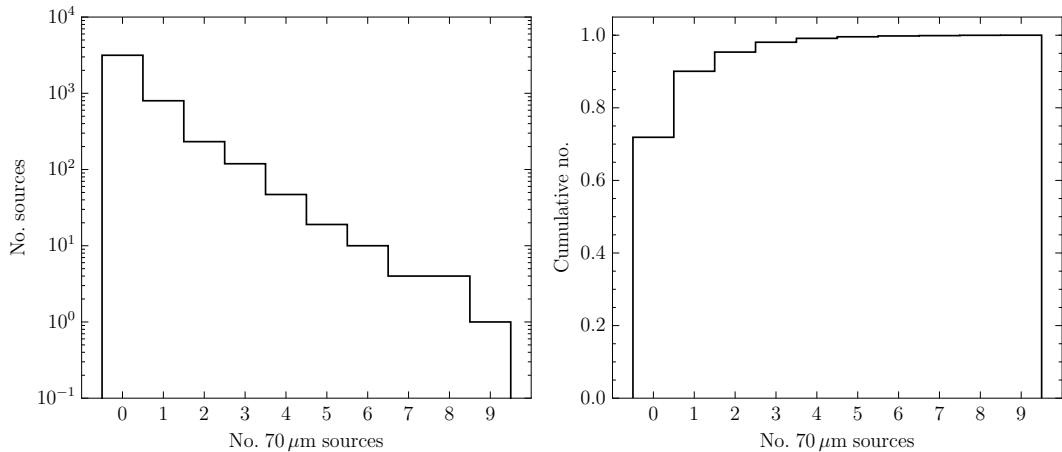


Figure 5.5: The multiplicity of 70 μm Hi-GAL sources with a CHIMPS clump association.

dependent on the accuracy of the association.

Many of the CHIMPS clumps were found to be associated with multiple 70 μm Hi-GAL sources, as shown in Figure 5.5 and, in these cases, the 70 μm flux of all associated sources was added up. The flux was converted to luminosity by:

$$L_{70} = 4\pi d_k^2 \Delta\nu \sum_n (S_{70})_n, \quad (5.1)$$

where d_k is the distance, $\Delta\nu$ is the bandwidth and S_{70} is the flux density of each source associated with the clump in question. This can be written in more appropriate units as:

$$L_{70} = 0.459 d_k^2 \Delta\nu \sum_n (S_{70})_n, \quad (5.2)$$

where L_{70} is the total 70 μm luminosity in units of L_\odot ($= 3.828 \times 10^{33}$ erg/s, Mamajek et al. 2015), d_k is the distance in kpc, $\Delta\nu$ is the bandwidth in Hz and the flux densities S_{70} have units of Jy. The PACS 70 μm band receives radiation in the wavelength range 60–85 μm (Poglitsch et al., 2010), yielding a bandwidth of 1470 GHz.

In this Section, the quantity $L_{70}/M_{13\text{CO}}$ is used as opposed to L_{70}/M (i.e. the clumps masses in ^{13}CO are used instead of clump masses in H_2) in order to avoid uncertainties in the abundance ratio of H_2 to ^{13}CO . As a guide, these quantities can be approximately converted by $L_{70}/M \sim 10^{-6} L_{70}/M_{13\text{CO}}$, which follows from the abundance ratios $X(^{12}\text{CO}/^{13}\text{CO}) = 77$ (Wilson & Rood, 1994) and $X(\text{H}_2/^{12}\text{CO}) = 1/8.5 \times 10^{-5}$ (Frerking, Langer & Wilson, 1982).

In Figure 5.6, the distribution of $L_{70}/M_{13\text{CO}}$ for all CHIMPS clumps with a Hi-GAL association is presented. In addition, a sub-sample of sources that have heliocentric distances of between 2 and 12 kpc, where 90% of the clump population reside (see Figure 4.2), is shown. This sub-sample has also been reduced to all of those clumps with masses greater than $1300 M_{\odot}$, which is the completeness limit at 12 kpc calculated using the formula in Section 4.5. The $L_{70}/M_{13\text{CO}}$ distribution appears to be lognormal, possibly indicating that it is controlled by similar processes to the distribution of clump formation efficiencies, defined as the ratio of total clump mass to cloud mass, found by Eden et al. (2012). A Shapiro–Wilk test for normality was carried out on $\log_{10}(L_{70}/M_{13\text{CO}})$ for both the full sample and the $2 < d_k < 12$ kpc sample, yielding P values of 0.035 and 0.048, respectively, indicating a deviation from normality at just over the 2σ level. This test would appear to reject the null hypothesis that the distribution is lognormal.

However, this rejection lies in somewhat of a statistical grey area, and deviations from normality could arise as a consequence of a number of biases. Rejecting the null hypothesis could only be done with a high level of confidence if the sample were known to be complete. The completeness limit applied to the CHIMPS clumps for the distance-limited sample, however, is not perfect since the CO sources are not all compact and Gaussian, and it is extremely difficult to describe

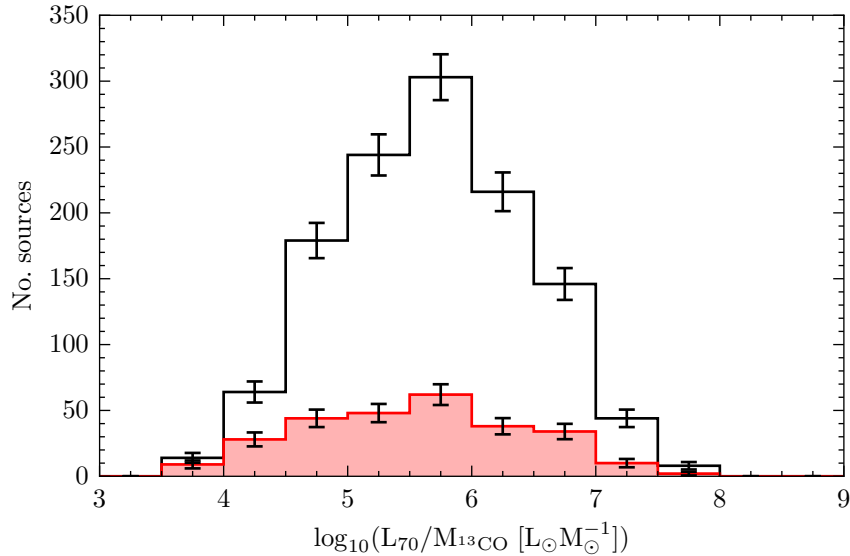


Figure 5.6: The distributions of $\log_{10} , L_{70}/M_{13\text{CO}}$ for all CHIMPS clumps with a Hi-GAL association (open histogram), and associations lying in the heliocentric distance range $2 < d_k < 12$ kpc with clump masses of greater than $1300 M_{\odot}$ (red histogram). The Poisson uncertainties are given for each bin.

a single limiting mass given the variety in morphologies of ^{13}CO (3–2) structures. The distribution could also be distorted in a similar way due to the completeness of the $70 \mu\text{m}$ source catalogue; either way, the deviation from normality is not large, so the evidence for a non-random effect on $L_{70}/M_{13\text{CO}}$ is marginal. If such an effect is present, it does not appear to be dominant.

5.2.2 L/M in the spiral arms

The position of the CHIMPS clumps in position–velocity space can allow them to be grouped into the spiral arms and inter-arm regions, given a certain tolerance in longitude and velocity. Continuing with the use of the spiral arm models of Taylor & Cordes (1993); Cordes (2004), any clumps falling within 15 km s^{-1} and 1.2 degrees of a spiral arm locus were assigned to that spiral arm. The 15 km s^{-1} velocity tolerance follows from the range of expected velocity deviations from

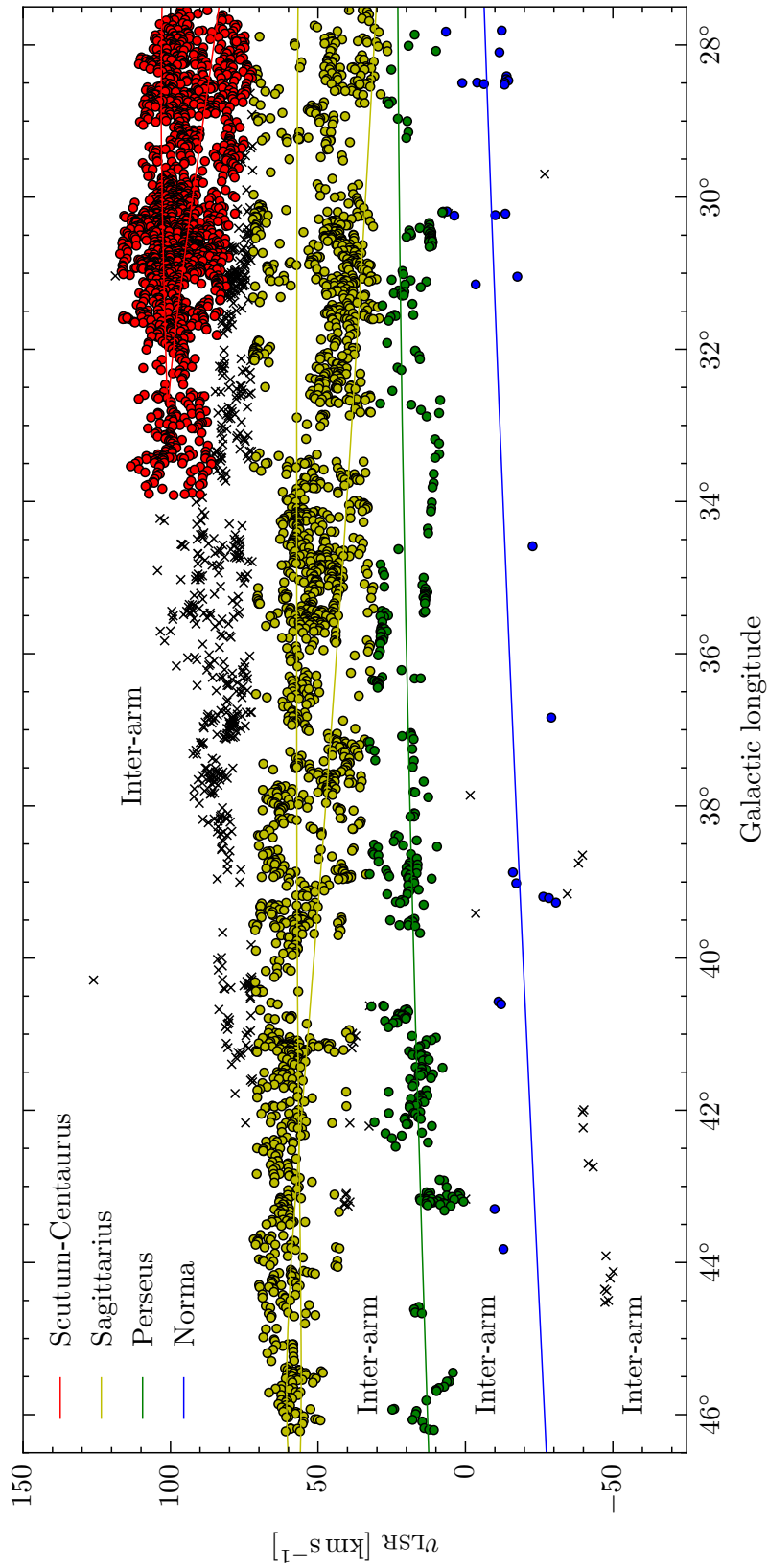


Figure 5.7: The spiral arm assignments of CHIMPS clumps in position-velocity space. The red, yellow, green and blue lines are the spiral arms of the Taylor & Cordes (1993) model, and associated CHIMPS clumps are matched to their colours.

Spiral arm assignment	No. sources
Scutum–Centaurus	1640
Sagittarius	1830
Perseus	352
Norma	28
Inter-arm assignment	No. sources
Scutum–Centaurus/Sagittarius	504
Sagittarius/Perseus	14
Perseus/Norma	4
Beyond Norma	16

Table 5.1: Spiral arm and inter-arm assignments for the 4,388 spatially resolved CHIMPS clumps.

circular orbits about the Galactic centre, as estimated by Clemens (1985) and Reid et al. (2009). The 1.2 degree tolerance in the longitude axis was introduced to allow a specific structure that appears coherent in position–velocity space, which extends from $\sim 33^\circ$ to 34° and 100 to 120 km s^{-1} in velocity (see Figure 2.8), and at the position of the Scutum–Centaurus tangent to be assigned to the Scutum–Centaurus arm.

The spiral arm assignments of all of the 4,388 CHIMPS clumps that are spatially resolved are illustrated in position–velocity space in Figure 5.7, with the number of sources assigned to each arm region listed in Table 5.1. Inspection of Figure 5.7 reveals a number of places where structures that are coherent in position–velocity space have been split up into separate spiral arms. This is a consequence of using these somewhat arbitrary criteria for what belongs to a spiral arm as well as the choice of spiral arm model, though it is extremely difficult to devise a better assignment scheme for such large-scale and dynamic structures as spiral arms. However, structures which appear to be split over two spiral arms, or arm and inter-arm regions might be expected of the spur structures seen

in external spiral galaxies such as M31 (e.g. Byrd, 1983), M51 (e.g. Elmegreen, 2007) and M81 (e.g. Kaufman et al., 1989), and produced in the simulations of e.g. Dobbs & Bonnell (2006) and Pettitt et al. (2015) who find that they may arise through the shear of dense gas assemblages as they exit spiral arms.

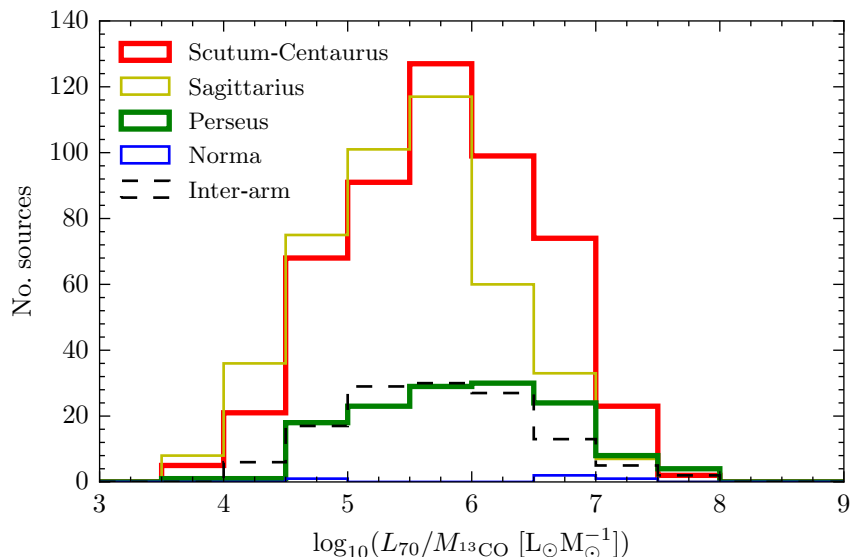


Figure 5.8: Distributions of $\log_{10}(L_{70}/M_{13\text{CO}})$ for the spiral arm sub-samples of clumps which have been designated according to their location in position–velocity space.

The distributions of clump $L_{70}/M_{13\text{CO}}$ measurements for the spiral arm-assigned sub-samples with heliocentric distances of more than 2 kpc are presented in Figure 5.8. Shapiro–Wilk tests were performed on the distributions of $\log_{10}(L_{70}/M_{13\text{CO}})$ for the Scutum–Centaurus, Sagittarius, Perseus, Norma and Inter-arm samples, yielding P-values of 0.5, 0.04, 0.6, 0.06 and 0.6, respectively. With the exception of the Sagittarius and Perseus arms, these sub-samples are consistent within $\sim 2\sigma$ of the null hypothesis that the $L_{70}/M_{13\text{CO}}$ values are log-normally distributed; the distributions for the Sagittarius and Norma arms show some deviations from normality. These sub-samples, however, have not been adjusted to account for mass completeness. Another visualisation of the spiral

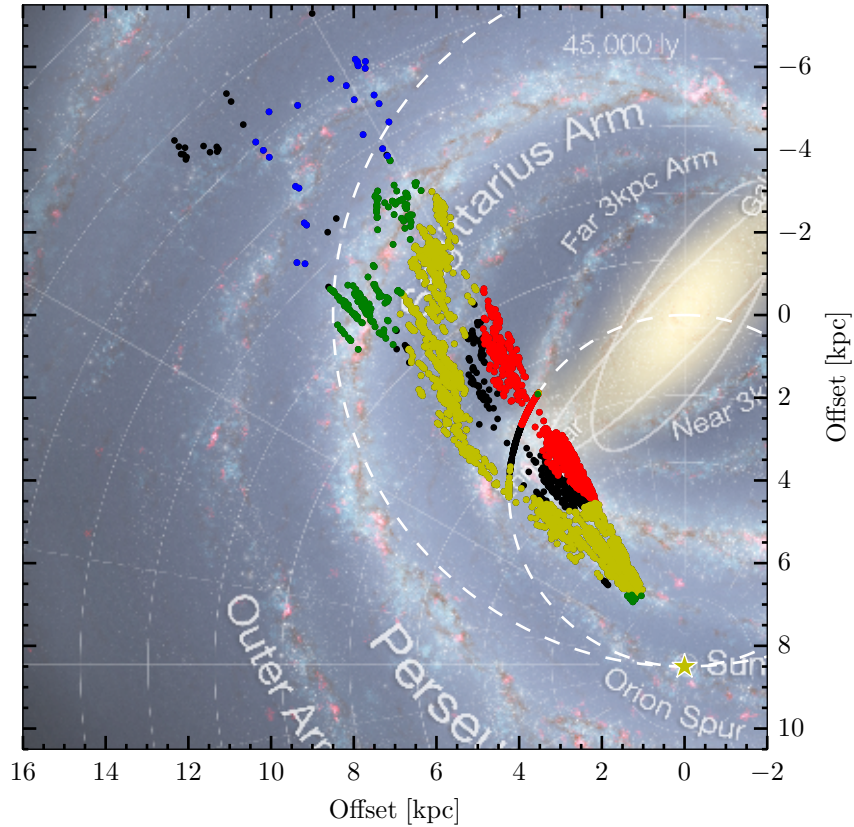


Figure 5.9: A top-down view of the spiral arm assignments of CHIMPS clumps. Clumps associated with the Scutum–Centaurus, Sagittarius, Perseus and Norma spiral arms are overlaid in red, yellow, green and blue, and inter-arm clumps are the black points. The underlying image is the illustration of Robert Hurt (see Figure 4.3).

arm assignment is presented as a top-down view of the Galaxy in Figure 5.9, where the spiral arm assignments are shown with a colour code. This Figure further demonstrates that spotting spiral arms in position–velocity space is not ideal, and the Perseus arm is particularly problematic because it passes through $v_{\text{LSR}} = 0 \text{ km s}^{-1}$, where local emission lies, and consequently a small number of local emission features have been grouped into the Perseus arm. These sources will be removed from the sample when completeness issues are taken into account.

There is a possibility that the deviations from normality in the distributions of $\log_{10}(L_{70}/M_{13\text{CO}})$ may be the result of distance biases. The Sagittarius sample

covers a large range of heliocentric distances, from 2 to 13 kpc, and consequently includes more low-mass clouds at the near side of the tangential velocity. The $\sim 2\sigma$ deviation from normality of the Norma sample, as the most distant arm, is likely to be caused by incompleteness issues. When the Sagittarius sample is split into the sources which have near-, tangential- and far-kinematic distance solutions, the Shapiro–Wilk P -values for these samples are 0.74, 0.40 and 0.02, respectively, indicating that the far sample holds the largest deviations from lognormality.

Distance and mass limits were placed upon the spiral arm and inter-arm sub-samples to account for some of the distance biases within. For each spiral arm, all clumps with a mass lower than the completeness limit, determined from Figure 4.10 at the furthest heliocentric distance in the sample, were removed. In addition to this, all clumps at a heliocentric distance of less than 2 kpc, which have large fractional errors on their masses, were also removed. The bulk of the sources in the inter-arm regions lie between the Scutum–Centaurus and Sagittarius arms, with the remainder being located at considerably greater distances. The inclusion of a small number of distant sources, where the completeness limit is higher, can significantly reduce the size of the sample, and for this reason the inter-arm sub-sample was reduced to those in the inter-arm region between the Scutum–Centaurus and Sagittarius arms. In Table 5.2 the means, standard deviations, and standard errors are quoted alongside the P -values from the Shapiro–Wilk test.

In these more complete sub-samples, there does appear to be some difference between spiral arms. The mean $\log_{10}(L_{70}/M_{13\text{CO}})$ of clumps in the Scutum–Centaurus arm is 5.34 ± 0.06 , which appears to be significantly lower than the corresponding measurements for the Sagittarius and Perseus arms of 5.84 ± 0.09

Spiral arm region	d_{\min} (kpc)	d_{\max} (kpc)	M_{\min} (M_{\odot})	Sample size	$\log_{10}(L_{70}/M_{13\text{CO}})$	μ	σ	$\Delta\mu$	Shapiro–Wilk P -value
Scutum–Centaurus	0	9.83	–	437	5.48	0.72	0.03	0.48	
Sagittarius	0	12.84	–	510	5.77	0.78	0.03	0.04	
Perseus	0	14.18	–	138	5.95	0.79	0.07	0.29	
Norma	0	15.73	–	4	6.52	0.96	0.55	0.06	
Inter-arm	0	14.31	–	129	5.73	0.77	0.06	0.63	
Scutum–Centaurus	2	9.83	875	187	5.34	0.77	0.06	0.25	
Sagittarius	2	12.48	1412	85	5.84	0.85	0.09	0.23	
Perseus	2	14.18	1821	15	6.06	1.06	0.28	0.48	
Norma	2	14.6	2001	1	4.88	–	–	–	
Inter-arm	2	9.70	852	28	5.67	0.68	0.13	0.98	

Table 5.2: Summary of the distributions of $\log_{10}(L_{70}/M_{13\text{CO}})$ for the spiral arm and inter-arm sub-samples for the CHIMPS clumps with one or more associated $70\ \mu\text{m}$ source.

and 6.06 ± 0.28 , respectively. The difference in the mean of these distributions is ~ 0.5 dex, corresponding to a factor of ~ 3 . The inter-arm sub-sample is consistent with all of the spiral arm sub-samples, but has a relatively large standard error on the mean due to a comparatively small sample size; these measurements can't be made for the Norma sub-sample which has only one clump with a mass above the completeness limit. If there is any difference on the efficiency between the arm and inter-arm regions, the sample is not large enough here to distinguish it. The distinction has been drawn here that the SFE is suppressed in the Scutum–Centaurus arm when compared to the Sagittarius and Perseus arms, but this can be stated conversely that the SFE is elevated in Sagittarius and Perseus – a result which has been reported in previous studies (Moore et al., 2012; Eden et al., 2015). This shall be discussed further in the next Chapter.

5.2.3 L/M as a function of Galactocentric distance

One of the most obvious tests that one might expect to show variations of star formation with Galactic environment is to look for trends with proximity to (or distance from) the Galactic centre. A number of studies have proposed that star formation is less efficient in high-pressure environments; Kruijssen et al. (2014) find that the low star formation rate per unit gas mass in the Milky Way's Central Molecular Zone (CMZ) could be explained by the high turbulent pressure causing an increase in the critical density required for star formation. Rathborne et al. (2014) reached a similar conclusion after observations of a CMZ molecular cloud which exhibits a low star formation rate despite having a very large column density. These propositions, combined with a turbulent and thermal pressure gradient in the Galaxy (e.g. Wolfire et al., 2003), would appear to predict that stars should be forming more efficiently in the Outer Galaxy compared to the

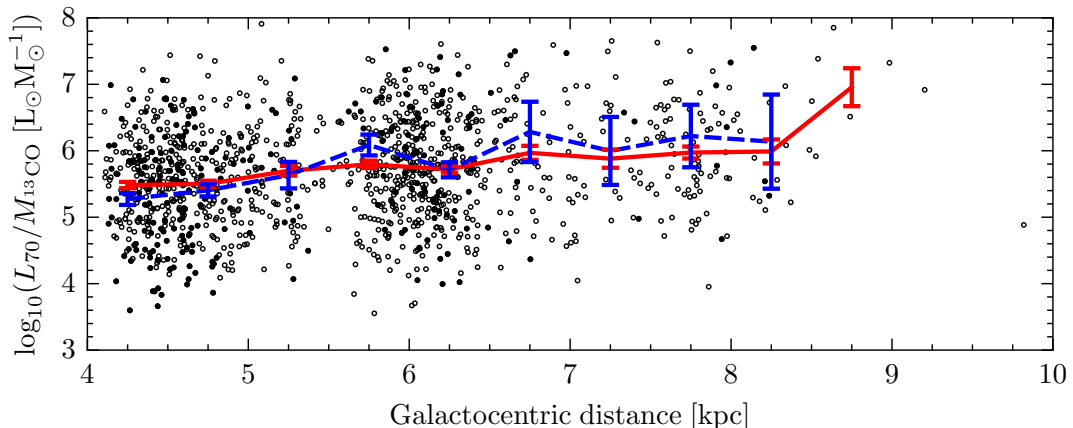


Figure 5.10: $L_{70}/M_{13\text{CO}}$ as a function of Galactocentric distance. The open circles is the full sample of 1,234 CHIMPS clumps with one or more $70\ \mu\text{m}$ association, and the filled circles are a sub-sample with heliocentric distances of between 2 and 12 kpc, and masses above $1300 M_{\odot}$. The red and blue-dashed lines show the mean values $\log_{10}(L_{70}/M_{13\text{CO}})$ within annular bins of 0.5 kpc width for the complete and distance- and mass-limited samples, respectively, and the error bars represent the standard errors on those means.

Inner Galaxy.

Figure 5.10 shows $L_{70}/M_{13\text{CO}}$ as a function of Galactocentric distance, for both the full sample of CHIMPS clumps with one or more $70\ \mu\text{m}$ association (open circles), and a sub-sample of sources with heliocentric distances of between 2 and 12 kpc, and masses greater than $1300 M_{\odot}$ (filled circles), the completeness limit at 12 kpc (see Figure 4.10). The solid red line displays the mean value of $\log_{10}(L_{70}/M_{13\text{CO}})$ in 0.5 kpc bins of the overall sample, while the red dashed line shows the trend of the mean $\log_{10}(L_{70}/M_{13\text{CO}})$ for the distance and mass-limited sample. The numerical results are presented in Table 5.3.

There appears to be a moderate increase in the average $L_{70}/M_{13\text{CO}}$ value moving outwards from the Galactic centre implying an increase in SFE, with an increase of an order of magnitude between 4 and 8 kpc. This is in agreement with a similar result found by Moore et al. (2012), who reported that the ratio of RMS luminosity to the mass of the ^{13}CO (1–0)-traced clouds of the GRS also increases

R_{GC} bin (kpc)	Full sample		Limited sample	
	$\log_{10}(L_{70}/M_{13CO})$ μ	$\Delta\mu$	$\log_{10}(L_{70}/M_{13CO})$ μ	$\Delta\mu$
4.0–4.5	5.48	0.05	5.27	0.09
4.5–5.0	5.50	0.05	5.40	0.09
5.0–5.5	5.70	0.07	5.63	0.20
5.5–6.0	5.80	0.06	6.09	0.16
6.0–6.5	5.72	0.05	5.71	0.11
6.5–7.0	5.97	0.11	6.28	0.45
7.0–7.5	5.88	0.14	6.00	0.51
7.5–8.0	5.97	0.09	6.22	0.47
8.0–8.5	5.98	0.18	6.14	0.71
8.5–9.0	6.96	0.29	–	–

Table 5.3: The mean $\log_{10}(L_{70}/M_{13CO})$ values and associated standard errors for the full sample, and distance and mass-limited determined from Galactocentric distance bins.

by a factor of ~ 10 over the same Galactocentric distance range. The distance and mass-limited sample is too small in the 8–8.5 kpc bin to tell whether the rise between 4 and 8.5 kpc is significant, but the rise in L_{70}/M_{13CO} between the comparatively well populated bins at 4–4.5 kpc and 6–6.5 kpc *is* significant; the mean and standard error in the 4–4.5 kpc bin is 5.27 ± 0.09 , and in the 6–6.5 kpc bin it is 5.71 ± 0.11 , and the rise is more than 3 times the quadrature sum of the standard errors. This result, and its implications are discussed in more details in Chapter 6.

Two high density groups of clumps are visible in Figure 5.10 with Galactocentric distances between ~ 4 and 5 kpc, and ~ 5.5 and 6.5 kpc, corresponding approximately to the positions of the Scutum–Centaurus and Sagittarius spiral arms. These two samples of the 70 μm -associated clump population, have similar ranges in heliocentric distance, covering $4 < d_k < 10$ kpc. After removing all clumps with masses less than the completeness limit at 10 kpc of $900 M_{\odot}$, the Scutum–Centaurus sample contains 192 clumps and the Sagittarius arm contains

117 clumps. The mean $\log_{10}(L_{70}/M_{13\text{CO}})$ for the Scutum–Centaurus and Sagittarius sub-samples are 5.35 ± 0.06 and 5.44 ± 0.07 , respectively. The apparent rise in SFE over this range on Galactocentric distance is not significant, as the measurements are consistent within the standard errors.

The uncertainty on the Galactocentric distance for each clump stems from the unknown random deviation of its line-of-sight velocity from the prediction of the adopted Galactic rotation curve model. By using the velocity dispersion of $\pm 15 \text{ km s}^{-1}$ for the uncertainty on the line-of-sight velocity, as was used to calculate the uncertainties on the heliocentric distances in Section 4.4, the mean uncertainty on the Galactocentric distances is found to be $\sim 0.5 \text{ kpc}$. These uncertainties simply have the effect of smearing out the spiral arms visible in the Galactocentric distance distribution and, in agreement with this, the two previously mentioned groups of clumps making up the Scutum–Centaurus and Sagittarius arms in Figure 5.10 have widths of $\sim 1 \text{ kpc}$. Over the full Galactocentric distance range, these uncertainties do not affect the conclusions presented here.

Chapter 6

Discussion and conclusions

The most basic results of the CHIMPS survey were presented in Chapter 2, and these are summarised in Section 6.1 of this Chapter. The emission was further analysed in Chapter 3, where the optical depths, excitation temperatures and column densities were determined on a voxel-by-voxel basis. The physical properties of the CHIMPS clumps have been described in Chapter 4, and in Section 6.3 they shall be placed in a more general context, and compared against the molecular structures identified in other surveys. In Chapter 5, the star formation associated with the CHIMPS clumps was estimated thereby allowing the calculation of star formation efficiency analogue $L_{70}/M_{13\text{CO}}$. The SFE measurements are discussed in Sections 6.4 and 6.5, with a particular emphasis on how these fit in with what has been learned of the CHIMPS sources themselves.

6.1 CHIMPS

In this thesis, the data from CHIMPS are presented. CHIMPS is a survey of the $J = 3-2$ rotational transition of ^{13}CO and C^{18}O in a region of the inner Galactic plane, spanning approximately $28^\circ \leq l \leq 46^\circ$ and $|b| \leq 0.5^\circ$, which is now publicly

available at <http://dx.doi.org/10.11570/16.0001>. The data have an angular resolution of 15 arcseconds and a spectral channel width of 0.5 km s^{-1} , with a bandwidth of 200 km s^{-1} . With a median rms of $\sim 0.6 \text{ K}$ in the $^{13}\text{CO} (3-2)$ spectra at this resolution, the sensitivity corresponds to a column density of roughly $N(^{13}\text{CO}) \sim 3 \times 10^{14} \text{ cm}^{-2}$ or $N(\text{H}_2) \sim 3 \times 10^{20} \text{ cm}^{-2}$ for optically thin gas at an excitation temperature of 10 K. The $\text{C}^{18}\text{O} (3-2)$ spectra have a median rms of 0.7 K per channel, corresponding to $N(\text{C}^{18}\text{O}) \sim 4 \times 10^{14} \text{ cm}^{-2}$ or $N(\text{H}_2) \sim 4 \times 10^{21} \text{ cm}^{-2}$.

The relatively low abundances of the two CHIMPS isotopologues compared to ^{12}CO (the relative abundances of ^{13}CO and C^{18}O compared to ^{12}CO are $\sim 10^{-2}$ and $\sim 10^{-3}$, respectively) mean that they become optically thick at much higher column densities. The CHIMPS data, therefore, may serve as an excellent resource for finding the dense substructures in molecular clouds that fuel star formation (Molinari et al., 2010b). When used in conjunction with other CO surveys such as COHRS (Dempsey, Thomas & Currie, 2013) and GRS (Jackson et al., 2006) which trace different gas components, these data will help to provide a clearer picture of star-formation, and molecular gas dynamics. CHIMPS also complements the wealth of submillimetre surveys such as the JPS, Hi-GAL, ATLASGAL, BGPS and infra-red surveys like *WISE*, GLIMPSE and MIPS GAL.

6.2 The Galactic structure according to CHIMPS

One of the most useful data products to have arisen from the CHIMPS survey is the position–velocity diagram, created from the latitude-integrated $^{13}\text{CO} (3-2)$ emission (see Figure 2.8), that shows Galactic structure with unprecedented clarity. While the range in longitude is CHIMPS is substantially less than the Dame,

Hartmann & Thaddeus (2001) CO $J = 1-0$ survey of the entire Galactic plane, the angular resolution is far higher (a factor of 30 improvement) and it identifies denser and more optically thin gas. Duarte-Cabral & Dobbs (2016) predict that the most massive GMCs are found in Galactic spiral arms, and the CHIMPS data therefore ought to be able to provide tighter constraints for spiral arm models. When used in conjunction with the aforementioned CO $J = 1-0$ data over the full Galactic plane, these data have the potential to produce a more accurate picture of the spiral structure in at least the first quadrant of the Milky Way.

The spiral arm models of Taylor & Cordes (1993), which were based on the model of Georgelin & Georgelin (1976) and updated in Cordes (2004) generally appear to match the CHIMPS $^{13}\text{CO} (3-2)$ emission in position–velocity space fairly well, though there are some discrepancies. In this model, for example, the Norma spiral arm appears to offset in velocity by $10-20 \text{ km s}^{-1}$, and it is not clear how the significant quantity of material between the Scutum–Centaurus and Sagittarius arms fits into the picture. While it would appear that this particular spiral arm model stands up well to modern data after two decades, at least over this range on longitude, there are a variety of more recent models that may be more appropriate to use.

It is important that the spiral structure of the Milky Way be established for studies of star formation in different Galactic environments. For instance, Ragan et al. (2014) identified a sample of giant molecular filaments in the Galactic plane, and associated them with spiral arm and inter-arm regions based on their location in position–velocity space with respect to the spiral arm model of Vallée (2008). Those spiral arm models do not completely agree with the structure seen in $^{13}\text{CO} (3-2)$ emission over the CHIMPS survey area; in Figure 6.1, the Vallée (2008) spiral arms have been overlaid on the CHIMPS $^{13}\text{CO} (3-2)$ emission in

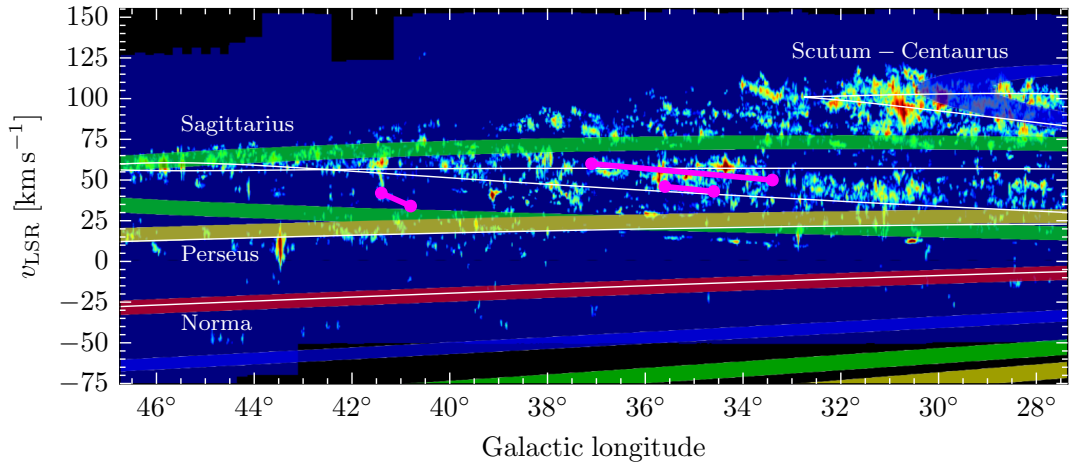


Figure 6.1: Position–velocity diagram for the ^{13}CO (3–2) CHIMPS data with an intensity scale matching that of Figure 2.8. The spiral arm model of Vallée (2008) has been overlaid, with the loci of the Scutum–Crux, Sagittarius–Carina, Perseus and Norma–Cygnus spiral arms appearing in blue, green, yellow and red, respectively. For comparison, the Taylor & Cordes (1993) spiral arm loci are overlaid with white lines. The three Ragan et al. (2014) giant molecular filaments in the survey area have been overlaid in magenta.

position–velocity space and it can be seen that, while the Perseus and Norma arms cover much of the same emission as the Taylor & Cordes (1993) models in this region of the sky, this particular model of the Sagittarius arm misses a large quantity of emission, and the Scutum–Crux tangent falls short in longitude of the W43 complex at $l \approx 31^\circ$. With this spiral arm model, Ragan et al. (2014) thereby deduced that the three identified giant molecular filaments which are in the CHIMPS survey are located in inter-arm environments, though comparison with the CHIMPS emission would appear to place at least two out of the three directly in what the Taylor & Cordes (1993) model identifies as the Sagittarius spiral arm.

6.3 The nature of the molecular structures identified in CHIMPS and its implications

6.3.1 Size and density

The CHIMPS survey constitutes one of the highest angular and spatial resolution studies of dense molecular gas over a significant area of the Galactic plane to date. The GRS molecular clouds were extracted from data smoothed to an angular resolution of 6 arcminutes, while the CHIMPS clumps were extracted from data with an effective resolution of 27.4 arcseconds. In the CHIMPS survey area, there are ~ 250 GRS molecular clouds with radii ranging from roughly 1 to 30 pc, whereas there are ~ 4400 spatially resolved CHIMPS clumps, and the majority have radii between ~ 0.05 and 5 pc. The order of magnitude difference in resolution is responsible for the difference in number and sizes of sources identified. This, however, is not only a matter of resolution; the critical density of the $J = 3-2$ transition is $\sim 10^4 \text{ cm}^{-3}$ at 10 K, compared to $\sim 5 \times 10^2 \text{ cm}^{-3}$ for the $J = 1-0$ transition, and consequently CHIMPS is sensitive to preferentially denser gas than GRS.

In Figure 6.2, the distribution of the mean density $n(\text{H}_2)$ of the CHIMPS clumps is compared to that of the molecular clouds found in the GRS (Roman-Duval et al., 2010) and the ATLASGAL clumps hosting high-mass YSOs and compact HII regions (Urquhart et al., 2014b). The CHIMPS clumps span a parameter space occupied by both of these surveys, with the most diffuse CHIMPS clumps having similar densities to the most diffuse GRS clouds, and the densest CHIMPS clumps roughly matching the density of the densest ATLASGAL clumps. It would appear that emission in CHIMPS shows both types of structures, which makes sense given that the thermal emission of the $J = 3-2$ transition traces dense gas

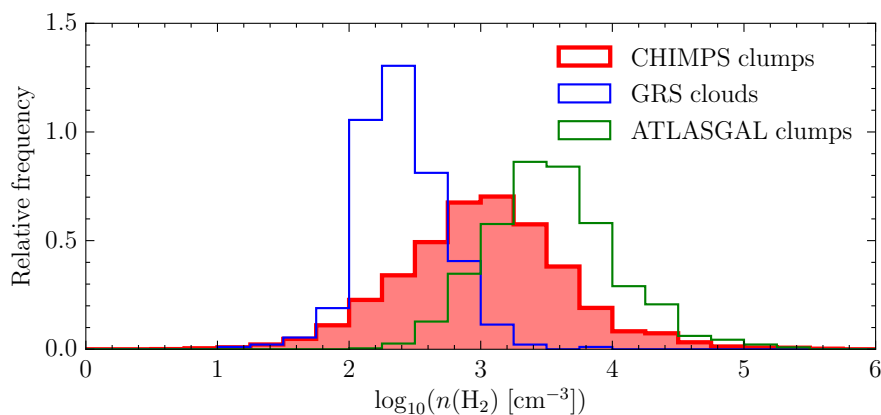


Figure 6.2: A comparison of the density distributions of molecular clouds from the GRS (Roman-Duval et al., 2010) and clumps from CHIMPS and ATLASGAL (Urquhart et al., 2014b). The bins have a width of 0.25 dex, and the areas have been normalised.

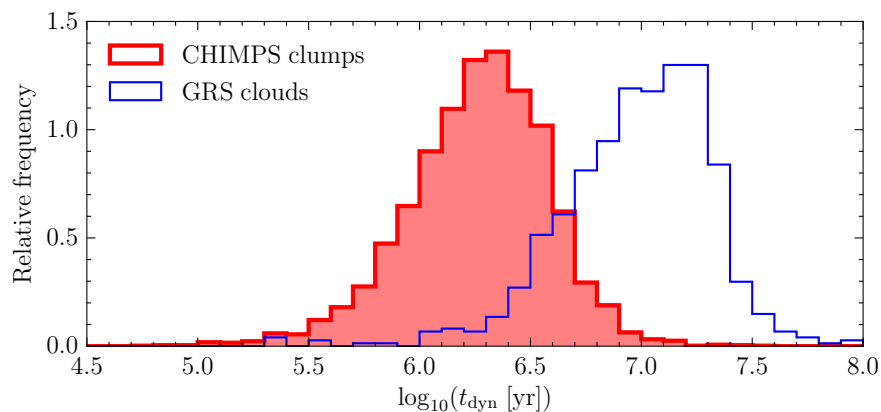


Figure 6.3: The dynamical timescales of the CHIMPS clumps and GRS clouds. The bin width is 0.1 dex, and the areas have been normalised.

similar to that traced by the 870 μm ATLASGAL dust emission, and extending to lower densities with a component of sub-thermal emission from molecular gas at lower densities, reaching into the GRS $J = 1-0$ density regime.

Since the structure of molecular clouds has been found to be hierarchical (e.g. Blitz & Stark, 1986; Rosolowsky et al., 2008) and possibly fractal (Falgarone, Phillips & Walker, 1991; Stutzki et al., 1998; Combes, 2000) in a number of preceding studies, it is unsurprising to find that the CHIMPS ‘clumps’ are smaller and denser than the molecular clouds of the GRS. The CHIMPS gas structures appear to be tracing some intervening density regime, covering both the molecular

cloud phase, and structures that are fragmenting to the scale of molecular clumps which overwhelmingly contain the sites of active star formation.

6.3.2 Timescales

The distributions of the dynamical timescales of CHIMPS clumps and GRS clouds, where $t_{\text{dyn}} = 2R/\sigma_{v_{\text{LSR}}}$ and $\sigma_{v_{\text{LSR}}}$ is the one-dimensional velocity dispersion, are compared in Figure 6.3. The peaks of the two distributions are separated by approximately an order of magnitude, suggesting that the GRS clouds are about 10 times as long-lived as the CHIMPS clumps. Otherwise, the shapes of the distributions are remarkably similar; they both have a range of approximately 2 orders of magnitude, and standard deviations of ~ 0.3 dex. The CHIMPS clumps have dynamical timescales that are easily long enough to form high-mass YSOs and compact HII regions, which have lifetimes of up to a few 10^5 years, and the most luminous high-mass YSOs have lifetimes of $\sim 7 \times 10^4$ years (Mottram et al., 2011).

The difference in timescales of the GRS clouds and the CHIMPS clumps gives a suggestion of the dynamic internal substructure of a cloud. Through the collation of observational evidence, Elmegreen (2000) found that star formation in molecular clouds operates over the space of only one or two dynamical timescales. If the structures seen in CHIMPS represent the dense interiors of the large-scale clouds seen in the GRS, then this would appear to suggest that while molecular clouds are transient objects in themselves, their interiors are changing on even shorter timescales, presumably driven by internal turbulence.

6.3.3 Pressure

This picture of the turbulent interiors of molecular clouds can be explored more directly by examining the turbulent and thermal pressure. The turbulent pressure was defined in Equation 4.20 and detailed in Section 4.6, and for comparison, the thermal pressure for each cloud can be calculated by:

$$P_{\text{therm}} = n(\text{H}_2)k_{\text{B}}T_{\text{ex}}, \quad (6.1)$$

where $n(\text{H}_2)$ is the average volumetric number density, k_{B} is Boltzmann's constant, and the gas is assumed to be in LTE where the gas temperature is given by the excitation temperature T_{ex} .

In Figure 6.4, the turbulent and thermal pressure of each CHIMPS clump is plotted as a function of Galactocentric distance. Wolfire et al. (2003) made predictions as to the behaviour of the turbulent and thermal pressure of the neutral HI gas as a function of Galactocentric distance, with both taking the form of similar modest exponential declines. In both cases, the mean logarithm of the pressure in 0.5 kpc bins is overlaid, and has been calculated for two samples; firstly, all CHIMPS clumps at heliocentric distances of > 2 kpc, and secondly, a distance and mass-limited sample of clumps which have heliocentric distances in the range $2 \text{ kpc} < d_{\text{k}} < 12 \text{ kpc}$ and clump masses of greater than $1300 M_{\odot}$ – the approximate completeness limit at 12 kpc. Neither the turbulent nor thermal pressures of CHIMPS clumps declines significantly over the range of Galactocentric distance covered, though the Wolfire et al. (2003) predictions from the neutral gas exhibit a decline by a factor of $\lesssim 5$ over the 6 kpc range in Galactocentric distances covered.

While the thermal pressure of the molecular gas in the CHIMPS clumps ap-

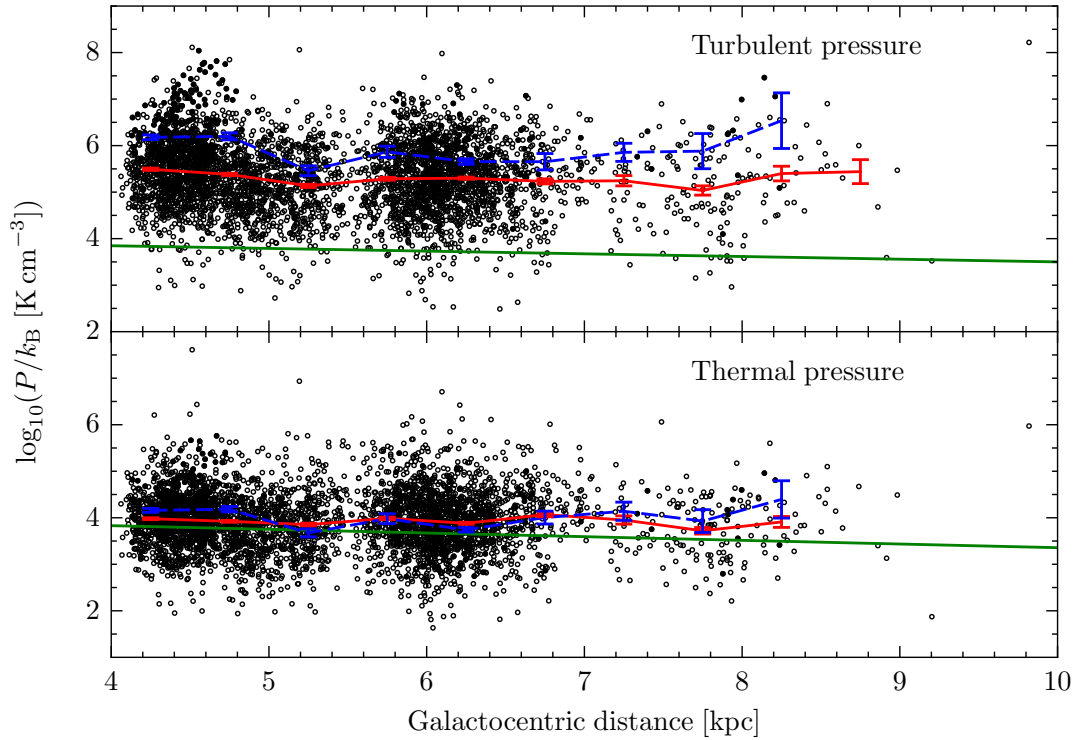


Figure 6.4: Variations in turbulent and thermal pressure as a function of Galactocentric distance. In both panels, the red line shows the mean value in 0.5 kpc bins for all CHIMPS clumps with a heliocentric distance of more than 2 kpc, while the blue dashed line shows the same trend for clumps with the additional constraints that they are closer than 12 kpc and have masses greater than $1300 M_{\odot}$. The error bars show the standard error on each bin. The green lines show the model of Wolfire et al. (2003) for the expected turbulent and thermal pressures of HI which exhibit a modest exponential decline at increasing distance from the Galactic centre.

appears to be in good agreement with the thermal pressure of the neutral gas, albeit with a small systematic offset of 0.5 dex (a factor of ~ 3), the turbulent pressures are significantly higher than the HI prediction. The mean turbulent pressures of clumps in the full sample and in the distance and mass-limited sample are enhanced by 1.6 and 2.2 dex, respectively, when compared to the mean Wolfire et al. (2003) prediction for HI over this range in Galactocentric radius. This suggests that the molecular clumps are in approximate thermal pressure equilibrium with the HI in the Galactic disc, but are considerably overpressurized with respect to

the turbulence of the neutral ISM.

The turbulent pressure is proportional to $n\sigma_v^2$, where n is the density and σ_v^2 is the velocity dispersion. If the mass and momentum are roughly conserved, then the velocity dispersion will not change between the neutral and molecular phases, implying that $P_{\text{turb}} \propto n$; an increase in the gas density from $10\text{--}100\text{ cm}^{-3}$ to $100\text{--}10^4\text{ cm}^{-3}$ at constant thermal pressure implies an increase in the turbulent pressure by the same factor. Since the gravitational pressure $P_g \propto R^{-4}$, and the mean density $n \propto R^{-3}$, gravity can still overcome the turbulent pressure in the centres of dense regions, and so clumps can remain internally gravitationally bound, even with such high turbulent pressure. This would seem to suggest that the formation of molecular clouds out of the neutral medium does not necessarily require collisional flows – they could simply form out of any thermal instability that results in a transition to the cold and dense phase.

6.3.4 Virial state

In Figure 4.11, the distribution of virial ratios is shown to indicate that the clumps are largely unbound considering their gravity and thermal pressure alone. This is also indicative of the transient and short-lived nature of the clumps, though there is the possibility of some additional effects keeping them in equilibrium; magnetic fields or external pressure are the obvious candidates that have not been accounted for in this calculation.

It is worth restating at this point that while the distribution of virial parameters would nominally indicate that largely gravitationally unbound structures make up the CHIMPS clumps, it is known that the masses are necessarily light on two fronts. Firstly, the $J = 3\text{--}2$ transition is not sensitive to the lower density gas that is recovered with the $J = 1\text{--}0$ transitions. Secondly, the CHIMPS

clumps are also likely to be systematically light in a distance-dependent manner due to the observational difficulties involved with $\text{C}^{18}\text{O}(3-2)$; the lower abundance of C^{18}O with respect to ^{13}CO and the lower sensitivity caused by lower atmospheric transmission mean that the optical depth of $^{13}\text{CO}(3-2)$ is not calculable in regions where $\text{C}^{18}\text{O}(3-2)$ is not detected but $^{13}\text{CO}(3-2)$ is and so the column density will be underestimated. These factors are likely to be responsible for the missing mass.

6.4 Variations in star formation efficiency

6.4.1 Variations between spiral arms

In Section 5.2.2, the sample of CHIMPS clumps with $70\ \mu\text{m}$ counterparts was divided into sub-samples based on their association with the Taylor & Cordes (1993) spiral arms in position–velocity space. The role that spiral arms play in star formation is currently unclear; spiral arms could simply be organising features that collect molecular gas (e.g. Elmegreen & Elmegreen, 1986), but do not otherwise effect the process of star formation, and that the increase in the surface density of the star formation rate associated with them is simply due to the enhanced surface density of molecular gas. It has also been suggested that spiral shocks could actually trigger star formation (e.g. Roberts, 1969; Bonnell et al., 2006).

When the CHIMPS spiral arm and inter-arm samples were reduced to contain only those clumps which have masses above the completeness limit, the mean $\log(L_{70}/M_{^{13}\text{CO}})$ of clumps in the Scutum–Centaurus arm was found to be a factor of $\sim 3-5$ lower than the same quantity for clumps belonging to both the Sagittarius and Perseus arms. This is similar to results found by Moore et al. (2012) and

Eden et al. (2015) who found that the mean SFE in the Sagittarius and Perseus arms are elevated by a factor of ~ 2 when compared to the Scutum–Centaurus arm. Those studies, however, found that the increases in SFE in the Perseus and Sagittarius arms were due to the presence of two extreme star-forming regions: W49 and W51. When W49 and W51 were removed from the sample, the SFEs were found to be unchanging across their samples between spiral arms and inter-arm regions. W51 is not in the CHIMPS sample, but W49 is, and it contributes 7 of the 15 sources in the distance and mass-limited Perseus sample. If W49 is removed from this sample, then the mean $L_{70}/M_{13\text{CO}}$ falls from 6.06 ± 0.28 to 5.74 ± 0.37 ; the elevation of SFE in the Perseus arm caused by W49 is not significant in this sample.

The Scutum–Centaurus sample covered by this survey largely contains sources located at or near the near-end of the long bar, where the orbits change from the bar-dominated region to the spiral arm-dominated region of the disc, and perhaps this special location might be responsible for a reduced SFE. Nguyen Luong et al. (2011) determine that the W43 star-forming region is located at the meeting point of the long bar and the Scutum–Centaurus arm, and find that the star formation rate is suppressed compared to the expectation from the assumed ‘classical’ SFE of 2% and the total gas mass. They suggest that W43 may be on the verge of a starburst where the star formation rate will dramatically increase in the future. Perhaps, then, this suggests a picture where the star formation rate of any given region is episodic, and that this study merely finds the Scutum–Centaurus sample at a temporal minimum of star formation rate.

James, Bretherton & Knapen (2009) and James & Percival (2016) have observed a ‘star formation desert’ in the bar-dominated regions of barred spiral galaxies where the star formation rate is suppressed, though it is unclear whether

this is caused by any change in star formation efficiency or is simply the result of a lower gas surface density. Is there any evidence for the Milky Way having a similar star formation desert, or a drop in the star formation efficiency in the bar-dominated centre? Roman-Duval et al. (2010) found that the surface density of molecular gas in the Milky Way does decrease markedly inside of the Galactocentric radius corresponding to the end of the long bar at ~ 4.5 kpc, though the GRS data do not extend into the Galactic centre. From those data, it is not clear whether the drop of molecular gas surface density represents a continuing trend into the centre, or whether it is only low only when compared to the build-up of molecular gas around the long bar's end at W43 that is included in their sample.

A study of the three-dimensional distribution of molecular gas traced by $^{12}\text{CO } J = 1-0$ in the Galaxy by Nakanishi & Sofue (2006) showed that the molecular gas surface density increases into the Galactic centre, with a small additional peak at a radius of ~ 5 where the long bar ends. A recent examination of archival H_2 and HI data by Koda, Scoville & Heyer (2016) found that the molecular gas fraction, $n(\text{H}_2)/(n(\text{HI} + \text{H}_2))$ varies strongly with Galactocentric distance with a $\sim 100\%$ molecular gas fraction in the Galactic centre that decreases to $\gtrsim 50\%$ at 6 kpc, and falling further to $\sim 10\text{-}20\%$ at 8.5 kpc, when averaged over the whole of the disc height. High-mass star formation has been observed to occur in the Near and Far 3kpc arms, at the very least, and Green et al. (2009) have identified 49 6.7 GHz methanol masers from the MMB spread over both arms but, with such large quantities of molecular gas present over the whole region, the overall star formation efficiency could still be low.

There are some issues with dividing up the CHIMPS clumps into spiral arms based on their position in position–velocity space. Firstly, this division must necessarily assume a spiral arm model, and for this study the model of Taylor &

Cordes (1993), updated in Cordes (2004) has been adopted. While this spiral arm model largely agrees well with the latitude-integrated position–velocity diagram for the CHIMPS ^{13}CO (3–2) data (see Figure 2.8), the Norma arm, for example, might be placed slightly differently. Issues also arise from the KDA which may be seen in Figure 5.9; the velocity tolerance in the Perseus arm allows objects in the Solar neighbourhood at $v_{\text{LSR}} \sim 0 \text{ km s}^{-1}$ to be erroneously drawn into its sample. Objects at heliocentric distances of less than 2 kpc have been removed from the samples for the study mentioned in the preceding paragraph, but this highlights some of the issues involved with this methodology.

6.4.2 Variations as a function of Galactocentric radius

The problems in identifying spiral arms lead naturally to a less model-dependent way of isolating spiral arms, which is to look for variations as a function of Galactocentric radius. As a survey of a limited sector of the Galactic plane, spiral features ought to show up as peaks in the Galactocentric radius distributions in CHIMPS. This has the additional advantage of being insensitive to the solution to the KDA; the v_{LSR} of a clump in emission maps onto a single Galactocentric distance, and depends only upon the rotation curve. In this work, the Galactic rotation curve of Brand & Blitz (1993) has been adopted.

In Figure 5.10 and Table 5.3 of Section 5.2.3, evidence was presented that SFE increases significantly with distance from the Galactic centre. The combination of this with the expectation of both turbulent and thermal pressures to decrease (e.g. Wolfire et al., 2003) over that range poses a question; can the increase in the SFE within CHIMPS clumps be explained by a lower turbulence? This could also be caused by the variation in abundance ratios of e.g. $X(^{12}\text{CO}/^{13}\text{CO})$ which have been predicted (e.g. Wilson & Rood, 1994) to increase with distance from

the Galactic centre. If this is, indeed, the case, then the implication is that molecular cloud masses calculated with a constant abundance ratio would be underestimated by a factor that increases with Galactocentric radius. This could account for the increasing $L_{70}/M_{13\text{CO}}$ to some extent. The value of $L_{70}/M_{13\text{CO}}$ was found to rise from 5.27 ± 0.09 to 5.71 ± 0.11 between the 4.0–4.5 and 6.0–6.5 kpc bins, a rise of $8 \pm 3\%$, which is well within the (large) error bars associated with the Wilson & Rood (1994) $X(^{12}\text{CO}/^{13}\text{CO})$ rise over the same range.

A number of studies over the last decade or so have proposed that turbulent pressure reduces the efficiency of star formation by increasing the column density threshold. In a study of numerical simulations of a gravitationally unbound molecular cloud, Clark & Bonnell (2004) found that in spite of the presence of a supersonic turbulence field, quiescent regions exist which are able to gravitationally collapse to form stars. They surmised that self-gravity is not a necessary condition for the evolution of GMCs, and that interiors do not become gravitationally bound until star formation occurs.

Kruijssen et al. (2014) studied the star formation in the Milky Way’s central molecular zone, and found that the SFR is suppressed by a factor of ≥ 10 when compared to predictions based on the quantity of dense gas contained therein. They suggest that the low SFR could be explained by the high turbulent pressure, which reaches $\sim 10^9 \text{ K cm}^{-3}$ in the CMZ, causing an increase in the volume density threshold required for star formation to occur. High resolution ALMA observations of the CMZ molecular cloud G0.253+0.016 by Rathborne et al. (2014) find a dearth of star formation activity despite having a vast reservoir of gas with a column density in excess of the proposed ‘universal’ column density threshold for star formation (e.g. Lada et al., 2012); the study supports the idea of a density threshold for star formation that is dependent upon the turbulent Mach number.

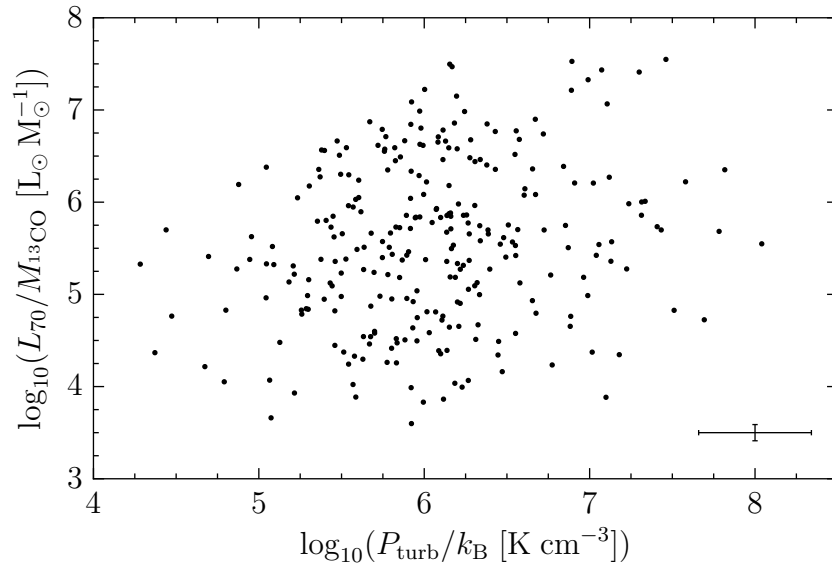


Figure 6.5: The CHIMPS clumps exhibit no significant correlation between turbulent pressure and $L_{70}/M_{13\text{CO}}$. The median error bar is shown in the lower right corner.

The relationship between the SFE analogue $L_{70}/M_{13\text{CO}}$ and turbulent pressure for the CHIMPS clumps is presented in Figure 6.5, measured for the distance and mass-limited sample which has a heliocentric distance range of $2 < d_k < 12$ kpc and a lower mass limit of $1300 M_\odot$. The Spearman rank-order correlation coefficient between $L_{70}/M_{13\text{CO}}$ and P_{turb} is $\rho = 0.19$ and, while the two-sided P -value for a hypothesis test whose null hypothesis is that they are uncorrelated is 0.0016 for the 275 clumps in the sample, there does not appear to be any significant correlation between SFE and turbulent pressure; these data do not show evidence for a turbulent pressure threshold for star formation. Furthermore, the scatter is significantly larger than the error bars, indicating that this lack of correlation is not simply an artefact of measurement uncertainties. It is possible, however, that a weak correlation has arisen as the consequence of a small selection effect or bias that has not been accounted for here.

6.5 The lognormality of L/M

The overall distribution of the star formation efficiency analogue $L_{70}/M_{13\text{CO}}$ was found to be approximately lognormal for individual clumps in Section 5.2. Eden et al. (2012) similarly found that the distribution of clump formation efficiencies implied by the dense gas fraction, calculated for a sample of BGPS clump residing within GRS molecular clouds, is also consistent with lognormality. Eden et al. (2015) also found lognormality in the SFE calculated from the ratio of the infrared luminosities of GLIMPSE and WISE-identified YSOs to the parent BGPS clump masses.

The division of the CHIMPS clump sample into spiral arms or Galactocentric distance bins in this study, has involved the grouping of sources in scales of ~ 0.5 kpc to several kpc, and the lack of differences between samples suggests that there are no significant changes on these spatial scales. When combined with the lognormal distributions in the star formation and clump formation efficiencies in the aforementioned studies, this would seem to suggest that it is local feedback mechanisms within molecular clouds that determine the star formation rate, and that the role played by spiral arms in *triggering* star formation – if any – is minor. It may be that there are a number of sub-samples of CHIMPS clumps within the overall lognormal $L_{70}/M_{13\text{CO}}$ distribution that do show variations with environment, and that they simply have not been identified yet. A method for finding these sub-samples is proposed in Section 7.3.

If it is indeed the case that the distributions of star and clump formation efficiencies within any reservoir of molecular gas are lognormal, then what is their origin? In general, lognormal distributions arise through the central limit theorem when the measured value of a quantity is the product of several independent multiplicative factors. The mere presence of these lognormal distributions indicates

that it will be a difficult task to tease apart the constituent contributing processes since they imply that there is not a single dominant mechanism controlling the SFE.

For example, Vazquez-Semadeni (1994) showed that the lognormal density probability distribution function of gas in a supersonically turbulent medium arises through the central limit theorem after successive shocks that alter the gas density through independent multiplicative factors. Log-normal column density probability distribution functions have been observed in many studies of molecular clouds (e.g. Schneider et al., 2013; Rathborne et al., 2014; Burkhart et al., 2015), though they tend to have a power-law tail at high column densities that is thought to correspond to regions that have become unstable to gravitational collapse. The characterisation of the internal density structure of molecular clouds as having a lognormal form, however, does not necessarily explain the lognormal star formation efficiency since it is, presumably, the power-law tail of gravity-dominated clumps that makes up the CHIMPS clump sample. This would only be the case if a critical column density threshold necessary for star formation applied in the lognormal regime, but the column density PDFs tend to exhibit a power-law tail where self-gravity, and also presumably the star formation, occurs.

Chapter 7

Future Work

7.1 Testing spiral arm models

The CHIMPS ^{13}CO (3–2) data could, in position–velocity space, allow a quality of fit to be calculated for spiral arm models in this area of the sky. If a tolerance is given in velocity about the predicted centres of the spiral arms, then the average ^{13}CO (3–2) emission profile could be integrated over discrete longitude bins, and given a model for the density distribution across the spiral arms (e.g. Roberts, 1969) the quality of fit could be calculated. One might expect that the velocity profile of emission averaged over a longitude bin ought to match the predicted profile when a good fit is found.

The top-down view of the Galaxy provided by a sample of star-forming regions with well known distances, such as those with methanol masers from the BeSSeL survey (Brunthaler et al., 2011), could also be used to determine spiral structure, and the CHIMPS clumps could be integrated into this sample. Images of face-on spiral galaxies could be used as a template for the distribution of star-forming regions within the Milky Way in this top-down view, and a sample

comprising spiral galaxies with varying strengths and numbers of spiral arms and with different winding angles could be used to find a best fit with the distribution of the Galactic sample of star forming regions and molecular clumps.

The strength of the CHIMPS data in tracing spiral structure could be further enhanced by increasing the longitude coverage in either or both directions.

7.2 Extracting the filamentary content of CHIMPS

In an analysis of low-density molecular gas traced by CO and high density molecular gas traced by NH₃, Goodman et al. (2014) found that the extremely high-aspect ratio filamentary IRDC discovered by Jackson et al. (2010), known as ‘Nessie’, may have an extent of up to ~ 400 pc. Many more large-scale filaments have since been identified by the combination of mid-infrared extinction features, followed up with spectra of molecular gas tracers, like CO, to identify any velocity coherence. Li et al. (2013) found a velocity-coherent 500 pc molecular ‘wisp’, with a mass of $\gtrsim 10^5 M_{\odot}$ located ~ 130 pc above the Galactic plane, that appears to have been disturbed by an expanding bubble structure. A study by Battersby et al. (2014) describes a giant molecular filament, known as G32.02+0.06, that is 80 pc in length and has a mass of $2 \times 10^5 M_{\odot}$, which is not quite in the Galactic mid-plane. The aforementioned Ragan et al. (2014) study identified 7 giant molecular filaments in the first Galactic quadrant that have lengths of ~ 100 pc and masses of 10^4 – $10^5 M_{\odot}$ and, using similar techniques, Abreu-Vicente et al. (2016) identified a further 9 comparably giant molecular filaments in the fourth Galactic quadrant with lengths of 80–160 pc.

Goodman et al. (2014) suggest, through comparisons with numerical simulations by Smith et al. (2014), that large-scale filaments like Nessie could be

the high-density crests of spiral arms. They draw the analogy that Nessie-like filaments are the ‘bones’ of the Milky Way’s structural ‘skeleton’. Such ‘bone’ structures should be expected to lie on the Galactic mid-plane, and in that regard the Li et al. (2013) wisp and the Battersby et al. (2014) filaments do not appear to be directly related to Galactic structure, but Goodman et al. (2014) and Ragan et al. (2014) find that Nessie runs directly along the Scutum–Centaurus spiral arm. The Smith et al. (2014) simulations do not include the effects of stellar feedback or magnetic fields, and the disruption of the mid-plane filaments that e.g. HII regions might disturb the Nessie-like filaments to create structures like the wisp of Li et al. (2013). Continuing the analogy, Zucker, Battersby & Goodman (2015) identified a further ten ‘bones’ and, although they are smaller and less massive than the Ragan et al. (2014) filaments, they are within 20 pc of the Galactic mid-plane and 6 of them run along the Scutum–Centaurus arm in position–position–velocity space.

The position–velocity diagrams of the ^{13}CO (3–2) emission within CHIMPS (see Figure 2.8) hint at the presence of similar filamentary structures. For example, a string of bright knots of emission can be seen extending from approximately $l = 33.2^\circ$, $v_{\text{LSR}} = 100 \text{ km s}^{-1}$ to $l = 34^\circ$ and $v_{\text{LSR}} = 110 \text{ km s}^{-1}$, and a string of similar (but less obvious) features appear to exist in the region between the Scutum–Centaurus and Sagittarius spiral arms, which were discussed in Section 2.2.4. This inter-arm emission may also describe a minor arm or spur, that have been produced in numerical simulations (e.g. Dobbs & Pringle, 2013; Pettitt et al., 2015; Dobbs, 2015; Duarte-Cabral & Dobbs, 2016), and can be seen in other galaxies, such as *Spitzer* observations of IC342, which is shown in Figure 7.1. A systematic search for filamentary structures in CHIMPS, using algorithms such as DisPerSE (Sousbie, 2011), getfilaments (Men’shchikov, 2013) or FILFINDER

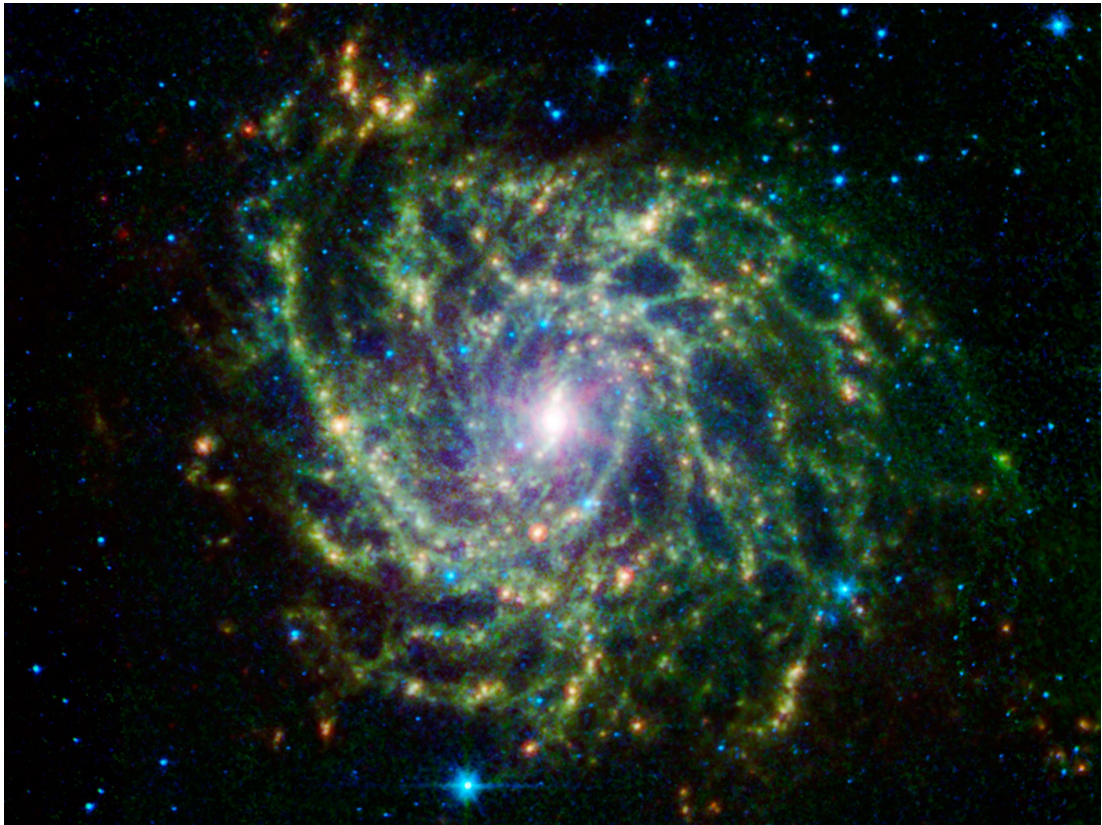


Figure 7.1: A composite image of the galaxy IC342, with data from *Spitzer* MIPS 24 μm (red), IRAC 5.8 and 8.0 μm (green) and 3.6 and 4.5 μm (blue) imaging. Image credit: NASA/JPL-Caltech.

(Koch & Rosolowsky, 2015) could allow further study of the relationship between large-scale filaments and spiral arms, which are very clear in the CHIMPS tracers. While the relatively high density of the $J = 3-2$ transition means that large-scale filaments, on the scale of several degrees, are not immediately obvious to the eye in the CHIMPS data, they may become clearer after smoothing, or might also be identifiable via the application of a minimum spanning-tree algorithm to the clump catalogue.

7.3 Identifying complexes of emission

The CHIMPS clump catalogue contains between four and five thousand entries, depending upon what criteria are used to filter out false positives. Distances were assigned to the majority of these sources in Chapter 4.3 by looking for nearby sources from other surveys in position–position–velocity space that have already had solutions to the KDA assigned to them. This was a necessary approach because the large number of CHIMPS clumps that have been identified would have made it a mammoth task to visually inspect a HI spectrum for each individual source if the KDAs were to be resolved by the HISA or HICA methods, and a further problem is that there are currently no HI Galactic plane surveys of comparable spatial resolution to CHIMPS. Moreover, there are a number of problems with kinematic distances, for which one must assume a Galactic rotation curve model and ignore peculiar velocity deviations from it. The most reliable way of establishing distances to sources within the plane of the Milky Way is by using very long baseline interferometry to obtain geometric parallax measurements, which have been touted as the ‘gold standard’ (e.g. Menten et al., 2007). Parallax distances are purely geometric calculations, and make no assumptions about the Galactic rotation curve, and are thus more robust than kinematic distance assignments.

If the CHIMPS clumps could be grouped into larger complexes, then not only would there be fewer HI spectra to be visually inspected for determination of kinematic distances, but the low spatial resolution HI spectra would be more suitable, and there may be an increased frequency of coincidence with a source with a geometric parallax distance assignment. One way of identifying complexes of discrete sources is through the use of friends-of-friends analysis, which was used by Wienen et al. (e.g. 2015) to group the ATLASGAL clumps into complexes.

Such analysis could lead to improvements in the reliability of distance determinations, reducing the distance uncertainty (in the case of associations of complexes with sources that have parallax-determined distances), and hence the uncertainty in mass, size and related properties.

In addition to the improvement that could be made in distance determinations, in Section 6.5 the possibility was raised that environmental variations in SFE might be lost in the grouping of CHIMPS clumps into overly large sub-samples that cover kiloparsec scales in spiral arms or Galactocentric distance bins. There may yet be sub-samples within the survey that exhibit environmental variations, but the physical connection between clumps has been lost due to the FellWalker source extraction that naturally breaks up emission regions into clumps that define density peaks. The more diffuse ambient emission that connects up emission peaks has been lost, though there are a number of other algorithms that can reduce this problem.

A further difficulty in working with observations in $^{13}\text{CO}(3-2)$ from the CHIMPS survey is that it is intrinsically difficult to adequately describe the irregular morphologies of extended dense gas structures in a catalogue (e.g. see Figure 5.4), and this may have implications for making associations with sources from complementary data sets. Source extraction algorithms such as FellWalker (Berry, 2015) and ClumpFind (Williams, de Geus & Blitz, 1994) tend to identify the peaks of emission within a region, but they struggle to identify groups of emission features which one would identify by eye. Other approaches have been found to have more convincing results, and the recently developed Spectral Clustering for Interstellar Molecular Emission Segmentation (SCIMES; Colombo et al., 2015) method is such a scheme, which adopts a similar approach to friends-of-friends analysis.

SCIMES uses cluster analysis to identify and connect emission regions with similar properties in high resolution data, describing the hierarchical structures of giant molecular clouds, for example, using dendrograms (see e.g. Rosolowsky et al., 2008). Colombo et al. (2015) demonstrated that the structures identified by SCIMES are robust against changes in the input dendrogram parameters, as well as variations in noise and spatial resolution. Duarte-Cabral & Dobbs (2016) used SCIMES to extract emission from synthetic observations generated for smoothed particle hydrodynamic (SPH) simulations of giant molecular clouds. The authors found that, in general, SCIMES was able to recover the simulated giant molecular clouds well, and was particularly good at extracting long filaments which are generally not recovered by FellWalker, for example. SCIMES would therefore appear to be ideally suited to extracting the complex emission from the CHIMPS data, and would allow a more robust study of the effects of Galactic environment, and mitigate the aforementioned problems with distance assignment.

7.4 Spatial frequency analysis

The $L_{70}/M_{13\text{CO}}$ data compiled in Chapter 5 could potentially hold some additional insights into the dominant mode of star formation over the survey area that may be encoded into the spatial distribution of rises and falls in the SFE analogue. Figure 7.2 shows longitudinal profiles for the $L_{70}/M_{13\text{CO}}$ measurements for all of the CHIMPS clumps that have $70\ \mu\text{m}$ Hi-GAL source associated with them. There may be spatial frequency signals encoded within these data that might be sensitive to a dominant mode of star formation; for example, if spiral arms are playing some role in enhancing or suppressing the SFE, then it might be expected that spatial frequencies corresponding to a spiral arm width or an inter-

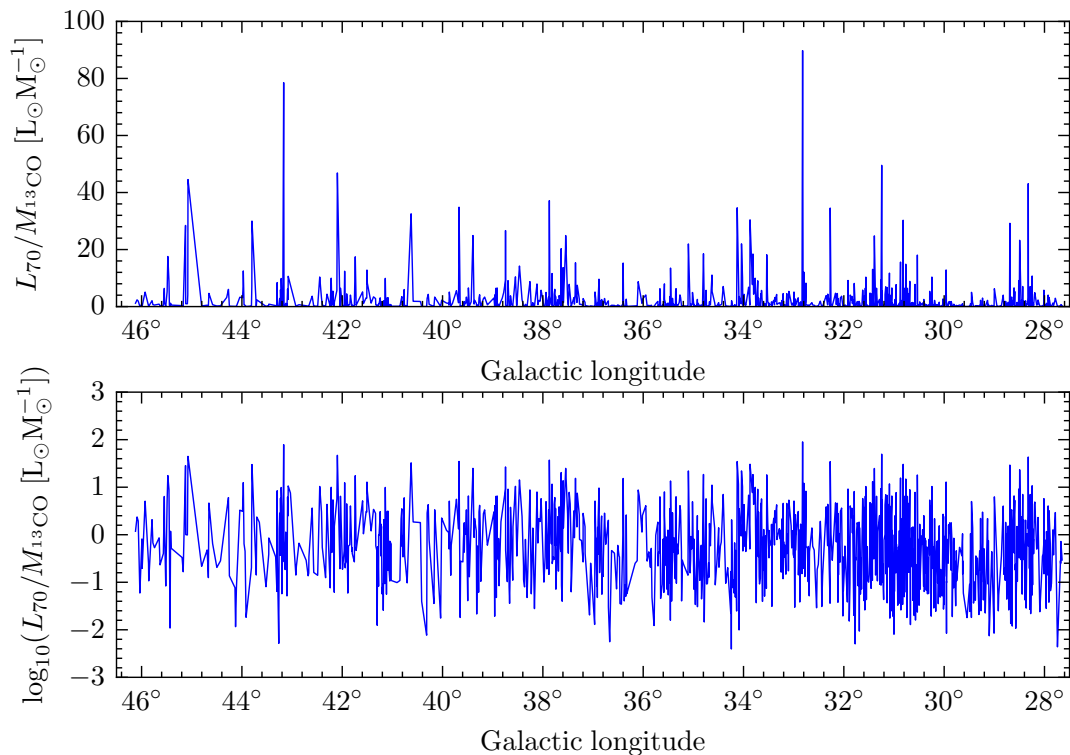


Figure 7.2: Longitudinal profiles of the $L_{70}/M_{13\text{CO}}$ measurements of all clumps with $70\ \mu\text{m}$ counterparts in CHIMPS. The top panel shows a linear scale of $L_{70}/M_{13\text{CO}}$, whereas in the bottom panel it is logarithmic. The blue lines connect the data points which have been ordered by longitude.

arm spacing might be present, and spatial frequency analysis techniques such as fast Fourier transforms could reveal those frequencies.

In any given longitude range, however, this Figure contains sources at many different distances along the line of sight, and thus the conversion from angular to spatial scale changes in a complicated fashion across this profile. This could be taken into account by dividing the $L_{70}/M_{13\text{CO}}$ sample into heliocentric distance-limited sub-samples that have similar spatial scales between clumps at the near and far bin edges, and these would provide transects that cover spiral arm and inter-arm regions. The profiles in Figure 7.2 simply trace the variation in $L_{70}/M_{13\text{CO}}$ from source-to-source which have been ordered by longitude, but

other profiles could be produced by averaging over longitude bins at different heliocentric distances.

Appendix A

Parameters used in the CHIMPS data reduction

A.1 ORAC-DR parameters

The following parameters were used in the reduction of each CHIMPS observation:

```
[REDUCE_SCIENCE_NARROWLINE]
BASELINE_LINEARITY=1
BASELINE_ORDER=4
BASELINE_LINEARITY_LINEWIDTH=1
PIXEL_SCALE=7.612
REBIN=0.5
```

¹ This parameter was altered for each individual observation, and was determined by inspecting the average spectrum of each raw time-series file. For

example, if a broad emission feature was visible with a 10 km s^{-1} linewidth at a velocity of 40 km s^{-1} , then this parameter would be set to ‘30:50’.

A.2 *FellWalker* parameters

The source extraction was carried out using the *FellWalker* algorithm (Berry, 2015) of CUPID:FINDCLUMPS, and the SNR cubes were the input data. Pixels with a $\text{SNR} < 3$ are regarded as noise, and all clumps must have a peak SNR of at least 5. The *FellWalker* parameters are listed below. The $^{13}\text{CO}(3-2)$ source extraction parameters were:

`FellWalker.AllowEdge=0`

`FellWalker.CleanIter=2`

`FellWalker.FlatSlope=1`

`FellWalker.FwhmBeam=3`

`FellWalker.MaxBad=0.05`

`FellWalker.MinDip=5`

`FellWalker.MinHeight=5`

`FellWalker.MinPix=16`

`FellWalker.MaxJump=4`

`FellWalker.Noise=3`

`FellWalker.RMS=1`

`FellWalker.VeloRes=1`

An identical parameter file was used for the C¹⁸O (3–2) source extraction, but with the following alterations:

```
FellWalker.MinDip=3
```

```
FellWalker.MinHeight=5
```

```
FellWalker.Noise=2
```

Appendix B

Radiative transfer analysis

The radiative transfer analysis used in Chapter 3 is derived in this Appendix and largely follows, with a few minor alterations, the derivation presented in Polychroni (2010), which was adapted from Moore (1989).

The absorption coefficient for a rotational transition between states $J = j \rightarrow i$ is:

$$\kappa(\nu_{ji}) = \frac{h\nu_{ji}}{4\pi} (n_i B_{ij} - n_j B_{ji}) \phi(\nu_{ji}), \quad (\text{B.1})$$

where h is Planck's constant, ν_{ji} is the frequency of the photon with the same energy as the difference between levels j and i , n_j and n_i define relative populations of the upper and lower levels, respectively, B_{ij} and B_{ji} are the Einstein absorption and stimulated emission coefficients of the two levels, respectively, and $\phi(\nu_{ji})$ is the line profile phase function of the transition. This can be re-written as:

$$\kappa(\nu_{ji}) = \frac{h\nu_{ji}}{4\pi} n_i B_{ij} \left(1 - \frac{n_j B_{ji}}{n_i B_{ij}} \right) \phi(\nu_{ji}), \quad (\text{B.2})$$

and since $g_i B_{ij} = g_j B_{ji}$, where g_i and g_j are the statistical weights of the two

levels:

$$\kappa(\nu_{ji}) = \frac{h\nu_{ji}}{4\pi} n_i B_{ij} \left(1 - \frac{n_j g_i}{n_i g_j} \right) \phi(\nu_{ji}). \quad (\text{B.3})$$

For a system in local thermodynamic equilibrium (LTE), the excitation of the particles is dominated by collisions, and the energy level populations are determined by the Boltzmann distribution, characterised by the excitation temperature T_{ex} :

$$\frac{n_j g_i}{n_i g_j} = e^{-h\nu_{ji}/k_{\text{B}}T_{\text{ex}}}, \quad (\text{B.4})$$

and so under the assumption that LTE applies, the absorption coefficient may be re-written as:

$$\kappa(\nu_{ji}) = \frac{h\nu_{ji}}{4\pi} n_i B_{ij} (1 - e^{-h\nu_{ji}/k_{\text{B}}T_{\text{ex}}}) \phi(\nu_{ji}). \quad (\text{B.5})$$

The Einstein A and B coefficients for spontaneous and stimulated emission are related by:

$$A_{ji} = \frac{2h\nu_{ji}^3}{c^2} B_{ji} = \frac{g_i}{g_j} B_{ij} \frac{2h\nu_{ji}^3}{c^2}, \quad (\text{B.6})$$

thus:

$$B_{ij} = \frac{g_j}{g_i} \frac{c^2}{2h\nu_{ji}^3} A_{ji}, \quad (\text{B.7})$$

from which the absorption coefficient can be re-stated as:

$$\kappa(\nu_{ji}) = \frac{c^2}{8\pi} \frac{g_j}{g_i} n_i \frac{A_{ji}}{\nu_{ji}^2} (1 - e^{-h\nu_{ji}/k_{\text{B}}T_{\text{ex}}}) \phi(\nu_{ji}). \quad (\text{B.8})$$

Generally where the total number of particles is n :

$$\frac{n_i}{n} = \frac{g_i}{Z} e^{-h\nu_{i0}/k_{\text{B}}T_{\text{ex}}}, \quad (\text{B.9})$$

for which Z is the partition function:

$$Z = \sum_{J=0}^{\infty} (2J+1) e^{-hBJ(J+1)/k_B T_{\text{ex}}}, \quad (\text{B.10})$$

where the substitution $\nu_{J0} = BJ(J+1)$ has been made. $B = h/8\pi^2 I$ is the rotation constant and I is the moment of inertia of the molecule. For $hB \ll k_B T_{\text{ex}}$, the expression for Z can be approximated by:

$$Z \approx \frac{k_B}{hB} \left(T_{\text{ex}} + \frac{hB}{3k_B} \right), \quad (\text{B.11})$$

assuming that the excitation temperature is the same for all transitions.

It is now possible to substitute for $n_i g_j / g_i$ in Equation B.8 from Equation B.9:

$$n_i \frac{g_j}{g_i} = \frac{g_j}{g_i} \frac{g_i}{Z} n e^{-h\nu_{i0}/k_B T_{\text{ex}}}, \quad (\text{B.12})$$

and Equation B.8 becomes:

$$\kappa(\nu_{ji}) = \frac{c^2}{8\pi} g_j \frac{1}{Z} e^{-h\nu_{i0}/k_B T_{\text{ex}}} \frac{A_{ji}}{\nu_{ji}^2} (1 - e^{-h\nu_{ji}/k_B T_{\text{ex}}}) n \phi(\nu_{ji}). \quad (\text{B.13})$$

The optical depth of the radiation is defined as:

$$d\tau(\nu) = \kappa(\nu) dx, \quad (\text{B.14})$$

and:

$$\tau(\nu) = \int \kappa(\nu) dx \approx \kappa(\nu) L, \quad (\text{B.15})$$

where L is the extent of the emission region along the line of sight. The optical

depth can now be written as:

$$\tau(\nu_{ji}) \approx \frac{c^2}{8\pi} g_j \frac{1}{Z} e^{-h\nu_{i0}/k_B T_{\text{ex}}} \frac{A_{ji}}{\nu_{ji}^2} (1 - e^{-h\nu_{ji}/k_B T_{\text{ex}}}) \phi(\nu_{ji}) N, \quad (\text{B.16})$$

where $N = nL$ is the column density of material contributing to the line emission.

By substituting $g_j = 2j + 1$ and $\nu_{i0} = Bi(i + 1)$, this becomes:

$$\tau(\nu_{ji}) = \frac{c^2}{8\pi} (2j + 1) \frac{1}{Z} e^{-hBi(i+1)/k_B T_{\text{ex}}} \frac{A_{ji}}{\nu_{ji}^2} (1 - e^{-h\nu_{ji}/k_B T_{\text{ex}}}) \phi(\nu_{ji}) N. \quad (\text{B.17})$$

Substituting for A_{ji} :

$$A_{ji} = \frac{16\pi^3}{3\epsilon_0 h c^3} \nu_{ji}^3 |\mu_{ij}|^2, \quad (\text{B.18})$$

where $|\mu_{ij}|^2$ is the dipole moment matrix element for the transition, summed over the three perpendicular directions in space. It can be shown that $|\mu_{ij}|^2 = \mu^2 j/(2i + 3)$ for $j \rightarrow i$, $j = i + 1$ where $2i + 3 = 2j + 1$ (Townes & Schawlow, 1955) and μ is the dipole moment of the molecule. Thus:

$$\tau(\nu_{ji}) = \frac{2\pi^2}{3\epsilon_0 h c} \frac{j}{Z} e^{-hBi(i+1)/k_B T_{\text{ex}}} \nu_{ji} \mu^2 (1 - e^{-h\nu_{ji}/k_B T_{\text{ex}}}) \phi(\nu_{ji}) N. \quad (\text{B.19})$$

In order to obtain an expression for the peak line optical depth, we can approximate $\int \tau(\nu) d\nu \approx \tau_0 \Delta\nu$, where τ_0 is the peak optical depth and $\Delta\nu = \sqrt{\pi/(4 \ln 2)} \times \text{FWHM} = 1.064 \times \text{FWHM}$ for a Gaussian line. For a Doppler broadened line, $\text{FWHM} = \Delta\nu = \nu_{ji} v/c$, where v is the velocity.

Therefore, for the $J = 3 \rightarrow 2$ and $J = 1 \rightarrow 0$ transitions, the optical depths from equation B.19 are:

$$\tau(\nu_{32}) = \frac{2\pi^2}{3\epsilon_0 h c} \frac{3}{Z} e^{-6hB/k_B T_{\text{ex}}} \frac{c}{v} \mu^2 (1 - e^{-h\nu_{32}/k_B T_{\text{ex}}}) N, \quad (\text{B.20})$$

and:

$$\tau(\nu_{10}) = \frac{2\pi^2}{3\epsilon_0 hc Z} e^{-hB \times 0 / k_B T_{\text{ex}}} \frac{c}{v} \mu^2 (1 - e^{-h\nu_{10}/k_B T_{\text{ex}}}) N. \quad (\text{B.21})$$

Hence the ratio of optical depths is:

$$\frac{\tau(\nu_{32})}{\tau(\nu_{10})} = 3 \frac{(1/Z)}{(1/Z)} e^{-6hB/k_B T_{\text{ex}}} \frac{(c/v)\mu^2}{(c/v)\mu^2} \left(\frac{1 - e^{-h\nu_{32}/k_B T_{\text{ex}}}}{1 - e^{-h\nu_{10}/k_B T_{\text{ex}}}} \right) \frac{N}{N}. \quad (\text{B.22})$$

Assuming that both the line shape and excitation temperature are the same for both transitions, Equation B.22 reduces to become:

$$\frac{\tau(\nu_{32})}{\tau(\nu_{10})} = 3e^{-6hB/k_B T_{\text{ex}}} \left(\frac{1 - e^{-h\nu_{32}/k_B T_{\text{ex}}}}{1 - e^{-h\nu_{10}/k_B T_{\text{ex}}}} \right), \quad (\text{B.23})$$

and with $B = \nu_{10}/2$, this becomes:

$$\frac{\tau(\nu_{32})}{\tau(\nu_{10})} = 3e^{-3h\nu_{10}/k_B T_{\text{ex}}} \left(\frac{1 - e^{-h\nu_{32}/k_B T_{\text{ex}}}}{1 - e^{-h\nu_{10}/k_B T_{\text{ex}}}} \right). \quad (\text{B.24})$$

The radiation temperature is given by:

$$T_R = \frac{c^2}{2k\nu^2} (I_\nu - I_{bg}), \quad (\text{B.25})$$

where I_{bg} is the intensity of the microwave background at the frequency of the line and:

$$I_\nu = \frac{2h\nu^3}{c^2} \frac{1}{e^{h\nu/k_B T_{\text{ex}}} - 1} (1 - e^{-\tau(\nu)}), \quad (\text{B.26})$$

hence:

$$T_R = \frac{h\nu}{k} \left(\frac{1}{e^{h\nu/k_B T_{\text{ex}}} - 1} - \frac{1}{e^{h\nu/k T_{bg}} - 1} \right) (1 - e^{-\tau(\nu)}). \quad (\text{B.27})$$

The radiation temperature ratio for $J = 3-2$ and $J = 1-0$ emission for the

same species is therefore:

$$\frac{T_{R_{32}}}{T_{R_{10}}} = \frac{1 - e^{-\tau_{32}}}{1 - e^{-\tau_{10}}} \frac{\nu_{32}}{\nu_{10}} \frac{(e^{h\nu_{32}/k_B T_{\text{ex}}} - 1)^{-1} - T_{\text{bg}32}}{(e^{h\nu_{10}/k_B T_{\text{ex}}} - 1)^{-1} - T_{\text{bg}10}}, \quad (\text{B.28})$$

where:

$$T_{\text{bg}32} = \frac{1}{e^{(h\nu_{32}/k_B T_{\text{bg}})} - 1}, \quad (\text{B.29})$$

and:

$$T_{\text{bg}10} = \frac{1}{e^{(h\nu_{10}/k_B T_{\text{bg}})} - 1}. \quad (\text{B.30})$$

From Equation B.17, an expression for the column density of gas emitting in the measured lines can be obtained in terms of the excitation temperature:

$$N_{ji} = \frac{8\pi}{c^2(2j+1)} Z e^{hBi(i+1)/k_B T_{\text{ex}}} \frac{\nu_{ji}^2}{A_{ji}} \left(\frac{1}{1 - e^{-h\nu_{ji}/k_B T_{\text{ex}}}} \right) \int \tau(\nu_{ji}) d\nu. \quad (\text{B.31})$$

By substituting Equation B.18 into Equation B.31:

$$N_{ji} = \frac{3\epsilon_0 hc}{2\pi\nu_{ji}\mu^2 j} Z e^{hBi(i+1)/k_B T_{\text{ex}}} \left(\frac{1}{1 - e^{-h\nu_{ji}/k_B T_{\text{ex}}}} \right) \int \tau(\nu_{ji}) d\nu, \quad (\text{B.32})$$

and correcting for the optical depth by introducing the multiplicative factor $\tau/(1 - e^{-\tau})$, and re-writing in terms of the velocity:

$$\begin{aligned} \int \tau(\nu) d\nu &= \int T_R(\nu) d\nu \frac{1}{J(T_{\text{ex}})} \frac{\tau}{1 - e^{-\tau}} \\ &= \frac{1}{J(T_{\text{ex}})} \frac{\tau}{1 - e^{-\tau}} \frac{\nu_{ji}}{c} \int T_R(v) dv, \end{aligned} \quad (\text{B.33})$$

where:

$$J(T_{\text{ex}}) = \frac{h\nu}{k} \left(\frac{1}{e^{h\nu/k_B T_{\text{ex}}} - 1} - \frac{1}{e^{h\nu/k_B T_{\text{bg}}} - 1} \right). \quad (\text{B.34})$$

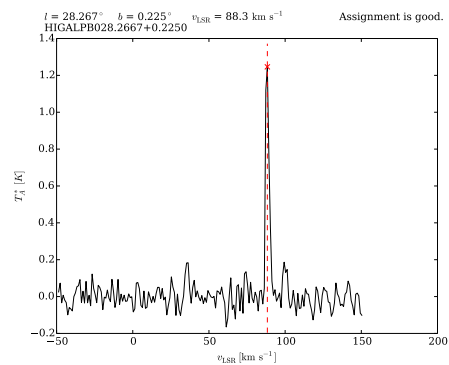
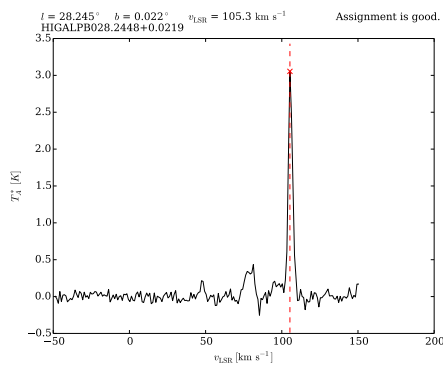
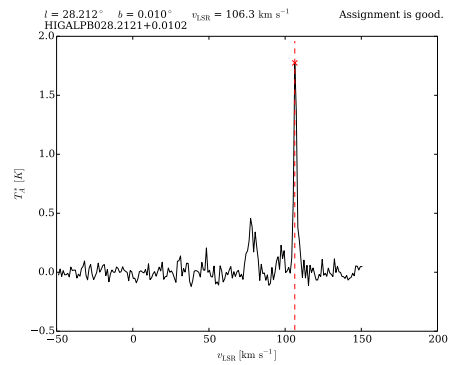
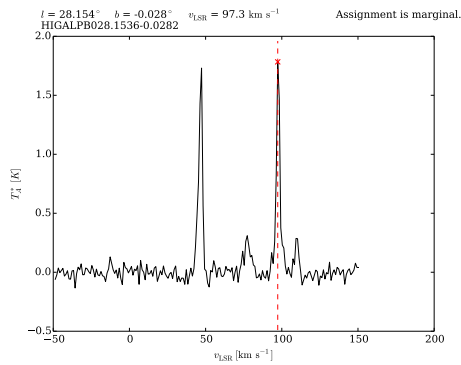
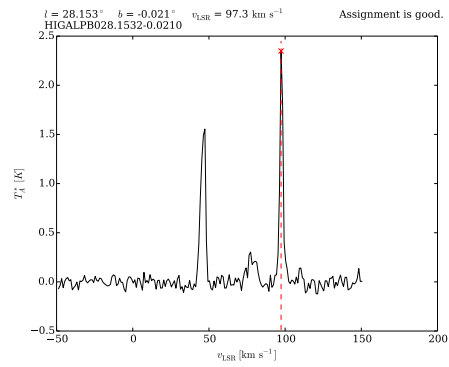
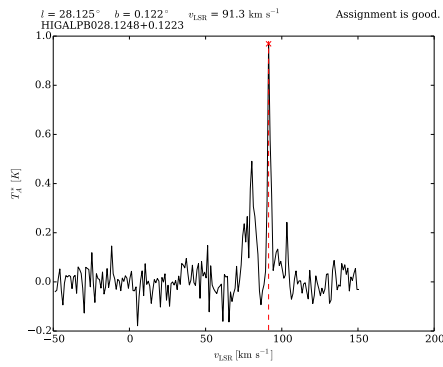
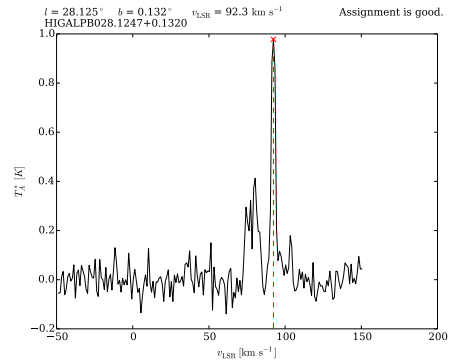
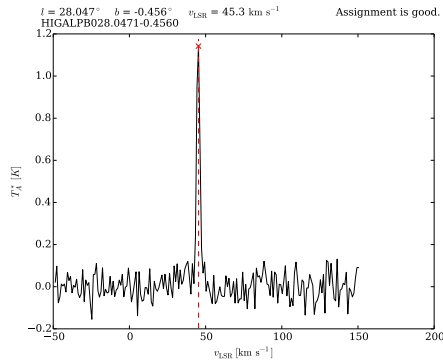
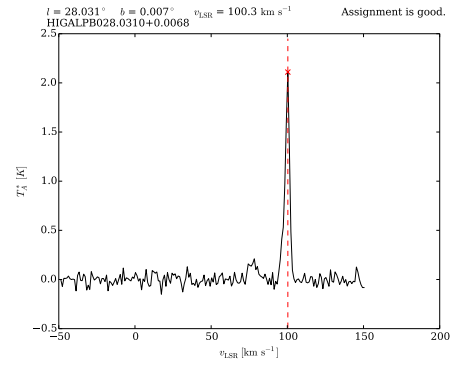
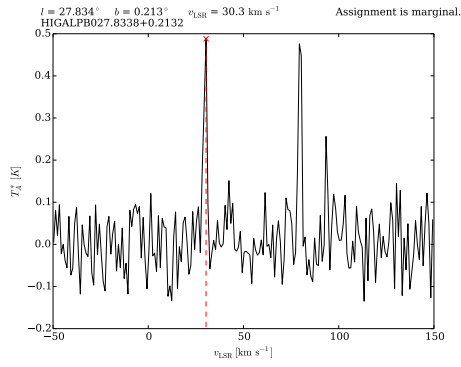
By combining Equations B.32, B.35 and B.34, the column density can now be calculated in terms of the radiation temperature, and as a function of velocity:

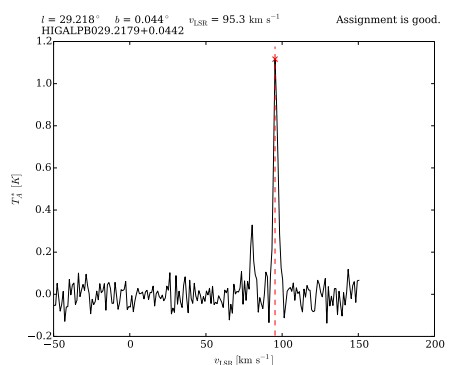
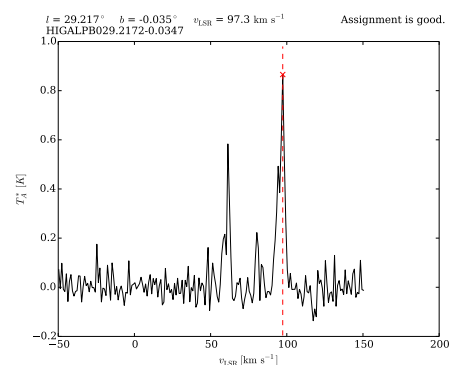
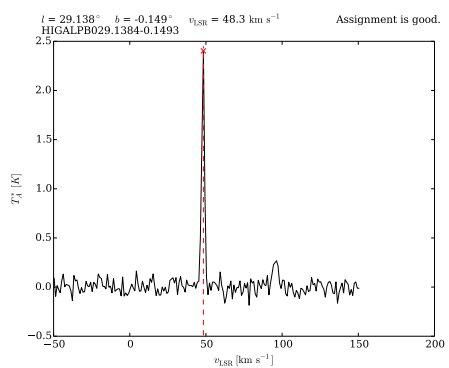
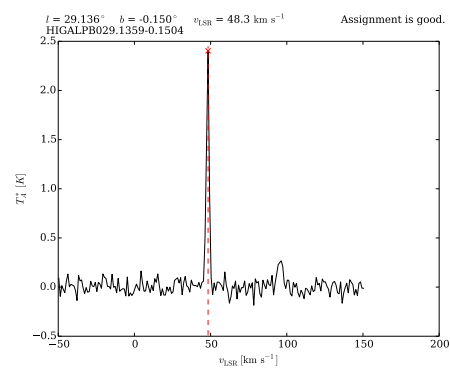
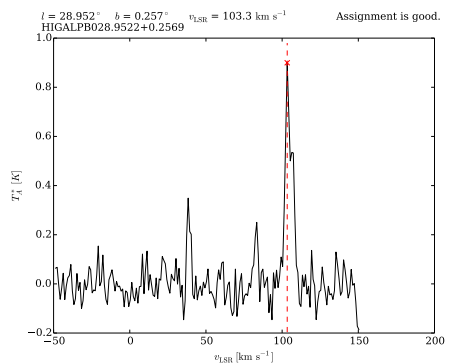
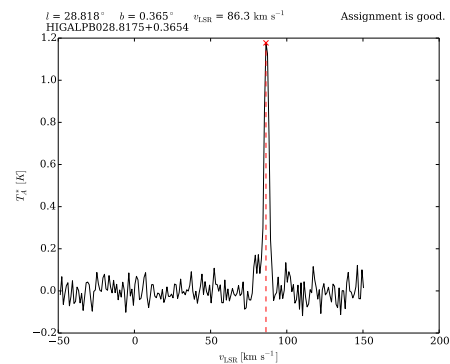
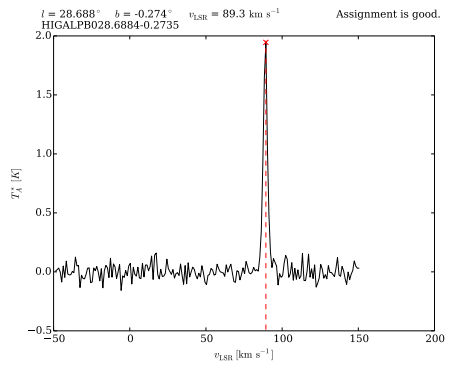
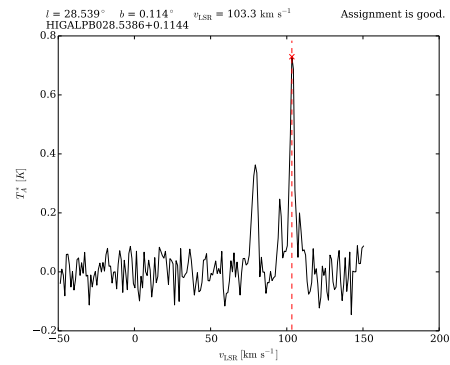
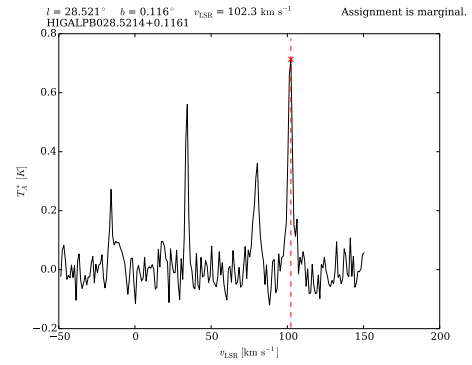
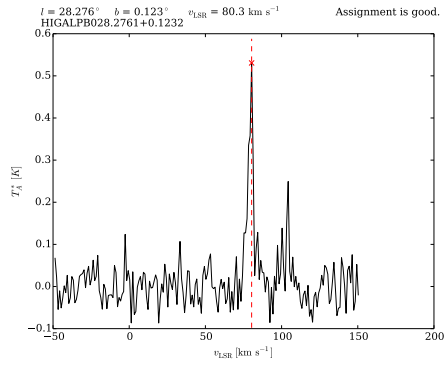
$$N_{ji} = \frac{3\epsilon_0 k_B}{2\pi\nu_{ji}\mu^2 j} Z e^{hBi(i+1)/k_B T_{\text{ex}}} \left(\frac{1}{1 - e^{-h\nu_{ji}/k_B T_{\text{ex}}}} \right) \left(\frac{1}{e^{h\nu_{ji}/k_B T_{\text{ex}}} - 1} - \frac{1}{e^{h\nu_{ji}/k_B T_{\text{bg}}} - 1} \right)^{-1} \frac{\tau}{1 - e^{-\tau}} \int T_R(v) dv. \quad (\text{B.35})$$

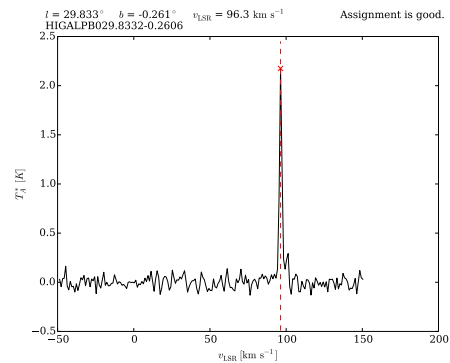
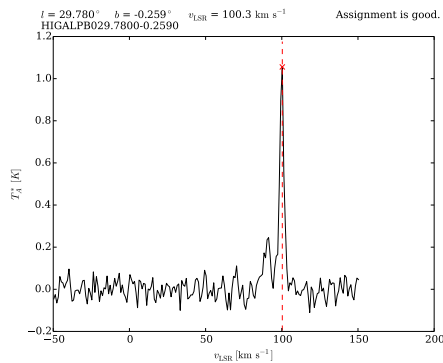
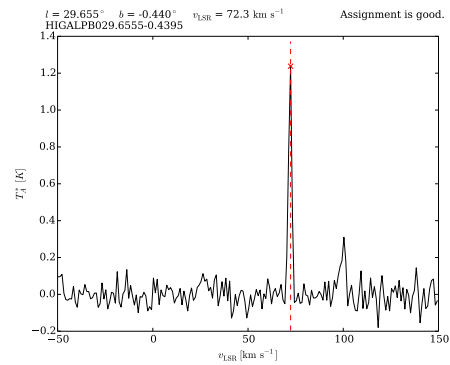
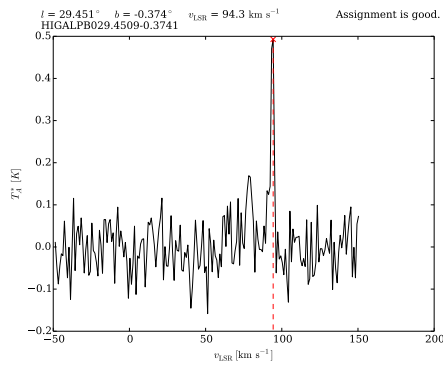
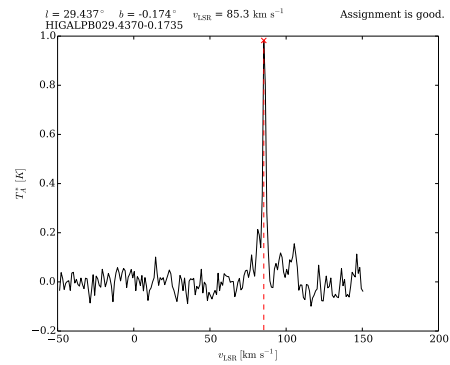
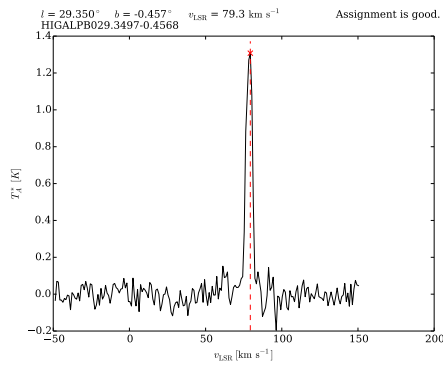
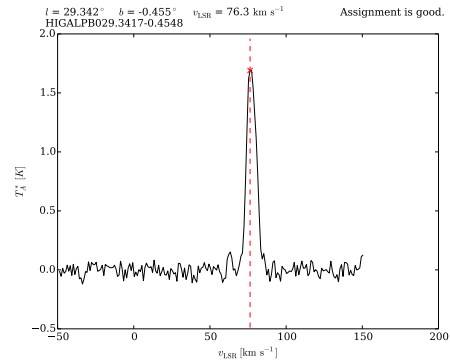
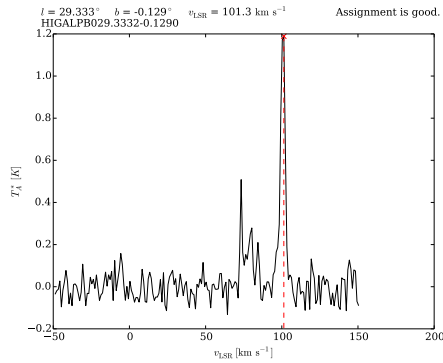
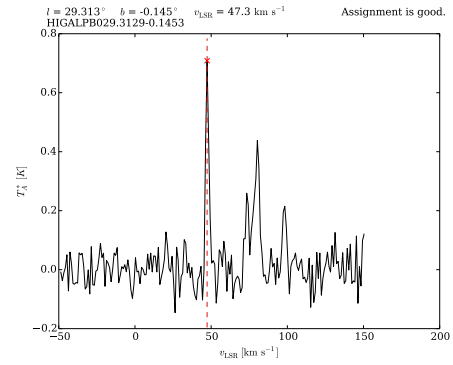
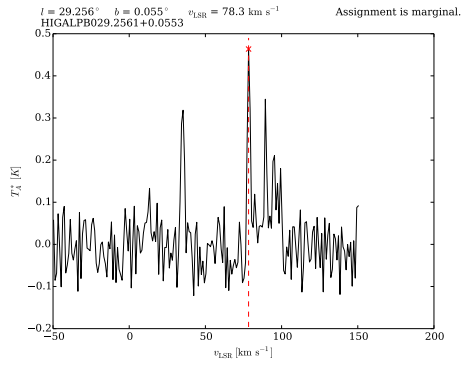
Appendix C

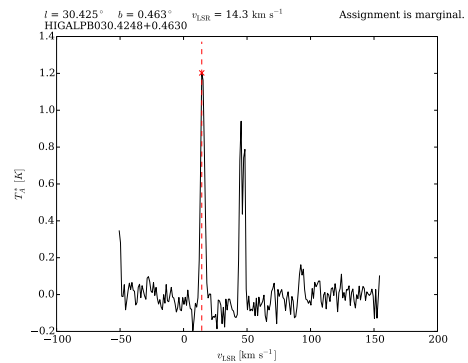
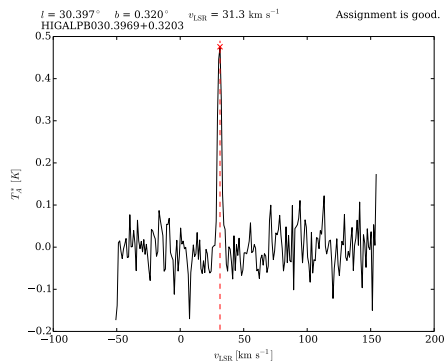
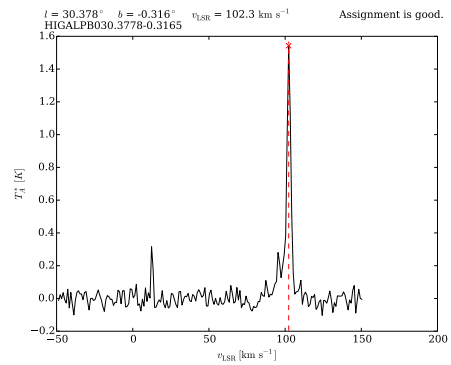
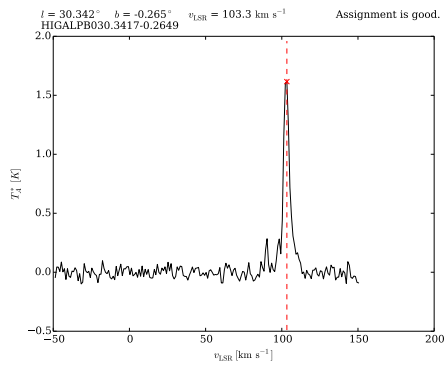
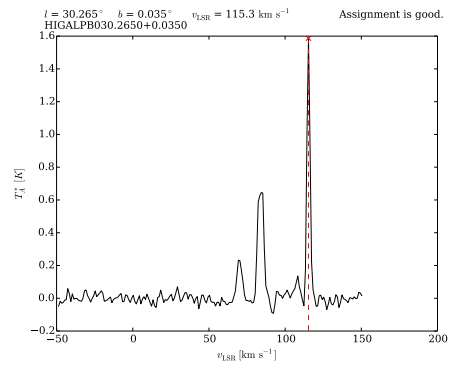
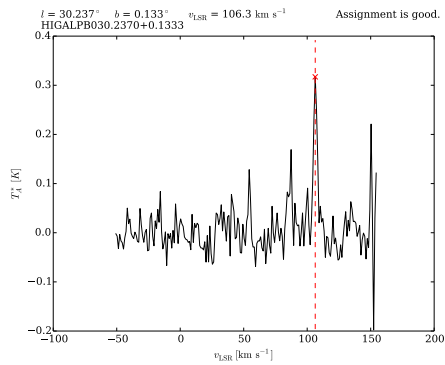
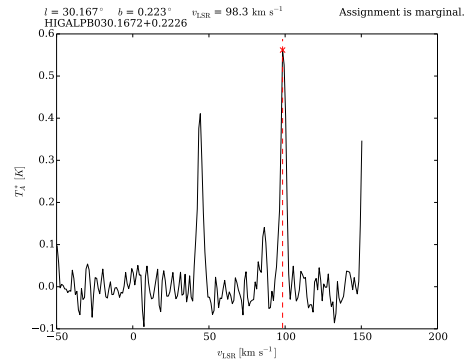
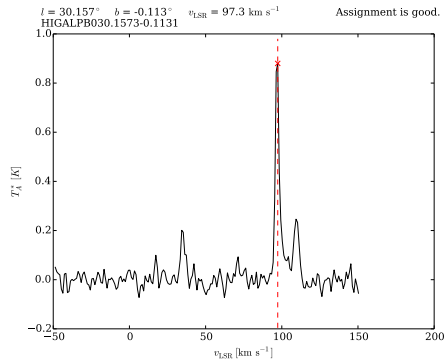
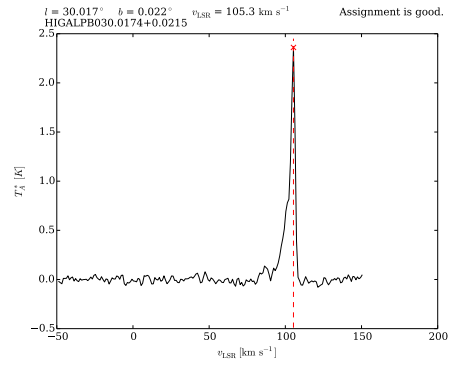
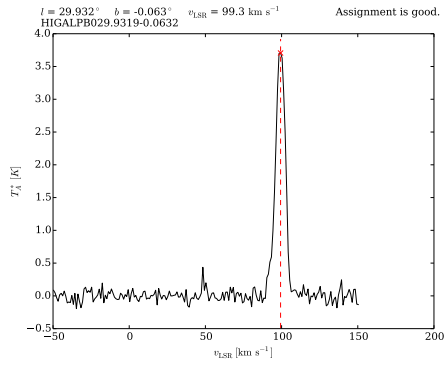
Hi-GAL 70 μm velocity assignments

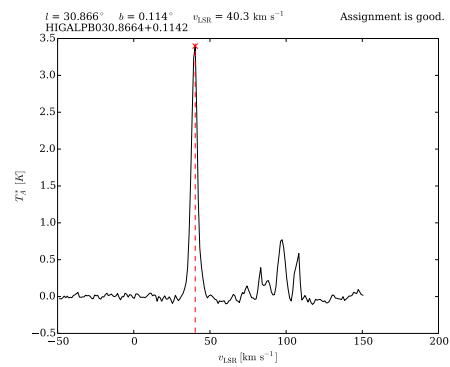
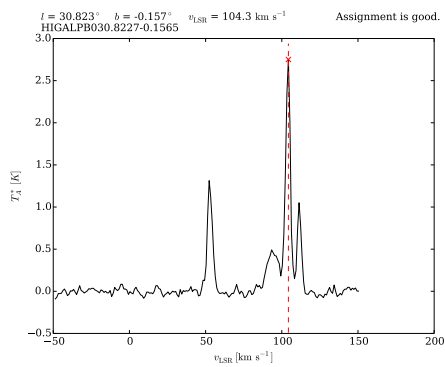
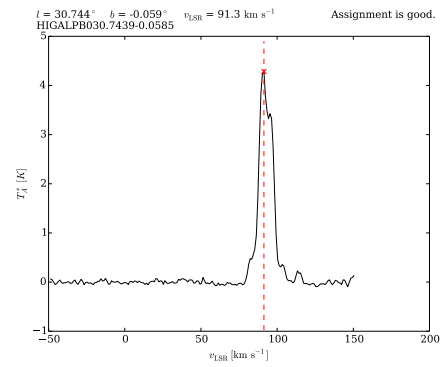
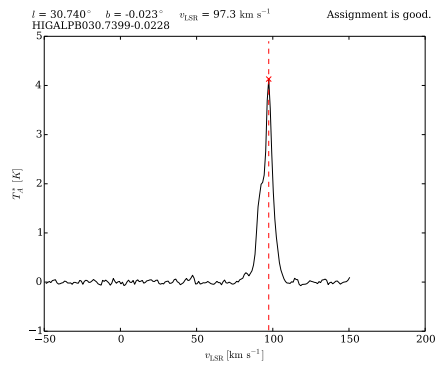
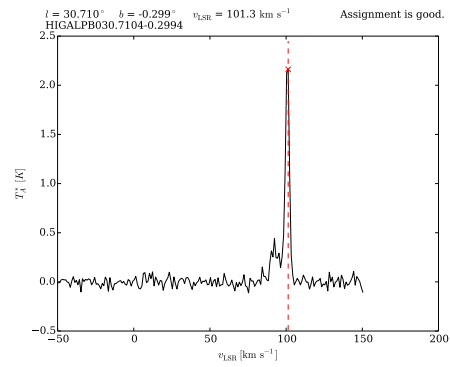
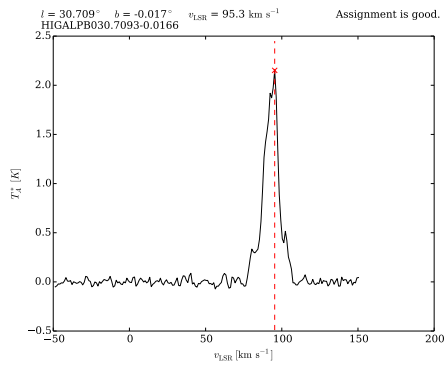
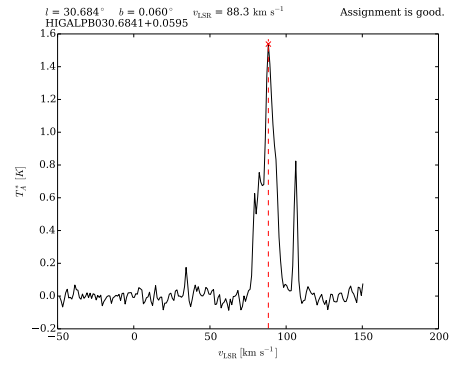
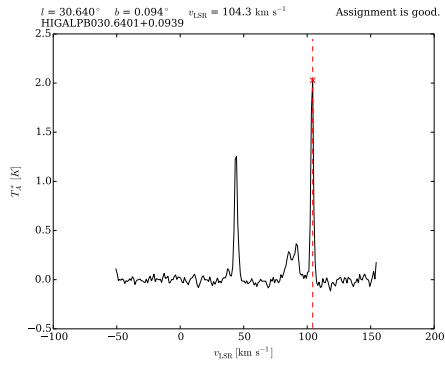
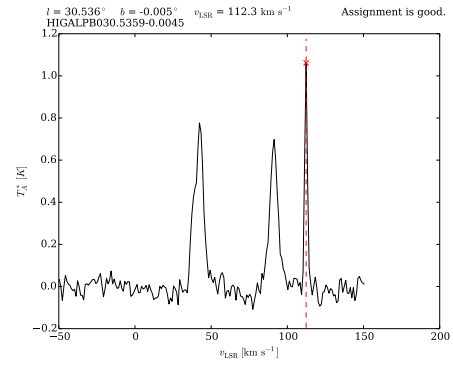
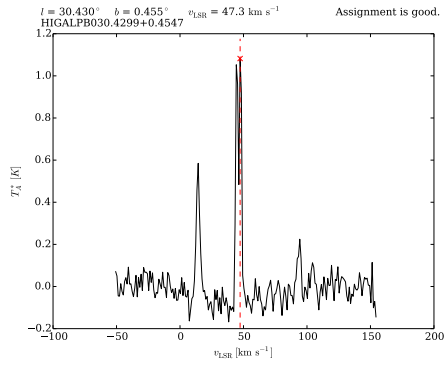
A sub-sample of ^{13}CO (3–2) spectra for 200 of the 2,031 Hi-GAL 70 μm sources associated with CHIMPS clumps in Section 5.1 are illustrated in the following pages. For each source, its centroid l and b coordinates are listed as in Molinari et al. (2016), along with its Hi-GAL designation, the v_{LSR} assigned from the CHIMPS ^{13}CO (3–2) spectrum, and a comment about the quality of the velocity assignment. Velocity assignments are graded good, marginal and poor. Assignments that were judged to be marginal were so graded because either there are multiple peaks of comparable peak T_{A}^* , or because the SNR was low.

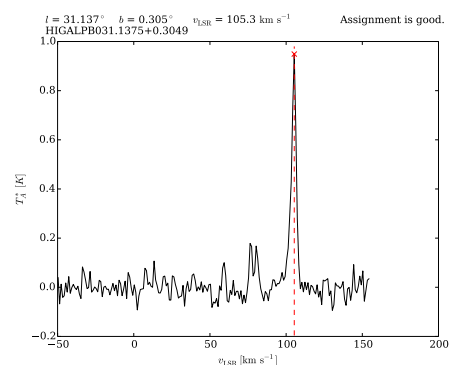
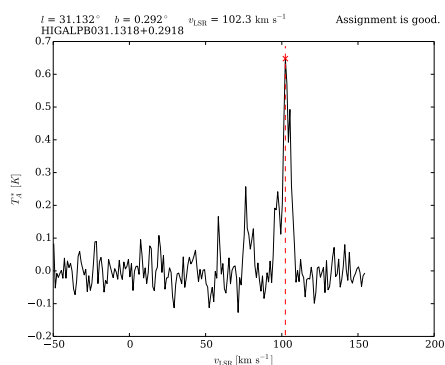
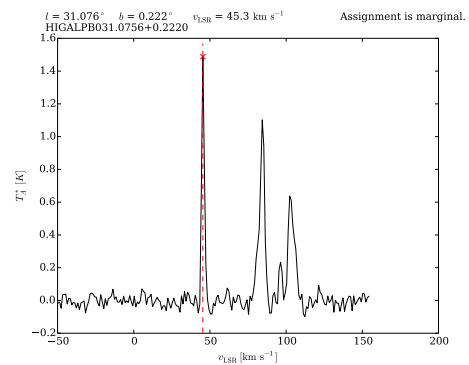
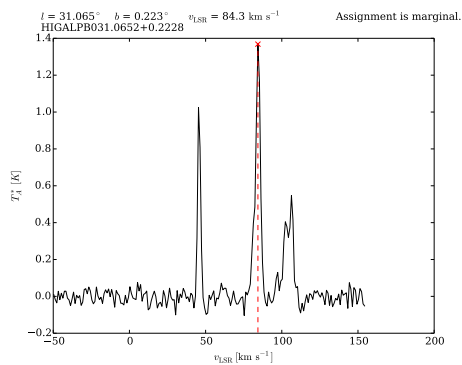
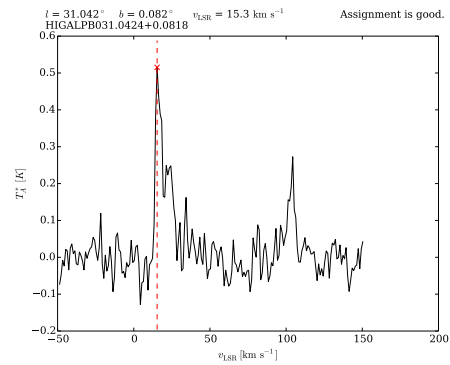
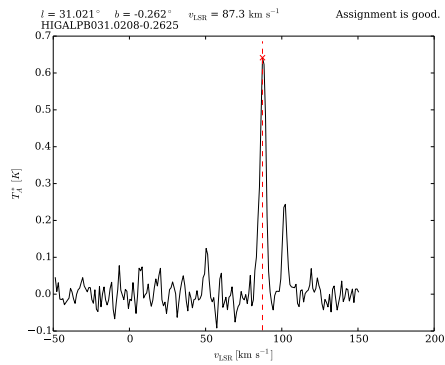
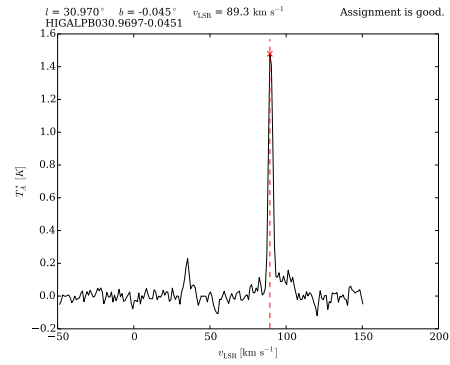
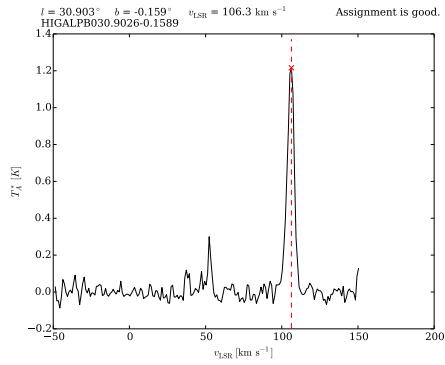
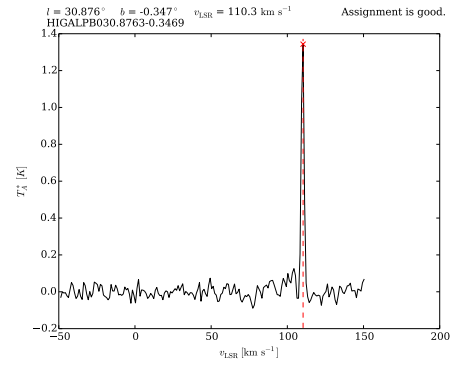
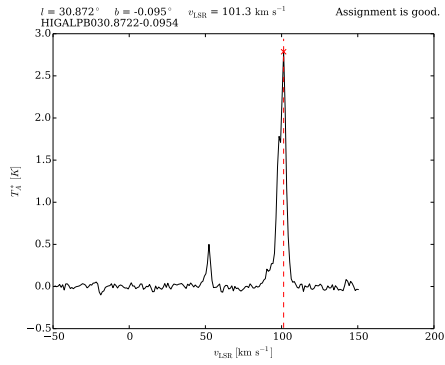


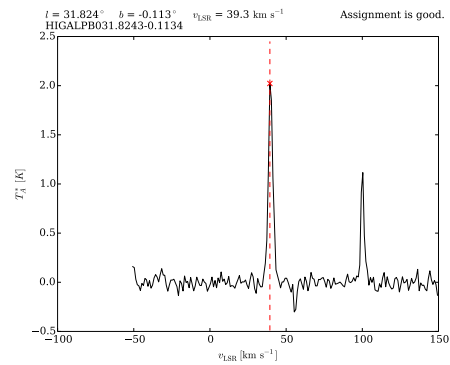
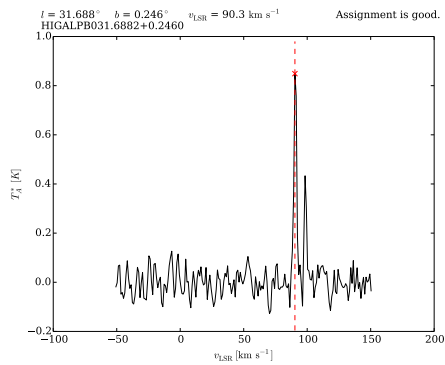
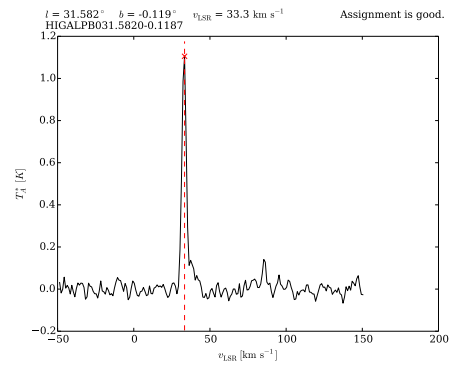
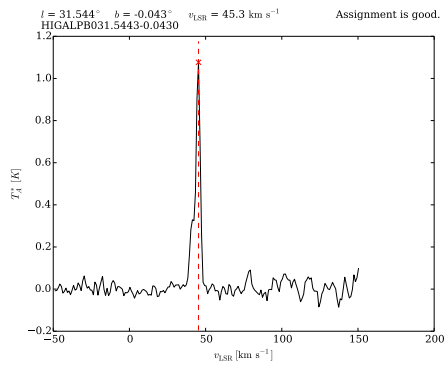
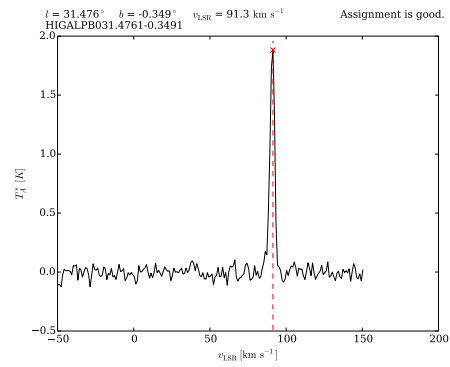
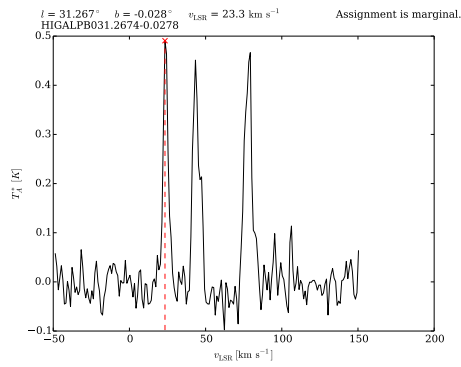
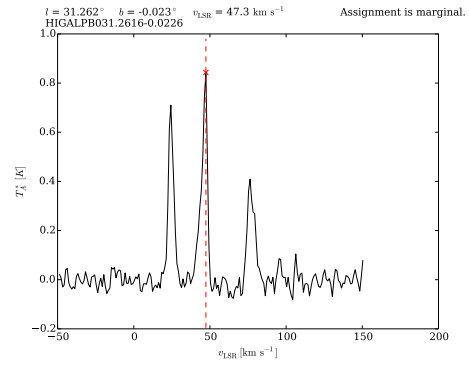
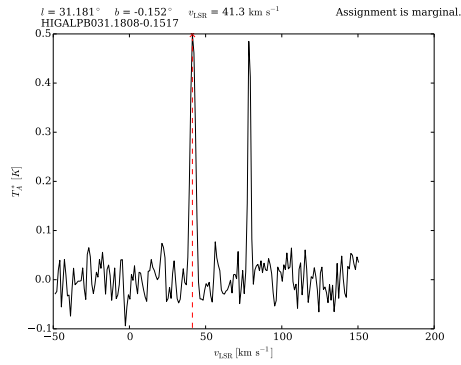
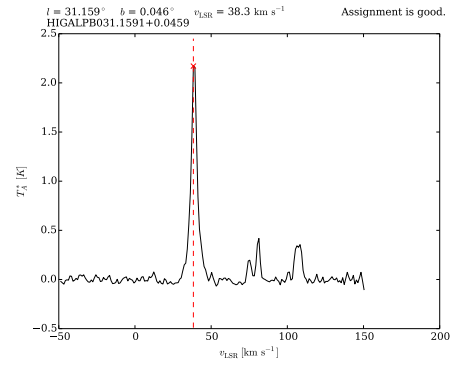
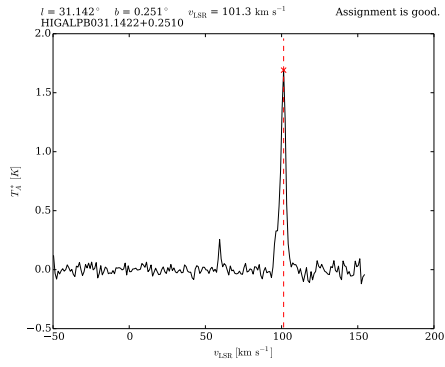


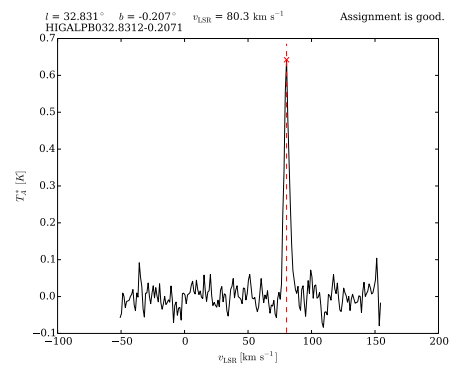
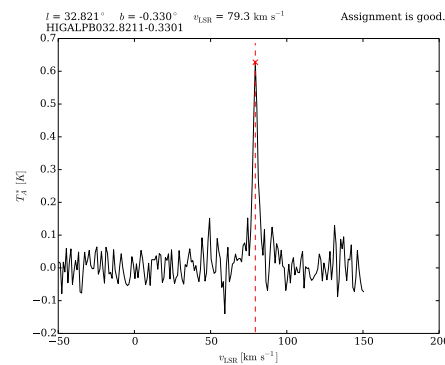
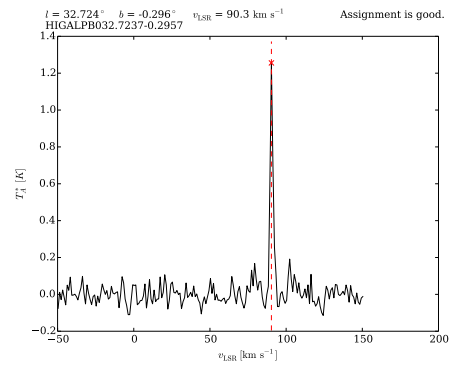
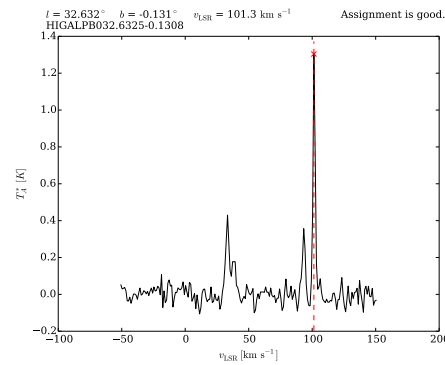
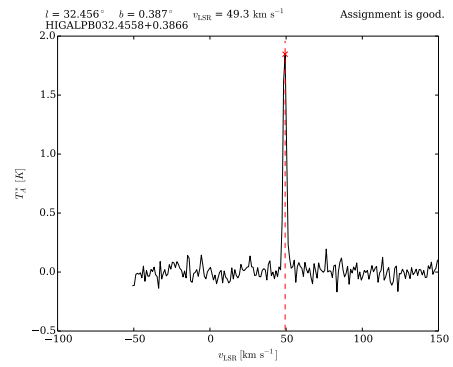
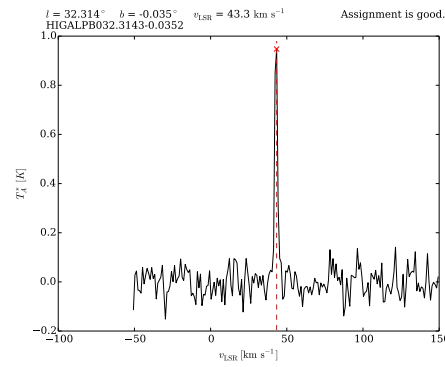
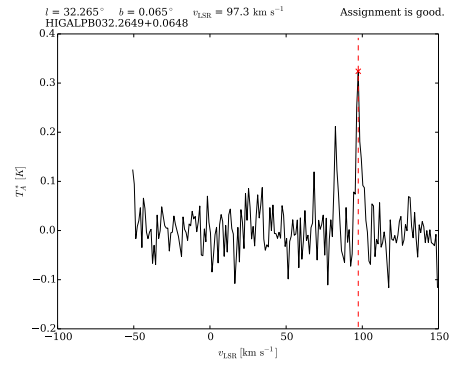
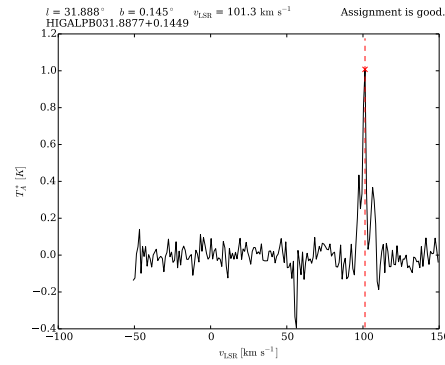
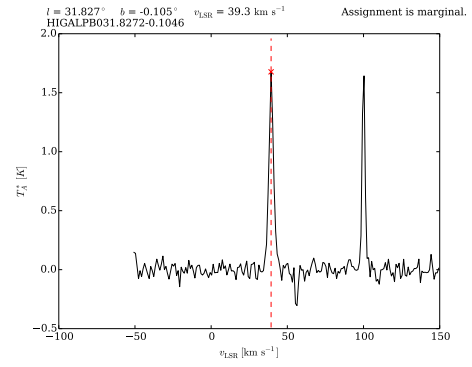
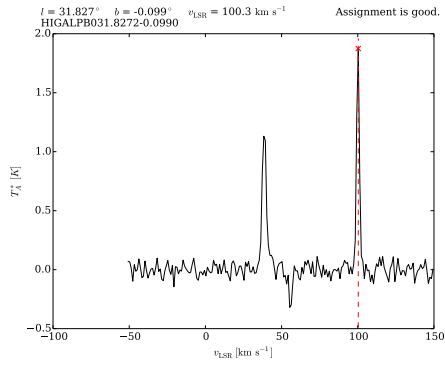


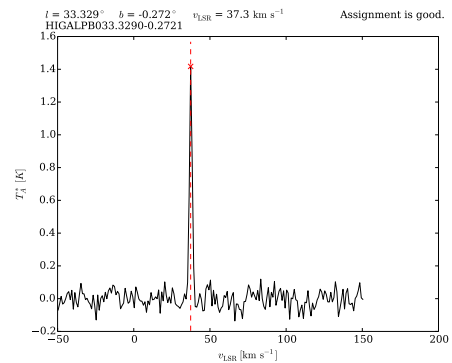
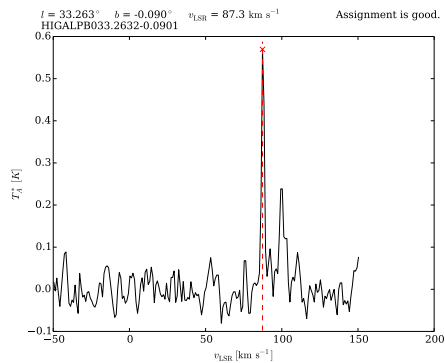
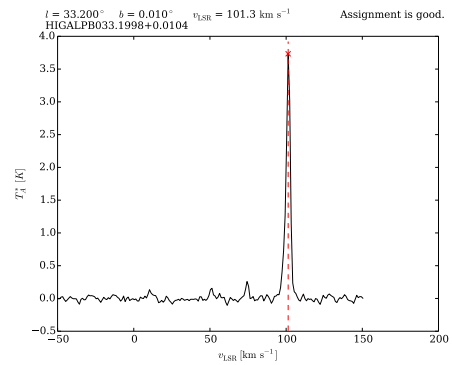
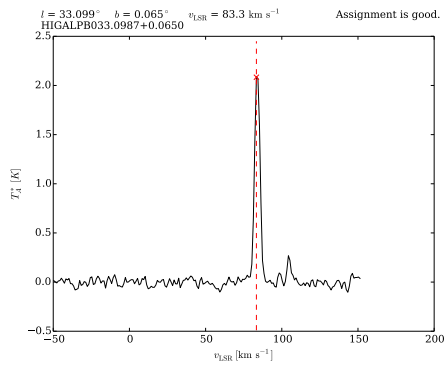
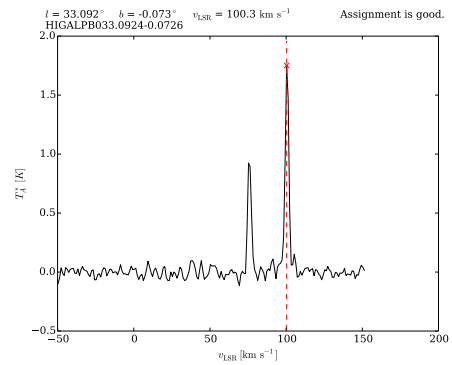
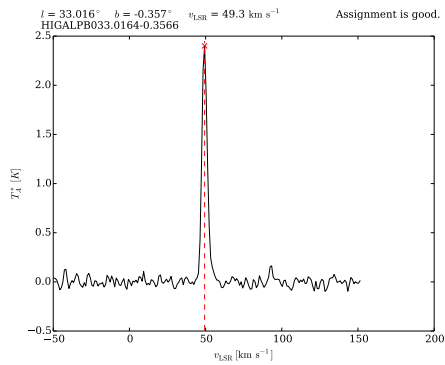
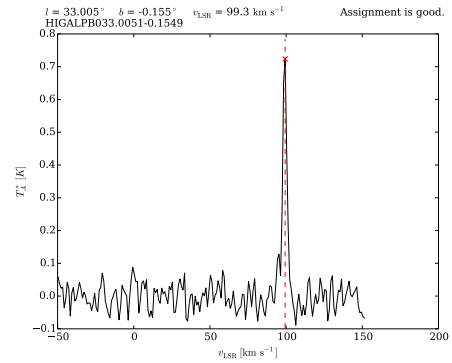
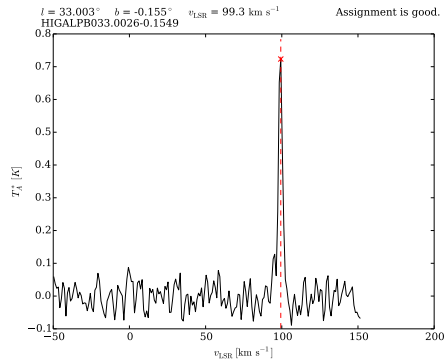
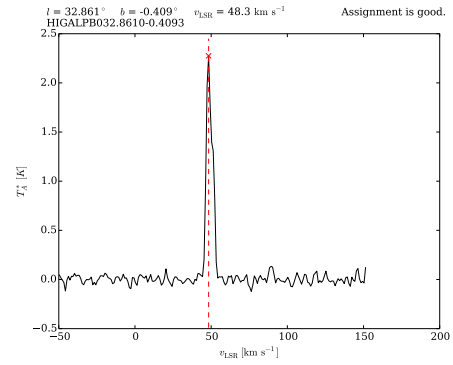
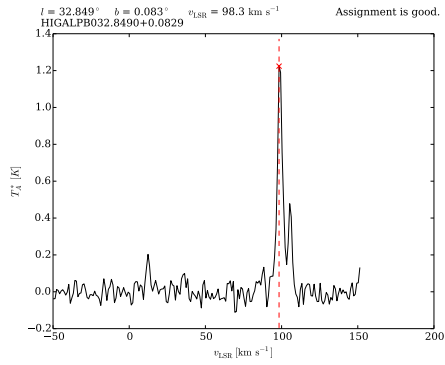


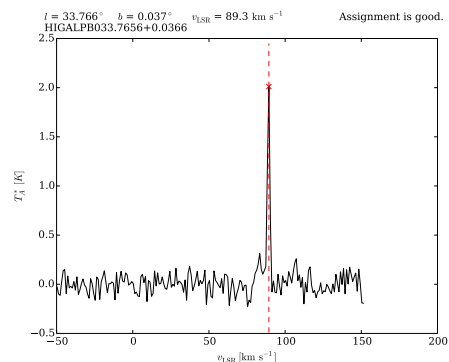
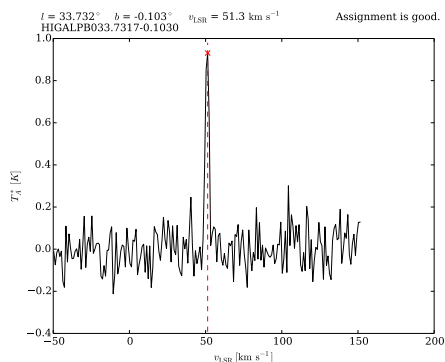
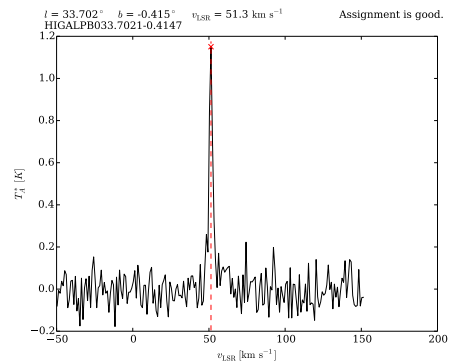
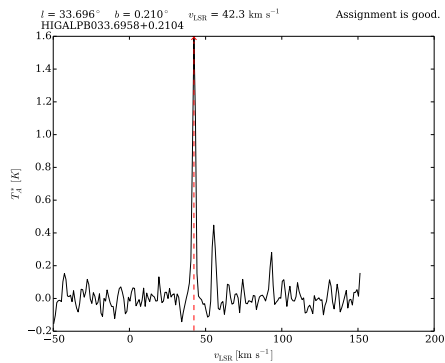
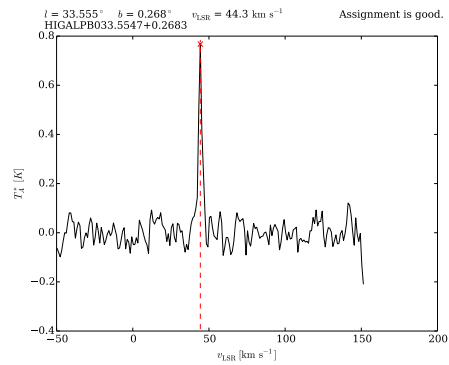
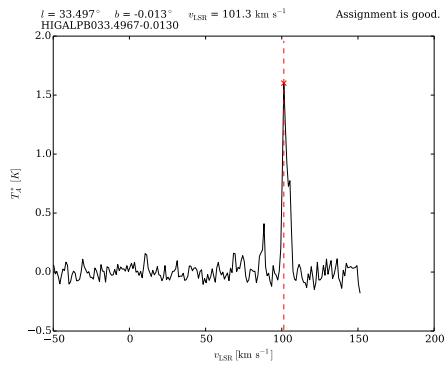
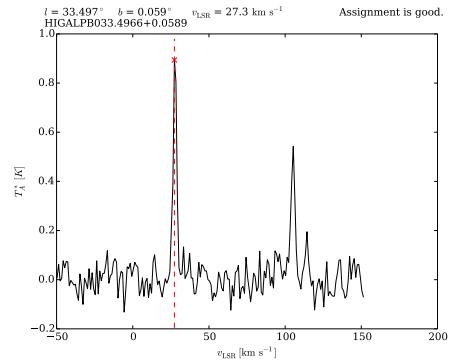
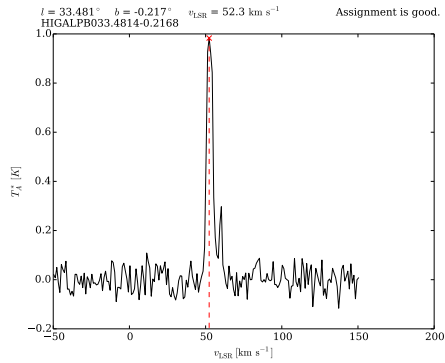
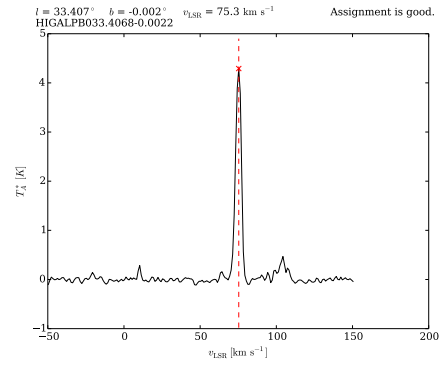
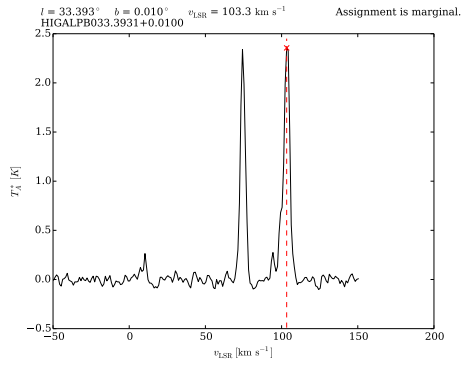


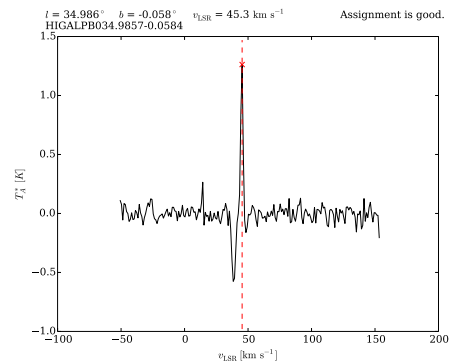
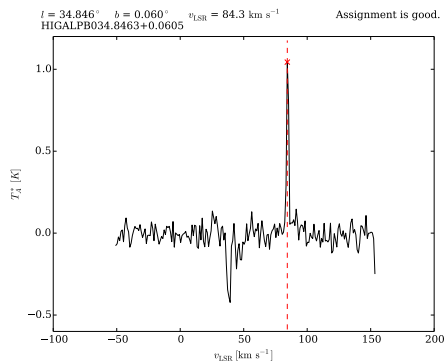
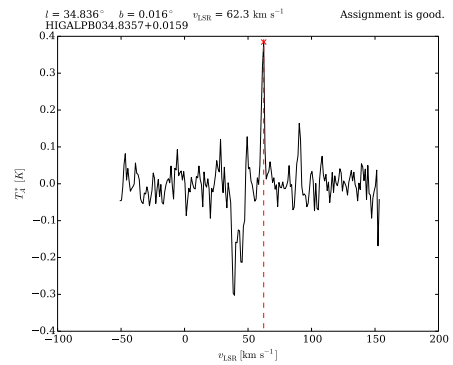
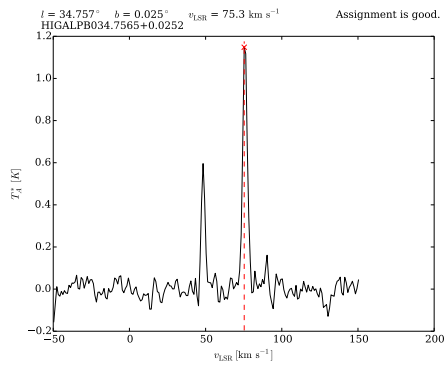
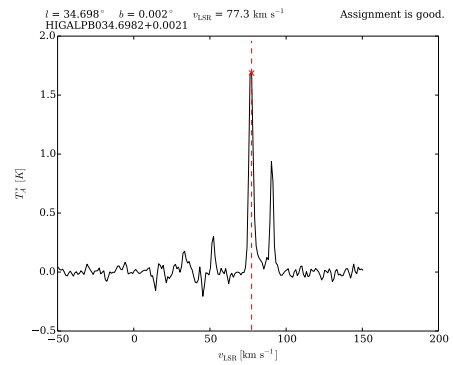
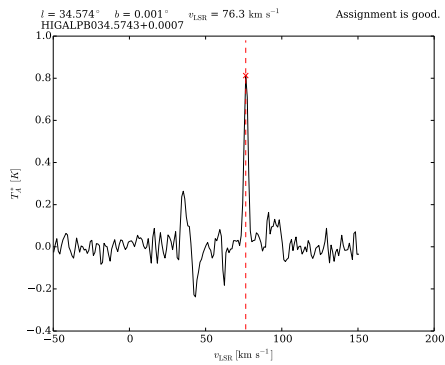
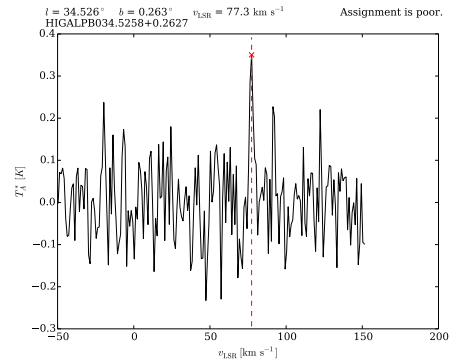
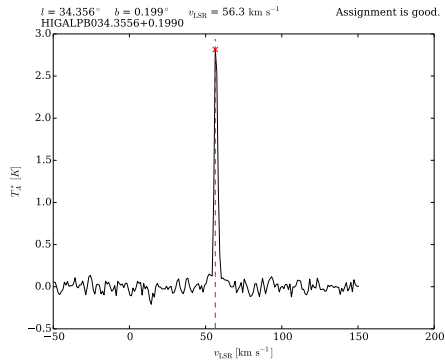
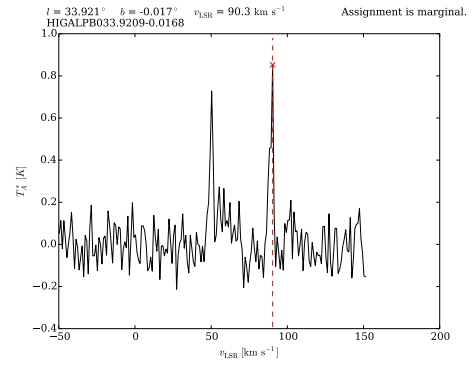
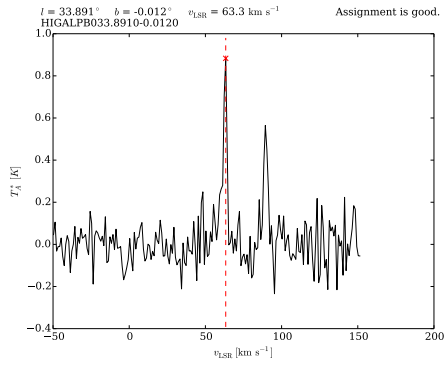


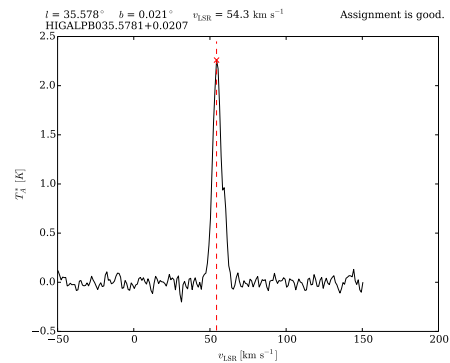
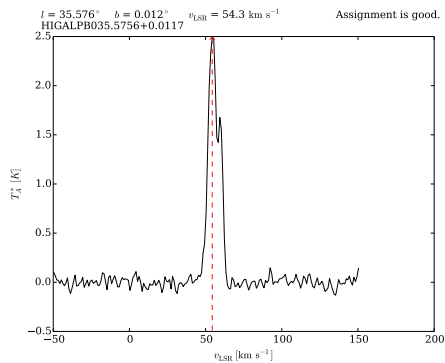
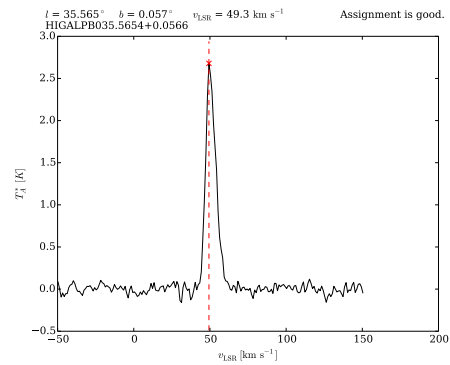
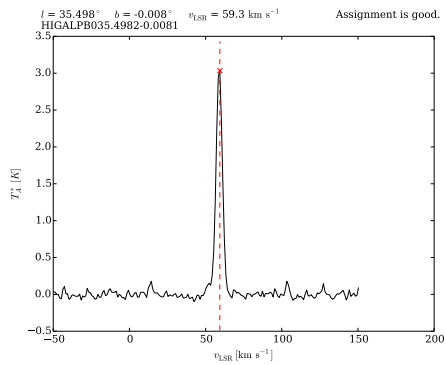
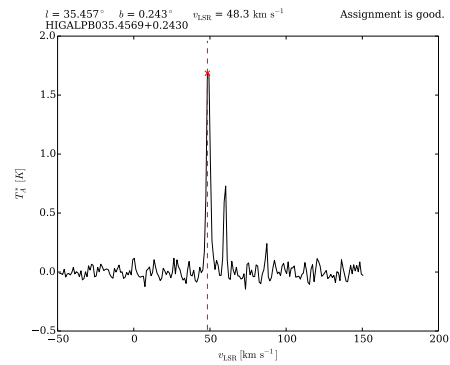
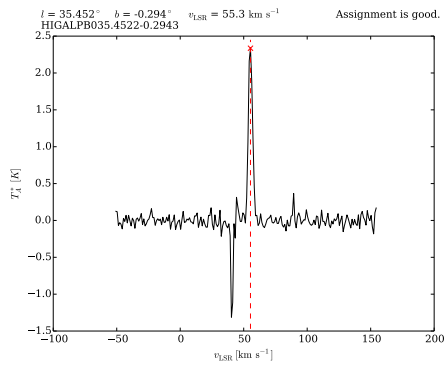
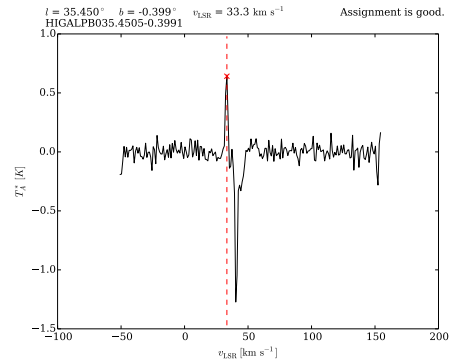
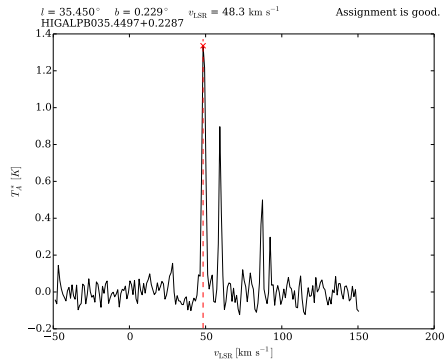
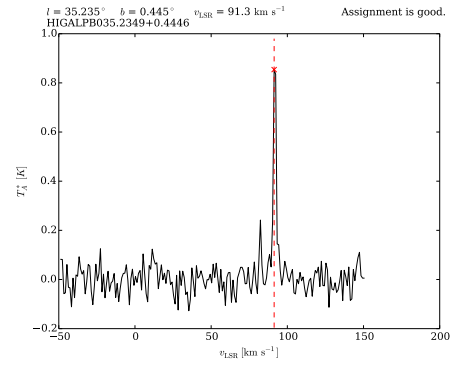
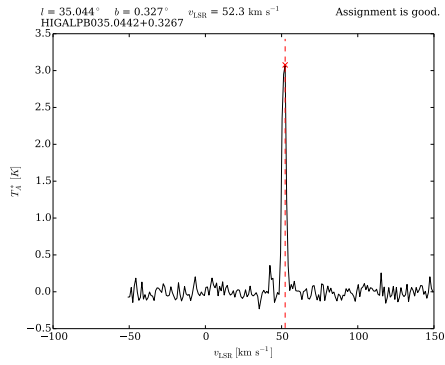


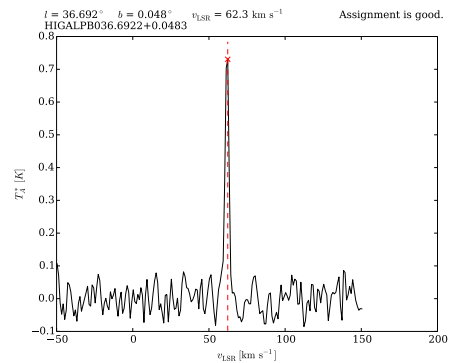
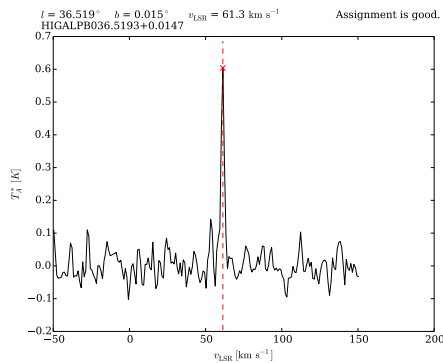
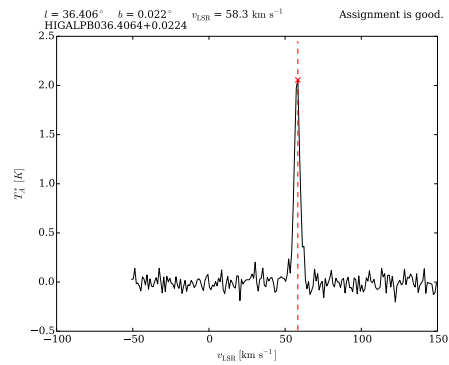
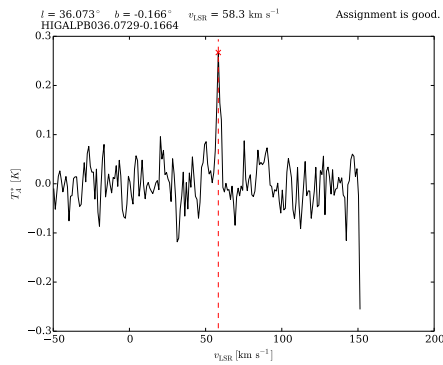
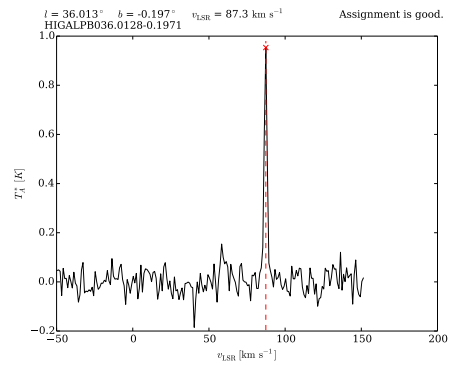
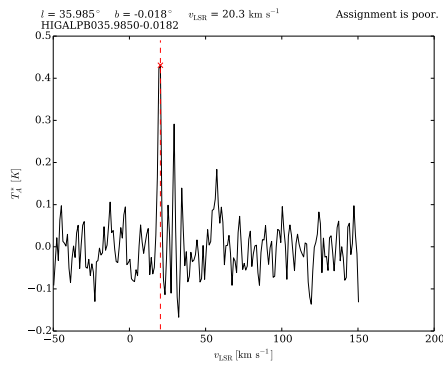
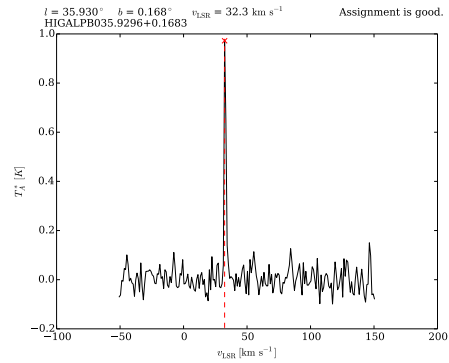
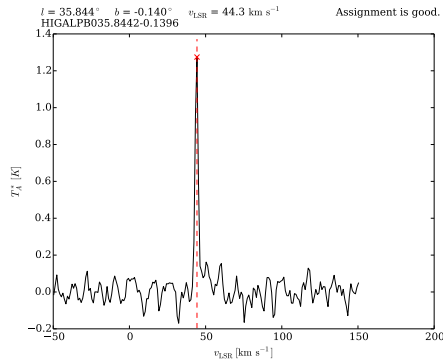
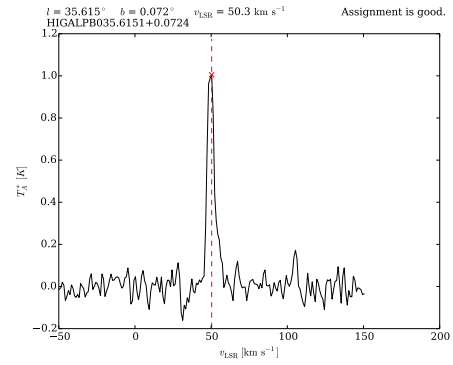
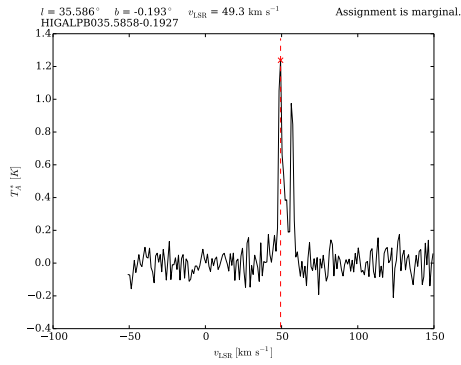


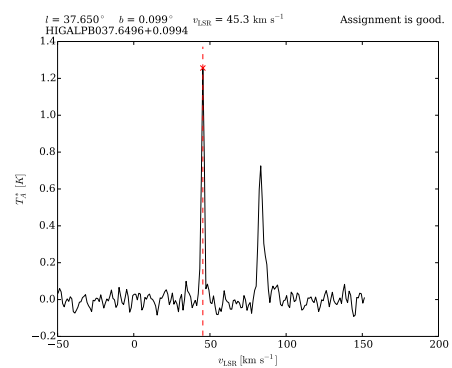
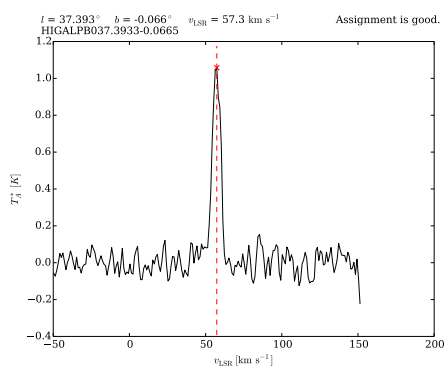
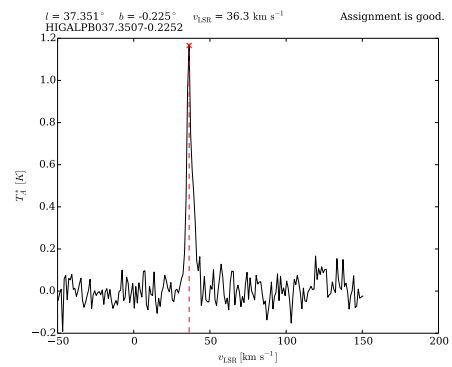
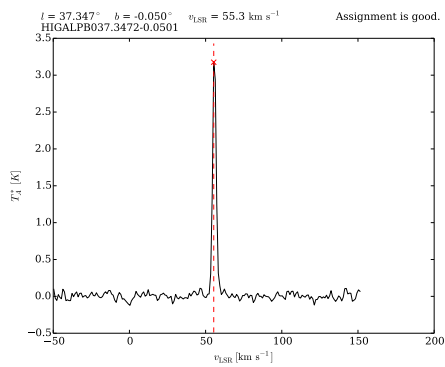
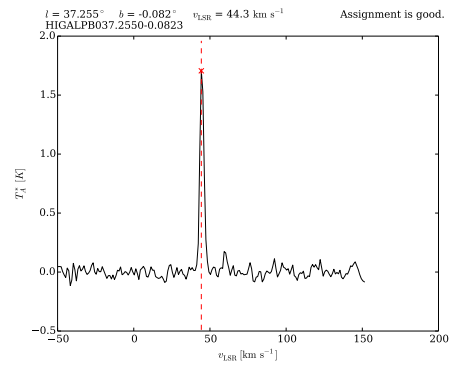
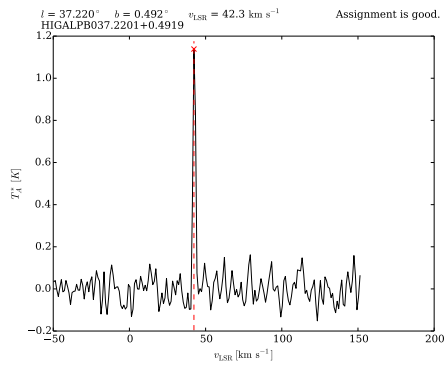
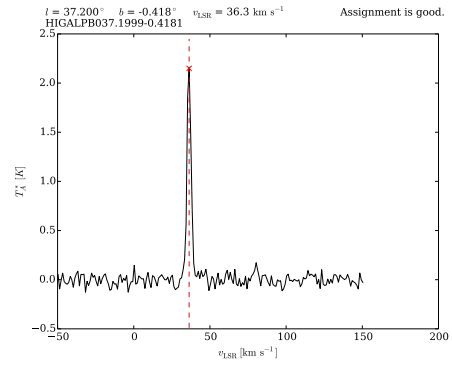
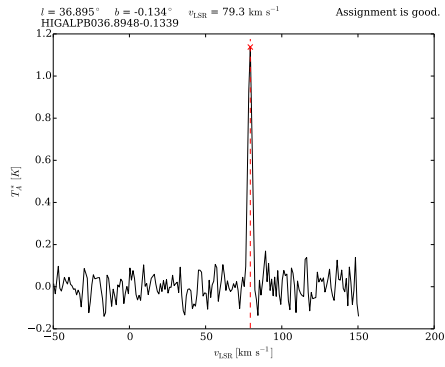
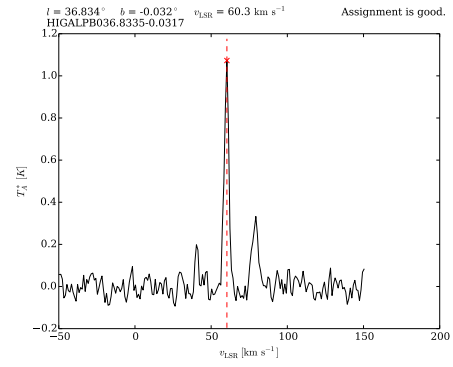
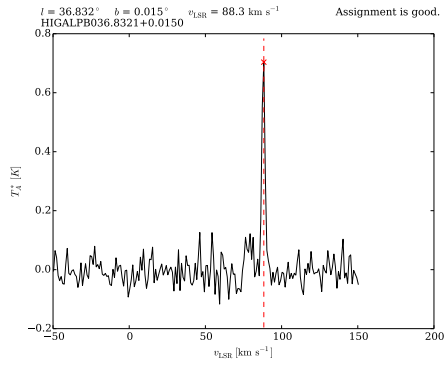


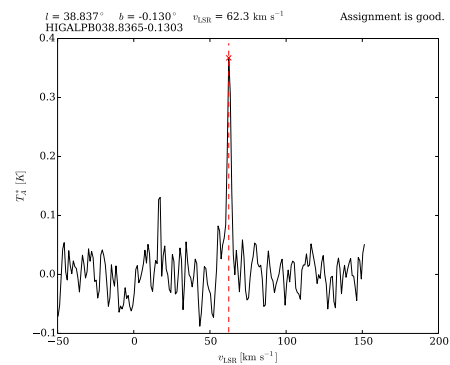
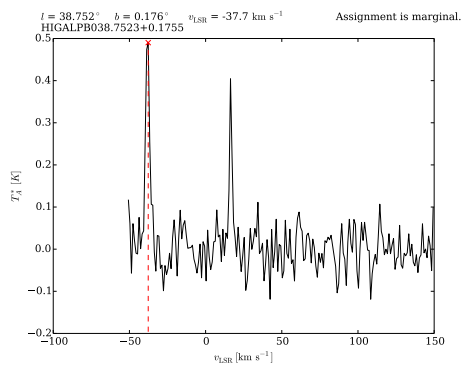
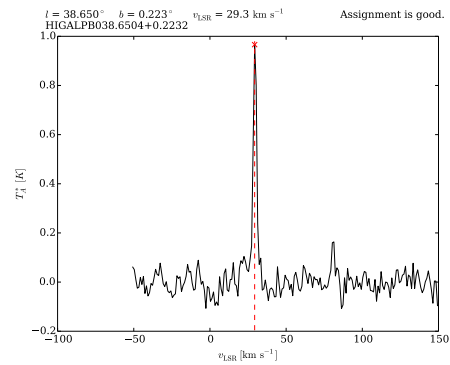
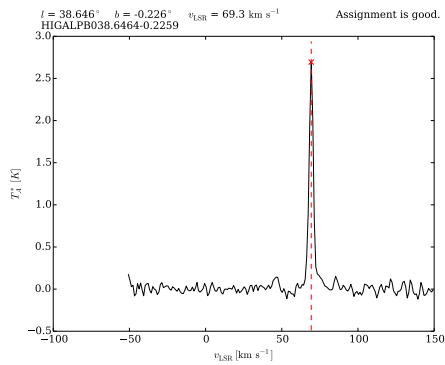
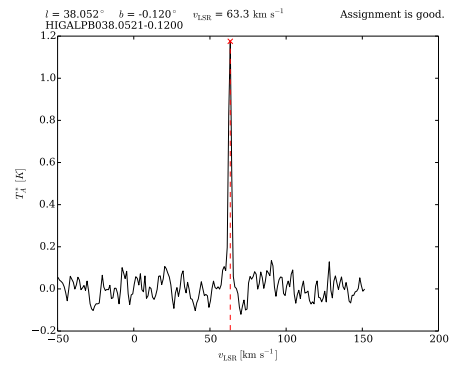
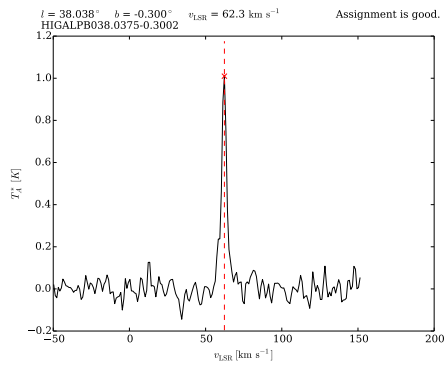
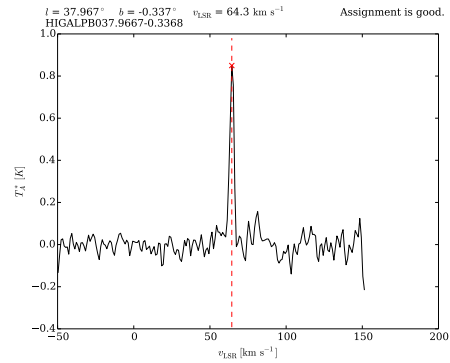
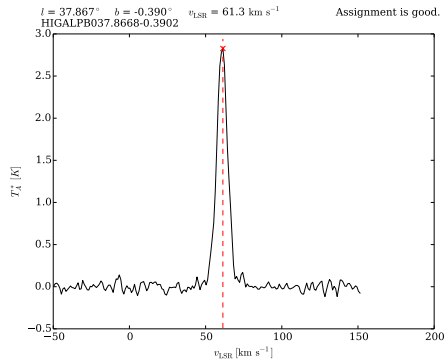
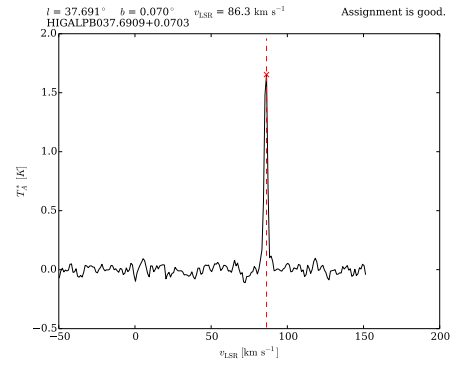
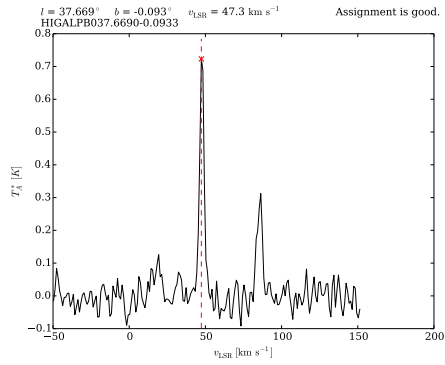


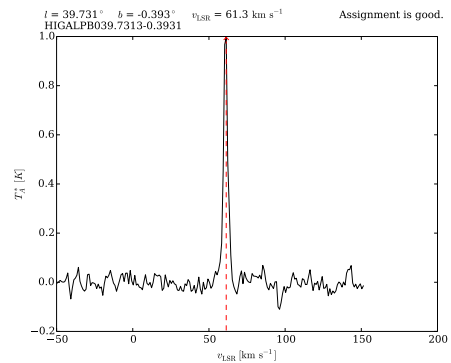
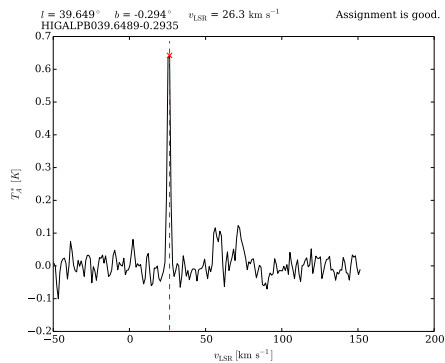
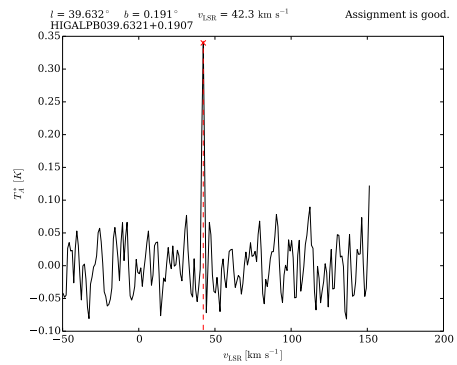
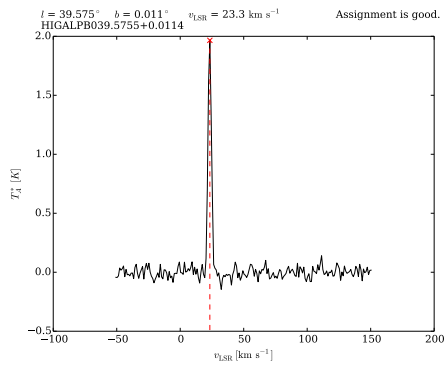
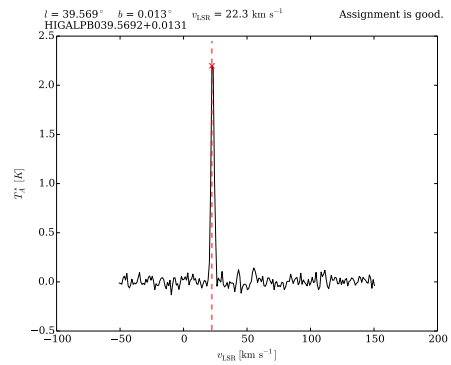
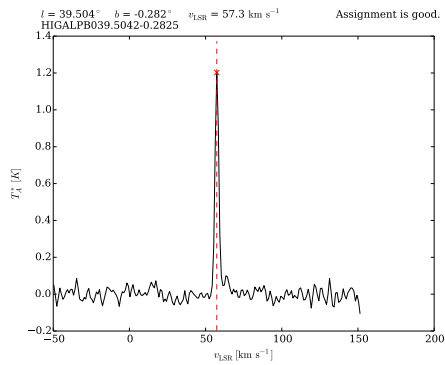
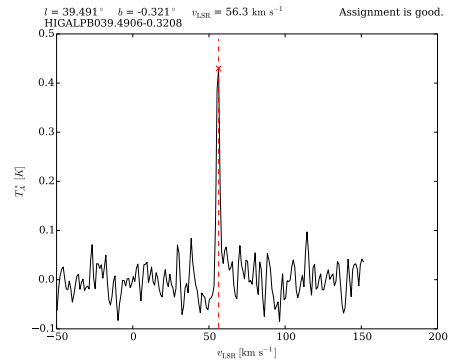
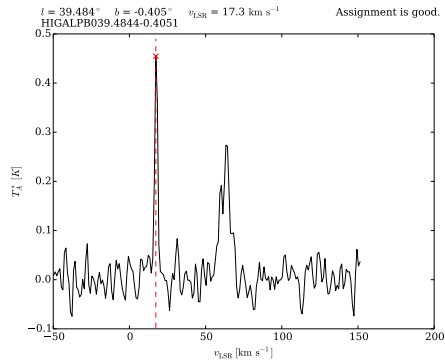
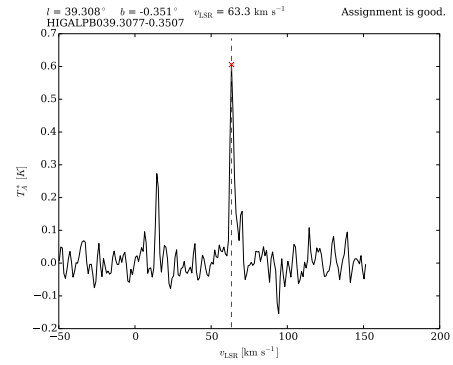
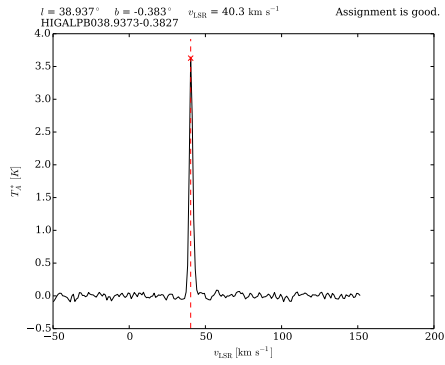


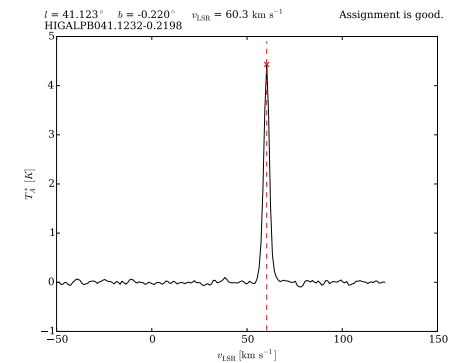
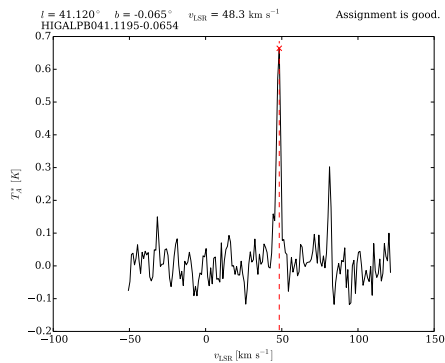
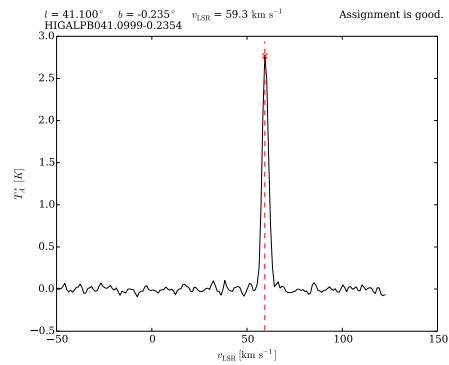
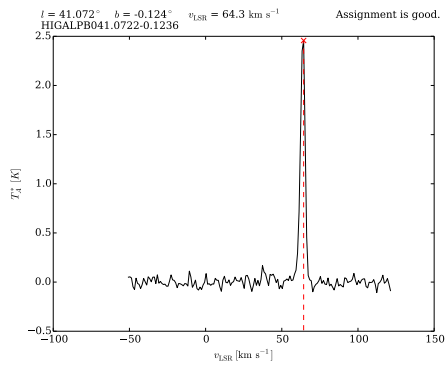
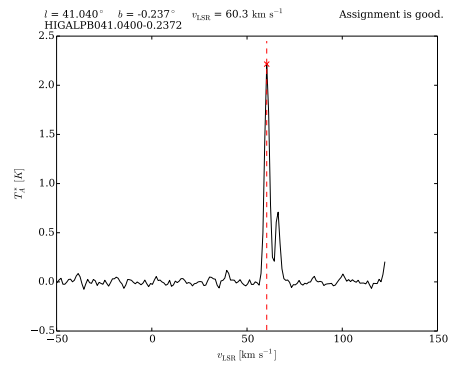
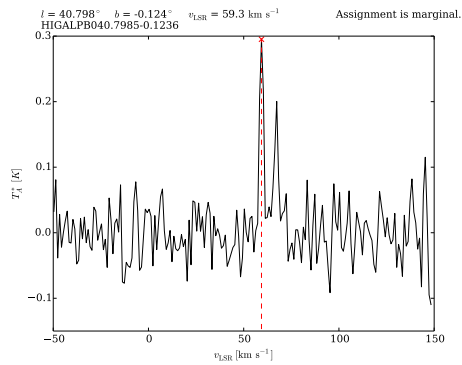
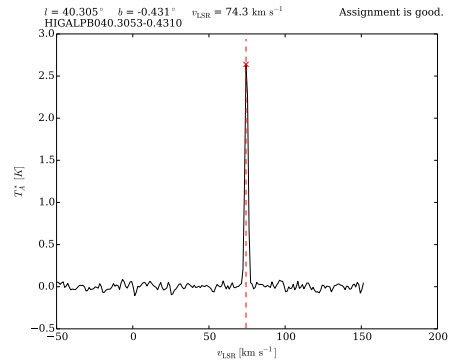
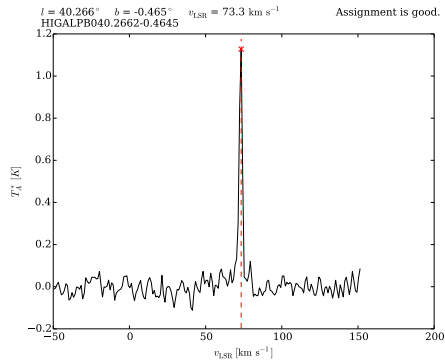
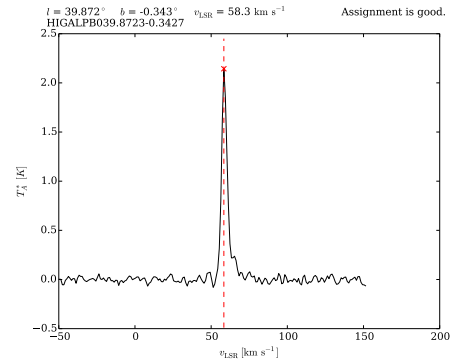
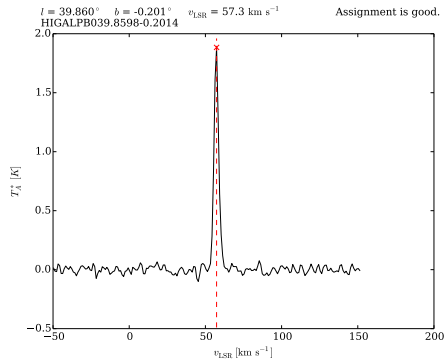


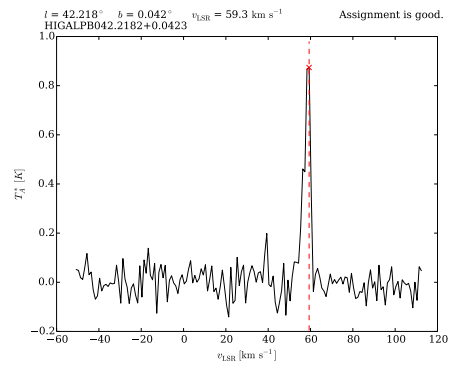
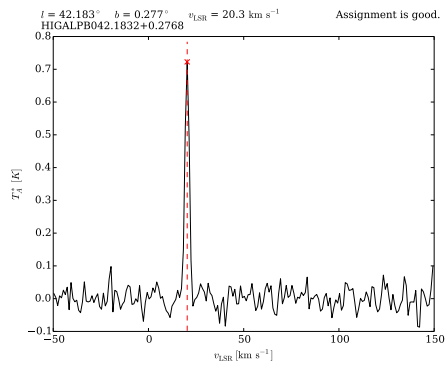
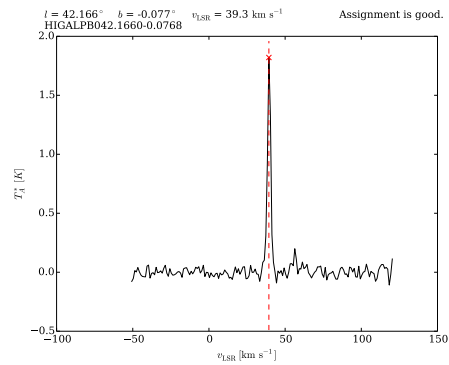
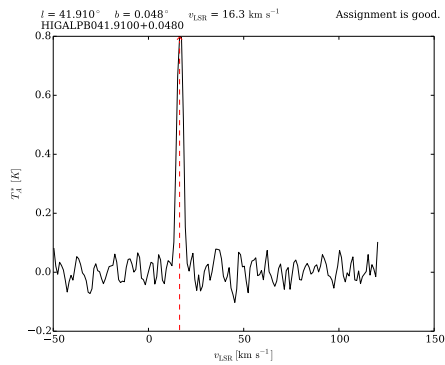
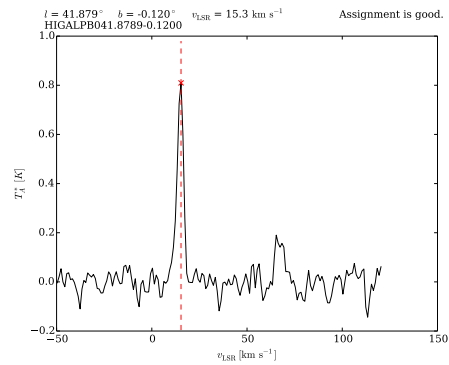
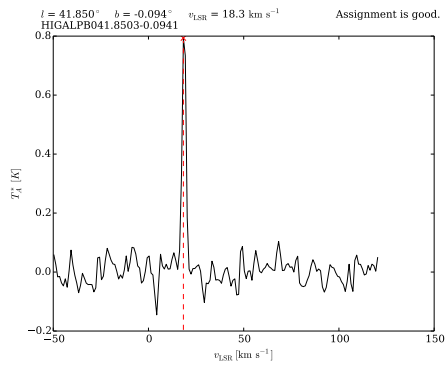
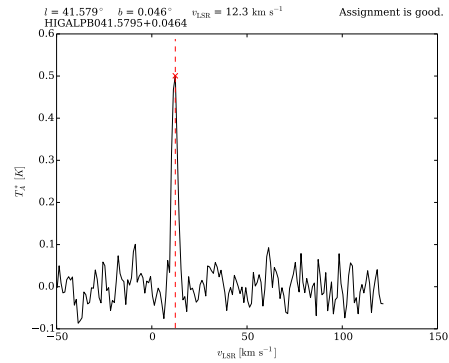
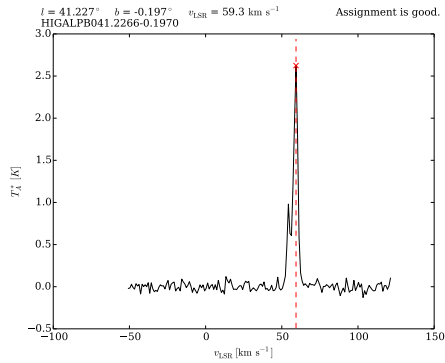
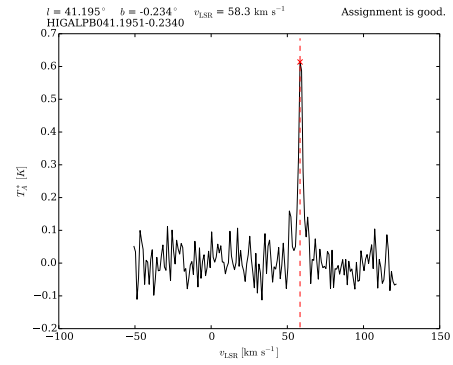
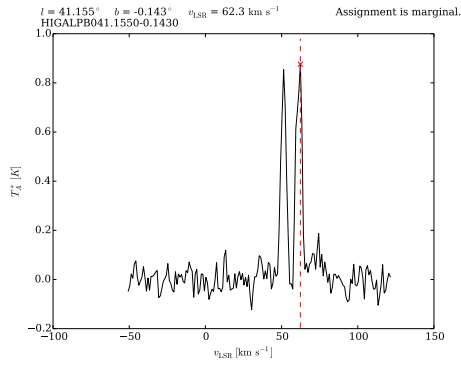


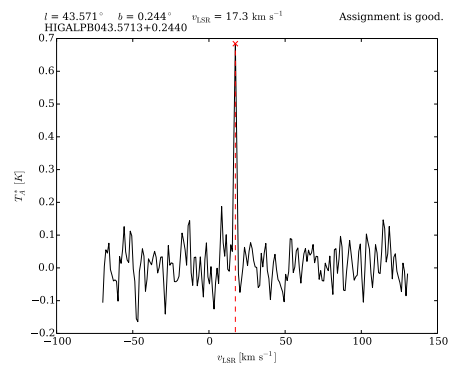
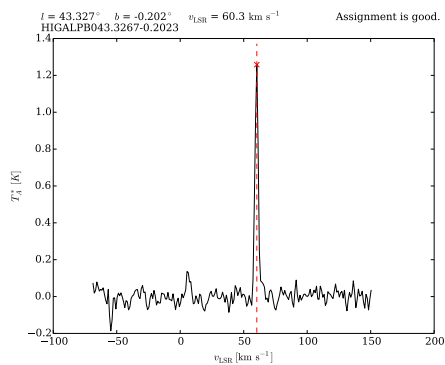
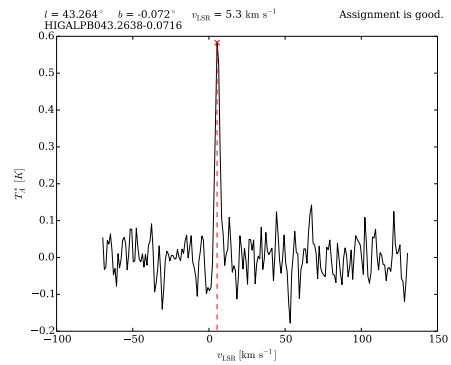
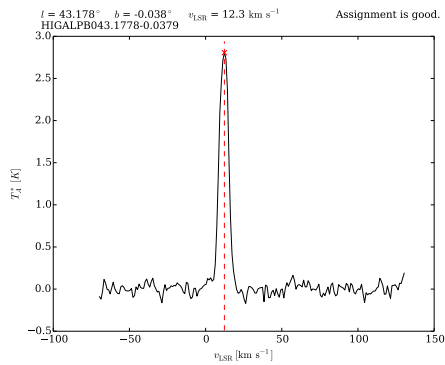
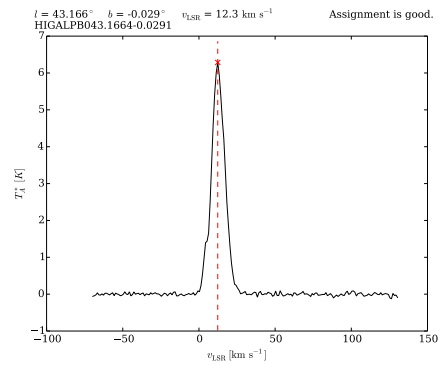
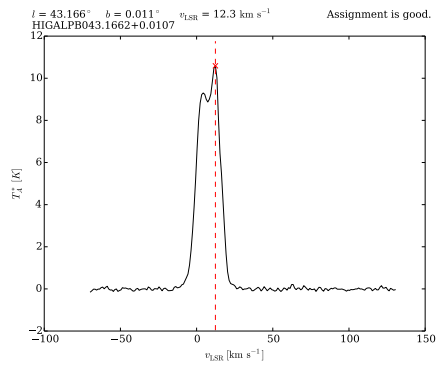
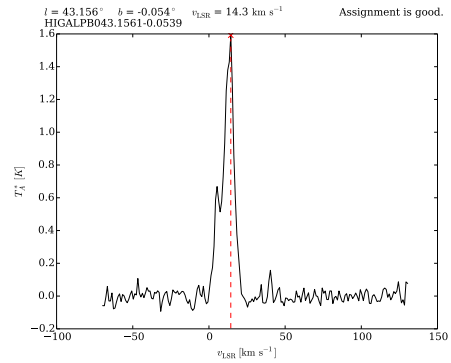
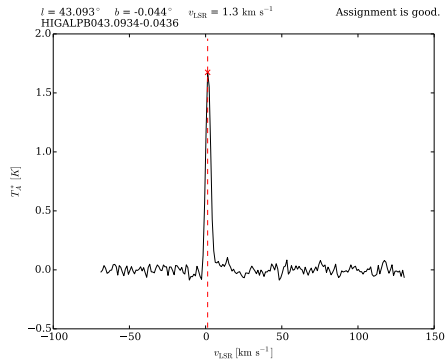
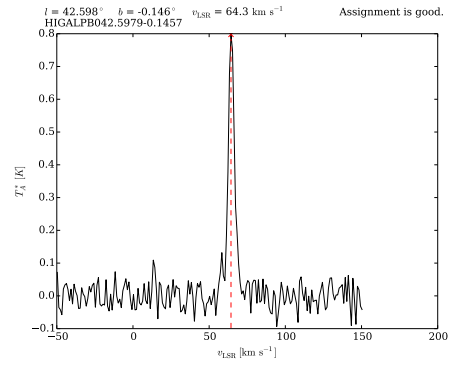
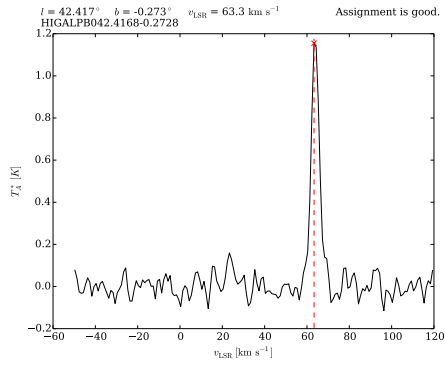


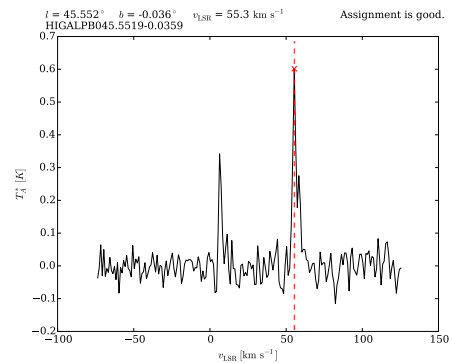
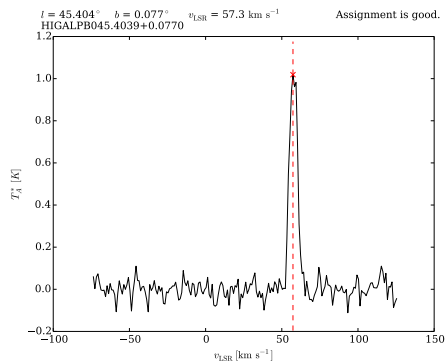
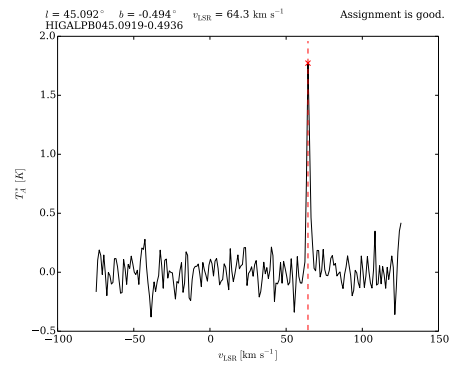
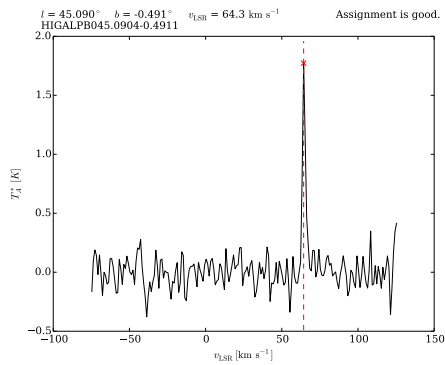
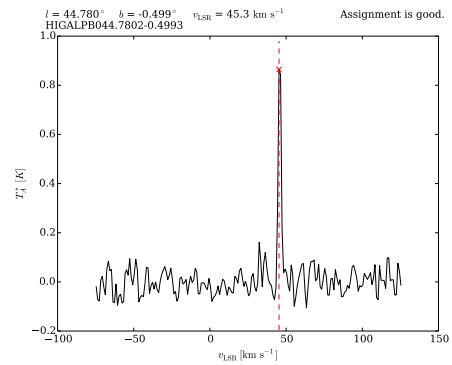
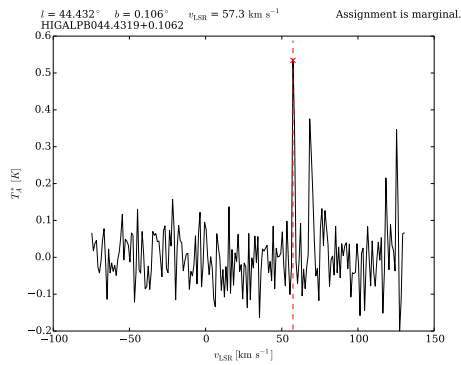
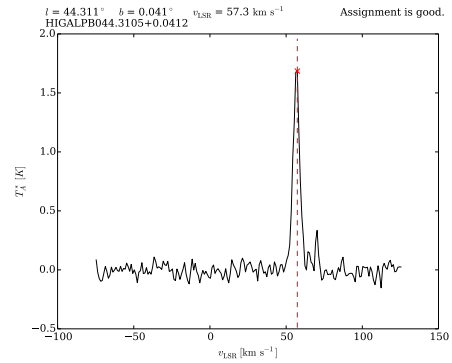
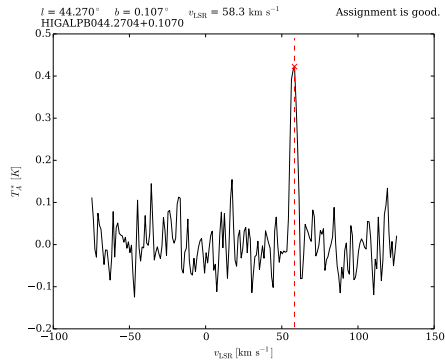
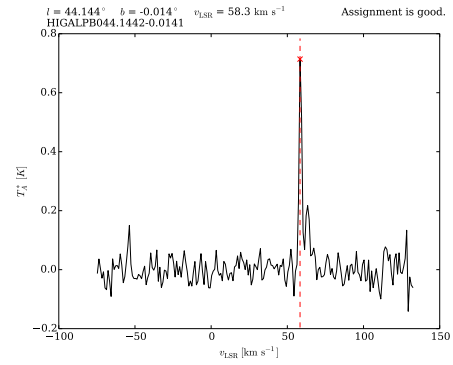
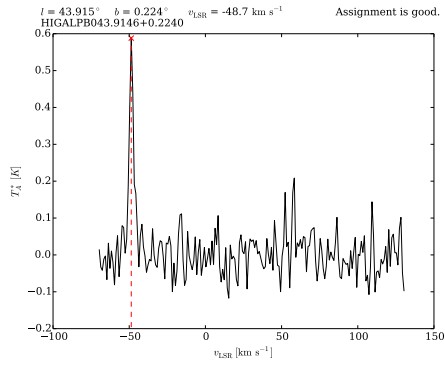












References

- Abreu-Vicente J., Ragan S., Kainulainen J., Henning T., Beuther H., Johnston K., 2016, *A&A*, 590, A131
- Aguirre J. E. et al., 2011, *ApJS*, 192, 4
- Akritas M. G., Bershady M. A., 1996, *ApJ*, 470, 706
- Allen C. W., 1973, *Astrophysical Quantities*. University of London, Athlone Press, 3rd ed.
- Amôres E. B., López-Corredoira M., González-Fernández C., Moitinho A., Minniti D., Gurovich S., 2013, *A&A*, 559, A11
- Anathpindika S. V., 2010, *MNRAS*, 405, 1431
- Anderson L. D., Bania T. M., 2009, *ApJ*, 690, 706
- André P., Di Francesco J., Ward-Thompson D., Inutsuka S.-I., Pudritz R. E., Pineda J. E., 2014, *Protostars and Planets VI*, 27
- André P. et al., 2010, *A&A*, 518, L102
- Arzoumanian D. et al., 2011, *A&A*, 529, L6
- Bahcall J. N., Bahcall S., 1985, *Nature*, 316, 706

- Baker P. L., Burton W. B., 1979, *A&AS*, 35, 129
- Bania T. M., Anderson L. D., Balser D. S., 2012, *ApJ*, 759, 96
- Barnes P. J., Muller E., Indermuehle B., O'Dougherty S. N., Lowe V., Cunningham M., Hernandez A. K., Fuller G. A., 2015, *ApJ*, 812, 6
- Bastian N., Covey K. R., Meyer M. R., 2010, *ARA&A*, 48, 339
- Battersby C., Ginsburg A., Bally J., Longmore S., Dunham M., Darling J., 2014, *ApJ*, 787, 113
- Benedettini M. et al., 2015, *MNRAS*, 453, 2036
- Benjamin R. A. et al., 2003, *PASP*, 115, 953
- Benjamin R. A. et al., 2005, *ApJL*, 630, L149
- Bergin E. A., Tafalla M., 2007, *ARA&A*, 45, 339
- Berlind A. A. et al., 2006, *ApJS*, 167, 1
- Berry D. S., 2015, *Astronomy and Computing*, 10, 22
- Berry D. S., Reinhold K., Jenness T., Economou F., 2007, in *Astronomical Society of the Pacific Conference Series*, Vol. 376, *Astronomical Data Analysis Software and Systems XVI*, Shaw R. A., Hill F., Bell D. J., eds., p. 425
- Bertoldi F., 1989, *ApJ*, 346, 735
- Bertoldi F., McKee C. F., 1992, *ApJ*, 395, 140
- Bigiel F. et al., 2016, *ApJL*, 822, L26
- Bihl S. et al., 2015, *A&A*, 580, A112

- Binney J., Gerhard O. E., Stark A. A., Bally J., Uchida K. I., 1991, *MNRAS*, 252, 210
- Bisbas T. G., Wunsch R., Whitworth A. P., Hubber D. A., Walch S., 2011, *ApJ*, 736, 142
- Blaauw A., 1985, in *IAU Symposium*, Vol. 106, *The Milky Way Galaxy*, van Woerden H., Allen R. J., Burton W. B., eds., pp. 335–341
- Blake G. A., Sutton E. C., Masson C. R., Phillips T. G., 1987, *ApJ*, 315, 621
- Blitz L., Shu F. H., 1980, *ApJ*, 238, 148
- Blitz L., Stark A. A., 1986, *ApJL*, 300, L89
- Bohlin R. C., Savage B. D., Drake J. F., 1978, *ApJ*, 224, 132
- Bolatto A. D., Leroy A. K., Rosolowsky E., Walter F., Blitz L., 2008, *ApJ*, 686, 948
- Bolatto A. D., Wolfire M., Leroy A. K., 2013, *ARA&A*, 51, 207
- Bonnell I. A., Bate M. R., 2006, *MNRAS*, 370, 488
- Bonnell I. A., Bate M. R., Clarke C. J., Pringle J. E., 2001, *MNRAS*, 323, 785
- Bonnell I. A., Dobbs C. L., Robitaille T. P., Pringle J. E., 2006, *MNRAS*, 365, 37
- Brand J., Blitz L., 1993, *A&A*, 275, 67
- Brand J., Wouterloot J. G. A., 1995, *A&A*, 303, 851
- Breen S. L., Ellingsen S. P., Caswell J. L., Green J. A., Voronkov M. A., Avison A., Fuller G. A., Quinn L. J., 2016, *MNRAS*, 459, 4066

- Breen S. L. et al., 2014, MNRAS, 438, 3368
- Breen S. L., Ellingsen S. P., Caswell J. L., Green J. A., Voronkov M. A., Fuller G. A., Quinn L. J., Avison A., 2012a, MNRAS, 426, 2189
- Breen S. L., Ellingsen S. P., Caswell J. L., Green J. A., Voronkov M. A., Fuller G. A., Quinn L. J., Avison A., 2012b, MNRAS, 421, 1703
- Breen S. L. et al., 2015, MNRAS, 450, 4109
- Brunthaler A. et al., 2011, *Astronomische Nachrichten*, 332, 461
- Buckle J. V. et al., 2009, MNRAS, 399, 1026
- Burkhart B., Lee M.-Y., Murray C. E., Stanimirović S., 2015, ApJL, 811, L28
- Byrd G. G., 1983, ApJ, 264, 464
- Carey S. J., Clark F. O., Egan M. P., Price S. D., Shipman R. F., Kuchar T. A., 1998, ApJ, 508, 721
- Caselli P., Walmsley C. M., Tafalla M., Dore L., Myers P. C., 1999, ApJL, 523, L165
- Caswell J. L. et al., 2010, MNRAS, 404, 1029
- Caswell J. L. et al., 2011, MNRAS, 417, 1964
- Churchwell E. et al., 2009, PASP, 121, 213
- Clark P. C., Bonnell I. A., 2004, MNRAS, 347, L36
- Clemens D. P., 1985, ApJ, 295, 422
- Clemens D. P., Barvainis R., 1988, ApJS, 68, 257

- Clemens D. P., Yun J. L., Heyer M. H., 1991, *ApJS*, 75, 877
- Colombo D., Rosolowsky E., Ginsburg A., Duarte-Cabral A., Hughes A., 2015, *MNRAS*, 454, 2067
- Combes F., 2000, *Advanced Series in Astrophysics and Cosmology*, 10, 143
- Commerçon B., Hennebelle P., Henning T., 2011, *ApJL*, 742, L9
- Contreras Y. et al., 2013, *A&A*, 549, A45
- Cordes J. M., 2004, in *Astronomical Society of the Pacific Conference Series*, Vol. 317, *Milky Way Surveys: The Structure and Evolution of our Galaxy*, Clemens D., Shah R., Brainerd T., eds., p. 211
- Currie M. J., 2013, in *Astronomical Society of the Pacific Conference Series*, Vol. 475, *Astronomical Data Analysis Software and Systems XXII*, Friedel D. N., ed., p. 341
- Currie M. J., Berry D. S., Jenness T., Gibb A. G., Bell G. S., Draper P. W., 2014, in *Astronomical Society of the Pacific Conference Series*, Vol. 485, *Astronomical Data Analysis Software and Systems XXIII*, Manset N., Forshay P., eds., p. 391
- Currie M. J., Draper P. W., Berry D. S., Jenness T., Cavanagh B., Economou F., 2008, in *Astronomical Society of the Pacific Conference Series*, Vol. 394, *Astronomical Data Analysis Software and Systems XVII*, Argyle R. W., Bunclark P. S., Lewis J. R., eds., p. 650
- Dale J. E., Haworth T. J., Bressert E., 2015, *MNRAS*, 450, 1199
- Dame T. M., Hartmann D., Thaddeus P., 2001, *ApJ*, 547, 792

- Dame T. M., Thaddeus P., 2008, *ApJL*, 683, L143
- Dame T. M. et al., 1987, *ApJ*, 322, 706
- Davies B., Hoare M. G., Lumsden S. L., Hosokawa T., Oudmaijer R. D., Urquhart J. S., Mottram J. C., Stead J., 2011, *MNRAS*, 416, 972
- de Vaucouleurs G., Malik G. M., 1969, *MNRAS*, 142, 387
- Dempsey J. T., Thomas H. S., Currie M. J., 2013, *ApJS*, 209, 8
- Dib S., Helou G., Moore T. J. T., Urquhart J. S., Dariush A., 2012, *ApJ*, 758, 125
- Dib S., Kim J., Vázquez-Semadeni E., Burkert A., Shadmehri M., 2007, *ApJ*, 661, 262
- Dobbs C. L., 2015, *MNRAS*, 447, 3390
- Dobbs C. L., Bonnell I. A., 2006, *MNRAS*, 367, 873
- Dobbs C. L., Bonnell I. A., Clark P. C., 2005, *MNRAS*, 360, 2
- Dobbs C. L., Bonnell I. A., Pringle J. E., 2006, *MNRAS*, 371, 1663
- Dobbs C. L., Burkert A., Pringle J. E., 2011, *MNRAS*, 413, 2935
- Dobbs C. L., Glover S. C. O., Clark P. C., Klessen R. S., 2008, *MNRAS*, 389, 1097
- Dobbs C. L., Pringle J. E., 2013, *MNRAS*, 432, 653
- Duarte-Cabral A., Dobbs C. L., 2016, *MNRAS*, 458, 3667
- Dunham M. K., Rosolowsky E., Evans, II N. J., Cyganowski C., Urquhart J. S., 2011, *ApJ*, 741, 110

- Dunham M. M., Crapsi A., Evans, II N. J., Bourke T. L., Huard T. L., Myers P. C., Kauffmann J., 2008, *ApJS*, 179, 249
- Dunham M. M. et al., 2006, *ApJ*, 651, 945
- Dwek E. et al., 1995, *ApJ*, 445, 716
- Eden D. J., Moore T. J. T., Morgan L. K., Thompson M. A., Urquhart J. S., 2013, *Monthly Notices of the Royal Astronomical Society*, 431, 1587
- Eden D. J., Moore T. J. T., Plume R., Morgan L. K., 2012, *MNRAS*, 422, 3178
- Eden D. J., Moore T. J. T., Urquhart J. S., Elia D., Plume R., Rigby A. J., Thompson M. A., 2015, *MNRAS*, 452, 289
- Ellsworth-Bowers T. P. et al., 2013, *ApJ*, 770, 39
- Ellsworth-Bowers T. P., Rosolowsky E., Glenn J., Ginsburg A., Evans, II N. J., Battersby C., Shirley Y. L., Svoboda B., 2015, *ApJ*, 799, 29
- Elmegreen B. G., 1979, *ApJ*, 231, 372
- Elmegreen B. G., 2000, *ApJ*, 530, 277
- Elmegreen B. G., 2007, *ApJ*, 668, 1064
- Elmegreen B. G., Elmegreen D. M., 1986, *ApJ*, 311, 554
- Elmegreen B. G., Lada C. J., 1977, *ApJ*, 214, 725
- Elmegreen B. G., Scalo J., 2004, *ARA&A*, 42, 211
- Falgarone E., Phillips T. G., Walker C. K., 1991, *ApJ*, 378, 186
- Feast M., Whitelock P., 1997, *MNRAS*, 291, 683

- Federrath C., 2016, MNRAS, 457, 375
- Fitzpatrick E. L., 1999, PASP, 111, 63
- Fixsen D. J., 2009, ApJ, 707, 916
- Flower D. R., Pineau Des Forêts G., Walmsley C. M., 2006, A&A, 449, 621
- Fontani F., Giannetti A., Beltrán M. T., Dodson R., Rioja M., Brand J., Caselli P., Cesaroni R., 2012, MNRAS, 423, 2342
- Foyle K., Rix H.-W., Walter F., Leroy A. K., 2010, ApJ, 725, 534
- Frerking M. A., Langer W. D., Wilson R. W., 1982, ApJ, 262, 590
- Fukui Y. et al., 2014, ApJ, 780, 36
- Fukui Y. et al., 2016, ApJ, 820, 26
- Furukawa N., Dawson J. R., Ohama A., Kawamura A., Mizuno N., Onishi T., Fukui Y., 2009, ApJL, 696, L115
- Galván-Madrid R. et al., 2013, ApJ, 779, 121
- Georgelin Y. M., Georgelin Y. P., 1976, A&A, 49, 57
- Gibb A. G., Jenness T., Economou F., 2013, Starlink User Note, 265
- Girart J. M., Frau P., Zhang Q., Koch P. M., Qiu K., Tang Y.-W., Lai S.-P., Ho P. T. P., 2013, ApJ, 772, 69
- Glassgold A. E., Langer W. D., 1973a, ApJL, 179, L147
- Glassgold A. E., Langer W. D., 1973b, ApJ, 186, 859
- Goldsmith P. F., Langer W. D., 1978, ApJ, 222, 881

- Goodman A. A. et al., 2014, *ApJ*, 797, 53
- Goodman A. A., Pineda J. E., Schnee S. L., 2009, *ApJ*, 692, 91
- Gould R. J., Salpeter E. E., 1963, *ApJ*, 138, 393
- Green J. A. et al., 2010, *MNRAS*, 409, 913
- Green J. A. et al., 2012, *MNRAS*, 420, 3108
- Green J. A., McClure-Griffiths N. M., Caswell J. L., Ellingsen S. P., Fuller G. A., Quinn L., Voronkov M. A., 2009, *ApJL*, 696, L156
- Hacar A., Kainulainen J., Tafalla M., Beuther H., Alves J., 2016, *A&A*, 587, A97
- Hacar A., Tafalla M., Kauffmann J., Kovács A., 2013, *A&A*, 554, A55
- Hammersley P. L., Garzón F., Mahoney T. J., López-Corredoira M., Torres M. A. P., 2000, *MNRAS*, 317, L45
- Hartmann L., Ballesteros-Paredes J., Bergin E. A., 2001, *ApJ*, 562, 852
- Heitsch F., Slyz A. D., Devriendt J. E. G., Hartmann L. W., Burkert A., 2006, *ApJ*, 648, 1052
- Hennebelle P., 2013, *A&A*, 556, A153
- Heyer M., Krawczyk C., Duval J., Jackson J. M., 2009, *ApJ*, 699, 1092
- Heyer M. H., Terebey S., 1998, *ApJ*, 502, 265
- Hillenbrand L. A., Hartmann L. W., 1998, *ApJ*, 492, 540
- Hoare M. G. et al., 2012, *PASP*, 124, 939
- Hocuk S., Cazaux S., Spaans M., 2014, *MNRAS*, 438, L56

- Hodge P. W., 1983, *PASP*, 95, 721
- Hofner P., Churchwell E., 1996, *A&AS*, 120, 283
- Hollenbach D., Salpeter E. E., 1971, *ApJ*, 163, 155
- Hosokawa T., Yorke H. W., Omukai K., 2010, *ApJ*, 721, 478
- Hou L. G., Han J. L., 2014, *A&A*, 569, A125
- Huchra J. P., Geller M. J., 1982, *ApJ*, 257, 423
- Inoue T., Fukui Y., 2013, *ApJL*, 774, L31
- Jackson J. M., Finn S. C., Chambers E. T., Rathborne J. M., Simon R., 2010, *ApJL*, 719, L185
- Jackson J. M. et al., 2006, *ApJS*, 163, 145
- James P. A., Bretherton C. F., Knapen J. H., 2009, *A&A*, 501, 207
- James P. A., Percival S. M., 2016, *MNRAS*, 457, 917
- Jenness T., Cavanagh B., Economou F., Berry D. S., 2008, in *Astronomical Society of the Pacific Conference Series*, Vol. 394, *Astronomical Data Analysis Software and Systems XVII*, Argyle R. W., Bunclark P. S., Lewis J. R., eds., p. 565
- Jenness T., Currie M. J., Tilanus R. P. J., Cavanagh B., Berry D. S., Leech J., Rizzi L., 2015, *MNRAS*, 453, 73
- Johnston K. G., Shepherd D. S., Aguirre J. E., Dunham M. K., Rosolowsky E., Wood K., 2009, *ApJ*, 707, 283

- Kainulainen J., Hacar A., Alves J., Beuther H., Bouy H., Tafalla M., 2016, *A&A*, 586, A27
- Kaufman M., Bash F. N., Hine B., Rots A. H., Elmegreen D. M., Hodge P. W., 1989, *ApJ*, 345, 674
- Kendrew S. et al., 2012, *ApJ*, 755, 71
- Kerr F. J., Lynden-Bell D., 1986, *MNRAS*, 221, 1023
- Kim W.-T., Ostriker E. C., 2006, *ApJ*, 646, 213
- Kimura T., Tosa M., 1996, *A&A*, 308, 979
- Kirk H., Klassen M., Pudritz R., Pillsworth S., 2015, *ApJ*, 802, 75
- Koch E. W., Rosolowsky E. W., 2015, *MNRAS*, 452, 3435
- Koda J., Scoville N., Heyer M., 2016, *ApJ*, 823, 76
- Könyves V. et al., 2015, *A&A*, 584, A91
- Kramer C., Stutzki J., Rohrig R., Corneliussen U., 1998, *A&A*, 329, 249
- Kruijssen J. M. D., Longmore S. N., Elmegreen B. G., Murray N., Bally J., Testi L., Kennicutt R. C., 2014, *MNRAS*, 440, 3370
- Krumholz M. R., McKee C. F., Klein R. I., 2005, *Nature*, 438, 332
- Kutner M. L., Ulich B. L., 1981, *ApJ*, 250, 341
- Kwan J., 1979, *ApJ*, 229, 567
- Lada C. J., Forbrich J., Lombardi M., Alves J. F., 2012, *ApJ*, 745, 190
- Langer W. D., Penzias A. A., 1990, *ApJ*, 357, 477

- Larson R. B., 1981, MNRAS, 194, 809
- Lee Y., Stark A. A., Kim H.-G., Moon D.-S., 2001, ApJS, 136, 137
- Li G.-X., Wyrowski F., Menten K., Belloche A., 2013, A&A, 559, A34
- Louvet F. et al., 2014, A&A, 570, A15
- Lucas P. W. et al., 2008, MNRAS, 391, 136
- Lumsden S. L., Hoare M. G., Urquhart J. S., Oudmaijer R. D., Davies B., Mottram J. C., Cooper H. D. B., Moore T. J. T., 2013, ApJS, 208, 11
- MacLaren I., Richardson K. M., Wolfendale A. W., 1988, ApJ, 333, 821
- Mamajek E. E. et al., 2015, ArXiv e-prints (arXiv: 1510.07674)
- Matthews L. D., Greenhill L. J., Goddi C., Chandler C. J., Humphreys E. M. L., Kunz M. W., 2010, ApJ, 708, 80
- McKee C. F., Tan J. C., 2003, ApJ, 585, 850
- Men'shchikov A., 2013, A&A, 560, A63
- Men'shchikov A. et al., 2010, A&A, 518, L103
- Menten K. M., 1991, ApJL, 380, L75
- Menten K. M., Reid M. J., Forbrich J., Brunthaler A., 2007, A&A, 474, 515
- Milam S. N., Savage C., Brewster M. A., Ziurys L. M., Wyckoff S., 2005, ApJ, 634, 1126
- Molinari S. et al., 2016, A&A, 591, A149
- Molinari S. et al., 2010a, A&A, 518, L100

- Molinari S. et al., 2010b, *PASP*, 122, 314
- Momose R., Okumura S. K., Koda J., Sawada T., 2010, *ApJ*, 721, 383
- Moore B., Frenk C. S., White S. D. M., 1993, *MNRAS*, 261, 827
- Moore T. J. T., 1989, PhD thesis, Edinburgh Univ. (Scotland).
- Moore T. J. T. et al., 2015, *MNRAS*, 453, 4264
- Moore T. J. T., Urquhart J. S., Morgan L. K., Thompson M. A., 2012, *Monthly Notices of the Royal Astronomical Society*, 426, 701
- Motte F., Schilke P., Lis D. C., 2003, *ApJ*, 582, 277
- Mottram J. C. et al., 2011, *ApJL*, 730, L33
- Myers A. T., McKee C. F., Cunningham A. J., Klein R. I., Krumholz M. R., 2013, *ApJ*, 766, 97
- Myers P. C., 2011, *ApJ*, 735, 82
- Myers P. C., Goodman A. A., 1988, *ApJ*, 329, 392
- Nagy Z., van der Tak F. F. S., Fuller G. A., Spaans M., Plume R., 2012, *A&A*, 542, A6
- Nakanishi H., Sofue Y., 2006, *PASJ*, 58, 847
- Nguyen Luong Q. et al., 2011, *A&A*, 529, A41
- Oort J. H., 1977, *ARA&A*, 15, 295
- Ossenkopf V., Henning T., 1994, *A&A*, 291, 943
- Ostriker E. C., Stone J. M., Gammie C. F., 2001, *ApJ*, 546, 980

- Padoan P., Haugbølle T., Nordlund Å., 2012, *ApJL*, 759, L27
- Padoan P., Juvela M., Goodman A. A., Nordlund Å., 2001, *ApJ*, 553, 227
- Padoan P., Nordlund Å., 2002, *ApJ*, 576, 870
- Paradis D., Dobashi K., Shimoikura T., Kawamura A., Onishi T., Fukui Y., Bernard J.-P., 2012, *A&A*, 543, A103
- Peretto N., Fuller G. A., 2009, *A&A*, 505, 405
- Peretto N. et al., 2013, *A&A*, 555, A112
- Pettitt A. R., Dobbs C. L., Acreman D. M., Bate M. R., 2015, *MNRAS*, 449, 3911
- Pickett H. M., Poynter R. L., Cohen E. A., Delitsky M. L., Pearson J. C., Muller H. S. P., 1998, *J. Quant. Spectrosc. & Rad. Transfer*, 60, 883
- Pilbratt G. L. et al., 2010, *A&A*, 518, L1
- Pillai T., Kauffmann J., Tan J. C., Goldsmith P. F., Carey S. J., Menten K. M., 2015, *ApJ*, 799, 74
- Pineda J. E., Goodman A. A., Arce H. G., Caselli P., Foster J. B., Myers P. C., Rosolowsky E. W., 2010, *ApJL*, 712, L116
- Plambeck R. L. et al., 2013, *ApJ*, 765, 40
- Planck Collaboration et al., 2011, *A&A*, 536, A1
- Poglitsch A. et al., 2010, *A&A*, 518, L2
- Polychroni D., 2010, PhD thesis, Liverpool John Moores University

- Polychroni D., Moore T. J. T., Allsopp J., 2012, MNRAS, 422, 2992
- Polychroni D. et al., 2013, ApJL, 777, L33
- Pon A. et al., 2016, A&A, 587, A96
- Purcell C. R. et al., 2013, ApJS, 205, 1
- Ragan S. E., Henning T., Tackenberg J., Beuther H., Johnston K. G., Kainulainen J., Linz H., 2014, A&A, 568, A73
- Rathborne J. M., Johnson A. M., Jackson J. M., Shah R. Y., Simon R., 2009, ApJS, 182, 131
- Rathborne J. M. et al., 2014, ApJL, 795, L25
- Reid M. J. et al., 2009, ApJ, 700, 137
- Rigby A. J. et al., 2016, MNRAS, 456, 2885
- Roberts H., van der Tak F. F. S., Fuller G. A., Plume R., Bayet E., 2011, A&A, 525, A107
- Roberts W. W., 1969, ApJ, 158, 123
- Roberts, Jr. W. W., 1972, ApJ, 173, 259
- Roberts, Jr. W. W., Stewart G. R., 1987, ApJ, 314, 10
- Roman-Duval J., Jackson J. M., Heyer M., Johnson A., Rathborne J., Shah R., Simon R., 2009, ApJ, 699, 1153
- Roman-Duval J., Jackson J. M., Heyer M., Rathborne J., Simon R., 2010, ApJ, 723, 492

- Rosolowsky E. et al., 2010, *ApJS*, 188, 123
- Rosolowsky E. W., Pineda J. E., Kauffmann J., Goodman A. A., 2008, *ApJ*, 679, 1338
- Scalo J., Elmegreen B. G., 2004, *ARA&A*, 42, 275
- Schilke P., 2016, in *EAS Publications Series*, Vol. 75, *EAS Publications Series*, pp. 227–235
- Schneider N. et al., 2013, *ApJL*, 766, L17
- Schneider N. et al., 2015, *MNRAS*, 453, 41
- Schneider N. et al., 2012, *A&A*, 540, L11
- Schneider S., Elmegreen B. G., 1979, *ApJS*, 41, 87
- Schöier F. L., van der Tak F. F. S., van Dishoeck E. F., Black J. H., 2005, *A&A*, 432, 369
- Schuller F. et al., 2009, *A&A*, 504, 415
- Scoville N. Z., Sargent A. I., Sanders D. B., Claussen M. J., Masson C. R., Lo K. Y., Phillips T. G., 1986, *ApJ*, 303, 416
- Seigar M. S., 2005, *MNRAS*, 361, L20
- Seigar M. S., James P. A., 2002, *MNRAS*, 337, 1113
- Shetty R., Beaumont C. N., Burton M. G., Kelly B. C., Klessen R. S., 2012, *MNRAS*, 425, 720
- Shu F. H., 1977, *ApJ*, 214, 488

- Sievers A. W., Mezger P. G., Bordeon M. A., Kreysa E., Haslam C. G. T., Lemke R., 1991, *A&A*, 251, 231
- Smith N., Whitney B. A., Conti P. S., de Pree C. G., Jackson J. M., 2009, *MNRAS*, 399, 952
- Smith R. J., Glover S. C. O., Clark P. C., Klessen R. S., Springel V., 2014, *MNRAS*, 441, 1628
- Smith R. J., Glover S. C. O., Klessen R. S., Fuller G. A., 2016, *MNRAS*, 455, 3640
- Sodroski T. J. et al., 1995, *ApJ*, 452, 262
- Solomon P. M., Rivolo A. R., Barrett J., Yahil A., 1987, *ApJ*, 319, 730
- Sousbie T., 2011, *MNRAS*, 414, 350
- Stahler S. W., Palla F., Ho P. T. P., 2000, *Protostars and Planets IV*, 327
- Stark A. A., Lee Y., 2006, *ApJL*, 641, L113
- Stenholm B., 1975, *A&A*, 39, 307
- Stil J. M. et al., 2006, *AJ*, 132, 1158
- Stutzki J., Bensch F., Heithausen A., Ossenkopf V., Zielinsky M., 1998, *A&A*, 336, 697
- Sugitani K. et al., 2011, *ApJ*, 734, 63
- Tafalla M., Hacar A., 2015, *A&A*, 574, A104
- Tan J. C., 2000, *ApJ*, 536, 173

- Tan J. C., Beltrán M. T., Caselli P., Fontani F., Fuente A., Krumholz M. R.,
McKee C. F., Stolte A., 2014, *Protostars and Planets VI*, 149
- Taylor J. H., Cordes J. M., 1993, *ApJ*, 411, 674
- Thompson M. A., Urquhart J. S., Moore T. J. T., Morgan L. K., 2012, *MNRAS*,
421, 408
- Torii K. et al., 2011, *ApJ*, 738, 46
- Townes C. H., Schawlow A. L., 1955, *Microwave Spectroscopy*. McGraw-Hill, NY
- Traficante A., Fuller G. A., Peretto N., Pineda J. E., Molinari S., 2015, *MNRAS*,
451, 3089
- Urquhart J. S., Figura C. C., Moore T. J. T., Hoare M. G., Lumsden S. L.,
Mottram J. C., Thompson M. A., Oudmaijer R. D., 2014a, *MNRAS*, 437, 1791
- Urquhart J. S. et al., 2012, *MNRAS*, 420, 1656
- Urquhart J. S. et al., 2014b, *MNRAS*, 443, 1555
- Urquhart J. S. et al., 2015, *MNRAS*, 446, 3461
- Urquhart J. S. et al., 2013a, *MNRAS*, 431, 1752
- Urquhart J. S. et al., 2013b, *MNRAS*, 435, 400
- Vallée J. P., 2008, *AJ*, 135, 1301
- Vazquez-Semadeni E., 1994, *ApJ*, 423, 681
- Vidali G., Roser J., Manicó G., Pirronello V., Perets H. B., Biham O., 2005,
Journal of Physics Conference Series, 6, 36

- Walsh A. J., Macdonald G. H., Alvey N. D. S., Burton M. G., Lee J.-K., 2003, *A&A*, 410, 597
- Whitworth A. P., Bhattal A. S., Chapman S. J., Disney M. J., Turner J. A., 1994, *MNRAS*, 268, 291
- Wienen M. et al., 2015, *A&A*, 579, A91
- Williams J. P., de Geus E. J., Blitz L., 1994, *ApJ*, 428, 693
- Williams J. P., McKee C. F., 1997, *ApJ*, 476, 166
- Wilson T. L., Rood R., 1994, *ARA&A*, 32, 191
- Wolfire M. G., Cassinelli J. P., 1987, *ApJ*, 319, 850
- Wolfire M. G., McKee C. F., Hollenbach D., Tielens A. G. G. M., 2003, *ApJ*, 587, 278
- Wright E. L. et al., 2010, *AJ*, 140, 1868
- Yang B., Stancil P. C., Balakrishnan N., Forrey R. C., 2010, *ApJ*, 718, 1062
- Zhang B. et al., 2014a, *ApJ*, 781, 89
- Zhang B., Reid M. J., Menten K. M., Zheng X. W., Brunthaler A., Dame T. M., Xu Y., 2013, *ApJ*, 775, 79
- Zhang Q. et al., 2014b, *ApJ*, 792, 116
- Zinnecker H., Yorke H. W., 2007, *ARA&A*, 45, 481
- Zucker C., Battersby C., Goodman A., 2015, *ApJ*, 815, 23